CRANFIELD UNIVERSITY

Michael Corsar

Tidal Turbine Modelling From the Perspective of Design and Operation

School of Water, Energy and Environment

PhD Thesis
Academic Year: 2015 - 2016

Supervisor: Dr. Joao Amaral Teixiera
June 2016

CRANFIELD UNIVERSITY

School of Water, Energy and Environment

PhD Thesis

Academic Year 2015 - 2016

Michael Corsar

Tidal Turbine Modelling From the Perspective of Design and Operation

Supervisor: Dr. Joao Amaral Teixiera
June 2016

ABSTRACT

The aim of this thesis is to study the effects of turbulent flow on a fixed pitch tidal current turbine from the perspective of turbine design and operation. A prototype turbine, Deltastream as it is known, is being developed by Tidal Energy Ltd for deployment in Ramsey Sound, Wales. It is well known that turbulence plays an important role in the fatigue life of marine turbines. Field measurements of tidal flow at the turbine site were analysed to establish the velocity spectra and turbulence intensity. This revealed a wide range of anisotropic turbulence which is dependent upon the tidal direction with intensities ranging from 5-20%.

A numerical turbine model based on momentum theory was constructed in a time marching formulation that accounts for the effects of dynamic inflow and rotationally augmented airfoil stall delay properties. The turbine rotor design allows for load alleviation by regulation of the turbine tip speed ratio. At flow velocities above the rated velocity the tip speed ratio can be increased to reduce turbine loads. The model has been combined with a novel rotor speed control algorithm that estimates unsteady turbine inflow velocity from turbine loading without the requirement for external sensing of flow speed. When the turbine is subjected to three dimensional turbulent inflow the rotor speed controller has been shown to significantly reduce the fatigue effect of unsteady, turbulent flow. The turbine blade design has been developed using the model established. Experimental validation studies were carried out at 1/16th scale in turbulent conditions.

Studies using the model have; identified the relationship between turbulence intensity and turbine fatigue load, established a controller schedule to significantly reduce fatigue loading and determined the blading fatigue life in realistic turbulent flows.

Keywords:

Turbulence, dynamic Inflow, fixed pitch turbine

ACKNOWLEDGEMENTS

I would like to thank profusely Dr. Joao Amaral Teixiera and Prof. David Mba for all their tremendous support, understanding, insight and friendship throughout this PhD.

I also greatly appreciate the support and encouragement I have received from Prof. Peri Pilidis who made it possible to finish the thesis.

Many thanks also to all my other colleagues who have been tremendously supportive and helpful.

TABLE OF CONTENTS

LIST OF FIGURES

LIST OF TABLES

LIST OF NOMENCLATURE

a - axial induction factor

a' – tangential induction factor

B – blade number

C_d – drag coefficient

C_l – lift coefficient

C_T – thrust coefficient

C_P – power coefficient

D – drag force

D_c – channel depth

k – reduced frequency

K – control gain

K_p – proportional control gain

L – lift force

L_x – eddy length scale

r - radius

U – mean axial flow velocity

u – instantaneous axial flow velocity

v - instantaneous cross-stream flow velocity

W – relative flow velocity

w - instantaneous vertical flow velocity

α – angle of attack

θ – pitch angle

ρ - density

σ - stress

τ - period

ω – angular velocity

ADCP – Acoustic Doppler Current Profiler

AoA – angle of attack

BEM – Blade Element Momentum

BM – bending moment

FE – Finite Element

RPM – revolutions per minute

TI – turbulence intensity

TKE – turbulence kinetic energy

TSR – tip speed ratio

1 Introduction

1.1 Project Aims and Objectives

The over-arching aim of this project is to assess the performance of a gravity stabilised, fixed pitch tidal turbine in turbulent flow. In conjunction with Cranfield's partner Tidal Energy Ltd, who are developing the Deltastream tidal turbine, this thesis aims to answer key questions in regard to the design and operation of the tidal turbine which will operate in a channel called Ramsey Sound. The aim of Tidal Energy Ltd is to commercialise the Deltastream to produce electricity to sell to the UK electricity network based in part on technical developments arising from this work.

The objectives of the project are as follows:

- Develop a model to analyse tidal turbine hydrodynamic loading.
- Analyse flow velocity data from Ramsey Sound in order to characterise the turbulent flow conditions in and implement a strategy to model it.
- Develop an improved turbine design that delivers enhanced performance using the modelling technique.
- Validate the model with literature sources and through experimental testing.
- Develop a control methodology to control peak and fatigue loads
- Establish design and operational modifications that will enhance performance, operability and fatigue life.

1.2 Thesis layout

The thesis is split into six chapters; 2) Literature Survey, 3) Methodology, 4) Model Validation, 5) Modelling of Turbine Operation and 6) Conclusions. The literature survey covers key aspects of the fundamentals of turbulent flow in relation to marine currents and outlines the state of the art in measurement techniques and analysis in tidal channels. It also covers techniques used in modelling tidal turbines and methods used in other industries that are applicable to this field. The final part of the literature survey describes composite material behaviour in the harsh marine environment. The thesis methodology outlines construction of the engineering models that make up the building blocks of the code developed to analyse turbine loading in turbulent flow conditions. The steps used to validate this code are described in Chapter 4 which includes a wide variety of literature sources plus experimental testing of a laboratory scale turbine test rig developed by the author. The validated model is then employed to run simulations to replicate Deltastream operating conditions from the perspective of operability, performance and fatigue life. Turbulence data from field measurements gathered at the turbine site are used to provide a set of realistic flow conditions in which to test the functioning of the Deltastream to assess its strengths and weaknesses. This includes a study on the fatigue performance in turbulent flow conditions. The thesis is concluded in Chapter 6 where the significant findings from the process are summarised.

1.3 Project Methodology

The methodology of the project is as follows:

- A literature survey covering the state of the art in tidal turbine design was carried out to ascertain the ongoing areas of research within the field. This was followed by a detailed survey of literature on marine flows and turbulence, turbine rotor modelling techniques and theory of composite materials

- Flow data from field measurements carried out in Ramsey Sound were analysed based on the knowledge gained on turbulent flows. This analysis formalised the definition of the turbine inflow conditions for later modelling.

- In parallel with the flow analysis the hydrodynamic model was developed. The code was written in a flexible manner so that a number of engineering sub-models could be applied and an adaptable control algorithm was used that could easily be changed to suit changing control strategies.

- Once the turbulence model and turbine model were completed they were validated against numerous literature sources and also using data from a test campaign undertaken to provide experimental data of a laboratory scale version of the Deltastream turbine.

- When validation was complete the code was applied to explore the operability and fatigue life of the Deltastream prototype in conditions replicating Ramsey Sound. The relationship between the turbulence intensity and the fatigue load was studied as were alternative control strategies aimed at improving turbine operability over as wide a range of flows as possible.

As mentioned the turbine code was developed and validated so that it could be applied to study the behaviour of the Deltastream turbine in turbulent flow. Figure 1 shows a simplified, high level flow diagram outlining how the key elements of the model fit together. The model is fed user inputs in the form of a turbine design and a particular set of flow conditions. The output is the unsteady turbine blade loads that can be used in post-processing routines to analyse turbine performance, operability and fatigue life.

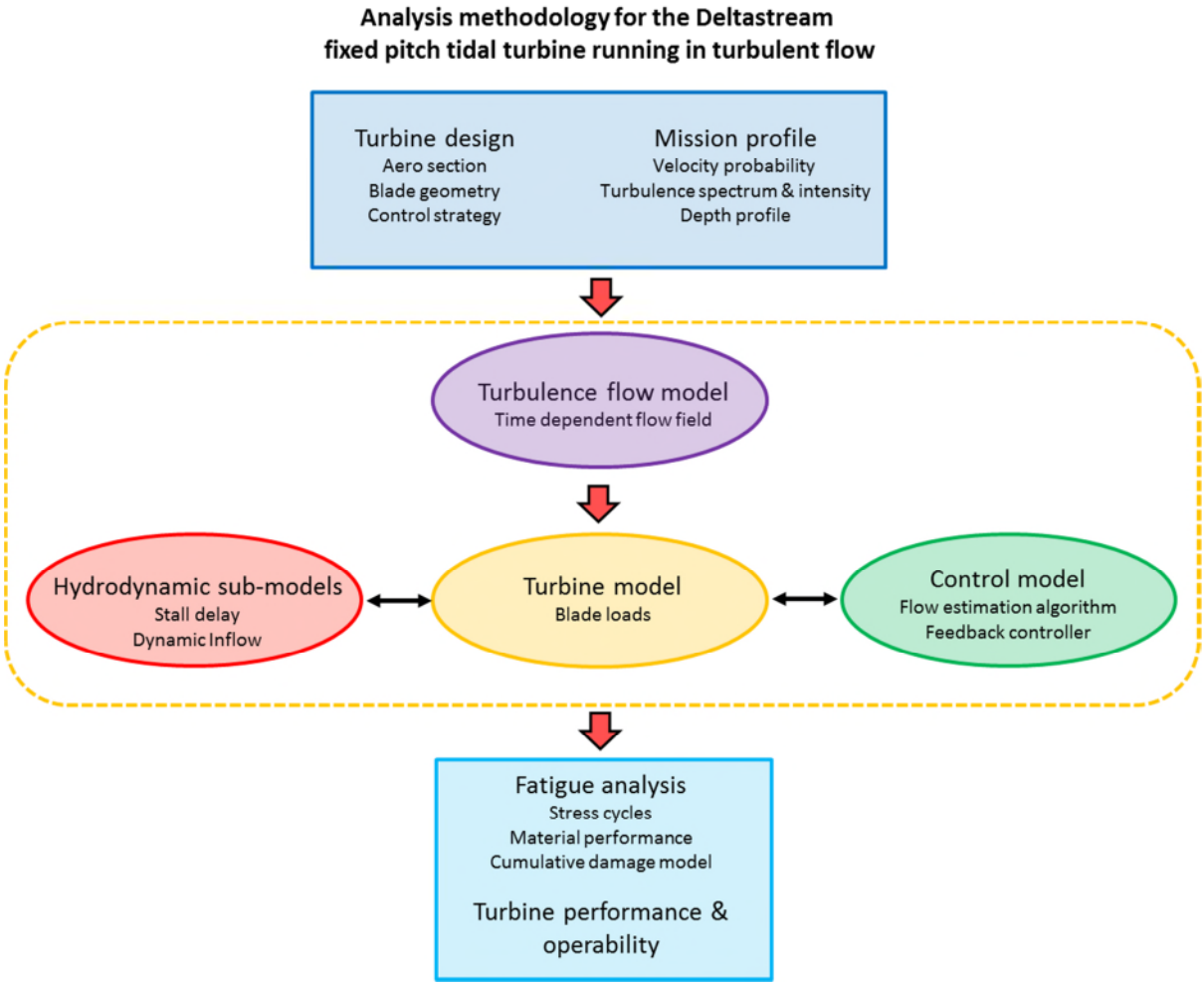

Figure 1 - Analysis methodology

The code is made up of a hydrodynamic turbine model, a turbulence inflow generator and a feedback controller. It has been found to be very flexible and accurate at determining turbine loads in turbulent flows.

1.4 Renewable Energy and Tidal Power

1.4.1 Sustainability

There has been much scientific research and political debate in recent years regarding the role of renewable energy technologies in both the UK and the world energy market as a means of providing greenhouse emission-free power.

In this debate renewable energy is defined as energy derived from naturally replenishing sources that are essentially infinite. In the case of tidal energy this energy comes from the gravitational influence that the Moon and Sun exert upon the Earth's oceans. Currently the majority of the UK's energy is the result of burning fossil fuels such as coal, oil and natural.

Modern energy policy in favour of renewables is driven by a three principle motivations. Firstly, fossil fuels are a finite resource that at some point will run out. Fossil fuels are formed by anaerobic decomposition of dead organisms over very long time scales measured in millions of years and are being used up at a much higher rate than they are being formed[1]. In 2007 approximately 88% of primary energy consumption came from fossil fuels either as coal, oil or gas[2]. Secondly, the security of a nation's energy supply is critical to the functioning of its economy. Reliance on energy imports from other countries increases risk and uncertainty within the economy. Thirdly, it is exceedingly likely that fossil fuel usage is altering the climate. The energy sector is by far the largest contributor to carbon dioxide emissions of any industry. In 2000 the world wide emissions of greenhouse gases was approximately 34 $GtCO_2e/y$, 74% of which was the result of energy production[3]. This includes electricity generation, industrial processes, domestic usage and transportation. Therefore energy reform is where the largest impact can be made in reducing CO_2 emissions.

While there is still debate over whether humans are actually changing the climate the argument for this is very robust;

- Burning fossil fuel leads to an increase in carbon dioxide levels in the atmosphere.
- Carbon dioxide is a greenhouse gas which changes the irradiance of the atmosphere thereby increasing the greenhouse effect.
- This increase leads to a rise of mean global temperatures.

Evidence that human activity is largely responsible for an increase in greenhouse gas concentration is shown Figure 2 in below.

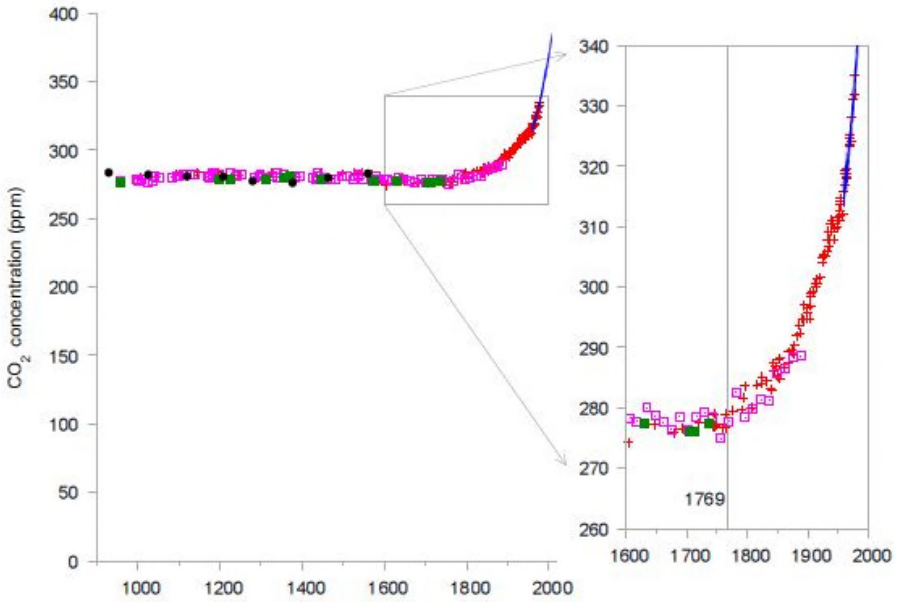

Figure 2 - Atmospheric CO2 concentration[4]

Figure 2 is a plot of CO_2 concentration in the atmosphere from 900AD until 2000AD. The data is gathered from analysis of air trapped in ice cores until 1977 and directly from the air since 1958. It is clear the concentration of atmospheric CO_2 remains constant at around 280ppm until just before1800 at which point it starts to increase. This coincides closely with the start of the industrial revolution when steam engines, powered by burning coal, started to provide energy for industry. It also corresponds with a steep rise in both world coal and oil production used in new industrial processes and a rapid increase in global population.

The effects of increasing the atmospheric concentration of CO_2 are difficult to predict but it is widely accepted that a doubling of concentration would lead to global surface warming of between 2 - 3.5°C[5]. This rise in temperature will occur over many decades or a century and will be more prominent at higher latitudes. Temperature data from the last few decades appears to confirm these predictions as shown in Figure 3. This charts four independently derived measurements of the change in land temperature with time. This shows a warming of approximately 1 degree since 1975.

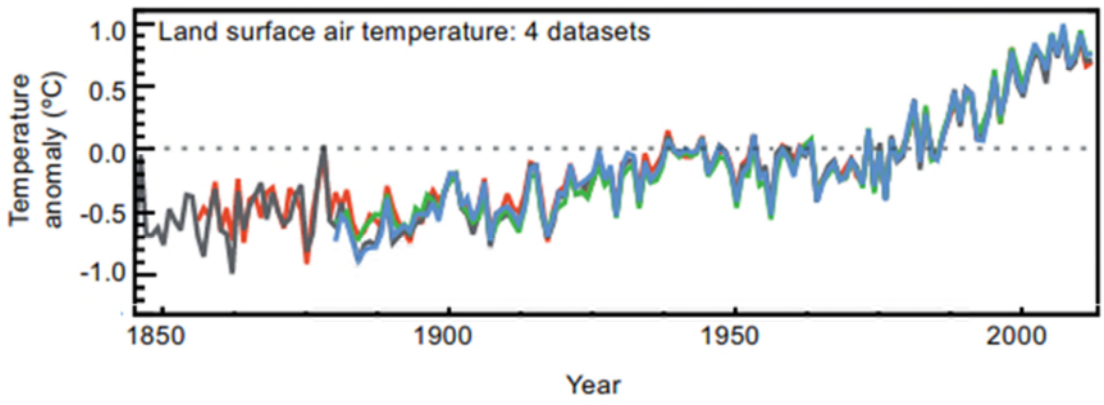

Figure 3 - Mean change in global land surface air temperature[6]

The UK government is keen to promote renewables growth as part of the solution to climate change and has developed a legislative framework that aims to support this. Marine renewable energy (wave and tidal) development is supported through a number of legislative measures, research efforts and financial incentives for developers and operators. The most prominent of these is the Renewables Obligation (RO) which was introduced as an amendment to the Utilities Bill in 2002[7] as a way to allow immature technologies to compete in the same energy market as existing fossil fuel sources.

1.4.2 Marine Energy

1.4.2.1 The tide

The tides are defined as the rise and fall of the oceans' surface under the dynamic influence of the gravity of the Earth, Moon and Sun system[8]. Newtonian or Equilibrium tidal theory draws on the concept of tidal "bulges" which form above the oceans covering the Earth's surface due to gravitational pull. Equilibrium theory assumes that the ocean covers the entire Earth's surface at a uniform depth. It does not account for the effects of land masses or the Coriolis Effect. Equilibrium theory adequately explains the two tidal cycles per day, known as the semidiurnal tidal range (M2), and the existence of spring and neap tides[9]. The moon orbits the Earth in a period of 27.3 days in the same direction as the rotation of the Earth about its polar axis. Due to the

superposition of the two bodies orbital pattern there is a complete tidal cycle approximately every 12.42 hours[10].

Equilibrium of a water particle occurs when the particle is in such a position that the gravitational potential of both the Earth and Moon act equally upon it. The Earth's potential can be expressed as:

$V_E = g\eta$

Equation 1

Here η is the height of the tidal bulge above the mean sea level.

Measurements have shown the height of the tidal bulge is typically around 0.6m above mean sea level due to the moon and around 0.3m due to the influence of the Sun. A number of tidal phenomena can be explained using this theory coupled with observations of the Sun-Moon-Earth system relative positions.

The difference in bulge height due to the Sun and Moon explains the variation in tidal range over the lunar cycle. The semidiurnal range varies over the course of approximately four weeks. At new and full moons the Sun, Moon and Earth are aligned with each other which reinforces the bulges causing Spring tides. Spring tides have a larger range than the mean tide i.e. greater amplitude high and low tides. At the end of the 1st and 3rd quarters of the lunar cycle the Sun and Moon are at 90° relative to the Earth which result in Neap tides which have a smaller range.

The moon is not in a circular orbit around the Earth and so its distance from the Earth varies with its orbital cycle thereby forcing the Spring and Neap tides. At its perigree, when the Moon is closest to the Earth, the tidal range is increased. The opposite occurs when it is at its apogee, when at its furthest position from the Earth. The result is approximately a 40% difference in tidal range over this cycle[11].

Equilibrium theory fails to account for local conditions that affect the tidal range in a specific location the most obvious of these being the influence that land masses have on the movement of the tidal bulges, which act as barriers

causing them to be diverted. Furthermore, the bathymetry of the sea bed can also significantly alter the local tidal range and phase of the tide which is highlighted in Figure 4 below.

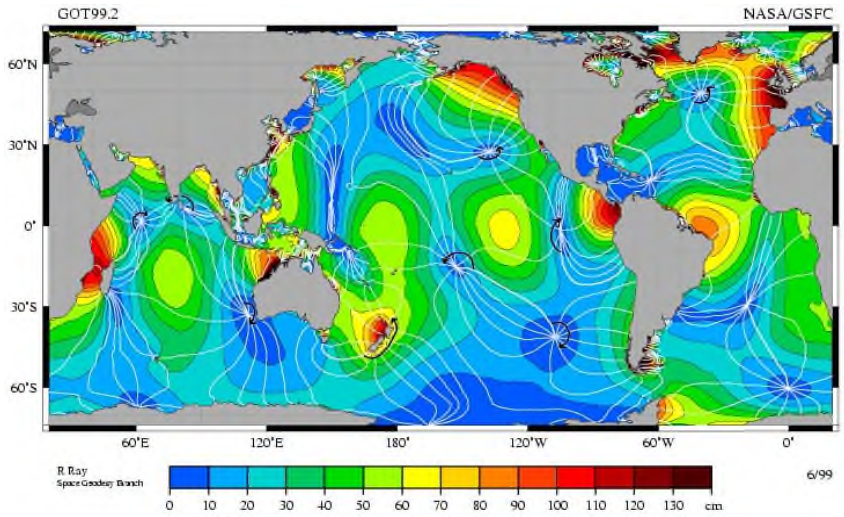

Figure 4 - Global tidal ranges[12]

This shows the range of the principle lunar semidiurnal constituent at different locations around the globe i.e. the range over a half day tidal cycle. This shows how the land masses greatly complicate the tidal range and change the phase of the tide. The white contours show lines of constant tidal phase i.e. where the tide is at the same point in its cycle. A further complicating factor is the Coriolis Effect which affects the tidal range in enclosed basins and channels. The UK and the West coast of France have some of the highest tidal ranges in the world.

1.5 The tidal resource

1.5.1 Energy potential

Tidal energy is in the form of long duration waves that travel from the deep oceans to shallow coastal seas and eventually hit land. This energy is mainly dissipated through turbulent mixing. The rate of energy dissipation in the Earth's

shelf seas is on average 2.5TW[13]. There are a number of estimates of the total flux arriving on the NW European shelf ranging from 215GW[14] to 250GW[15]. Most authors agree that it is safe to assume that there is an average flux of 200GW dissipated around the British Isles. However, studies into the power that can be feasibly harnessed surmise that it is substantially lower than the total flux. Depending upon the modelling method used studies show that the UK tidal stream average power resource lies between 2.1GW[16] and 3.9GW[17]. This leads to a figure for the technically extractable annual power of around 18TWh/yr[18]. Generally guidelines suggest that suitable tidal stream resource locations have a depth greater than 20m and a peak current of 1.5-2m/s or higher. This limits the number of individual sites around the UK suitable for tidal power extraction to approximately 40.

The average UK consumption of electrical power is approximately 40GW[19] therefore; tidal stream energy represents a resource potential of 5-10% of UK demand. Unlike wind driven renewable energy resources tidal energy is very predictable. While wind energy can only be forecast some hours ahead and wave energy by several days, it is possible to determine the flux at a particular tidal location many decades in the future. The phase, magnitude and direction of the current can all be predicted with a reasonable degree of accuracy which would be of huge benefit for scheduling power supply in a large electrical network.

1.5.2 Tidal resource description

Previous discussion has covered the cause of tidal currents and also the potential available for extraction in quite a general manner, this section covers the aspects more relevant to tidal stream power. There are three cases that describe different tidal flows from which it is technically feasible to extract power.

- The first case is a tidal current streaming through a narrow channel. As the water passes through a restriction, by continuity, the flow must accelerate thereby increasing kinetic flux. An example of such as case is the Strangford Lough Narrows in Northern Ireland where the Lough connects to the Irish Sea via a 7km channel. The channel narrows from 2.25km wide to only 500m resulting in a maximum flow speed of 3.5m/s.

- In some cases the tidal current is driven by a difference in surface elevation between two bodies of water which creates a pressure gradient in an adjoining channel. Such hydraulic currents occur if the bodies of water have tidal ranges that are out of phase with each other such as the Naruto Strait in Japan. Here there is a five hour phase lag over a short channel that creates a 1m head difference across the channel resulting in a peak current of 5m/s[20].

- The third case is due to constructive interference between waves that meet in a channel that is open to the ocean at one end. This occurs when the channel length coincides with the wave speed so that the outgoing reflected tidal wave encounters the incoming one thereby positively reinforcing each other to create a larger amplitude wave.

The theory of power extraction from the air by horizontal axis wind turbines is well established and much of it can be applied to tidal turbines. Power from the wind generally takes place in the presence of a single boundary, the ground. The relative size of the wind turbine is small compared to the atmosphere so that its presence creates a negligible reduction in the energy of the atmosphere. However, in the case of a tidal stream turbine the flow is constrained on three sides by the channel and the total energy of the flow is much closer in magnitude to that which can be extracted by the device.

Energy extraction from a tidal stream differs from the atmosphere because tidal currents are bounded, finite systems with no capacity for energy replenishment from other sources, whereas the atmospheric energy source is considered almost infinite[21]. This means that as energy is extracted from the flow the mean velocity of the flow will decrease. Therefore the greater the quantity of energy extracted from the channel (e.g. by an array of devices) the greater the

reduction in flow speed over the entire channel not just in the wake of the device[22]. This suggests there is an optimum level of power extraction that a tidal channel can support[23].

The tidal current resource is perceived as large but the magnitude of the exploitable proportion is subject to constant revision as a greater understanding of the resource is formed. As improvements in the understanding of the effects of energy extraction on the flow dynamics of a tidal current are better understood in terms of the limitations of a hydraulic channel changes are being made to the way the resource is assessed. However a widely accepted method is the Flux Methodology as applied by the Carbon Trust in their latest assessment of UK resource[24]. The Flux method results in a total resource value for each site which is the product of the time varying power flux and the cross sectional channel area. The viable percentage of kinetic flux that can be extracted from a site is determined by the Significant Impact Factor (SIF). Only a fraction of the total channel energy can be extracted without significant alteration to the flow speed. This fraction is dependent upon the type of tidal current being considered. For channels where a head difference drives a hydraulic current only up to 10% of the kinetic flux can be extracted before there are significant reductions to the flow speed. On the other hand for channels where the head is not the driving factor this value can be as high as 50%[25]. Therefore a unique SIF is applied to each potential site being examined in order to assess it individual resource.

Generally tidal resource description is represented using curves showing predictable tidal current variations far into the future which is true of the mean velocity. However, Figure 5 shows a more detailed account of tidal flow. This is a contour plot of velocity in a fast flowing tidal channel comprising several minutes of data at a sampling rate of 10Hz. The horizontal velocity is measured in mm/s and the channel depth is approximately 40m. This demonstrates that the flow contains many complex turbulent eddies with dimensions comparable to the size of a tidal energy device. In fact these eddies can be similar to the

dimensions of the turbine blades in many cases[26]. This causes a major impact on system design from the perspective of reliability and turbine control as large scale flow unsteadiness will be delivered constantly to the turbine driving high cycle fatigue. Therefore an understanding of this unsteadiness is critical in the design of tidal energy devices if there are to have a long design life.

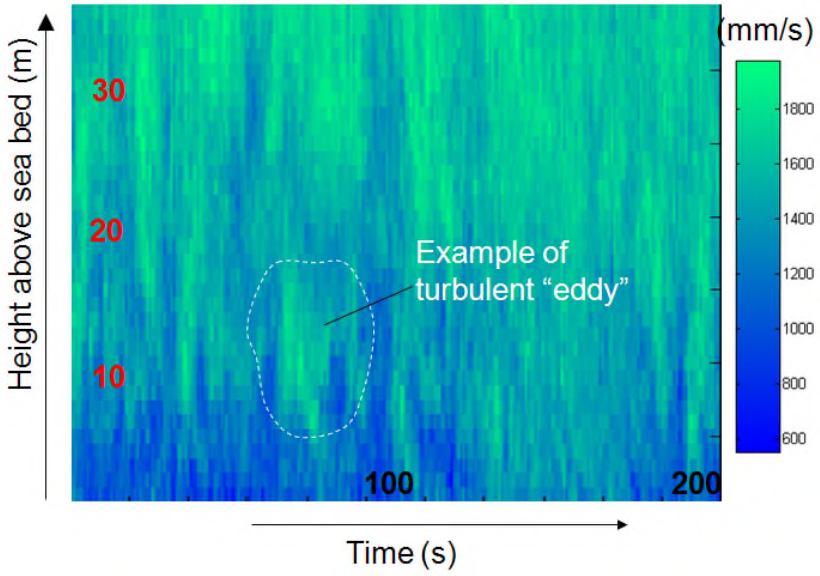

Figure 5 - Turbulence in the water column[27]

Figure 6 shows a time series taken mid-channel in the Fall of Warness, Orkney which is a site of interest for the development of tidal power systems. The measurement device sampled at 2Hz to capture the velocity variations caused by turbulence in the water. The data is measured for approximately three hours which is half a tidal cycle. The mean rise and fall in velocity consistent with the semi-diurnal cycle is evident with the mean flow cycling between zero and 2m/s. Additionally, there are significant variations over much shorter times scales which is attributable to turbulence. The turbulent fluctuations appear to fluctuate with amplitudes of 25-40% of the magnitude of the mean flow which will create considerable fluctuations in load for any turbine extracting power in this flow. The characterisation of turbulence and a discussion of the measurement techniques is described in greater detail in sections 2.2.1 and 2.2.2.

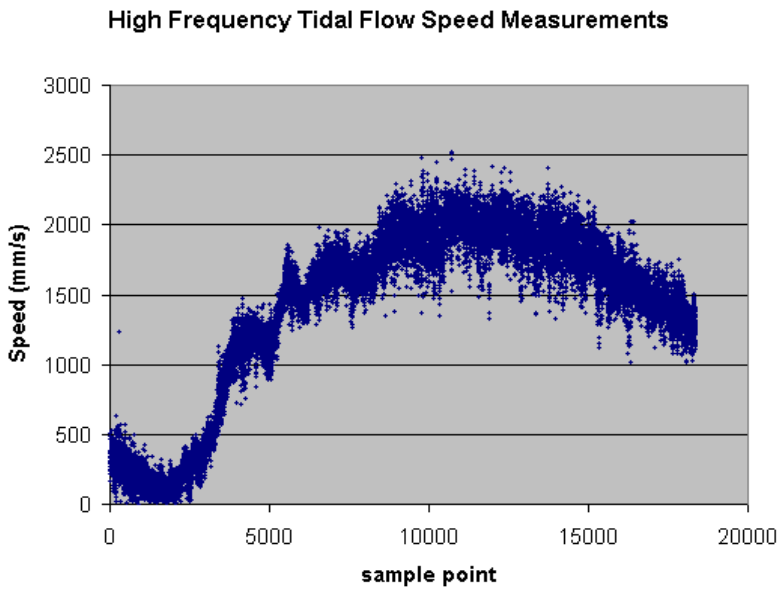

Figure 6 - Velocity fluctuations due to turbulence[28]

1.6 Tidal Stream Technology Review

1.6.1 Tidal Devices

While tidal stream turbine technology is still in its early stages there have been a variety of full scale prototype devices operated around Europe and North America. Over the last decade technical advances have moved the technology from small scale laboratory experiments to full scale prototypes and high level demonstrators operating in offshore channels. This was assisted by the opening of new facilities such as the European Marine Energy Centre (EMEC) in Orkney[29]. The aim of EMEC is to provide temporary berths for device developers to test full sized machines in a fast flowing tidal environment without having any peripheral concerns such as environmental assessments, planning applications, installation problems or connection to an electrical network.

Converting the kinetic energy of a moving fluid to electrical power is not a new challenge. Much of the basic theory from the Danish wind turbine model applies to the tidal power industry[30]. Wind power is similar to tidal power but there are significant differences in the design drivers for tidal turbines that will define the

size and strength of tidal turbines. The density of water is more than 800 times (ρ_{air} ~ 1.22kg/m^3 and ρ_{tide}~ 1025kg/m^3) that of air which leads to a more power dense working flow and hence tidal turbines are smaller machines for the same power output even though the velocity of the working fluid is much lower than in wind energy. Generally it is considered that the mean spring peak tidal velocity should be 2m/s or higher as a requirement for commercial viability. This is compared to 12-15m/s for the rated wind speed of a multi-megawatt wind turbine. Analysis of the tidal energy market shows that developers are selecting around 2.5-2.6m/s as the rated tidal velocity for their machinery. For example Tidal Generation Ltd's 'Deepgen', Marine Current Turbines Ltd's 'Seagen' and Atlantis Resources 'AK series' turbine are rated at 2.7m/s, 2.4m/s and 2.6m/s respectively and are all 1MWe machines. The ratio of wind to tidal turbine rotor diameters can be estimated by rearranging the power equation:

$$P = {}^{1}/_{2}\,\rho C_p \pi R^2 U^3$$

Equation 2

Where C_p is turbine power coefficient, R is rotor radius and U is fluid velocity. If it assumed that Cp and P is be equal for both wind and tidal devices this can be re-written as the ratio of the radii of wind turbine to tidal turbine as follows:

$$\frac{R_W}{R_T} = \sqrt{\frac{\rho_T}{\rho_R}\left(\frac{U_T}{U_W}\right)^3}$$

Equation 3

A wind turbine will therefore have a diameter three times larger for the same output power considering the aforementioned densities and velocities. This non-dimensional analysis can be extended further to consider the thrust ratio of wind versus tidal turbines. If it is assumed that the power coefficient of both machines is identical and from momentum theory it is known that peak power that can be extracted from a moving fluid is when axial induction factor, a = 0.3 i.e. the flow in the free stream is reduced by 30% after passing through the rotor plane. Furthermore, as power is the product of thrust and velocity it can therefore be estimated that the tidal turbine thrust load will be approximately 4.6 time higher

than for the wind turbine (when both turbines are running in their respected rated flows)[29]

There are several distinct tidal stream device concepts currently under development; vertical and horizontal axis turbines plus linear lift flap devices. As was seen with the development of the wind industry it is the horizontal axis devices that appear to be the most successful. Horizontal axis turbines come in a variety of forms but are by far the furthest developed of any concept. They can be split into three categories; 1- floating but moored to the sea bed, 2- gravity base resting on the sea bed or 3- mounted on foundations in the sea bed. Furthermore some designs employ a duct around the rotor in an effort to increase device performance.

The following is a list of examples of leading horizontal axis devices at various stages of development[31]:

- SeaGen developed by Marine Current Turbines Ltd is a full scale prototype mounted on monopole foundations in Strangford Lough (N.I.). It is a twin rotor system with an installed capacity of 1.2MW delivered by two twin bladed rotors. It achieves bi-directional operation through pitch control of the blades. It was installed and achieved full power in 2009
- Tidal Stream Turbine developed by Hammerfest Strom AS in Norway is a 300kW, 3 bladed turbine mounted on a tripod frame with foundations. It was installed in Kvalsundet (N. Norway) in 2003 and was the world's first grid connected tidal turbine. Hammerfest Strom UK has an agreement with Scottish power to deploy a 1MW version of the original prototype.
- Free Flow Turbines developed by Verdant Power is a 3 bladed, 4.68m diameter device mounted on the river bed. There are a number of these devices deployed in the New York East River generating around 1MWh/day to the local grid.
- Open Centre Turbine developed by Open-Hydro Ltd is an open centre 6m diameter rotor in a ducting. A 250kW prototype device was installed at EMEC in 2006 and was the first to connect to the UK grid in 2008. The

latest version of the turbine was installed in 2014 and has run for 10,000hrs.

- Lunar Energy Tidal Turbine developed by Lunar Energy Ltd is a 1.2MW ducted, gravity base concept device. It uses an 11.5m diameter bi-directional rotor.
- Evopod developed by Ocean Flow Energy Ltd is a 5 bladed, floating device moored to the sea floor. In 2014 a ¼ scale mono turbine was deployed in Sanda Sound, Scotland with a 37kW rated output.
- In 2013 Alstom deployed a 1MW turbine, which was a derivative of their earlier Deepgen turbine, at EMEC. In late 2014 they reported a total cumulative export of over 1GWh. Currently a 1.4MW machine is in development.

The devices utilising sea bed foundations are the most advanced with many at the full scale prototype stage but it remains to be seen if the other concepts will prevail as the industry grows. The aim of the other concepts is to avoid expensive marine foundations in order to produce electricity at a lower cost but therefore have to overcome the large loads imposed by the marine environment in other ways. Furthermore due to the nature of the location in which they operate successful devices will be those that can achieve a cheap system of maintenance in the hostile environment[32].

1.7 The Deltastream Turbine

The Deltastream turbine is a concept device being developed by Tidal Energy Ltd. Cranfield University has undertaken consultancy work on aspects of the rotor turbomachinery design and control system. The Deltastream concept is a gravity stabilised device that will rest on the sea-bed with no positive anchorage or foundation system to hold it in place. Figure 7 shows a full scale commercial device concept drawing which has three turbine nacelles mounted upon a steel triangular frame with a total rated capacity of 1.2MWe. Each rotor will have a diameter of approximately 15-18m and be rated at 400-500kW in a 2m/s tide.

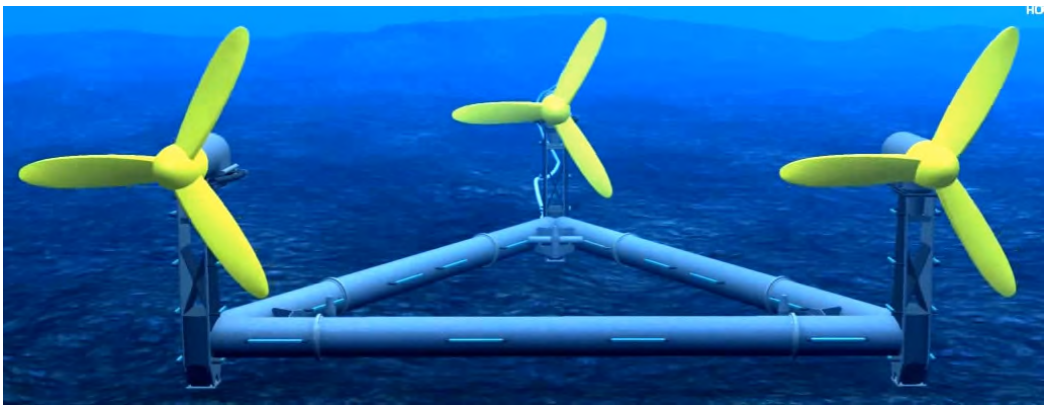

Figure 7 - The Deltastream Turbine [33]

The device will rest in a tripod configuration on three feet and will be held in place under its own weight. The combined weight of the steel frame, towers, nacelles and rotors will be in the region of 300T or more plus the frame will be flooded with sea water. The entire device can be assembled on land and then deployed in a tidal channel using a barge to lower it to the sea bed at slack water. The device will be deployed at the northern end of a channel called Ramsey Sound (near St. David's Head, Wales) as circled in Figure 8. The Ebb tide flows North to South and the Flood tide the reverse. The Flood tide is known to be more turbulent than the Ebb due to topographical obstructions to the flow.

Figure 8 - Deltastream in Ramsey Sound[34]

In order to operate in both Ebb and Flood tides it utilises a hydraulic yaw system on each nacelle that rotates the rotor around the tower axis[35]. The blades will be fabricated from moulded glass fibre reinforced plastic composite and will be fixed to a central hub mounted to the step up gear box drive shaft. A variable speed rotor will be employed to control the turbine load and power but there will be no facility for blade pitch control. It is important to note that this is not a stall regulated design. A full description of the rotor turbomachinery design philosophy follows in Chapter 4 (section 4.2.3) where the prototype turbine design is explained. The prototype device has been constructed by Tidal Energy Ltd as shown in Figure 9 below which at this time is ready for performance testing.

Figure 9 - Prototype Deltastream tidal turbine [32]

The prototype device is a full scale development machine that is comprised of a single turbine, nacelle and tower with a modified frame designed to be a pre-commercial demonstrator that will be able to prove virtually all the design assumptions but at a lower financial risk than a three turbine machine. The three bladed rotor shown in Figure 10 below was designed by the author using a methodology which is fully explained in chapter 4. This design is the development of an early rotor which has been conceived as an initial concept to provide a starting place for design calculations. The author improved the power to thrust ratio of the original rotor based on new learning gained over the course of the project the details of which are explained in Chapter 4.

Figure 10 - Prototype Deltastream turbine rotor [32]

The drive train and slew mechanism is shown in Figure 11 below. The rotor blades are attached to a cast iron hub mounted onto the input shaft of a step up gear box which then drives onto the electrical generator. The hub and blade mounting arrangement is shown in Figure 11 below. This also shows some of the construction of the blades which are comprised of a spar cap running the full length of each blade to support the loads which is covered by a leading edge and trailing edge fairing which are moulded into an airfoil shape required to generate lift.

Figure 11 - Hub mounted blades [32]

The slew mechanism consists of two double acting hydraulic rams which yaw the rotor and drive train frame through 180 degrees allowing for three mode states. The turbine can face the Ebb flow, the Flood flow or it can be in a parked mode facing 90 degrees out of the flow which is an effective way of feathering the rotor when the turbine is not producing power. This can only be activated at slack water or at very low tidal velocities.

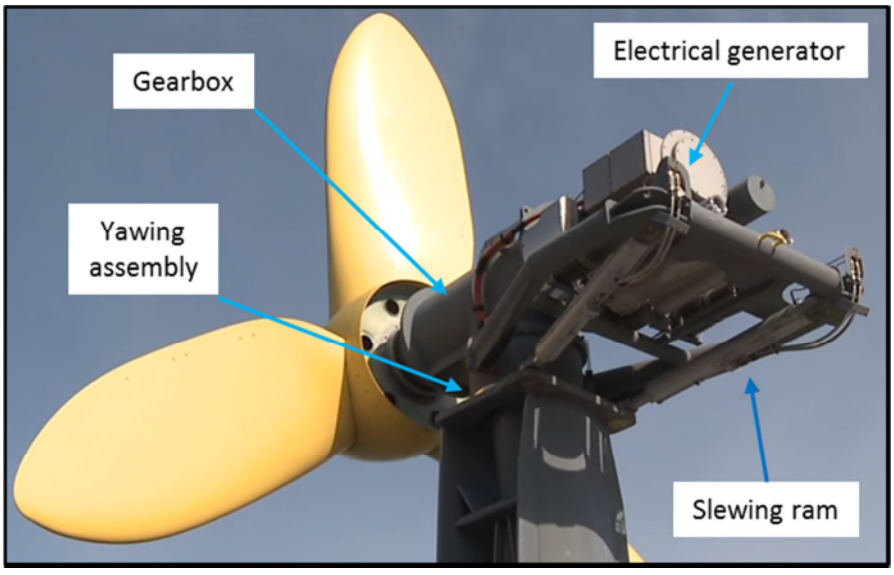

Figure 12 - Drive train and slew mechanism [32]

To ensure reliability of the friction force used to counteract the horizontal rotor thrust load the turbine frame is mounted on steel feet as shown in Figure 13

below. The feet are designed to provide high levels of friction regardless of the sea bed condition by ensuring the pressure is high at the point of contact.

Figure 13 - Tripod foot [32]

The critical design constraint on the Deltastream that must be met before full scale testing can commence is to ensure that the device remains firmly located on the sea bed. As there is no method of fixing to the sea bed the device is held in place under its own weight. Therefore the thrust force, caused by the rotor loads, must always be less than the available frictional resistance. The friction coefficient values used in this work are taken from a geographic survey of the seabed at the turbine site in Ramsey Sound carried out on the behalf of Tidal Energy Ltd by Atkins Global (Geotech). The survey established the likely minimum static coefficient of friction is 0.35 which is used throughout the rest of this work[36]. Furthermore the turbine will be subject to high levels of cyclic loading and so it is imperative the device has a robust, failsafe mechanism to quickly mitigate excessive unsteady forces.

The thrust is limited by the design of the rotor blades and the choice of operating speed. A large pitch angle has been used in the blade design as it was found that as pitch increases the turbine thrust can be reduced by increasing rotor RPM[36]. As pitch is increased the peak C_P lies at decreasing TSRs. For the highly pitched Deltastream blades the operating speed is necessarily low. There are additional benefits to reducing the turbine speed; running at lower tip speeds ensures cavitation is unlikely and furthermore it satisfies environmental concerns over blade impact with marine mammals.

A three bladed rotor was used in order to achieve a trade-off between reducing tip loss and using robust blades. Increasing rotor solidity with more blades results in a slower rotor, which reduces losses, but this requires slender blades which are susceptible to high stresses from extreme loads and impact damage from debris in the flow. The Deltastream rotor design has been validated through model scale testing in a circulating water column facility which is covered, along with the design methodology, in detail in Chapter 4.

1.8 Tidal technology research

There are a wide variety of research areas currently being pursued with the aim of further developing tidal power technology. Of particular interest to this project is the way the tidal environment interacts with the turbine rotor. Therefore a good deal of emphasis has been placed on characterising the resource and the methods used to model how this affects the tidal device. The methods listed in this section are expanded upon in later sections.

A study was undertaken using a generic 2MW turbine model to determine the sensitivity of tidal turbines to fatigue loading from waves and turbulence[37]. The study was undertaken using the GH Tidal Bladed design package that models the device for a given resource description. A time history of the blade loads was used in the fatigue life prediction method. The fatigue load criticality was then compared with the extreme loading conditions to determine which factor drives design. A combination of turbulence intensity and co-linear waves

superimposed with a range of tidal current velocities was used as the source of the unsteady fatigue loading. The result of the study was a strong correlation between fatigue damage and channel turbulence intensity and to some extent wave velocity. It highlights the importance of characterising the resource at the site and also states there will be benefits of using load mitigating control systems.

Aerodynamic models, such as BEM theory, are considered as a computationally efficient way of determining rotor performance. In order to enhance the accuracy of such models a study has been carried out into the effect the boundary conditions play in the prediction of rotor performance[38]. The study considers three models using different boundaries; 1- the standard BEM theory with no boundaries, 2- flow where all the boundaries are rigid i.e. a blockage correction and 3- a channel where the free surface can deform. In the third model by allowing the free surface to deform a more realistic downstream pressure distribution can be modelled. The type of boundaries used is most pronounced when the ratio of the channel area to rotor swept area is small. This demonstrates the importance of incorporating the boundaries when modelling an array of devices across a channel.

In addition to the classic aerodynamic models CFD (see Chapter 2) is an important tool used in the research of tidal devices. In particular it lends itself to detailed studies of the flow field around the turbine blades and has been used in conjunction with experimental studies of turbine performance[39]. A CFD model was validated against experimental data from the testing of a model scale device in order that further studies into flow separation could be undertaken without requiring more testing. The CFD simulation included a validated model of the test facilities. The study found that the Reynold's Stress Model best suited this type of simulation as it modelled anisotropic turbulence in the rotor wake. Good correlation between experimental values of rotor power and thrust were achieved using this model.

A further enhancement of the modelling methods used in the analysis of turbine rotors is in coupling the aerodynamic models to an optimisation scheme. This

approach has been used in the design of a wind turbine that delivers lower cost electricity than those that are designed using traditional methods[40]. This numerical method uses multiple design constraints in order to solve the objective function which is to find the minimum cost of energy possible. This is determined from a combination of design constraints and the extreme loads, fatigue loads and the annual energy production. The rotor shape aerodynamic model was a semi-empirical approach in order to save computational resource. Two optimisation techniques were considered; firstly sequential linear programming (SLP) and secondly the method of feasible directions (MFD). SLP was found to be fast but in some cases offered non-viable designs. In such cases the MFD approach was used as a correction to the SLP method but was not used as the primary method because of slow convergence. Based upon existing designs this technique reduced the cost of energy by around 3.5%.

Most of the methods that are used to model rotor performance are based upon the characteristics of the airfoils used for the rotor blades. Work has been undertaken on the lift, drag and cavitation behaviour of two dimensional sections that may be viable for tidal turbine blades[41]. A panel code, Xfoil, was used in conjunction with an experimental method in a cavitation tunnel to study four NACA profiles. This demonstrated that the range of applicability of the panel code was limited to low angles of incidence. Furthermore the experimental method revealed an envelope of cavitation free operation for each of the profiles tested and the conditions in the marine environment that this envelope would apply.

2 Literature Survey

This chapter looks in detail at the methods used to model turbine rotor loading, details of the turbulent fluid environment and how composite materials are affected by the marine environment.

2.1 Modelling Techniques for Helicopter, Wind Turbine and Tidal Turbine Rotors

2.1.1 The Actuator Disc Model

This simple model attributed to Betz (1926)[42] considers the rotor as a simple permeable disc that absorbs force from the flow and which simplifies much of the real flow phenomena created by the rotor. It is based on linear momentum theory and makes a number of assumptions:

1 – The flow is steady, homogeneous and incompressible

2 – There is no friction drag

3 – The turbine has an infinite number of blades

4 – There is uniform thrust over the rotor disc

5 – There is no rotation of wake flow

6 – The static pressure far up- and down-stream are equal to the ambient static pressure

The rotor extracts power by causing a step change in static pressure across the swept surface (see Figure 14). There is a decrease in flow velocity across this plane proportional to the decrease in kinetic energy of the flow (which has been transferred to the rotor).

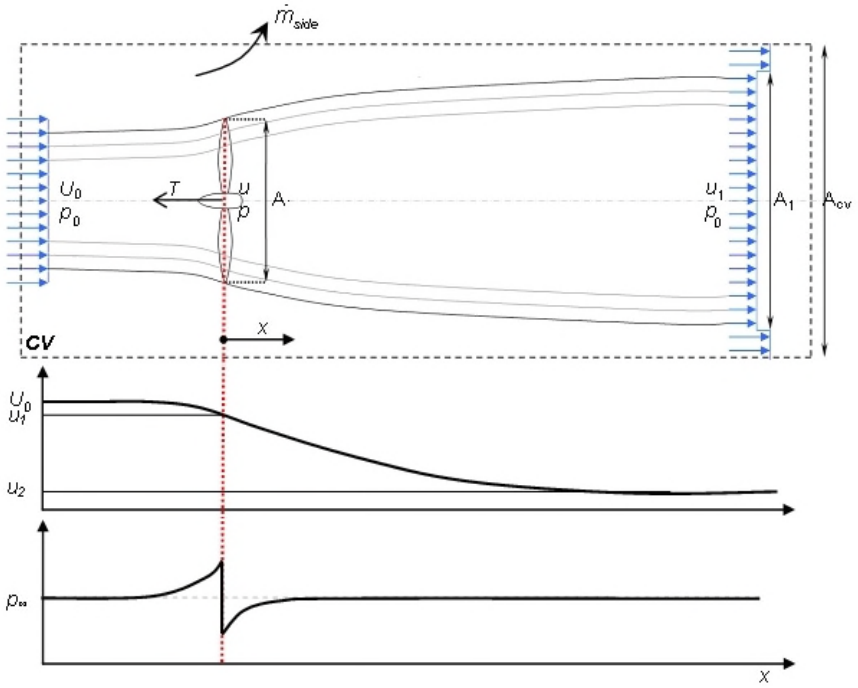

Figure 14 - Velocity and pressure across disc[43]

The static pressure rises just up-stream of the rotor as the fluid slows down. There is then an abrupt pressure drop across the plane of the rotor followed by a gradual return to the initial state in the far wake. In the control volume above, **CV** (Figure 14), it is assumed that Bernoulli can be applied upstream of the rotor and again downstream (but not across the rotor):

$$P_0 + {}^1\!/_2\,\rho U_0^2 = P + {}^1\!/_2\,\rho u^2$$

Equation 4

The net pressure on the control volume boundary is zero as it follows the streamlines. The power can be expressed in terms of the rate of momentum transfer:

$$P = \dot{m}\left({}^1\!/_2\,U_0^2 + \frac{P_0}{\rho} - {}^1\!/_2\,u_1^2 - \frac{P_0}{\rho}\right)$$

Equation 5

The power and thrust equations can be written in terms of induction factor:

$$P = 2\rho U_0^3 a(1-a)^2 A$$

Equation 6

$$T = 2\rho U_0^2 a(1-a)A$$

Equation 7

It is therefore possible to express the power, C_P, and thrust, C_T, coefficients as follows:

$$C_P = \frac{P}{1/2\,\rho U_0^3 A} = 4a(1-a)^2$$

Equation 8

$$C_T = \frac{T}{1/2\,\rho U_0^2 A} = 4a(1-a)$$

Equation 9

The C_P function is maximised when a = 1/3 which results in a maximum value of C_P = 16/27. Furthermore the C_T function is maximised when a = 1/2 as shown in Figure 15 below. This shows that the thrust coefficient can equal unity. A full derivation of these equations can be found in Manwell[42].

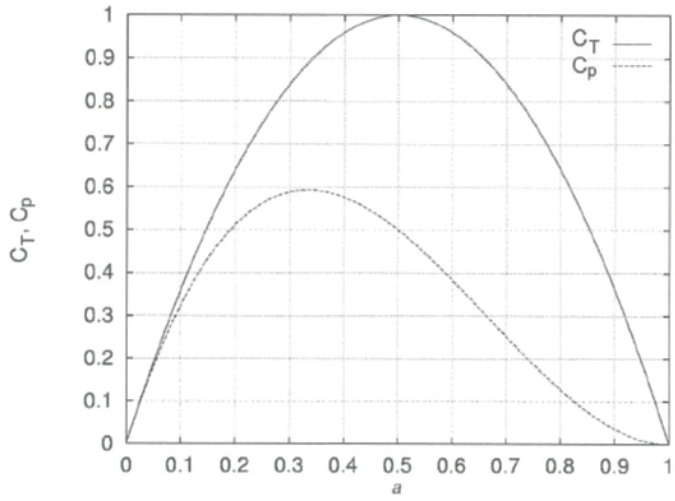

Figure 15 - Cp and Ct curves for an ideal turbine[44]

This predicts that the maximum possible efficiency of an ideal rotor is approximately 59%. When analysing a real rotor the actuator disc model is only valid between a = 0 and approximately a=0.4 otherwise the theory predicts the velocity in the wake will become negative. This model does not account for the tangential velocity component which results from the rotation of a real rotor. Momentum theory is discussed in further detail later in this chapter.

2.1.2 Vortex Wake Methods

As many fluid dynamic phenomena are essentially incompressible, isothermal, single-phase turbulent flows their governing equations can be simplified by re-writing the N-S equations in terms of vorticity which is the basis of all vortex methods. In Equation 10 below the curl of the N-S equation is written such that it gives the transport equation in terms of vorticity:

$$\frac{\partial w}{\partial t} + u.\nabla w = w.\nabla u + \nu\nabla^2 w$$ [45]

Equation 10

Where u is the three component velocity vector, ν is the kinematic viscosity and w is vorticity. Two of the benefits of this formulation are the absence of the pressure term and the automatic satisfaction of the continuity equation i.e. $\nabla.u = 0$. This allows for the simplification of numerical methods that are designed to solve the N-S equations.

In the context of turbine modelling the vortex wake method is an explicit treatment of the rotor wake that represents the wake in terms of the circulation and spatial location of vortical elements trailed from the blades into the wake and subsequently convected downstream[46]. It is assumed that the flow is incompressible and behaves according to potential flow theory. All the vorticity is concentrated within vortex filaments trailing from the blades. The induced flow velocity field is then calculated using the Biot-Savart law in order that the blade aerodynamic loads can be calculated. The Biot-Savart law is used in fluid flow problems to calculate the velocity induced by a vortex filament as follows:

$$u = \frac{\Gamma}{2\pi r}$$ [xliii]

Equation 11

Where Γ is the strength of the vortex and r is the perpendicular distance between the point of interest and the vortex line.

The method is split into two categories; prescribed wake models and free wake models. For the prescribed wake technique the positions of the vortical elements are specified before the calculation commences based upon empirical evidence[47]. This limits it to being a postdictive method as its scope is limited to being used where the conditions have previously been tested. Furthermore it is only valid for steady flow conditions.

Conversely, the free wake method is a predictive technique where the wake elements are tracked by Lagrangian markers, inherent to the discretisation scheme, and are allowed to convect and deform freely under the action of the local velocity field. The result is a much more computationally demanding model as the Biot-Savart law must be solved a great many times.

The solution to the vortex model is based on a Lagrangian discretised, finite-difference representation of the governing equations of the wake which is used to track in time the progression of the vortex elements as they convect in the wake. The convection of these elements follows the relationship:

$$\frac{d\vec{r}(\psi,\xi)}{dt} = \vec{V}\left(\vec{r}(\psi,\xi)\right)$$

Equation 12

In Equation 12 $\vec{r}(\psi,\xi)$ defines the position vector of a marker lying on a vortex filament, trailed from the blade when it was located at an azimuth angle, ψ, at time, t. The angle referenced at t_0 is $\xi = \Omega(t - t_0)$. Formally the governing equation of the free wake is written as:

$$\frac{\delta\vec{r}(\psi,\xi)}{\delta\psi} + \frac{\delta\vec{r}(\psi,\xi)}{\delta\xi} = \frac{1}{\Omega}\vec{V}\left(\vec{r}(\psi,\xi)\right)$$

Equation 13[48]

Here $\vec{V}$ is the total induced velocity of the flow field. This is the summation of the free-stream flow, the induced flow contributions from the vortex filaments plus all other sources such as turbulence. Once the induced velocity has been determined the blade loads are determined from the aerodynamic lift and drag coefficients for the blade airfoil. This method is not in wide use in the wind industry due to the difficulty in formulating a suitable integration methodology for the free vortex wake equations that is numerically accurate, stable and versatile.

2.1.3 CFD methods

Computational Fluid Dynamics (CFD) is a section of fluid mechanics that uses numerical methods to solve large fluid flow problems. Generally codes are based on some form of the Navier-Stokes (NS) equations or the Euler equations. Since the late 1990's CFD codes have been sufficiently advanced to be of practical interest for use in the wind industry. Solvers for the analysis of wind rotors have been developed from those used previously in aerospace applications but using the incompressible NS equations because of the low Mach numbers encountered in wind turbine aerodynamics[49].

It is well known that the NS equation cannot be solved directly for most practical cases and so turbulence modelling must be introduced to close the problem. In general Reynold's Averaged NS (RANS) equations are used to provide an approximate solution to the problem. The most successful turbulence model used for wind rotor modelling is the k-omega model developed by Menter[50]. It has been shown however that RANS fails to model stalled flow at high flow speeds and a move to a more accurate solution is required such as that offered by the Detached Eddy Simulation (DES)[51]. The DES is very computationally demanding as it requires much finer meshes and time accurate algorithms.

The CFD process requires a digital representation of the structure being studied in order that some form of mesh can be formed around it. For wind rotor applications to produce a high quality grid a multi-block grid configuration is

required. This allows for very small cells to be placed in the boundary layer of the blade so that the laminar sub-layer can be resolved at the high Reynold's numbers encountered over the chord of the blades[52].

The CFD technique proved itself as an invaluable tool in rotor applications during the blind comparison study organised by the National Renewable Energy Laboratory (NREL) in 2000. In this study CFD simulation results were compared with wind tunnel tests of the NREL phase VI turbine undertaken in the NASA Ames wind tunnel. One model in particular proved, a Detached Eddy Simulation model run in EllipSys 3D solver by Sorensen, to deliver results close to the results measured in the wind tunnel tests including in conditions of extreme stall[53]. CFD can also be used in the study of aerodynamic effects of geometry details including blade tips and roots which is a significant advantage over the Engineering models which are not capable of providing such details.

In an effort to reduce computational cost without sacrificing fidelity, CFD viscous solvers have been coupled with other solution methods such as potential flow codes to study, for instance, the aerodynamics of airfoils in unsteady flow. In this case the viscous model was required to resolve the turbulent boundary layer formed as a result of leading edge separation[54].

2.1.4 Blade Element Momentum Theory

The blade element momentum (BEM) theory is well established and has been used widely for modelling the behaviour of marine propellers, helicopter rotors and wind turbines. Because of their relative simplicity BEM methods are the mainstay of the wind power industry[55]. Validation studies have shown the BEM approaches can give good preliminary predictions of loads as well as an insight into factors affecting performance such as blade planform and twist[56]. Validation studies have shown that BEM models can be accurate when modelling axial conditions if blade angle of attack is small and the model being used[57]. The theory is an analytical approach for solving the rotor inflow based upon combining momentum theory and blade element theory to predict the

performance characteristics of a rotor[58]. Momentum theory is used to calculate the inflow conditions for each blade section and then blade element theory is applied to determine the fluid loads imposed by the flow conditions over the blades. The blade is modelled as a discrete number of radial nodes which form contiguous annular sections[59]. By integration of the fluid loads acting upon each section the thrust and torque of the entire blade can be determined. At each radial section thrust and torque are determined by equating the fluid momentum changes with the blade forces determined from lift and drag coefficients unique to the specific blade airfoil for a particular Reynold's number[60].

In the classical momentum approach each blade element is thought of as an independent stream-tube, the lateral boundaries of which consists of stream-lines that do not allow flow into or out of the section[61]. Furthermore the force on the blade is constant over the whole annulus which assumes the rotor has an infinite number of blades. Therefore one must, in addition to accounting for the airfoil section Reynold's number dependency, also apply empirical factors to better predict a number of radially dependent effects that can occur due to rotation and non-uniform flow fields. Real blades experience a span-wise pressure gradient caused by, for example, a roll-off in blade force towards the tips due to the tip vortex which can be corrected for by using both a tip loss factor and by including the solidity ratio[62]. A second radial effect not accounted for by classical BEM theory is the effect of boundary layer pumping that can lead to delayed stall characteristics resulting in an under prediction of power (which is discussed in more detail later in this chapter). The assumptions of momentum theory apply for axial flow conditions at low angle of attack such as for non-yawed flows and when circulations along the blades are uniform.

The BEM theory can be used to calculate the loads upon each rotor blade for a set of input conditions. These inputs include; the parametric blade geometry, aerodynamic section data (Cl and Cd) and the incident flow velocity to the rotor plane. Momentum theory is applied to determine the relative flow velocity (W) to each airfoil section then element theory is used to calculate the lift and drag forces. The forces are then integrated over the length of each blade to

determine the torque and thrust loads. In order to calculate the relative flow velocity vector so element theory can be applied, the axial and tangential induction factors, a and a', are determined by an iterative procedure described in Chapter 3.

Figure 16 shows the velocity triangles for a blade element, the plane of rotation is perpendicular to the direction of thrust.

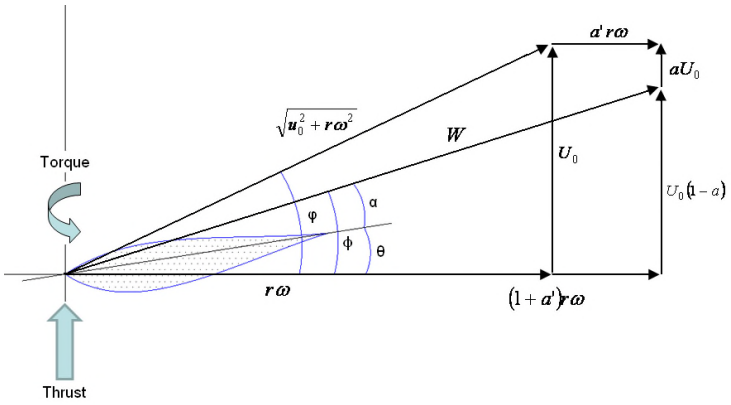

Figure 16 - Airfoil velocity triangles

Here U_o refers to the axial fluid flow velocity and rω is the velocity of the blade. The relative flow velocity over the section, W, is at a flow angle, Φ, to the plane of rotation. The flow angle is the sum of the angle of attack, α, of the airfoil and the twist angle, θ, of the blade, which changes over the length of the blade. The lift and drag coefficients are applied to the relative flow velocity and local chord in order to realise the lift and drag forces per section.

Determination of the axial and tangential flow factors is achieved computationally by iteration the detail of which is described in section 3.2.1.. In order to calculate the relative flow velocity over the section the flow angle, Φ, must be known, however this is a function of the induction factors. Therefore an initial guess of the induction factors is made and applied to the BEM algorithm. The outputs of the algorithm are the new values of the induction factors which are applied to the next iteration. Upon convergence the induction factors are

used to predict the flow angle over the section in order that the angle of attack can be determined.

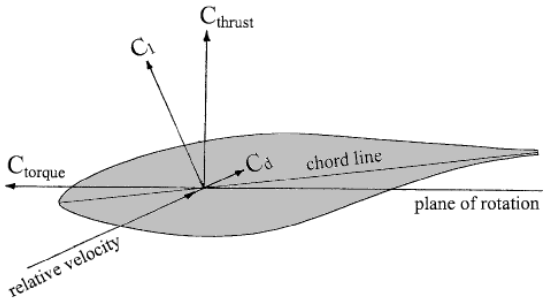

Figure 17 - Radial section loads

Figure 17 shows the load vectors as determined by element theory, where Cl and Cd are the lift and drag coefficients. The torque (Ctorque) and thrust (Cthrust) coefficients are parallel and perpendicular respectively to the plane of rotation of the blade and it is these that are used to determine the power and thrust of the rotor. This approach is applied to each element over the length of each blade and by integration over the length of each blade the total thrust and torque is determined. A full description of the BEM algorithm used by the author can be found in chapter 3.

2.1.4.1 Validity

The BEM approach has a number of limitations, the most prominent of which is its range of validity. The method works well at low and moderate tip speed ratios but becomes less reliable at high tip speed ratios where the wake expansion is large and becomes dominated by turbulence[63]. Therefore the BEM method is most effective for analysing rotor geometries around to their design point. This is when the stream-tube assumption for each radial annulus holds true because the rotor is operating in what is known as the windmill state as shown in Figure 18 below[64]. In this state the condition that streamlines carry fluid elements from the far upstream to the far downstream holds true[65]. The windmill state occurs over a range of axial induction factors from 0 to 0.4.

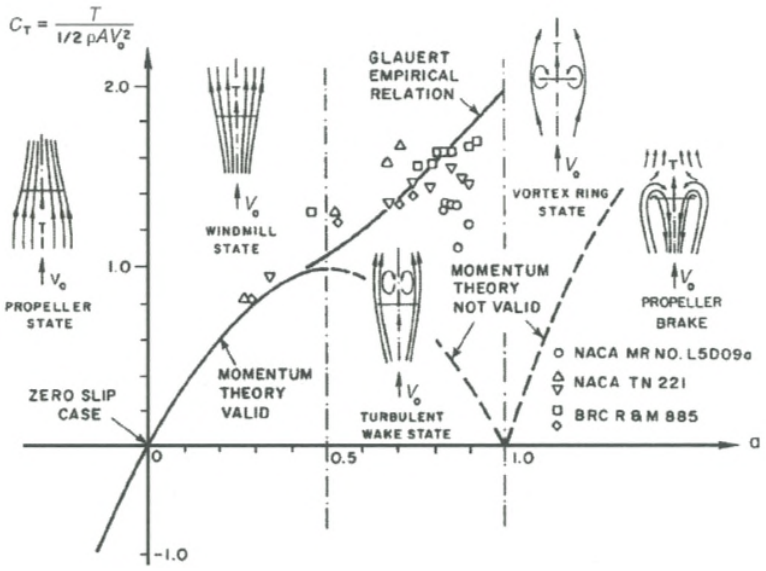

Figure 18 - Rotor states

When the turbine is heavily loaded, typically at high tip speed ratios (particularly for stall controlled machines), the rotor is said to be operating in the turbulent wake state. Here recirculation occurs in the wake, behind the blades, and the stream-tubes start to choke due to the large expansion behind the rotor[66]. This causes momentum theory to break down and further empirical relationships must be applied such as that proposed by Glauert to determine the thrust coefficient in this regime[67]. This serves to highlight the 2D nature of the model. As previously stated the model assumes each annulus section is independent of all other sections which is valid when operating in the windmill state but not when fluid from outside the wake starts mixing with fluid passing through the rotor[68]. With turbulent mixing affecting the wake the flow becomes increasingly three dimensional in nature to the point where the model is no longer a valid interpretation as the assumption that the net pressure on the control volume boundary is equal to zero no longer holds. Eventually, as the blade load continues to increase the axial induction factor reaches unity and in theory the rotor becomes impermeable to the flow[69]. This is known as the vortex ring state and represents reverse thrusting propellers. Momentum theory cannot be used

in this regime however this of little interest to tidal turbine research as rotors operating in the vortex ring state transfer energy to the flow.

2.1.5 Engineering sub-models

There are a number of augmentations that can be applied to BEM theory that can extend its range of validity, improve its accuracy and account for non-steady flow conditions such as turbulence.

2.1.5.1 Stall delay due to rotation

As previously mentioned the use of two dimensional aerodynamic section data with BEM techniques can lead to an under-prediction of peak and post peak power production in stall regulated turbines. A well-documented example of this is the UAE rotor which was tested in the NASA Ames large wind tunnel (see Chapter 4). This stems from inadequate aerodynamic modelling of the 3D effects that blade rotation impose upon a blade in stall.

Studies on the boundary layer development of wind turbine blades have shown that boundary layer separation is delayed due to rotation. The effects of rotation were first observed on test results from aircraft propeller blades[70] and has since been widely studied on helicopter and wind turbine blades[71,72]. For example Ronsten took pressure measurements on both non-rotating and rotating blades and then calculated the airfoil section coefficients for both cases[73]. Figure 19 below shows the difference between the non-rotating (NRB) and rotating (RB) cases with the lift coefficient measured at 30% of blade span. The lift coefficient of the rotating case is very clearly enhanced at the same angle of attack that the non-rotating case has already stalled and the maximum value of lift is both significantly higher and at a delayed. The effects of rotation are most pronounced in the blade root region where the angle of attack tends to be highest, by design, because of the lower rotational velocity.

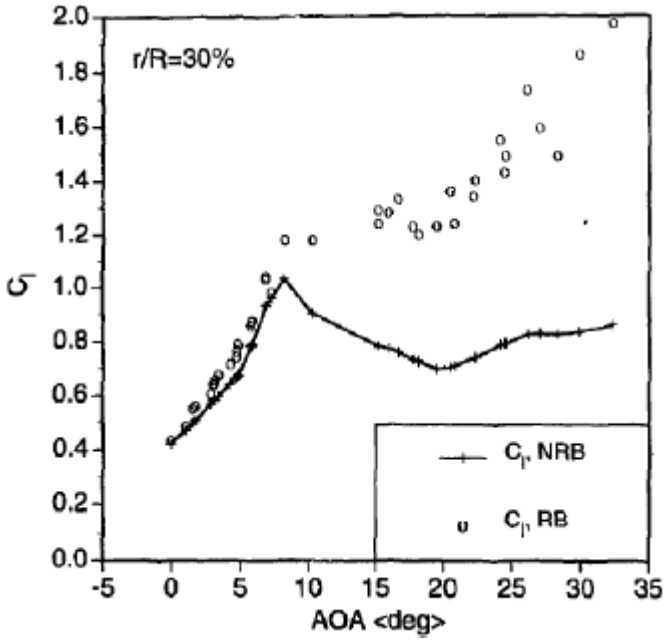

Figure 19 - Non-rotating and rotating Cl

Experimental results show that separated flow on a rotating blade has a strong radial component which is not observed when the boundary layer is attached. CFD simulations designed to replicate the experimental conditions of the NREL UAE rotor show how the flow over the blade surfaces are affected by rotation. Figure 20 shows the results of a simulation run in CFD in partially stalled conditions[74]. Here the streamlines over the suction surface show radial flow in the direction of the tip which are strongest in the root region.

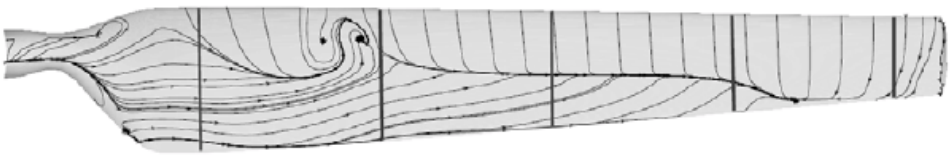

Figure 20 - UAE rotor streamlines

Rotation has two main effects; firstly it increases the radial pressure distribution along the span and secondly it introduces centrifugal and Coriolis forces in the rotating reference frame. The dynamic pressure and the centrifugal force result in a span-wise pressure gradient that directs flow in the direction of the tip[75]. The Coriolis effect, caused by the rotating frame when observed from the by the incoming flow, acts as a positive pressure gradient in the chord-wise direction

which actively delays stall and in some cases on the inboard sections of blades the boundary layer can be completely stabilised against separation[76]. When the boundary layer separates (stationary flow in the boundary layer) the radial component of flow is much larger than when attached and there is little chord-wise flow. The radial flow is not observed when the flow is attached because the fluid moves rapidly over the blade with little time for radial forces to act. However, when the boundary layer stagnates the centrifugal force has time to have a radial pumping effect when it acts on the slower moving flow resulting in enhanced lift in the stalled region[7175].

Several models have been developed to account for rotational effects based upon both experimental observations and numerical results. Analytical work shows that the centrifugal component of force is a function of the ratio of chord length to radial position (c/r)[77] and all stall delay models take this into account. These conventional models have the general form:

$$\boldsymbol{C_{l,3d} = C_{l,2d} + f_{cl}(\frac{c}{r}, \ldots)\Delta C_l}$$

Equation 14

Where $C_{l,3d}$ is the corrected lift coefficient, $C_{l,2d}$ is 2d test data, f_{cl} is a function relating c/r and other variables to the difference in C_l if the section were not to stall and the stall point from the 2d data. These models have been developed over time and have applications in helicopter aerodynamics, aircraft propellers and wind turbine blades.

One of the most established for use with wind turbine aerodynamic data is that developed by Snel. Only the lift coefficient is modified in the 3D correction which is based upon Equation 15:

$$\boldsymbol{C_{l,3d} = C_{l,2d} + A(c/r)^B\left(C_{l,lin} - C_{l,2d}\right)}$$

Equation 15

Where the coefficients A = 3 and exponent B = 2. $C_{l,lin}$ is an imagined projection of the section lift if the gradient of the C_l line remained constant for angles of

attack greater than the angle of stall i.e. the linear portion extended beyond the stall margin as if the section did not stall.

A new approach was developed by Bak[76] from analysis of the UAE rotor tests where the 3D corrections were applied based upon the pressure distribution over the airfoil and it is the change in pressure between the stalled flow and the 2D wind tunnel data that is modelled. This method relies to a greater extent on estimating the physics of the flow than the conventional models. The change in pressure is described by the product of a shape function and an amplification function of the form:

$$\Delta C_p = \boldsymbol{Amplification}\left(\frac{c}{r}, \frac{r}{R}, \alpha, \theta\right) \boldsymbol{x\ Shape}\left(\frac{x}{c}, \alpha\right)$$

Equation 16

Where the amplification function is based upon a description of the force balance acting upon the flow; the dynamic pressure, centrifugal force and Coriolis effect. The amplification function accounts for the local chord length (c/r), radius (r/R), blade twist (θ) and angle of attack (α). While the shape function is based upon the angle of attack and the chord-wise position (x/c).

Three conventional stall delay models (Snel, Lindenburg and Chav. + Hansen) and the new pressure based approach (Bak) were compared with experimental data from the NREL UAE rotor[78] with varying success. Figure 21 below shows the lift coefficient predictions of the four models at 80% of the blade radius with the 2d wind tunnel measurements and the 3d rotational measurements. As rotation has little effect on the aerodynamic performance at this point of the blade all the models and the 3d data match closely with the 2d data.

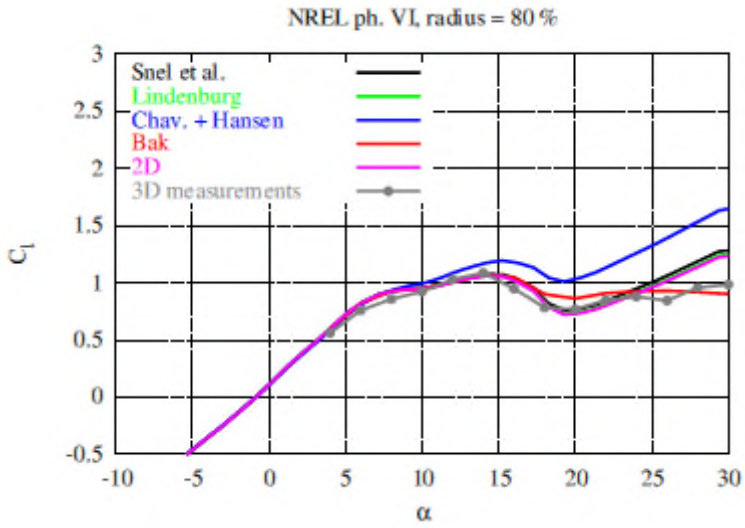

Figure 21 - Cl data - 80% radius

Figure 22 shows the predictions for 30% blade span where rotation has a strong bearing upon the performance of the blade as can be seen from the large difference between the 2d and 3d data in the post stall region. For this portion of the blade both Snel and Bak are in reasonable agreement with the 3d measurement data. The other two models under-predict and over-predict the 3d data by a considerable margin.

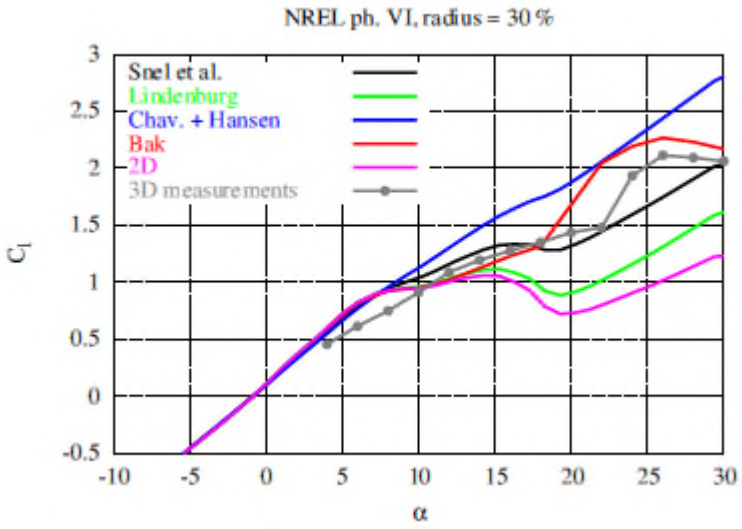

Figure 22 - Cl data - 30% radius

The application of these models is clear from Figure 23 which shows the curve of measured power vs wind speed for the UAE rotor. This shows the same trend between the models as Figure 22 with Lindenburg tending to under-predict power post stall while Chav. + Hansen considerably over-predicts the power beyond 9m/s wind speed. Both Snel and Bak provide the closest approximation to the 3d data but both tend to under-predict the power at high wind speeds. It has been shown for other rotors that Snel and Bak provide the best agreement of the four models with very little separating the two models[76].

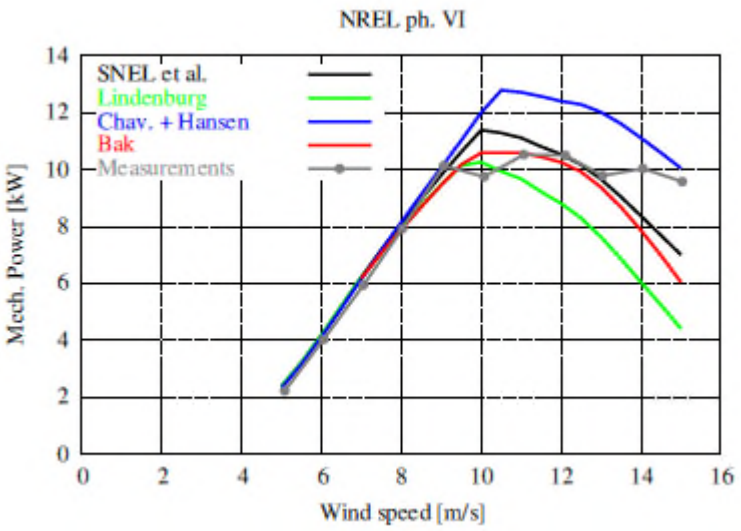

Figure 23 - UAE rotor - Power predictions

Due to its simplicity and performance in comparisons with other models the Snel stall delay model has been applied to section aerodynamic data which is discussed in later sections. The Bak model may provide better results for calculation of thrust loads in heavily loaded rotors but this is mainly relevant to stall controlled rotors.

2.1.5.2 Dynamic Inflow

A dynamic inflow model is used to account for the influence on the rotor of unsteady changes in the inflow conditions. Models of this type were originally developed for application in helicopter research into the effects of variable blade pitch on thrust load[79]. Classic BEM theory employed in time marching

formulations by their nature assume that the blade wake reacts instantaneously to changes in blade loading conditions (resulting from unsteady changes in the flow). They are generally known as equilibrium wake models. However, unsteady changes in blade loading result in changes to the wake vorticity at the blade trailing edge which take a finite length of time to manifest before a new equilibrium is reached. It has been shown this delay has a characteristic timescale on the order of D/U, where D is the rotor diameter and U is the free stream velocity. Therefore changes to the blade loading for full scale machines will take place over a period of a number of seconds. In wind turbine engineering this corresponds to turbulent gusts, blade pitch actions and some yawed operations.

A dynamic inflow model can be applied along with the BEM method to allow for quantification of the unsteady aerodynamic forces caused by the changing inflow across a rotor disc. It is important to model these unsteady effects as they can result in large load reversals which impact turbine fatigue life. Unsteadiness of an interaction with a flow is defined by a parameter known as reduced frequency. The interaction is considered unsteady when the reduced frequency is greater than 0.05 and highly unsteady above 0.2[80]. The reduced frequency is defined as follows:

$$\boldsymbol{k = \frac{\omega c}{2V}}$$

Equation 17

Where ω is the characteristic frequency of the flow, c is a relevant characteristic length scale such as blade chord and V is the mean flow velocity[81]. Hence it offers a definition in terms of the fluctuating component of the flow and the size of the object in the flow. Due to the relatively slow rotational velocity of tidal turbines perturbations in the incident flow velocity will result in high values of reduced frequency. For example turbulent fluctuations corresponding to the size of the blades will result in values of k on the order of 0.25 for a turbine with a 15m diameter rotor using Equation 17 with a turbine blade size of 2m in flows of 2m/s.

Several models have been developed that can be applied in conjunction with BEM theory that use an empirical approximation to model the delayed effects of wake vorticity that occurs when there is rapid fluctuation in the blade inflow conditions such as happens during blade pitching or in coherent wind gusts. As part of the EU sponsored programme EC Joule, which is discussed in Chapter 4, several models were validated against data from experimental testing of a 2MW turbine operating under fluctuating inflow conditions. Seven models were compared in this study[158] however only three are applicable for use as sub-models of a BEM code. These models are; the differential equation model developed at the Netherlands Energy Research Foundation (ECN de), the Bladed sub-model developed by Garrad Hassan (GH) and the model presented by the Technical University of Denmark (TUDk).

The ECN de model is a development of the ECN cylindrical wake model (ECN iw). The ECN iw model calculates the axial and tangential induced velocities from a vortex sheet description of the wake using the Biot-Savart law and therefore the time delay is accounted for inherently. Although the ECN de model calculates the induced velocity using BEM theory with the addition of a time derivative of the induced velocity to model the inflow behaviour the time constant of the derivative is taken from the equations of the cylindrical wake model which makes it difficult to use with the BEM code without knowledge of the ECN iw model.

The sub-model within Bladed was developed from dynamic inflow models applied helicopter aerodynamics. Work by Carpenter which was developed by Pitt and Peters[82] show that the thrust on a helicopter rotor can be defined as:

$$T = m_A \dot{v} + 2\pi R^2 \rho v \left(v - w + {}^{2}/_{3}\, \dot{\beta} R \right)$$

Equation 18

Where w is the steady vertical aircraft velocity, m_A is the apparent added mass of air, β is the blade flap angle and v is the inflow perturbation velocity. The apparent added mass is a construct to account for the effect of fluid

accelerating through the rotor plane resulting in an additional force on the blade. In the Bladed model, which has been posed in terms of a wind turbine rotor, the elemental thrust on a blade section is defined as:

$$\boldsymbol{dT = 2U_{\infty} am + U_{\infty} m_A \dot{a}}$$

Equation 19

Where m is the mass flow through the plane of the rotor, U_{∞} is the free stream velocity and m_A is known as the apparent added mass. This model is consistent with BEM theory and is inexpensive to compute but was found to under-predict the effects of dynamic inflow for wind turbines in this study.

In the third model, TUDk, initial values for the induced velocities are calculated using BEM theory and are then passed through a set of differential equations that incorporate a lag term into the model. This lag filter is applied by two differential equations of the form:

$$\boldsymbol{y + \tau_1 \frac{dy}{dt} = x + k\tau_1 \frac{dx}{dt}}$$

Equation 20

$$\boldsymbol{z + \tau_2 \frac{dz}{dt} = y}$$

Equation 21

Where τ_1 and τ_2 are the two time constants, one short and one long, which are defined as:

$$\boldsymbol{\tau_1 = \frac{1.1}{(1-1.3a)} \frac{R}{U}}$$

Equation 22

$$\boldsymbol{\tau_2 = \left[0.39 - 0.26 \left(\frac{r}{R}\right)^2\right] \tau_1}$$

Equation 23

The first constant, τ_1, accounts for the inflow conditions to the whole rotor while the second accounts for the radial dependency of the time delay. τ_1 is

proportional to the characteristic timescale relating to the size of the rotor, R, and the incoming flow speed, U. It also takes into account the loaded state of the blade in terms of the induction factor, a, as τ_1 increases with induction factor i.e. when the rotor is heavily loaded the time constant is larger than when its lightly loaded. τ_2 is proportional to τ_1 and defines the time constant for each elemental blade section. At the tip there is little delay as the tip vortex dominates flow in this region. The value of τ_2 increases according to an inverse square law so that it is maximised at the blade root. The result of this is that the value of τ_2 increases from 13% of the value of τ_1 at the tip to 39% at the centre of the rotor plane.

These models (plus four others not described here) were the subject of a validation study aimed at predicting the time dependent loading response of a 2MW turbine to pitching transients during the JOULE programme. Figure 24 shows the rotor torque predictions of the seven models plus the experimental data from the turbine with the three models of interest highlighted. Figure 25 is the equivalent for the blade bending moment.

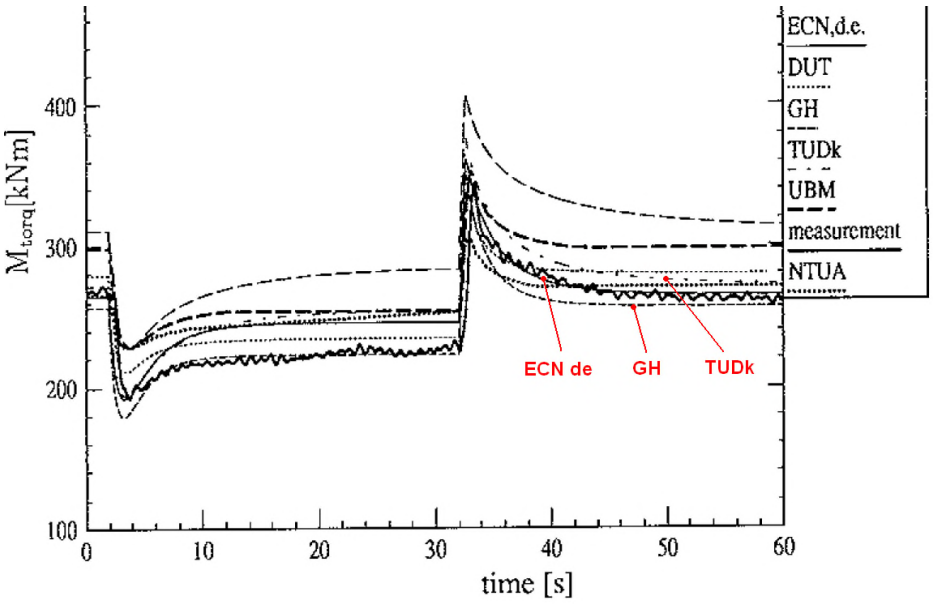

Figure 24 - Dynamic Inflow - Torque predictions

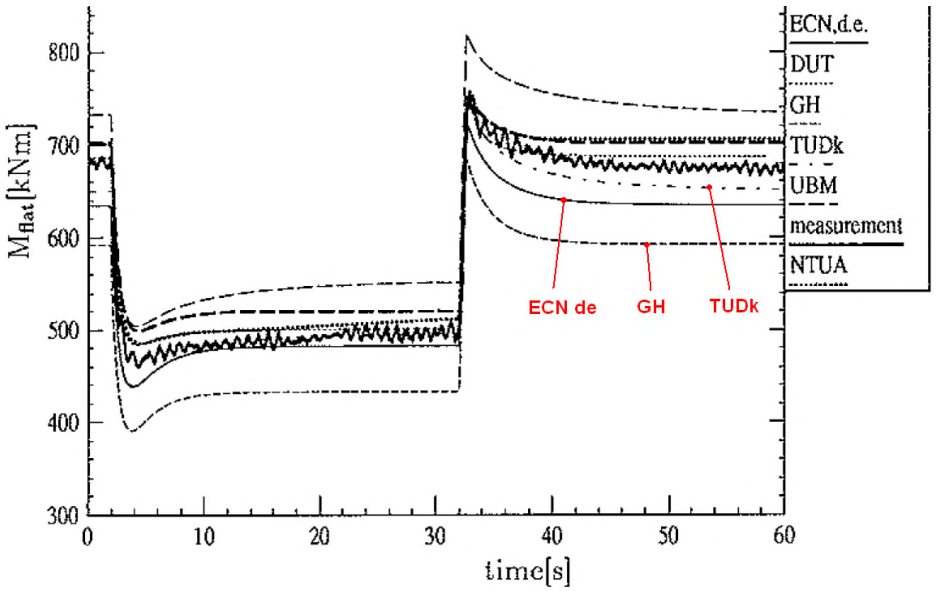

Figure 25 - Dynamic Inflow - Bending predictions

They show the relative performance of each model and quantify how closely they predict the measured loads on the turbine. A full description of the experimental conditions is given in the section on the code validation process. Figure 24 shows that all three codes predict the torque to within 15% of the experimental value (GH) with the ECN de model matching the experimental data most closely (approx. 5%). A much larger discrepancy is seen in Figure 25 where all three models under-predict the measurements with the GH model in particular showing a large difference. Generally the TUDk model is in good agreement with the experimental data and compares well with the more complex lifting line vortex models (the other codes being compared). Therefore based upon its compatibility with BEM theory, relative simplicity and validation performance this code was implemented as a sub-model within the BEM code.

2.1.5.3 Dynamic stall

Dynamic stall is a physically complex phenomenon but if viewed simplistically as a 2d process, dynamic stall initiates when the lifting surface alpha dynamically exceeds the static stall threshold. Soon thereafter unsteady boundary layer separation gives rise to a small but energetic dynamic stall

vortex. This vortex quickly grows, convects rapidly downstream and soon sheds from the lifting surface. During this process the vortex generates a region of low pressure on the lifting surface causing dramatic lift amplification beyond static levels followed by an abrupt deep stall at the vortex shedding[83].

Aerodynamic bodies subjected to pitching or plunging motion can exhibit a stalling behaviour that departs from that experienced by a static wing in stall. This phenomenon, known as dynamic stall, is generally accompanied by a dramatic decrease in lift and pitching moment. As a result aero-elasticity in unsteady airfoils has been a focus of experimental and theoretical study for many decades. Theodorsen's potential flow approximation for unsteady lifting and pitching airfoils[84] was one of the first analytical approaches to analyse fixed wings operating below stall in the attached flow regime. The occurrence of stall flutter of propellers, compressors and rotor wings and the continuous optimisation of helicopter design led to the need for analysis of unsteady aerodynamic forces in the stalled region. The most commonly cited model used in helicopter applications is the Beddoes-Leishman (B-L) of which there are several formulations. A complete dynamic stall model for unsteady lift, drag and moment is detailed in Leishman[85].

In recent times it has become increasingly necessary to consider non-steady loading in the wind turbine industry as blades become ever more slender and control systems are able to respond more rapidly to changes in loading. There are versions of the B-L model that have been applied to wind turbine aero-elasticity which are typically simplified to neglect compressibility and leading edge stall. As wind turbines are slow speed machines with maximum tip speed velocities on the order of 80m/s compressibility can be safely ignored. Furthermore the airfoil sections implemented in wind turbine blades tend to be thick and so leading edge stall is unlikely to occur.

Under stationary conditions the lift coefficient represents the lift force on an airfoil which acts at the aerodynamic centre of the section which tends to be at the forward quarter-chord point. The lift coefficient is approximately a linear function of the angle of attack, α, over a small range. For large angles of attack

the flow pattern changes and the lift coefficient will pass through a maximum before dropping off as the section enters static stall. Under non-stationary conditions, when the angle of attack varies rapidly, a completely different flow pattern emerges.

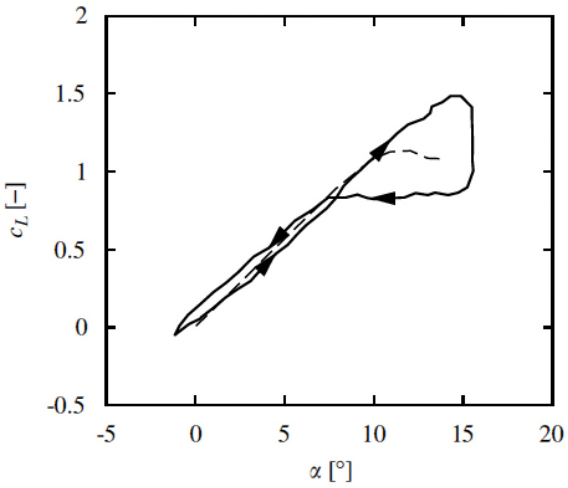

Figure 26 - Lift coefficient under static and dynamic conditions[86]

In Figure 26 the dashed line represents static conditions and the solid line dynamic conditions. This shows that dynamic stall conditions can lead to an increased range of attached flow and follows a different pattern for increasing and decreasing angle of attack. The reason for stall in static conditions is because the airfoil experiences trailing edge separation when above a critical angle of attack. However, in dynamic stall conditions leading edge separation is often induced instead, as shown in Figure 27 below, which results in the non-linear lift behaviour.

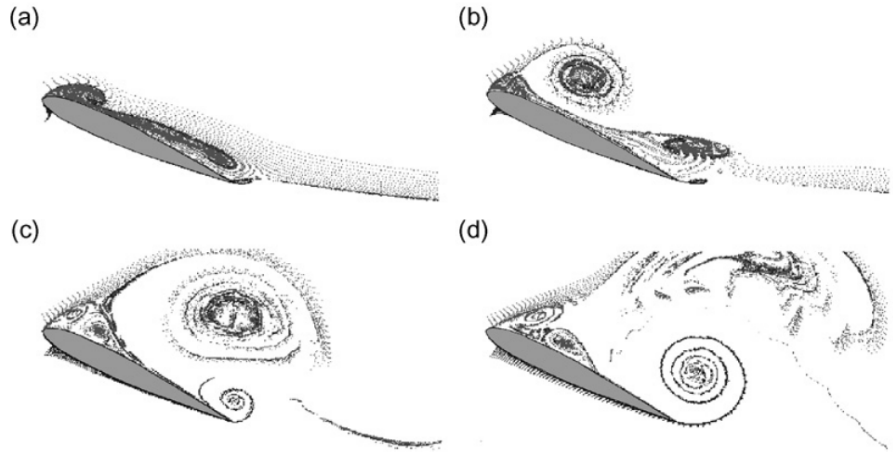

Figure 27 – CFD flow visualisation during dynamic stall conditions

In (a) leading edge separation of the boundary layer begins, followed by a build-up of a leading edge vortex in (b). Then in (c) the leading edge vortex detaches and there is a build-up of a trailing edge vortex which then detaches in (d) and the leading edge vortex breaks down. The result of the detached leading edge vortex is an initial period of enhanced lift followed by a dramatic loss of lift once the vortex has diffused. At low pitch velocities where the rate of change of angle of attack is small leading edge separation is not problematic but in cases where the rate of change is high, based upon the reduced frequency, dynamic stall must be considered. Unsteady effects on wind turbines are particularly acute because large flow perturbations resulting in high values of reduced frequency are often to be found. This is because rotor speeds are relatively low, compared to other turbomachinery, and so any changes in atmospheric conditions will result in significant changes to the angle of attack[87].

The majority of models reviewed in a blind trial controlled by the NREL were found to be inadequate at predicting the effects of dynamic stall as both large over and under-predictions of turbine torque were calculated by these models[88]. The most widely used model used in wind turbine analysis is the Leishman-Beddoes model which is capable of representing the unsteady lift, pitching moment and drag characteristics of an airfoil undergoing dynamic stall. The complete model can be split into four parts[89]:

1 – An attached flow model for the unsteady, linear air-loads

2 – A separated flow model for the non-linear air-loads

3 – A dynamic stall onset model

4 – A dynamic stall model for the vortex induced air-loads

To represent the effects of dynamic stall the model emulates the dynamic effects on the air-loads of the accretion of vorticity into a concentrated leading edge vortex, the passage of this vortex over the surface of the airfoil and its convection downstream[90]. The dynamic stall model is employed based upon certain flow conditions being met as defined by the Reynold's number and the rate of change of movement of the separation point.

The Leishman-Beddoes model is advantageous in that the number of empirical constants required for accurate performance is low compared with other models. There are only four constants relating to time lag effects that cannot be derived from the static airfoil data. Two are time constants used in the second sub-model and one in the third model. The fourth is a non-dimensional time period used to determine the duration of the dynamic stall process.

2.2 Turbulent flow

In this section the origin and nature of turbulent flow is introduced. This is followed by a discussion on the types of turbulence that affect marine turbines. The techniques that have been conceived and developed to provide a means of modelling this complex phenomenon are detailed. The technique used by the author in the development of this turbine model is described in greater detail. The chapter is then rounded out with a review of site specific flow data from literature sources that highlight the importance of being able to effectively model turbulence in order to predict tidal turbine loading.

2.2.1 Introduction to turbulence

Turbulent flow is almost always three dimensional and disordered in time and space however sometimes it may be simplified as quasi two dimensional. Furthermore it may exhibit well organised structures. Turbulence arises in flows as the result of internal instabilities when some critical value of Reynold's number is reached. A common source of instability in a flow is shear between layers of fluid such as found in the boundary layer near a wall. Turbulence is not a feature of fluids but of flows and hence most of the dynamics of turbulence is similar in all fluids (including gases) and is independent of fluid properties[91].

Turbulent flow is unstable by its very nature as small perturbations are amplified due to non-linearity in the governing equations of motion. This makes the flow somewhat unpredictable meaning precise deterministic predictions are impossible[92]. It is considered a stochastic process where there is always some level of indeterminacy even if the initial conditions are known[93]. Two properties common to all turbulent flows are that; they mix transported quantities far more rapidly than if only molecular diffusion were involved and they occur over a wide range of spatial length-scales.

Reynolds established that flow can be characterised by a single non-dimensional parameter now known as the Reynolds number, Re. This is generally defined as $Re = {}^{UL}/_{\upsilon}$ where U and L are a characteristic velocity and length while υ is the kinematic viscosity[94]. Turbulent flow has a very high Reynolds number[87]. At high Reynolds numbers there is a separation in the behaviour of the scales of turbulent motion. Large scale motions are influenced by the geometry of the fluid boundaries and control the transport and mixing[90]. The small scales are determined by the rate at which energy is received from the large scales on one side and by viscosity on the other. The energy of the flow is distributed over a range of wave numbers, or eddy sizes, known as the energy cascade as proposed by Richardson. A turbulent flow contains a wide range of eddies interacting with each other. An eddy does not have a precise definition but is assumed to be a turbulent motion within a region of size, l, that is coherent within this region[90]. A continuous transport of energy from the mean

flow to large eddies and down through a series of reducing eddies takes place. The turbulent kinetic energy, k, of the flow can be expressed as:

$$k = \frac{1}{2}(u'^2+v'^2+w'^2) = \int_0^\infty E(k)dk \quad [87]$$

Equation 24

$E(k)dk$ is dependent upon viscosity, dissipation rate, integral length scale, wave number and strain rate. The wave number is used to describe the dynamics of flow in a spectral form and is formally defined as:

$$\boldsymbol{\gamma = 2\pi/L}$$

Equation 25

Where L is a dimension typical of the fluid structures. The smallest wave numbers are associated with the largest scale structures of the flow. Wave numbers on the order 0.1 to 1 would coincide with eddies of interest to tidal turbine modelling. Kolmogorov proposed that for fully turbulent flows at intermediate wave numbers the magnitude of the eddies is independent of both the energy containing, large scale eddies as well as the small scale molecular viscosity[87]. This intermediate zone is known as the inertial sub-range and suggests that the small scale motions, known as the Kolmogorov scale, are universal and independent of local flow constraining geometry[90].

The three-dimensional energy spectrum for homogeneous, isotropic turbulence can be approximated as follows:

$$E(k) = C_k \varepsilon^{2/3} k^{-5/3} \quad [95]$$

Equation 26

Where ε is the dissipation rate of kinetic energy and C_k is the Kolmogorov constant with values typically ranging between 1.4 and 2.2 (based on experimental observations). The energy spectrum is illustrated in Figure 28 below which shows a plot of the energy cascade with log-log axes. Here wave number is plotted on the horizontal axis and turbulent energy on the vertical. The largest eddies are found at the lowest wave numbers where mixing and

fluid transport occur. The largest eddy size is governed by the flow configuration and is generally of the same order of scale as the fluid domain. In the region of highest energy the typical size of eddies is known as the integral length scale.

At the opposite extreme viscosity dominates the smallest fluid motions where kinetic energy is dissipated into heat by molecular diffusion. In-between is a region called the inertial sub-range and is universal to all turbulent flows. The gradient of the slope of the energy in this range has been found to follow the -5/3 law proposed by Kolmogorov in 1942. However, the size of the smallest eddies decreases as Reynolds number increases[87].

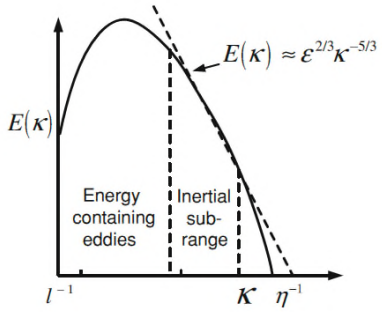

Figure 28 - Energy spectrum for fully turbulent flow[86]

The features of the energy cascade are best described as a non-equilibrium process. In the case of turbulent flow the situation arises where there is no time dependence (i.e. steady state) but currents of the conserved variables are flowing, driven by injection at one boundary and subtraction at another as described by Figure 29 below. As the dynamics of the system are dissipative, by fluid viscosity dissipating kinetic energy to heat, there must be addition of energy into the system at some point to maintain the steady state. It has been found that the large scale eddies receive energy from the bulk flow[90].

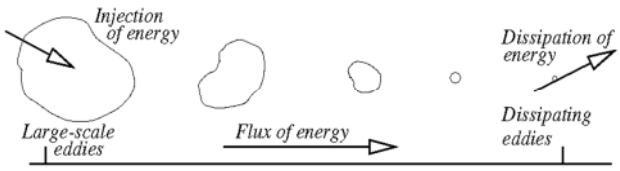

Figure 29 - Energy cascade

Therefore turbulence cannot maintain itself and is damped out unless energy is supplied externally from its environment. This understanding of the energy cascade places dissipation at the end of a sequences of processes and so the rate of dissipation, ε, is defined by the first process in the sequence i.e. energy transfer from the largest eddies. Experimental observations back up this up and show that ε is proportional to u^3/l and is independent of viscosity at the high Reynolds numbers required for fully turbulent flow[90].

2.2.2 Review of turbulence in tidal flows

There is much interest in understanding marine turbulence as it plays a decisive role in the performance and reliability of tidal power devices[96]. A detailed description of velocity inflow conditions across the entire rotor plane is required to be able to better predict unsteady loads. This is analogous to the wind turbine industry where it has been shown that the turbulence intensity and the velocity spectra can be correlated with performance and fatigue. At present numerical models can routinely only simulate part of the flow because it is not possible to directly model turbulence down to the smallest scales of motion due to computational resource limitations[97]. The design of turbines therefore relies on inflow estimations based on field observations from tidal locations. A limited number of studies have been carried out to date at tidal sites where the aim has been to measure the ambient turbulence which is the natural turbulence of the site without the presence of turbines[98]. Typically these studies only acquire data at one point in the flow, often close to the hub height of a turbine.

As discussed in the previous section turbulence is a manifestation of the flow which results from instabilities arising from shearing of the fluid. Turbulence develops in flows that are above the critical Reynold's number which is dependent upon the local geometry of the flow boundary. There are several elements which affect this including the tidal velocity, the roughness of the sea bed and the pressure distribution of the external flow. Near the sea bed flow velocity decreases giving rise to the classic boundary shear layer profile. Increasing sea bed roughness will promote the transition to turbulence because it reduces the critical Reynold's number. Due to the natural tendency of the fluid to resist shear forces the flow is torn by the shear stresses in energetic three dimensional eddies. Topographical irregularities will also affect the site turbulence distribution as they may lead to non-equilibrium turbulence where large scale eddies form and convect downstream without significant mixing[93]. Evidence for this comes from the significant differences observed in the velocity spectra at tidal sites dependent upon the direction of the tide. Measurements of turbulence in the Puget Sound in British Columbia show changes in the level of turbulence intensity and anisotropy of the velocity for the same site during different tides[93].

Studies of tidal flow are normally conducted using acoustic measurement techniques with the most common instrument for taking velocity measurements in tidal channels being the Acoustic Doppler Current Profiler (ADCP) which is a type of sonar device used to measure and record water current velocity. The transducer emits an ultrasonic acoustic burst at a specific frequency into the water column. The pulse scatters off particles suspended in the water and returns to the ADCP measurement head with a slightly phase shifted frequency which is caused by the Doppler Effect arising from the difference in beam speed after it has reflected of the suspended particle. Normally such a device has several measurement heads (typically 4) all of which transmit and then receive acoustic bursts or pings generated along a narrow beam. The ADCP device is operated from the sea bed and the beams are inclined at 20-30° from vertical in a symmetric pattern known as the Janus configuration as shown in Figure 30 below.

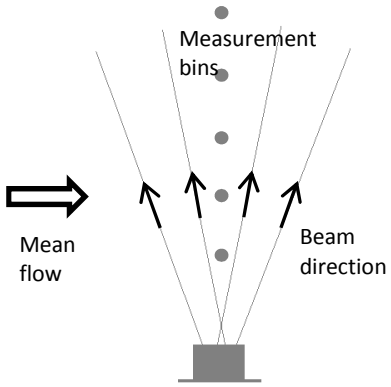

Figure 30 – ADCP schematic

ADCP's are able to measure the depth profile of the channel velocity by applying run-time windowing of the back scattered acoustic pings for each of the beams[99]. The result is a time history of the velocities in the along-beam direction at multiple measurement volumes between the sea-bed and the water surface. These evenly spaced volumes, or measurement bins, are calculated through the post-processing of the acoustic signal which determines the range of the returning signal based on time of flight which is why a pulsed rather than a continuous signal is necessary. The size of the spacing is a compromise between resolution and the statistical uncertainty in each velocity measurement as the velocity reported is the mean velocity for the whole volume[100]. In the process of converting the beam velocities into the flow velocity components in Cartesian coordinates, which is accomplished from the trigonometric relationships between the beams, the assumption is made that the flow is horizontally homogeneous from one beam to the next[94]. This results in a degree of averaging of the velocity field between the beams such that the high frequency turbulent velocity fluctuations are not possible which has been shown to affect measurements in the isotropic integral sub-range[101].

Other methods of analysis have been developed in order to study the turbulence of the flow. Reynold's stress and turbulent kinetic energy (TKE) production can be derived from ADCP's with four beams using the variance method[102] of post processing. However, the variance method also assumes that the turbulence has horizontally homogenous properties over the distance

between the beams[94]. Therefore the length scale of the turbulence being measured should be sufficiently large before it can be statistically characterised using ADCP velocity estimates. A further pre-condition is that the beams have vertical orientation, any deviation from the vertical results in errors in the measurement estimates[97]. In practise this is not possible so all measurements are influenced by a systematic error dependent upon the beam angle.

ADCP measurements have been documented at several tidal sites in areas of high kinetic flux with particular attention being paid to the turbulence intensity and the velocity spectra. A study in the Sound of Islay in Scotland reported intensity levels of around 9.5-10.3% at peak flow speeds in excess of 2m/s. The anisotropy of the stream-wise flow was also determined as $\sigma_u:\sigma_v:\sigma_w$= 1:0.75:0.56 which is very similar to the Kaimal model frequency spectra[92]. This is comparable with results from the Fall of Warness, Orkney, where turbulence intensity measured at 1.5m/s mean tidal speed ranges from 7.9-8.7%. Several studies from the Puget Sound suggest turbulence falls in the range of 8.4-11.4% dependent upon flow speed (in the range 1-3m/s) as shown in Figure 31 below. This shows data for two different sites (Nodule Point and Admiralty Head) in the Puget Sound using three different velocity measurement techniques including an ADCP. The data suggests that turbulence intensity follows a log normal relationship with flow velocity.

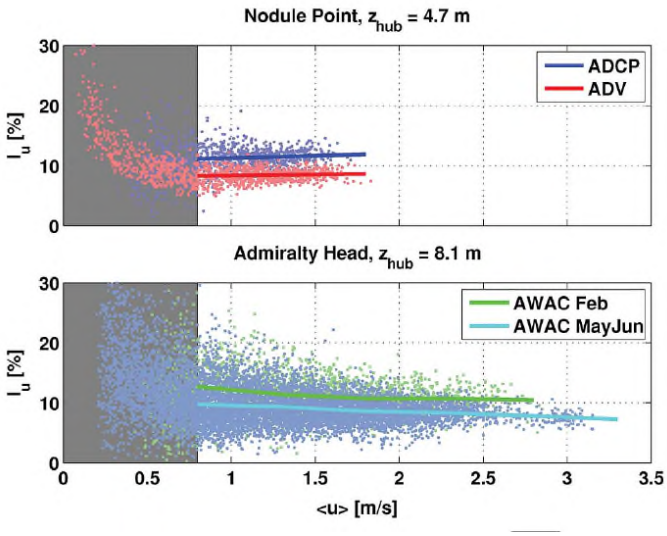

Figure 31 - Turbulence in Puget Sound [93]

Care must be exercised when using TI as compared to RMS velocities. As the mean flow speed tends to zero, TI will tend to an infinite value. Therefore below a certain threshold (around 0.5-1m/s) TI is not a useful measure. Whereas using simply the root mean square (RMS) velocity would give a true representation of the magnitude of the fluctuating velocity components across all flows. However, as flows below 1m/s are not considered useful by the tidal energy industry this does not pose a problem when comparing these literature sources. The velocity spectra for Nodule Point are shown in Figure 32 below with log-log axes which exhibit three distinct regions. The low frequency region exhibits evidence of large, anisotropic eddies for the horizontal flow while the mid-range frequencies show the classic $f^{-5/3}$ relationship with frequency suggesting isotropic turbulence for both horizontal and vertical flow in an inertial sub-range which would be expected. At the highest frequencies the signal tends to become dominated by Doppler noise and is not an effective measure of turbulence.

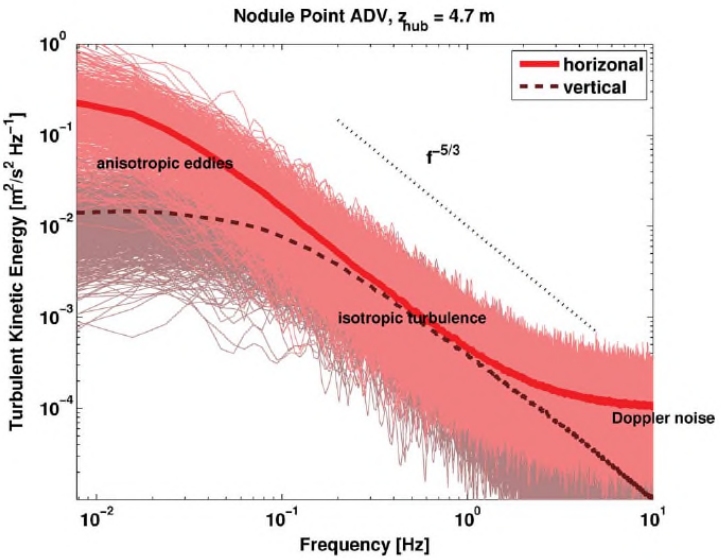

Figure 32 - Three dimensional velocity spectra [93]

The large eddies characterise the low frequency region in the range 0.01-0.1 Hz. It has been found by some authors that these eddies tend often to be anisotropic in the locations of study i.e. one velocity in particular tends to

dominate. While other studies have shown that tidal flow compares closely with general boundary layer power laws (e.g. Kaimal curves). There appears to be no universal law to describe tidal flow[103]. This is reinforced by data from Strangford Narrows in Ireland where turbulence intensity ranges from 3.2-7.1% which is dependent upon flow direction and mean velocity suggesting there is no global turbulence constant but it is dependent upon localised variations in topography[104].

In order to assess the turbulence eddy size the frequency spectra can be converted to length scale using Taylor's frozen field hypothesis according to:

$$L_u = \frac{\bar{u}}{f}$$

Equation 27

Which is only valid within the frequency band of coherent motion because at higher frequencies the turbulence is moving faster than it is advected and the lengthscale will be aliased. It is also restricted to the horizontal stream-wise flow component[92].

The studies also show that turbulence intensity decreases monotonically with elevation above the seabed as would be expected in well-developed boundary layer flow as demonstrated by Figure 33 below. This shows a difference of around 4.5% intensity over the 15m measurement elevation from data taken in the Puget Sound which shows the non-slack water over-all average superimposed in bold over a number of 5 minute records.

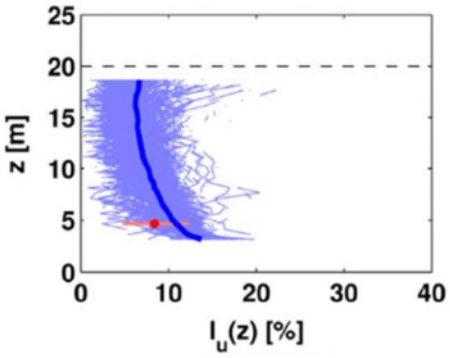

Figure 33 - Vertical profile of turbulence intensity [93]

The area weighted average of the turbulence intensity can be calculated as follows:

$$\boldsymbol{TI}_u = \frac{1}{\pi R^2} \sum \frac{I_u(z)|z-z_{hub}|(\Delta z)^2}{\sqrt{R^2 - |z-z_{hub}|^2}}$$

Equation 28

Where R is the turbine radius and z is the elevation above the seabed. However, in practise when the hub height and radius of full scale turbines are considered the difference between the area weighted average and the simple hub height value is negligible.

2.2.3 Stochastic turbulent flow field simulation

Although turbulence tends to be unpredictable in the time domain it can be well characterised in the frequency domain. Energy spectra have been theoretically derived by Kolmogorov. When the Reynold's number is sufficiently high the flow is locally homogeneous, isotropic and in a state of statistical equilibrium. In this condition turbulence can be uniquely determined by the dissipation rate and the viscosity. However, marine flows tend to be anisotropic due to other influences such as eddies from vortex shedding caused by the nature of the local bathymetry; therefore the existing methods for simulating data sets of turbulent flow rely on empirical representations of the flow. For instance the spectral density function of the atmospheric wind is shown in Figure 34 below on a log scale. The left hand side of the figure shows the energy content of processes that take place on the order of days and are driven by seasonal changes. The

right hand part of the plot shows the spectral density of processes attributable to turbulence in the flow which occur over the range of a fraction of a second to several minutes. The central part of the spectrum shows little activity as the dynamics of the flow are stationary. This range extends from approximately 5 minutes to 5 hours where the averaged statistics show little activity.

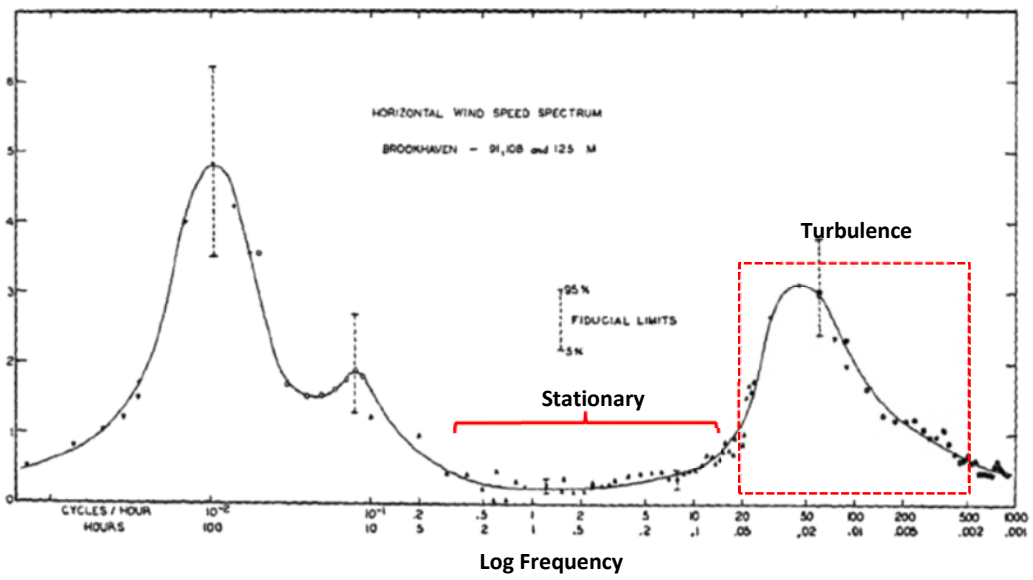

Figure 34 - van der Hoven spectrum[105]

A similar approach can be taken with tidal flows to show the frequency content of important processes. Because turbulence is common to both flows the energy content of the high frequency part of the spectrum is somewhat similar to that of the atmospheric wind. However, processes which are very different than those relating to the wind drive tidal flows and so the very low frequency term spectral components appear more closely related to the example spectrum shown in Figure 35 below. This shows the dominant tidal harmonic frequencies that are linked to the behaviour of the tide over periods of several days. However, as the spectral content of the flow at these very low frequencies does not impact upon high frequency turbulence modelling it will not be discussed further in this section.

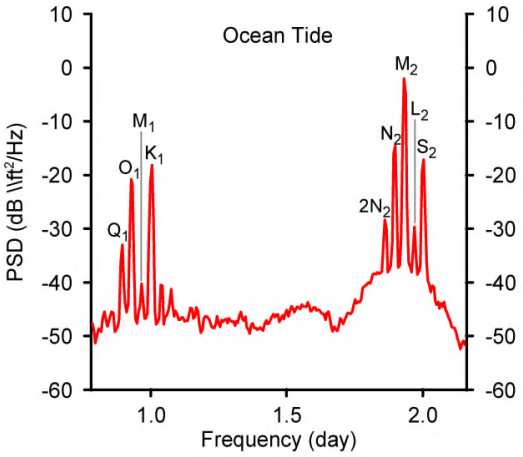

Figure 35 - Typical tidal power spectrum

As mentioned statistical models of real world turbulence must be derived from direct observations. The von Karman spectrum is an example of a good description of turbulence in wind tunnels[106]. The velocity spectrum in terms of frequency is defined as follows:

$$S_u(f) = \frac{4\sigma_u^2 L\sqrt{u}}{\left(1+71\left(fL\sqrt{u}\right)^2\right)^{5/6}}$$

Equation 29

Where σ is the standard deviation of the velocity component, L is the length scale and u is the stationary mean flow velocity. It is generally applicable over a frequency range of approximately 1 and 0.001 Hz which matches the frequency range over which wall bounded turbulence tends to occur due to shear. However, the Kaimal spectrum provides a better description of boundary layer turbulence intensity which fit empirical observations[107]. The Kaimal spectrum is defined as a function of the cyclic frequency as follows:

$$S_K(f) = \frac{4\sigma_K^2 L_K/\overline{u_{hub}}}{(1+6fL_K/\overline{u_{hub}})^{5/3}}$$

Equation 30

Where K = u, v & w are the stream-wise, cross-stream and vertical components of the velocity standard deviation respectively. The velocity component ratios are for the Kaimal spectra are; $\sigma_v = 0.8\sigma_u$ & $\sigma_w = 0.5\sigma_u$. L_k represents the

component integral length scale and f is the cyclic frequency. The Kaimal model assumes that the Richardson number, Ri = 0 as the model is only valid for neutral boundary layer flow. The Richardson number is a dimensionless ratio of the fluid buoyancy to flow shear gradient:

$$Ri = \frac{g}{\rho} \frac{\nabla \rho}{(\nabla u)^2}$$

Equation 31

Where g is the acceleration due to gravity, ρ is the fluid density and u is a characteristic flow velocity. When Ri is much less than unity buoyancy is not important to the flow physics but when Ri is much greater than unity buoyancy starts to dominate the fluid as there is very little kinetic energy to mix the flow. It is generally considered that when R<0.25 flow is turbulent and when R>1 flow is laminar and the flow becomes stratified. An example of estuarial channel flow is shown in Figure 36 below which plots Ri over a range of channel depths with Ri = 0.25 & 1 marked in red. Between the surface and 10m there is evidence of surface mixing from wave action but between 10-40m the flow is generally laminar as Ri is between 1-10. Below 40m Ri tends to decrease as turbulence increases with proximity to the sea bed. This indicates that fast flowing tidal channels cannot be stratified as the turbulent boundary layer extends to virtually the full depth and so the assumption of neutral buoyancy is completely valid for modelling of turbine inflow.

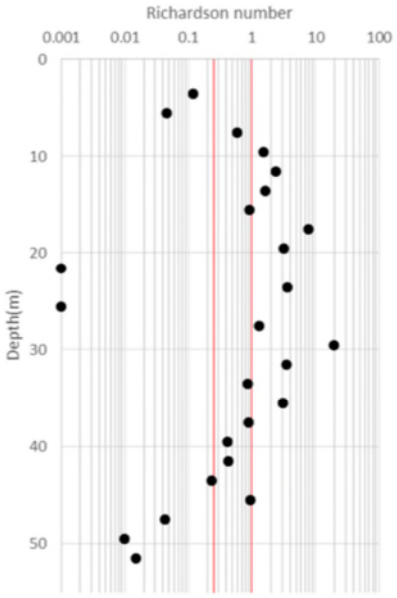

Figure 36 - Vertical profile of Richardson number[108]

The Kaimal model requires knowledge of the component length-scales. In atmospheric wind modelling the length-scale is dependent upon proximity to the ground as at higher altitudes the turbulence becomes isotropic but this is irrelevant to tidal modelling where the hub height will always be in a layer of anisotropic turbulence caused by the boundary layer. The integral length scale can be estimated by autocorrelation of the measured velocity with time. This technique is expanded upon in Chapter 3.

2.2.4 Coherence

Coherent structures are large scale fluidic masses within a turbulent flow which have phase correlated vorticity over their spatial volume. They are superimposed over the three dimensional random fluctuations which characterise stationary turbulence processes. In these regions the fluid has an organised, phase correlated structure over its spatial extent[109]. The evolutionary nature of coherent turbulence results in surges of non-stationary flow that last several seconds.

Generally in atmospheric turbulent flow the coherent structures have a specific spatiotemporal structure such that its kinetic energy resides in discrete frequency bands. A turbine rotor blade that passes through such a structure will encounter fluctuating turbulent kinetic energy levels which are a function of the rotor speed, the mean flow speed and the size of the coherent structure. The consequence of such encounters are that short period, impulse loads are induced on the blade, the magnitude and frequency of which will have ramifications for the turbine sub-systems in terms of stress and vibration[110].

In order to simulate high-stress turbine operating conditions it is important to include coherent structures with the frequency of occurrence derived from site specific data. If these are neglected from simulations the level of higher frequency energy in the flow may be an order of magnitude less than found from experimental data when coherence is present. The following (Figure 37) shows the superposition of stream-wise, cross-stream and vertical velocity components of a coherent turbulent structure over the random turbulent background. The background turbulence was simulated using the synthetic spectral Kaimal model while the coherent structure was added directly from a DNS simulation[111].

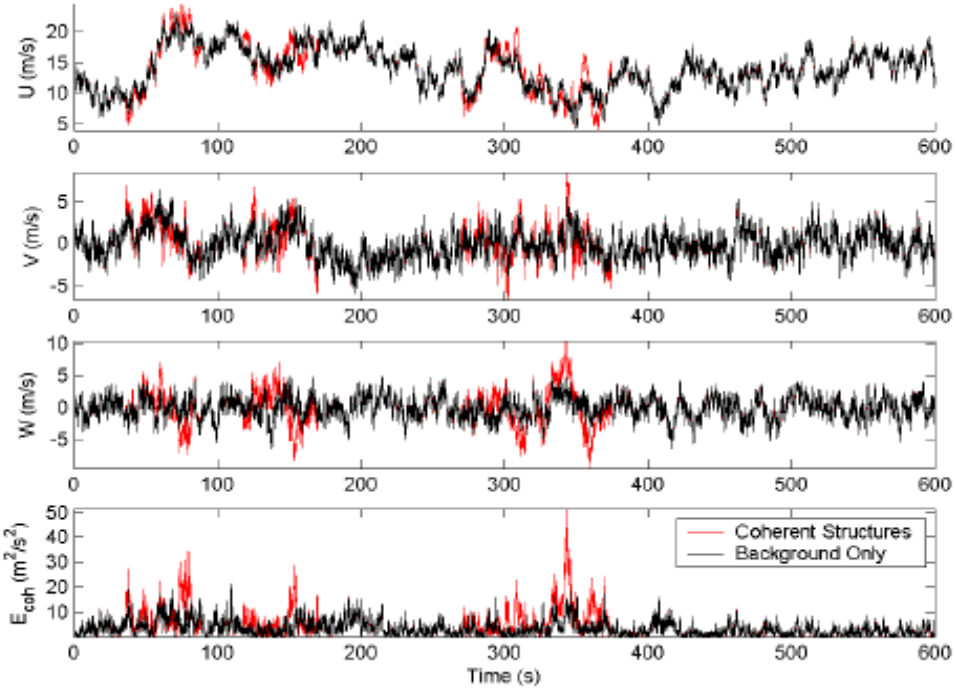

Figure 37 - Superposition of a coherent structure[105]

The first three plots show the velocity components (u, v & w) and the fourth shows the turbulent kinetic energy (TKE) of the flow as a time history. From this it evident these coherent events can be identified by the elevated levels of TKE which is significantly above that of the random turbulence.

Turbulence is a stochastic process and therefore its statistical description becomes stationary given a long enough data set. The presence of coherent structures represents non-stationary processes which are non-homogeneous in time and space. It has been found that many of their attributes can be modelled as Poisson and lognormal probabilistic processes. The point within a time series where a coherent event occurs can be described by a Poisson distribution at a non-constant rate. In general statistical analysis the Poisson distribution is used to model discrete events that occur independently of each other and so is well suited for this application. The length of time over which a coherent event occurs was found to be log normally distributed from measurements at wind turbine sites[105].

Coherence can be accounted for in simulations of turbulent flow fields when flow at a given point is influenced by its neighbouring points. In general terms the spatial coherence between two points is defined as:

$$Coh_{i,j}(f) = \frac{|S_{ij}(f)|}{\sqrt{S_{ii}(f)S_{jj}(f)}}$$

Equation 32

Where S_{ii} is the power spectral density and S_{ij} is the cross spectral density and allows quantification of the correlation between the two points. This is controlled by the following coherence function in the Kaimal model:

$$\mathrm{Coh}(\mathrm{r},\mathrm{f}) = \exp[-\mathrm{a}((\mathrm{f} * \mathrm{r}/\mathrm{V_{hub}})^2 + (0.12\mathrm{r}/\mathrm{L_c})^2)^{0.5}]$$ [112]

Equation 33

Where r is the separation between i and j, a is the coherence decrement equal to 12 and L_c is the length-scale. The Kaimal model has been implemented in a numerical turbulent flow field simulation tool called Turbsim that has been used to generate the turbine inflow for the hydrodynamic model. Turbsim is a third party model developed by Scandia National laboratories and its implementation are described in detail in Chapter 3.

2.3 Composite Materials in the Marine Environment

2.3.1 Introduction to Composites

Composite materials provide well know advantages in aeronautical applications[113] and the emerging field of marine renewables is now embracing composite materials because of their high strength and stiffness to weight ratios combined with their apparent non-corrosive properties in the severe salt water marine environment[114]. Glass fibre reinforced polymers (GFRP) are being employed as materials in the blades of tidal turbines and the energy absorption interfaces of wave devices[115]. The structural properties of GFRP are dependent upon several aspects such as the ratio of fibre to polymer matrix, the type of fibre and type of matrix materials and how the fibres are orientated. Therefore in comparison to conventional engineering materials they are more complex to manufacture and component failure is more complicated to predict[116]. However, the advantages of fibre reinforced materials often outweigh the complexities as one of the main benefits is the capability to create a component which has the fibre alignment adapted to the specific direction of loading allowing the material to be used to it maximum advantage[110]. Composites have been used in the construction of wind turbine blades for many years for their strength and stiffness properties. Both glass and carbon fibre reinforced thermosetting resins have shown strong fatigue resistance over decades of use[117].

In general composite materials that may be employed for use in the tidal industry compare well in terms of their material properties as well as on a raw cost basis as outlined in Table 1 below. This shows why glass fibre reinforced polymers are promising as materials for blade structures as they exhibit a stiffness to weight ratio around 20% higher than steel for a similar unit cost. Furthermore one of the main advantages is their ability to produce components with anisotropic strength properties with the stiffness aligned with the major loading axis as this further improves their strength to weight ratio compared to isotropic metallic materials. In terms of strength composite reinforcing materials can be ranked as follows from high to low; high modulus carbon, Kevlar, S-glass and E-glass.

Material	Density, kg/m^3	Young's Modulus, GPa	Cost, £/kg
E-glass fibre	2,500	70-90	2.6-2.8
Carbon fibre	1,800	230-517	50-70
Plain steel	7,800	210	0.33-0.65
Stainless steel	7,700	200-300	2.0-2.5
Titanium	4,500	115	10-12

Table 1 - Comparison of material data [108]

2.3.2 Stress Life Approach to Fatigue

It is critical that components can be designed to withstand fatigue loading and two common approaches are typically adopted to determine life dependent upon the particular cyclic conditions. These are stress life methods and strain life methods. Stress life methods are most useful in high cycle fatigue conditions where the applied stress results in elastic deformation and plastic strain will only occur at micro-scales around the defect crack tip. For low fatigue cycles the scatter in experimental data becomes increasingly large such that a strain life approach must be used. In this regime the loading will result in a combination of elastic and plastic deformation at the macro-scale[115]. The threshold between the two approaches tends to be around 10^4 cycles.

The Wohler S-N diagram forms the basis of the stress life approach which is a plot of nominal cyclic stress amplitude (S) versus cycles to failure (N) for a particular material often displayed on a log-log axis. Some materials such as low alloy steels and titanium alloys display a fatigue or endurance limit below which the material will not fail as shown by curve A in Figure 98 below. However most materials do not exhibit a well-defined endurance limit and tend to display a continually reducing S-N response as per curve B.

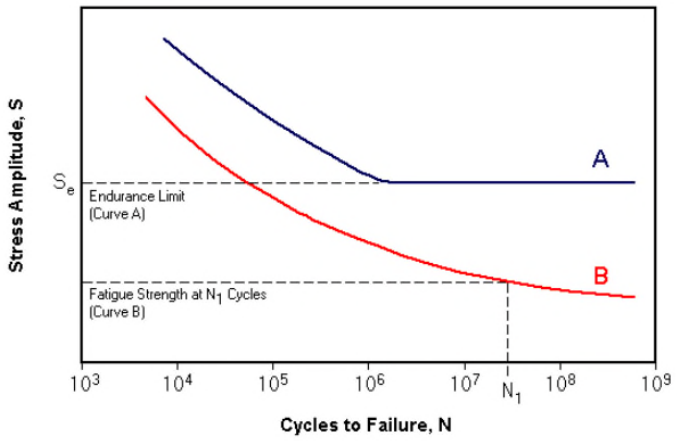

Figure 38 - Typical S-N curve [116120]

In many cases an arbitrarily defined, effective endurance limit is outlined as the stress at failure at 10^8 cycles for practical purposes such as time required to carry out material testing etc. In addition to the material properties there a number of other factors that influence the fatigue performance of a component including; surface finish, load type, temperature, mean and residual stresses, stress concentrations and the material environment. In corrosive environments no material has been found to exhibit an endurance limit[1165].

In high cycle fatigue analysis there are two main cycle counting methods that have been applied successfully; reservoir counting and rainflow counting. While rainflow counting is considered the industry standard, reservoir counting is an alternative form of cycle counting suitable for short stress histories[118]. Cycle counting is employed to reduce a spectrum of fluctuating stresses to a simplified set of well-behaved stress reversals[119]. It is effective with broadband time series where large cycles are interspersed with small cycles that have varying mean load such that reversals become somewhat ambiguous for example in stochastic processes. The method allows complex situations with local stress reversals to be accounted for in a consistent manner. For fatigue calculations rainflow counting is generally deemed superior to other methods however, the main drawback is that it does not account for the sequence of stress cycles. Although studies show that the effect of the sequence tends to be diminished

when many time histories are considered and to date no better procedure exists[120].

The rainflow method defines a stress cycle as a closed stress or strain hysteresis loop which allows the mean and range of each stress cycle can be determined as shown in Figure 39 below. The data series is prepared for counting by selecting ‘peaks’ and ‘valleys’ with small, insignificant stress cycles being discarded. The rainflow algorithm then counts the number of closed stress hysteresis loops in the time series and the results are presented as a cycle count matrix of mean and alternating stress versus count. The wind turbine industry standard algorithm conforms to ASME E 1049-85 and has been employed for fatigue analysis for many years.

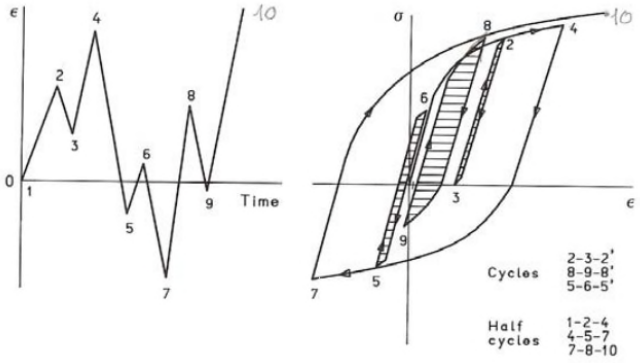

a) *b)*

Figure 39 - a) stress time series b) stress hysteresis loop[121]

2.3.3 Fatigue in Composites

The failure mechanisms associated with composite materials are more complex than metals, due to their anisotropic characteristics, such as delamination and interfacial de-bonding between the fibres and matrix[122]. Unlike metals their damage growth and failure mechanisms are not as well defined from an analytical perspective[113]. Fatigue causes extensive damage throughout the specimen volume leading to failure from general degradation[123]. Composite

failure generally grows from a damage zone where the failure mechanisms include fibre breakage, fibre pull-out, matrix cracking as well as delamination and de-bonding. The fatigue failure may be defined as either loss of adequate stiffness or of adequate strength. In GFRP damage commences with interfacial de-bonding which then tends to propagate under repeated load cycles to fibre breakage. Therefore resin stiffness is a key factor in controlling the propagation of cracks[111] Evidence for this comes from studies which show that epoxy resins, reinforced with glass fibres, are more fatigue resistant than vinyl-ester resins[124].

The static strength of composites is determined primarily by the fibre reinforcement orientation and the volume fraction between fibres and resin. The construction and orientation of the reinforcement plays a role in determining performance as generally larger quantities of thinner plies perform better than fewer layers of thick ply[125]. Conversely the fatigue strength under high cycle fatigue is determined by the properties of the polymer matrix[109]. A further complicating factor when considering the strength of tidal turbine blades is that studies carried out in both air and sea water show that sea water ageing of the composites reduces the fatigue life[126]. Glass fibres are prone to water diffusion over time when immersed in sea water which in combination with mechanical stress will result in premature failure[127]. This mechanism is known as stress corrosion cracking and is the most important feature of the fatigue life when immersed in sea water[128].

Immersion of both glass/epoxy and carbon/epoxy composites in sea water over prolonged periods will lead to water absorption by diffusion. Moisture diffusion into the matrix can plasticise and swell the polymer network which tends to decrease the surface free energy and increase the free volume thereby reducing the glass transition temperature[129]. This is a reversible process and the material will recover its properties once it has been dried out. However, on the other hand hydrolysis and micro-cracking can also occur after periods of long immersion. Hydrolysis leads to polymer weight loss and micro-cracking will cause degradation of the material properties and speed up the diffusion process. Water will diffuse into the polymer matrix even in the absence of

porosity and the diffusion rate is dependent upon the matrix chemistry. Although temperature controls the rate of diffusion the final equilibrium moisture content of the material is not dependent upon diffusivity[125]. Experimental measurements of the effect of sea water immersion has shown that both E-glass/epoxy and carbon/epoxy composites exhibit a similar level of weight gain. Although the rate of weight gain is temperature dependent a typical sample at 20°C would gain approximately 0.5% per year up to the saturation point as shown in Figure 40 below[130].

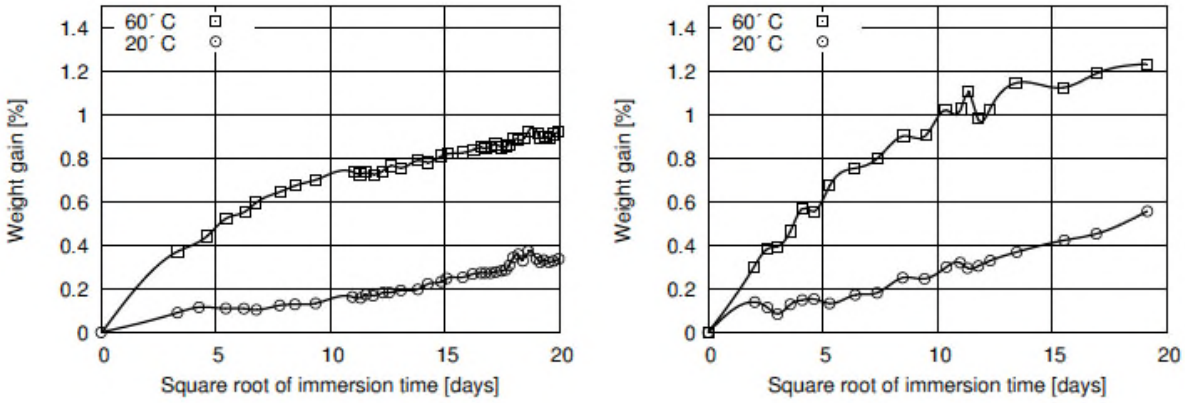

a) b)

Figure 40 - Rate of moisture diffusion a) E-glass b) carbon

The weight gain saturation point is dependent upon the resin material but tends to fall in the region of 1-5% of total weight[126]. As well as affecting the material static strength the fatigue life behaviour and mode of failure are also dependent upon sea water ageing as clearly illustrated in Figure 41 below which shows reduction in an E-glass/epoxy component flexural strength with immersion time. This demonstrates a 56% reduction in flexural strength after 100 days of immersion furthermore the failure mode changes from compression initially to tension by around 50 days[130].

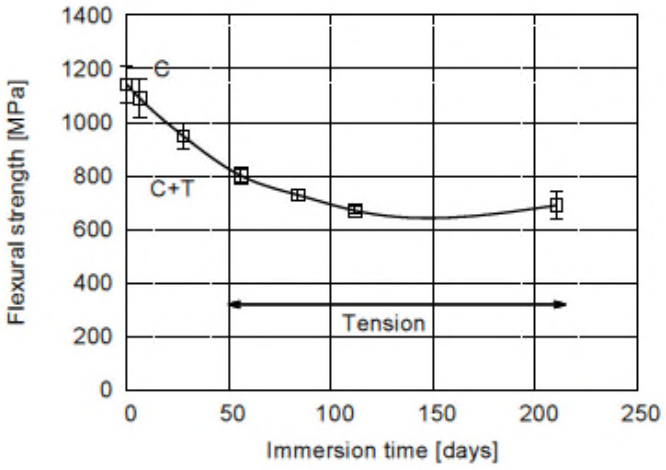

Figure 41 - Reduction in flexural strength

Furthermore the reduction in fatigue life for E-glass/epoxy is presented in Figure 42 where a new sample is compared with a sample aged for three months at 20°C. This shows a very large reduction in fatigue strength for the aged sample with samples failing at only 75% of the applied stress for 104 cycles in comparison with the new samples. Once again there was a failure mode change from compression to tension which suggests that there may be a stress corrosion mechanism underlies the reduction in strength[131].

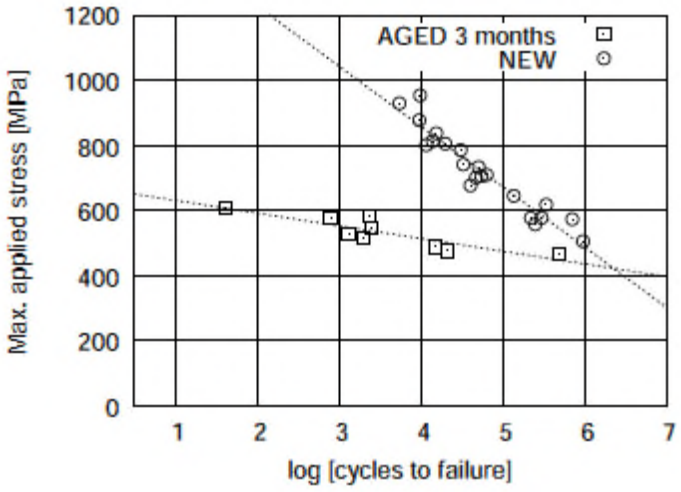

Figure 42 - Reduction in fatigue life

The nature of the fatigue load influences the life of the material depending upon the ratio between the cyclic amplitude and the mean stress, whether there is any significant off axis loading and also the sequence of the load cycles[132]. Studies have shown that in laboratory tests that random load spectra reduce component life by more than 50% as compared to an ordered load application[133].

2.4 Control Theory

Proportional Integral Derivative (PID) controllers are very commonly implemented in a wide variety of engineering applications for the control of plant. A typical example of a simple control model is shown schematically in Figure 43. PID control is predicated on the feedback of the value of the variable under control to the controller. This allows for comparison of the measured output with the desired operating point, known as the set-point, so that a change can be made to the system to adjust the output towards the set-point. The level of the response is based upon the difference between the set-point and the measured variable, known as the system error. The controller will apply corrective action such that the error tends to zero.

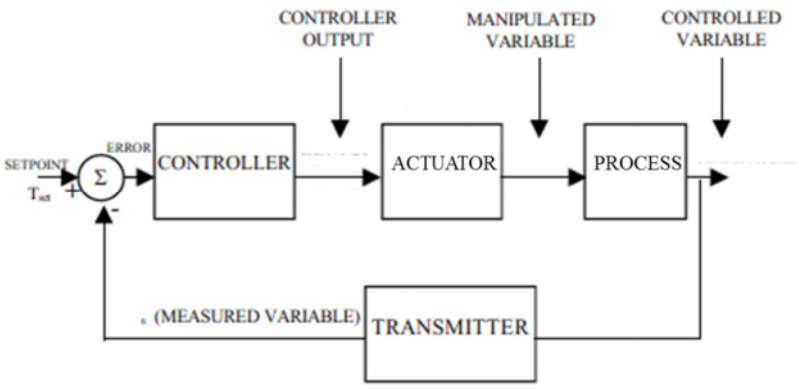

Figure 43 - Typical feedback control loop[134]

The controller can utilise Proportional, PI (Proportional-Integral) or PID control depending upon the dynamic response of the system. The controller output

determines how the actuator responds to physically alter the process. The output of the process is measured and then fed back to the controller.

When modelling control systems the Laplace transform is generally used to represent the dynamic relationship between the input and output of the process.

$$\boldsymbol{F(s) = \int_0^\infty f(t)e^{-st}\,dt} \qquad \textbf{Equation 34}$$

Where F(s) is the Laplace transform and f(t) is the inverse Laplace transform. S is known as the Laplace variable. This is useful when considering a system that is modelled as a first order differential equation in the form:

$$\boldsymbol{a_1\frac{dx(t)}{dt} + a_2x(t) = b_1u(t), x(0) = 0} \qquad \textbf{Equation 35}$$

Where u is the input variable and x is the output variable. Taking the Laplace transform of each side gives:

$$\boldsymbol{a_1[sx(s) - x(0)] + a_2x(s) = b_2u(s)} \qquad \textbf{Equation 36}$$

Rearranging in terms of the input variable:

$$\boldsymbol{x(s) = \left(\frac{b_1}{a_1s+a_2}\right)u(s)} \qquad \textbf{Equation 37}$$

Which can be simplified to:

$$\boldsymbol{x(s) = \frac{K}{\tau s+1}u(s)} \qquad \textbf{Equation 38}$$

Where K is defined as the gain of the system and τ is the time constant.

$$\boldsymbol{G(s) = \frac{K}{\tau s+1}} \qquad \textbf{Equation 39}$$

This expression is called the system transfer function and captures the dynamic between the input and output variables. This is an effective way of modelling the process element of the system.

In terms of the control model this is generally written in the ideal form as:

$$\boldsymbol{m(t) = K\left[e(t) + \frac{1}{\tau_I}\int e\,dt + \tau_D\frac{de}{dt}\right]} \qquad \textbf{Equation 40}$$

Where e is the system error. While the proportional control element is present in all control systems the addition of an integral and derivative term may be beneficial. The integral term accounts for the accumulated error in the past to reduce the steady state error of a controller output due to a constant disturbance that cannot be corrected for by using proportional control alone. The derivative term takes consideration of the rate of change in the error and will change the controller gain in response which tends to add stability to the system.

A feedback controller will alter the stability characteristics of a system which is a crucial feature in control modelling. There are a number of techniques to assess stability but the most common approach was developed by a combination of Zeigler and Nichols (Z-N). The Z-N standard method provides the values shown in Table 2 below in order to design the controller[135].

Controller	K_p	τ_i	τ_d
P	$0.5K_u$	-	-
PI	$0.45K_u$	$\tau_u/1.2$	-
PID	$0.6K_u$	$\tau_u/2$	$\tau_u/8$
Some overshoot	$0.33K_u$	$\tau_u/2$	$\tau_u/3$
No overshoot	$0.2K_u$	$\tau_u/2$	$\tau_u/3$

Table 2 - Zeigler-Nichols feedback coefficients [149]

The application of these coefficients in the model assumes a controller transfer function of the form:

$$G(s) = K_p\left(1 + {}^{\tau_i}/_{s} + {}^{\tau_d}/_{s}\right)$$

Equation 41

Where K_p is the system gain and τ_i and τ_d are the integral and derivative time constants respectively. Thus the proportional, integral and derivative terms are additive and must be summed by the controller to deliver the disturbance rejection. In order to assess the performance of the controller quantitative measures must be applied to analyse the system response. The Figure 44 below illustrates the system reaction with feedback control where A is the change in process variable, B is the amplitude of the first peak in overshoot and C is the second peak. The settling time is the time taken for the system to reach within 5% of the new steady state value also known as the 95% response time. From these definitions several performance metrics can be calculated including the Overshoot ratio:

$$OR = \frac{B}{A}$$

And the Decay ratio:

$$DR = \frac{C}{B}$$

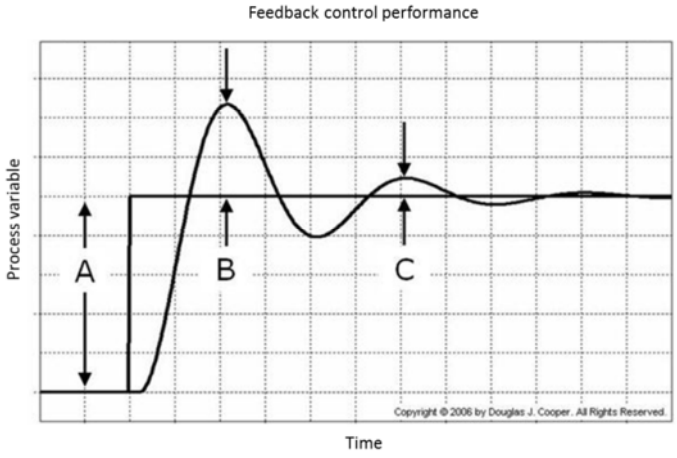

Figure 44 - Feedback performance

In many systems, including the standard Z-N tuning approach, the design value for the decay ratio is 0.25 which means the system is somewhat underdamped and will exhibit overshoots before the disturbance is dampened out completely.

In the case of the Deltastream overshoots are not welcome as this will add to the cyclic load profile and further shorten the device service life.

3 Methodology

This chapter outlines the methodology used to design and analyse the Deltastream tidal turbine in terms of performance, fatigue life and operability in turbulent flows. The literature survey conducted in Chapter 2 cited the various key elements involved in the modelling of the turbine in terms of the fluid environment, computation of the hydrodynamic loads and the fatigue modelling of the composite blades. This chapter outlines how these elements have been used to build a model and develop a process to capture the interaction of the turbine with the turbulent flow in Ramsey Sound. The modelling of the turbine is broken into five distinct sections; 1) hydrodynamic turbine model, 2) turbulent flow field model, 3) turbine control model, 4) stress analysis procedure and the 5) fatigue life analysis. The first three models have been integrated to provide a time dependent method of calculating turbine loading in turbulent flow that produces a series of rotor loads. It should be noted that the turbulent flow field generator, known as Turbsim, is a code developed at Sandia National Laboratories and is discussion in detail in section 3.4.7. The fourth and fifth models are used in a post-processing scheme to estimate fatigue life based on these load simulations as a means of comparing the damage caused by a particular set of flow and turbine variables. Each of the five aspects of the modelling process are described here in terms of the practical implementation of the theory and the justifications for assumptions made in adopting or simplifying a procedure.

3.1 Modelling overview

The proceeding section lays out the key aspects of the construction of the hydrodynamic code which was assembled in parts from the literature review of helicopter and wind turbine aerodynamics. The description of the way in which the code computes blade loads and details of the sub-models used to enhance the classic momentum theory are presented. This is followed in Chapter 4 with

a number of validation studies which are used as the means of determining the accuracy of the code and to draw attention to any potential weaknesses.

The hydrodynamic code cannot be viewed in isolation from the turbulence inflow model or the turbine speed control model. To aid in the introductory explanation a simplified flow diagram of the structure and organisation of the model is presented in Figure 45. This shows how the Matlab scripts that build the code interact with each other and with the text files used to store inputs and outputs to and from the code. The main script (1) is used to control the interaction of the models in terms of the flow of data and the scheduling of the calculation steps. The hydrodynamic code has been written in time marching formulation to take advantage of the form of the turbulent flow data delivered from the Turbsim model which is initially produced as a large three dimensional matrix and then converted by the code for distribution to the hydrodynamic calculation stages in discrete time steps of the evolving turbulent flow. When a simulation is started using script (2) the data from the user generated simulation input file is read into the main script (1) to prime the simulation by loading all data from input and properties files and a Turbsim input file is automatically generated. The Turbsim executable (3) is then called to run to create a dataset in accordance with the input file just created. A full description of the Turbsim model follows later in this chapter. Once the Turbsim model has completed its runtime execution the main script initiates the translation algorithm of the flow data from the binary data files and then loads the three flow velocity components into the Matlab workspace. In a separate operation the stall delay model translates the 2D static airfoil data to a 3D approximation for use with the momentum model. The 3D data is then stored for future use in other simulations if required. Once this point has been reached the simulation has been initialised and the main time marching algorithm instigates within a while loop that runs for the duration of the availability of turbulent flow field data.

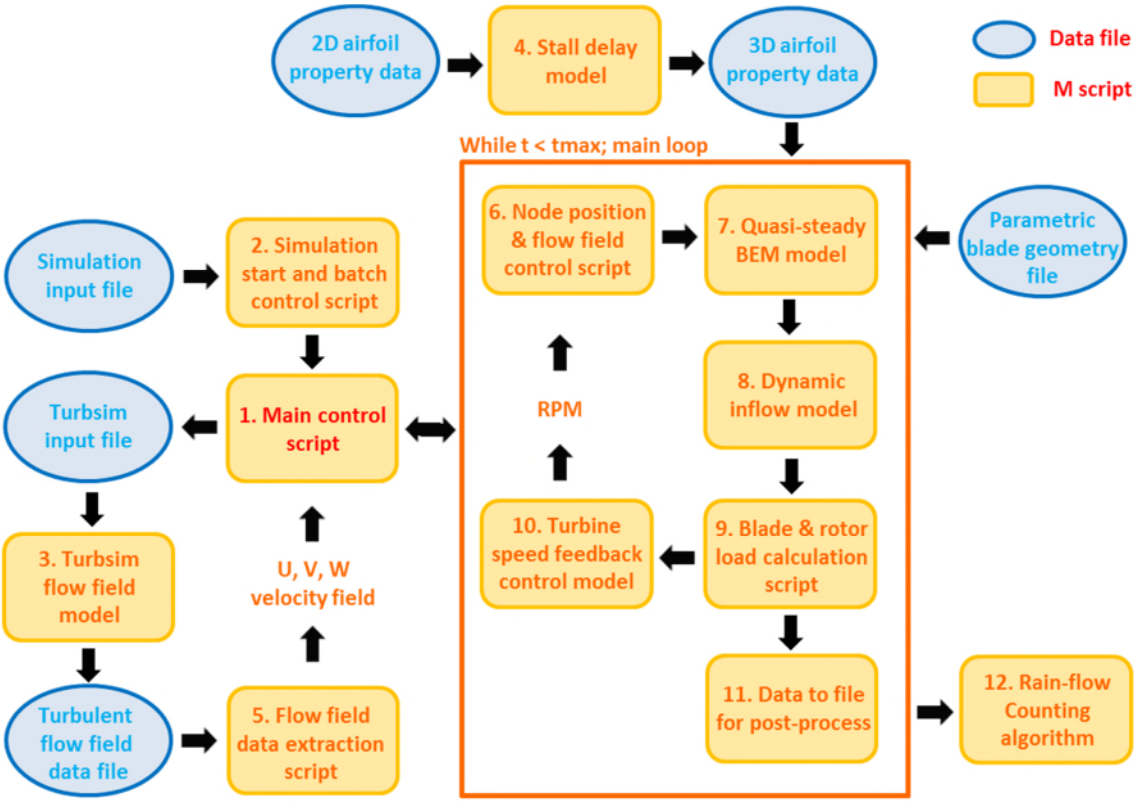

Figure 45 - Simplified flow diagram of Matlab model

The calculation nodes are assigned flow data at each time step using script (6) which tracks the turbine node positions dependent upon their rotation in space to allow two dimensional interpolation of the flow to match with blade position. This ensures each calculation node has a new velocity vector assigned each time step in accordance with the position of the rotor in terms of the flow plane. This data is then fed through scripts (7), (8) and (9) which carry out the calculations of the hydrodynamic model algorithm so that the blade and turbine loads are determined at which point the data is written to an asci file by the script (11). The Quasi-steady model uses the classical BEM formulation written in a time marching scheme. This reacts instantaneously to changes to the inflow conditions with no respect for the rate of change or total magnitude of the change. Modelling of the time dependent effects of changes to the inflow are modelled using the dynamic inflow model with the quasi steady BEM result being the input to this model. The turbine control model (10) uses the torque calculation output of (9) to determine the rotor speed response to the time step load and apply a correction via the controller gain within the feedback loop to try

and match the turbine RPM with the control set point. This new rotor speed then becomes one of the inputs to (6) at the start of the next time step. At this point the blade loads are available for post-processing in terms of stress analysis, rainflow counting and fatigue life calculations. With the basis of the model now in context the proceeding sections cover in much greater detail the operation of each element.

3.2 Hydrodynamic model

3.2.1 Blade Element Momentum Theory

The core of the model calculates the loads upon each rotor blade for a set of input conditions. The input conditions include; the parametric geometry of the blade, aerodynamic section data (Cl and Cd) and the incident flow velocity to the rotor plane. Momentum theory is applied to determine the relative flow velocity (W) to each airfoil section then element theory is used to calculate the lift and drag forces. Finally the forces are integrated over the length of each blade to determine the torque and thrust loads.

In order to calculate the relative flow velocity vector so element theory can be applied, the axial and tangential induction factors, a and a', must be determined (see below). In

Figure 16 the plane of rotation is perpendicular to the direction of thrust.

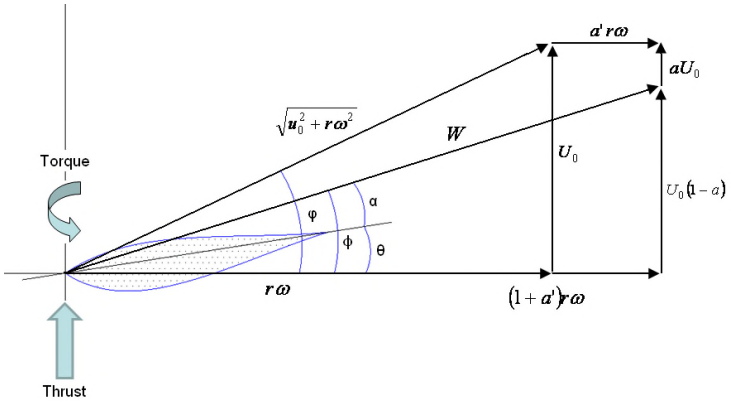

Figure 46 - Airfoil velocity triangles

Here U_o refers to the axial fluid flow velocity and rω is the velocity of the blade. The relative flow velocity over the section, W, is at a flow angle, Φ, to the plane of rotation. The flow angle is the sum of the angle of attack, α, of the airfoil and the twist angle, θ, of the blade, which changes over the length of the blade. The lift and drag coefficients are applied to the relative flow velocity and local chord in order to calculate lift and drag forces on each section.

Determination of the axial and tangential flow factors is achieved through a process of iteration. In order to calculate the relative flow velocity over the section the flow angle, Φ, must be known, however this is a function of the induction factors. Therefore an initial guess of the induction factors is made and applied to the BEM algorithm. The outputs of the algorithm are the new values of the induction factors which are applied to the next iteration. Upon convergence the induction factors are used to predict the flow angle over the section in order that the angle of attack can be determined. For a given airfoil section for which the lift and drag coefficients are known in terms of α, it is possible to determine the loads on the section caused by lift and drag.

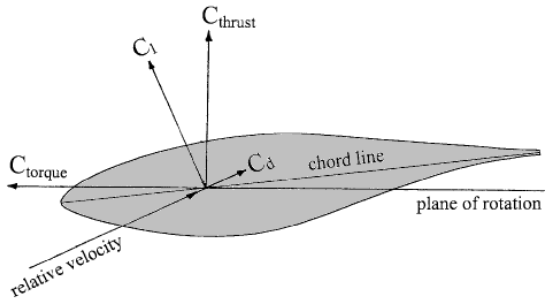

Figure 47 - Radial section loads

Figure 17 shows the load vectors as determined by element theory, where C_l and C_d are the lift and drag coefficients. The torque (C_{torque}) and thrust (C_{thrust}) coefficients are parallel and perpendicular respectively to the plane of rotation of the blade and it is these that are used to determine the power and thrust of the rotor. This approach is applied to each element over the length of each blade if the inflow velocity and rotor velocity are known. By integrations over the length of the blades the total blade thrust and torque forces can then be determined. The rotor power is a function of the torque and speed of the rotor.

As previously discussed the induction factors are determined using momentum theory in order to calculate the relative flow velocity. The following is an outline of the iteration process used to calculate a and a'. The initial values of a and a' are substituted into:

$$\boldsymbol{\Phi = \mathbf{atan}\left[\frac{U(1-a)}{\omega r(1+a')}\right]}$$

Equation 42

Here Φ is the local flow angle onto the rotating blade. From this angle of attack, α, can be found from:

$$\boldsymbol{\alpha = \Phi - \theta}$$

Equation 43

Where θ is the local twist angle of the blade. The lift and drag coefficients are calculated by interpolation. The appropriate coefficient is matched with the angle of attack from a lookup table linked to the appropriate airfoil. Next the thrust and torque coefficients are calculated as follows:

$$C_{thrust} = C_l cos\Phi + C_d sin\Phi$$

$$C_{torque} = C_l sin\Phi - C_d cos\Phi$$

Equation 44

The induction factors are shown in a simplified form as follows:

$$a = \frac{g1}{1+g1}$$

Equation 45

$$a' = \frac{g2}{1-g2}$$

Equation 46

Where a is the axial induction factor and a' the tangential induction factor.

The use of g1 and g2 is for algebraic simplicity only and are defined as:

$$g1 = \frac{cB}{8\pi F r sin^2\Phi}\left[\frac{\left(C_{thrust} - \left(cBC_{torque}^2\right)\right)}{(8\pi r sin^2\Phi)}\right]$$

Equation 47[136]

$$g2 = \frac{cBC_{torque}}{8\pi r sin\Phi cos\Phi}$$

Equation 48

Where B is the blade number, c is the local chord length and r is the radial blade position. The tip loss factor, F, is calculated from:

$$F = \frac{2}{\pi} acos(e^{-f})$$

Equation 49

Where f is as below:

$$f = \frac{1}{2} B\left[\frac{(R-r)}{r sin\Phi}\right]$$

Equation 50

The tip loss factor is used to account for the loss in lift at the blade tips due to three dimensional effects associated with the vortex wake that is not modelled by BEM theory. A relaxation scheme has been applied to the algorithm in order to aid convergence. In numerical algebra implementation of successive relaxation is a means to solve linear systems of equations that results in fast convergence.

The relaxation is applied as follows:

$$a_{new} = a + w(a_{initial} - a)$$

$$a'_{new} = a' + w(a'_{initial} - a')$$

Equation 51

Here w is the relaxation factor. It was found that when w = 0.2 convergence was always stable. These new induction factors are then used in Equation 42 as part of the new iteration loop. The results of the iteration procedure are monitored until the difference between the new and previous results drops below a predefined value, at which point the process is halted. Then the thrust and torque coefficients are recalculated and are used as inputs to calculate the blade loads. The relative flow velocity is calculated as:

$$W = \sqrt{{U_o}^2(1-a)^2 + r^2\omega^2(1+a')^2}$$

Equation 52

The lift and drag forces can then be computed from:

$$L = \frac{1}{2}\rho c C_l W^2$$

Equation 53

$$D = \frac{1}{2}\rho c C_d W^2$$

Equation 54

The section thrust and torque forces are then determined using the lift and drag forces:

$$P_{thrust} = Lcos\Phi + Dsin\Phi$$

Equation 55[137]

$$P_{torque} = L\,sin\Phi - Dcos\Phi$$

Equation 56

By summation of the sectional thrust forces, P_{thrust}, over the length of the blade the total blade thrust is determined. Similarly the total torque on the blade is determined by summing the sectional torque forces, P_{torque}, and multiplying by the radial position.

The coefficient of performance, C_P, is a measure of how much power the rotor extracts from the total available kinetic flux and is calculated as follows:

$$C_P = \frac{P_{rotor}}{0.5\rho A U^3}$$

Equation 57

In Equation 57, A is the total swept area of the rotor and U is the mean flow speed through the swept area. The thrust coefficient is calculated in a similar manner:

$$C_T = \frac{T_{rotor}}{0.5\rho A U^2}$$

Equation 58

This is the ratio of rotor thrust to total thrust that can be exerted on a solid disc in the flow of swept area A. It is possible that the value of C_T can exceed unity for a heavily loaded rotor at high TSR.

3.3 Unsteady hydrodynamic code

The following sections break down the individual models used within the hydrodynamic code.

3.3.1 Velocity flow field matrix

The inflow conditions to a turbine are critical to the behaviour of the device as this is what drives the rotor. As previously discussed the velocity distribution in a tidal channel varies enormously in space and time due to a number of dynamic effects. The fluctuations in the inflow conditions occur over a wide range of frequencies depending upon the mechanism driving the flow. Turbulence eddies of a length scale that affects the rotor load occur on a time scale of several seconds which is similar to the surface wave induced velocities that permeate to the depth of the rotor. Furthermore, the velocity shear profile of the channel varies with current velocity over a timescale of minutes to hours. An effect not

caused by the tidal environment is the velocity deficit upstream of the turbine tower caused by the blockage to the flow. Due to rotational sampling the blades experience a fluctuating load which is dependent upon the rotor speed. Therefore, before the blade loads can be calculated the overall velocity flow field must be represented in the code in a manner that closely resembles the tidal environment. Control over the parameters governing the flow field is also important in order that different aspects can be studied and related with how the turbine behaves.

The code represents the flow field based upon the diameter of the turbine rotor being studied. An empty square matrix of dimensions equal to the rotor diameter is created initially and then populated with values of flow depending upon which flow models are active to create a matrix of the overall flow field at the rotor plane. Currently the code has five different flow sub-models that can be used to build up a complex flow velocity array. All the models calculate the velocity profiles based upon the size of the flow field so that the spatial distribution of velocity magnitude is not distorted.

3.3.2 Shear profile model

The velocity depth profile of the channel is based upon a power law description of the form:

$$U_{current} = U_{surface}\left(z/d\right)^{1/n}$$

Equation 59

The profile models the velocity shear profile with depth where z is the depth below the surface and d is the total channel depth. The constant n varies depending upon the state of the tide but generally a value of 7 – 10 is used for most flows. If the site specific data is available the exponent can be time-dependent to better model how the shear profile changes with current velocity and turbulence intensity. Site specific data of average shear profiles are presented in section 3.4.6.

3.3.3 Dynamic Inflow model

The dynamic inflow solver sub-model (see section 2.1.5.2) was incorporated into the time-marching unsteady BEM code in the following manner as developed by Øye[138]. The two differential equations are re-written in terms of the induced velocity, W:

$$\boldsymbol{W_{int} + \tau_1 \frac{dW_{int}}{dt} = W_{qs} + k\tau_1 \frac{dW_{qs}}{dt}}$$

Equation 60

$$\boldsymbol{W + \tau_2 \frac{dW}{dt} = W_{int}}$$

Equation 61

Where W_{int} is the intermediate velocity, W_{qs} is the quasi-steady velocity calculated by the BEM algorithm and W is the filtered time dependent induced velocity. The analytical solution of this velocity is calculated assuming the time-step is small compared to the time scale of the filter:

$$\boldsymbol{H = W_{qs}^{i} + k\tau_1 \frac{W_{qs}^{i} - W_{qs}^{i-1}}{\Delta t}}$$

Equation 62

$$\boldsymbol{W_{int}^{i} = H + \left(W_{int}^{i-1} - H\right) exp\left(\frac{-\Delta t}{\tau_1}\right)}$$

Equation 63

$$\boldsymbol{W^{i} = W_{int}^{i} + \left(W^{i-1} - W_{int}^{i}\right) exp\left(\frac{-\Delta t}{\tau_2}\right)}$$

Equation 64

The filtered value of the induced velocity is then used to calculate the relative flow velocity and blade angle of attack so that the node loads can be determined in the same manner as when using the equilibrium wake formulation of the unsteady BEM code. The effects of this model are only observed when the inflow conditions to the blade change by a considerable magnitude and frequency. If the inflow conditions are constant in time the value of W is equal to W_{qs} as the time-dependent variables within the differential equation tend to zero

in this case. Validation of this model as implemented in the BEM code is presented in a later section (CEC JOULE 1 project).

The sub-model was incorporated into the time-marching unsteady BEM code in the following manner as developed by Øye[139]. The two differential equations are re-written in terms of the induced velocity, W:

$$\boldsymbol{W_{int} + \tau_1 \frac{dW_{int}}{dt} = W_{qs} + k\tau_1 \frac{dW_{qs}}{dt}}$$

Equation 65

$$\boldsymbol{W + \tau_2 \frac{dW}{dt} = W_{int}}$$

Equation 66

Where W_{int} is the intermediate velocity, W_{qs} is the quasi-steady velocity calculated by the BEM algorithm and W is the filtered time dependent induced velocity. The analytical solution of this velocity is calculated assuming the time-step is small compared to the time scale of the filter:

$$\boldsymbol{H = W_{qs}^{i} + k\tau_1 \frac{W_{qs}^{i} - W_{qs}^{i-1}}{\Delta t}}$$

Equation 67

$$\boldsymbol{W_{int}^{i} = H + \left(W_{int}^{i-1} - H\right) exp\left(\frac{-\Delta t}{\tau_1}\right)}$$

Equation 68

$$\boldsymbol{W^{i} = W_{int}^{i} + \left(W^{i-1} - W_{int}^{i}\right) exp\left(\frac{-\Delta t}{\tau_2}\right)}$$

Equation 69

The filtered value of the induced velocity is then used to calculate the relative flow velocity and blade angle of attack so that the node loads can be determined in the same manner as when using the equilibrium wake formulation of the unsteady BEM code. The effects of this model are only observed when the inflow conditions to the blade change by a considerable magnitude and frequency. If the inflow conditions are constant in time the value of W is equal to W_{qs} as the time-dependent variables within the differential equation tend to zero

in this case. Validation of this model as implemented in the BEM code is presented in a later section (CEC JOULE 1 project).

3.4 Analysis of Turbulent Flow

3.4.1 Velocity Measurements

The data used in this analysis was gathered from Ramsey Sound at the location that Deltastream is to be installed over a 28 hour period that included five peak flows, two in Ebb and three in Flood. The sampling rate was 2Hz and the data was separated into 10 minute sets of 1200 velocity measurements to ensure stationary statistics. This is trade-off between acquiring a data set long enough for reliability in the calculation of the turbulence characteristics but not too long that it included any component of the semi-diurnal frequency. The mean flow velocity for each bin at the turbine hub height is shown in Figure 48 below. The positive velocity values refer to the Flood tide which runs north to south and the negative values refer to the Ebb tide whose direction is almost 180° to the Flood.

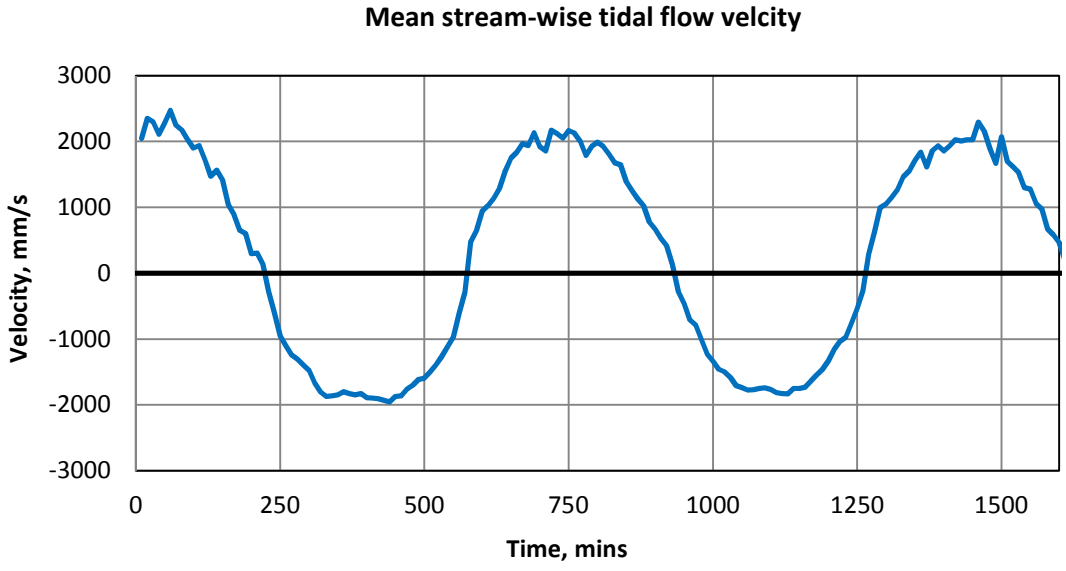

Figure 48 - Mean hub flow

The data is captured over a spring tide which ensures a wide range of flow velocities are available for analysis. The Flood tide peak velocities tend to be approximately 20% higher than for the peak Ebb flow which suggests that a higher energy content of up to twice the kinetic flux is available. However, detailed analysis shows that the Flood tide has a much higher level of turbulence than the Ebb which will result in much larger dynamic turbine loads.

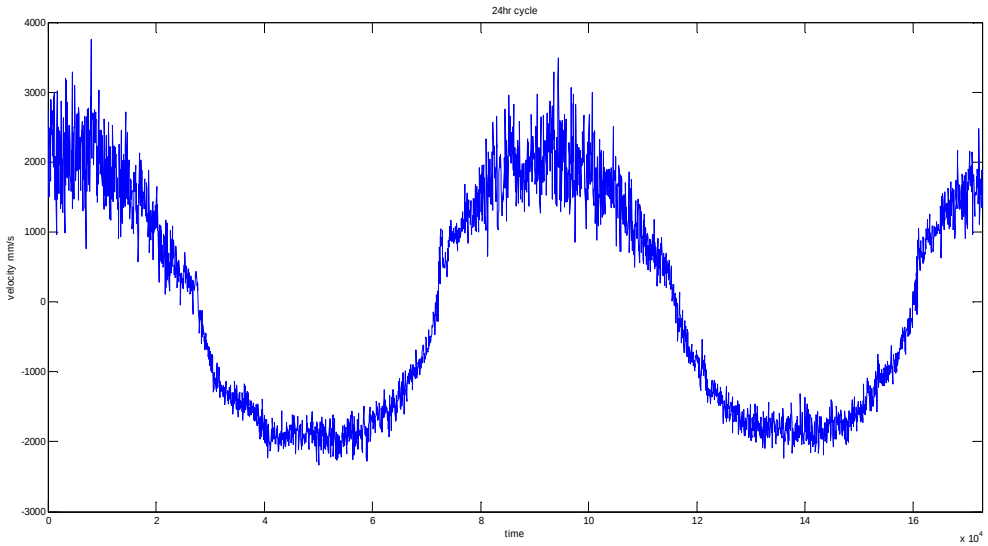

Figure 49 - Hub flow with turbulence

Figure 49 above shows the same plot as Figure 48 but without any averaging to reduce the velocity to its stationary mean which intuitively demonstrates the unsteadiness of the velocity. First to be noticed is the large fluctuations in velocity around the mean value which are almost equivalent to the mean velocity, secondly these fluctuations occur at a high frequency on the order of a few seconds which suggests a rapidly changing flow environment. Finally, there is a marked difference in the level of unsteadiness between the Flood flow and the Ebb flow suggesting the turbulence strongly dependent upon flow direction.

In order to understand the velocity distribution for both the Ebb and Flood flows a histogram of velocity magnitude is plotted in Figure 50 for the Ebb and Figure 51 for the Flood. Overlaid on each histogram is a Gaussian probability distribution function conforming to the variance and mean values of the velocity data set. In both cases the distribution of velocity appears in close agreement

with the normal distribution for all three Cartesian directions. Further analysis of the stationary statistics reveals that the Flood velocity distribution has a much larger variance than the Ebb as shown in Table 3 below. This is a quantification of the spread of the data from the mean value and confirms what can be observed qualitatively in Figure 49. Furthermore the standard deviation of the Flood data is considerably higher than the Ebb which indicates a wider spread of the bulk of the data around the mean.

Stream-wise	Ebb	Flood
Stnd Dev.	0.175	0.495
Variance	3	25
Skew	0.064	0.325
Kurtosis	2.9	3.6

Table 3 - stationary properties

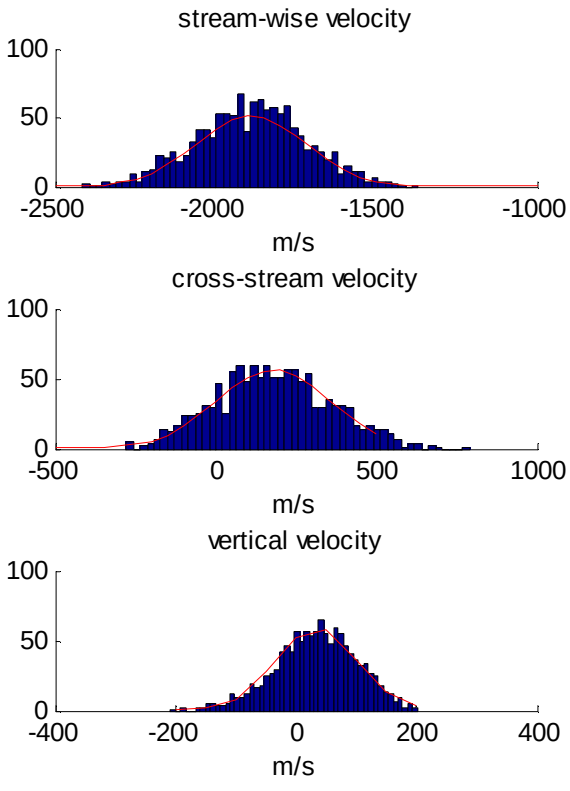

Figure 50 - Ebb velocity PDF

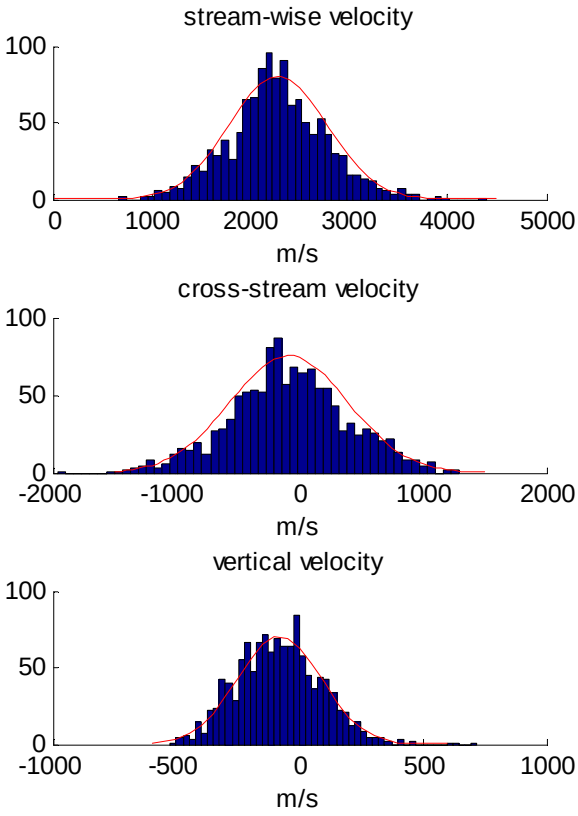

Figure 51 – Flood velocity PDF

Although the Flood flow velocities exhibit a much greater variability than the Ebb flow an evaluation of the kurtosis of both data sets shows that the distribution is not peaked to favour a particular velocity. Both the Flood and Ebb flows have a kurtosis value close to 3 which is expected for a normal distribution. The skewness value of the Flood data indicates a slight skew in favour of higher flow velocities although the magnitude is small while there is no skew associated with the Ebb data. However, possibly the most important consideration from this analysis is the ratio of the standard deviations for each flow.

Tide	σ_u	σ_v	σ_w
Flood	0.175	0.128	0.084

Ebb	0.495	0.208	0.079

Table 4 - velocity component standard deviation

Therefore the standard deviation ratios for each tide are 1:0.42:0.16 for Flood and 1:0.73:0.48 for Ebb. This indicates the turbulence is anisotropic and the Ebb tide ratio is very similar to the values used for the Kaimal spectra (see Chapter 2). The stream-wise component of the Flood tide appears to be far more dominate in comparison to Ebb but spectral analysis is required for further comparison in this respect.

3.4.2 Turbulence Intensity

Another very important statistic used to classify turbulence is the turbulence intensity of the flow. This is the ratio of the r.m.s. of the instantaneous velocity to the mean velocity and is defined as follows:

$$TI = \frac{\sqrt{\frac{1}{3}(u'^2+v'^2+w'^2)}}{\bar{U}} \quad 141$$

Equation 70

Where u' is the instantaneous fluctuating component of the flow and $\bar{U}$ is the mean of a stationary data set (for a given channel depth over the 10 minute period of the data set).

The TI was determined for each of the 10 minute data sets for both the Ebb and Flood flows over the extent of the rotor plane for three of the depth bins (bins 2, 10 & 17) to understand the distribution of turbulence in the channel. Figure 52 shows the TI for the hub height bin against flow speed for the Ebb tide. This shows there is strong link between TI and flow velocity with TI decreasing for increases in flow speed above mean flows of 1m/s. Flows below 1m/s are largely irrelevant to tidal turbine due to the low power density. Therefore turbulence in the turbine working flow range is between 5.5 and 11.5% which are very similar to the values taken from literature as discussed in Chapter 2.

Observations from several site surveys indicate that the turbulence can lie anywhere between 3.2 and 11.4% with 8-10% being typical but this is dependent upon flow velocity and direction of tide.

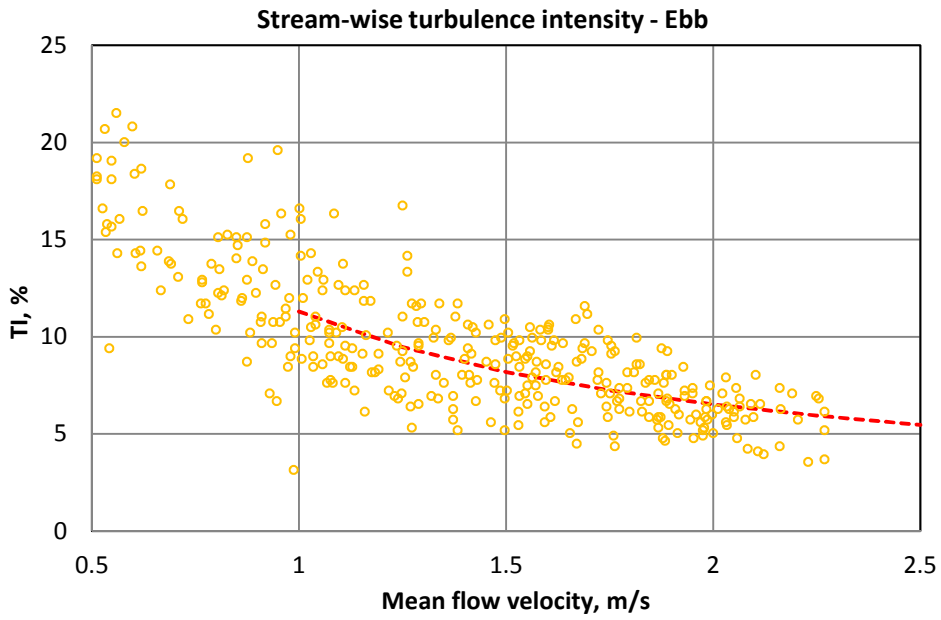

Figure 52 - TI Ebb flow

In contrast for the same plot of Flood tide TI the distribution is not as strongly correlated with flow speed as shown in Figure 53. For flow above 1m/s as flow speed increases TI does not decrease as quickly and there is greater variability around the mean line. The turbulence level is also much higher than the Ebb tide ranging from 13-19% which is also much higher than many of the reported literature sources. This is evidence to support the hypothesis that mechanisms other than classical boundary layer shear is contributing to turbulence in the Flood tide direction. For example large scale bathymetry and topology will generate turbulent structures as described by Figure 54. This is further supported by Figure 8 (Chapter 1) which shows a map of Ramsey Sound. The Deltastream turbine will be positioned at the head of the channel. Therefore on Flood tides (South to North flow) the flow will be obstructed by all the

bathymetric features of the tidal channel. This includes a line of large rocks which protrudes mid-way into the channel that will generate large scale vorticity. The Flood tide is therefore not a representative example of turbulent flow in tidal channels.

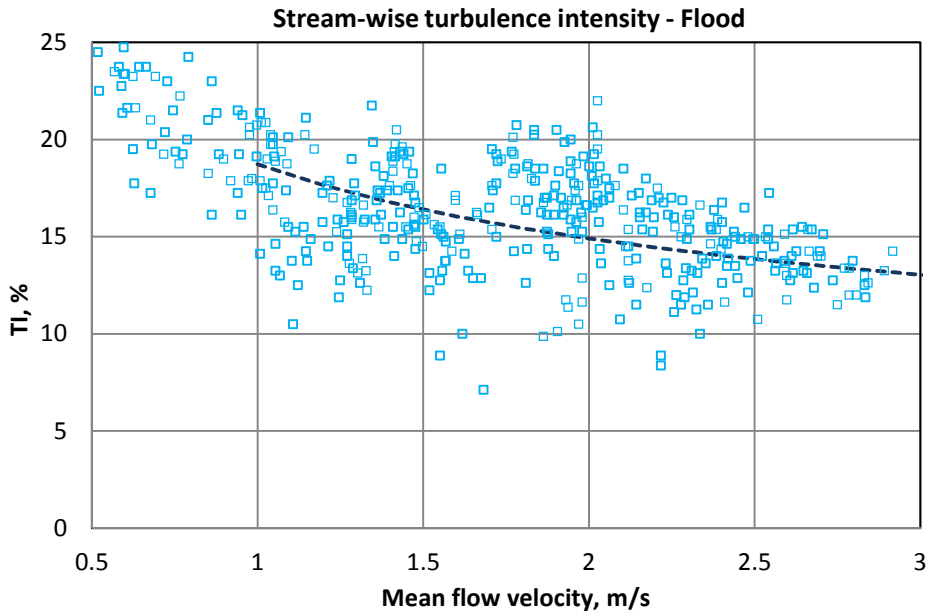

Figure 53 - TI Flood flow

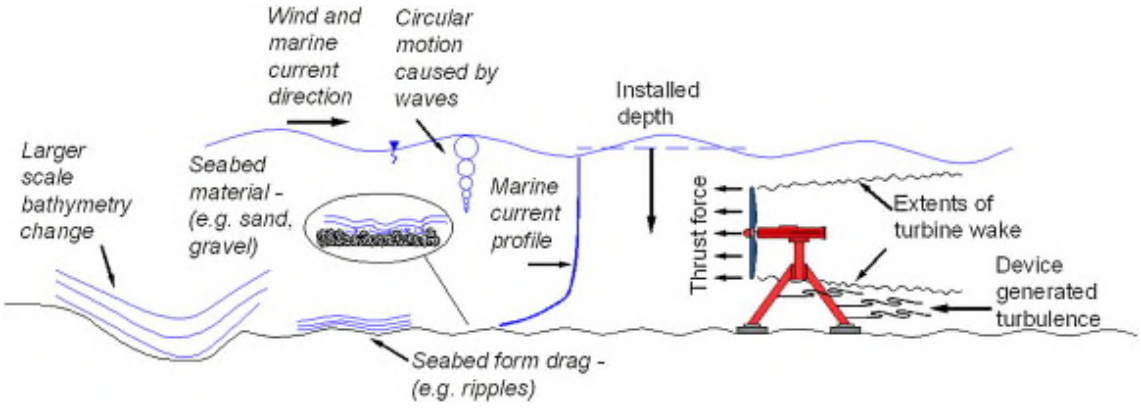

Figure 54 - Mechanisms of turbulence generation[140]

The TI was also examined in terms of channel depth to determine if its behaviour changes over the rotor inflow plane. There is little evidence of any correlation for the Flood tide however the data from the Ebb flow shown in Figure 55 indicates that TI increases with depth. For a mean velocity of 2m/s the TI in the Ebb flow is 10% at BDC and around 6-7% at hub height and at TDC. This would be expected given that sea bed friction is driving the height of the turbulent boundary layer. This also matches with observation from the Puget Sound that showed that the differences in turbulence across the rotor plane were not particularly significant although it is possible to determine the area weighted average as described in Chapter 2

Understanding how the turbulence relates to flow speed allows for calculation of the number of hours per year a turbine will experience a particular level of turbulence. It is critically important to adequately model the turbulence level of the flow as it is the key driver in high cycle fatigue loading on the device. If the approach taken is too conservative in estimating the turbulence level it will dramatically affect the design of the device in favour of stronger components which will naturally drive up the cost of energy.

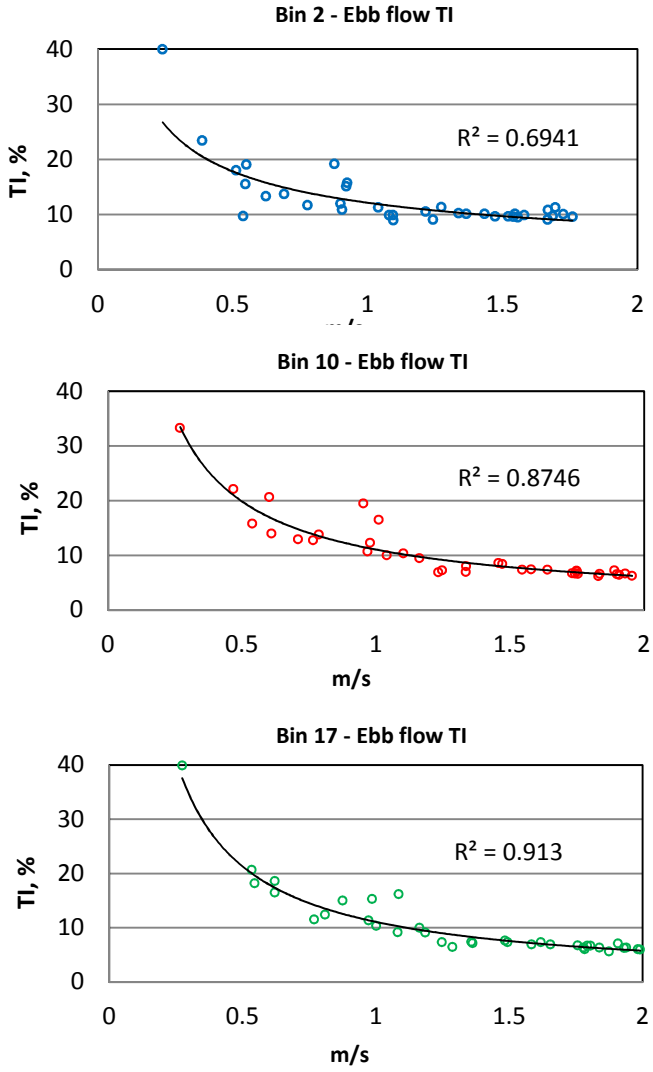

Figure 55 - TI depth behaviour Ebb

3.4.3 Integral length scales

Turbulent motion occurs over a range of velocities and length scales known as the energy cascade as turbulent flow is composed of eddies of many different sizes. An eddy is described as a localised region in the flow of coherent fluid motion which has a characteristic size and velocity. As the flow is unstable the largest eddies break up and their energy is transferred into smaller eddies in an inviscid manner. This process repeats itself down the range of length scales

until the eddies become small and the kinetic energy is dissipated through molecular viscosity at low Reynolds numbers.

Characterisation of the larger scale turbulent motions is achieved by determining the distance over which the longitudinal flow velocity is correlated. This is accomplished by applying a two point auto-correlation function to two sets of velocity measurements which have been recorded simultaneously at some distance apart. The resulting cross correlation coefficient is an indication of the strength of the relationship of the two velocities sets. With the ADCP data the Pearson product moment coefficient is used which is defined as follows:

$$R_{xy} = \frac{cov(X,Y)}{\sigma_x \sigma_y} = \frac{E\left[(X-\mu_x)\left(Y-\mu_y\right)\right]}{\sigma_x \sigma_y}$$

Equation 71

Where X and Y are the random variables, cov is the covariance function of the random variables, σ is the standard deviation and μ is the expected value of the random variables.

The longitudinal integral length scale is defined as the integral of the cross correlation function with respect to the distance between the measurements as follows:

$$L_{11}(x,y,r) = \int_0^\infty R_{xy}(x,y)dr$$

Equation 72

Where x and y are the velocity data sets separated by some distance r. This can be solved by calculating the area under the curve of the correlation function shown in Figure 56 below. This shows the values of R_{xy} plotted against r, the spacing between the measurements, and clearly demonstrates how the strength of the relationship between measurements decreases with spacing as the signals become less similar with distance.

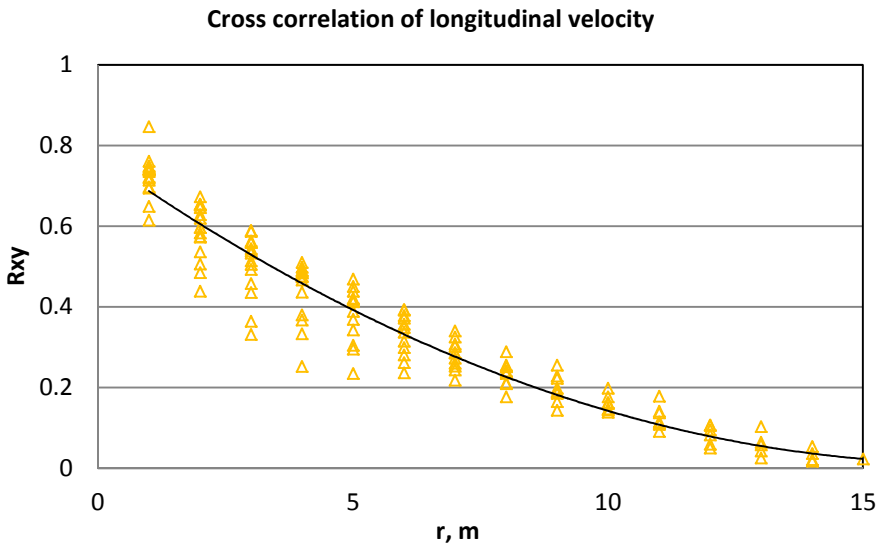

Figure 56 - Cross correlation coefficient

The integral length scale was calculated for both the Ebb and Flood flow for a number of the stationary data bins using this technique applied to the stream-wise velocity of the 18 depth bins. The results of which are shown in Figure 57 and Figure 58 where the longitudinal integral length scale is plotted against turbulence intensity. Figure 57 shows the length scale of the Ebb flow which appears to be invariant with the level of turbulence (6 to 10%) with a mean value of 4.72m. Figure 58 shows that the Flood flow length scale is proportional to the turbulence level but the relationship is weak. The mean length scale for the Flood longitudinal flow is 6.51m which is approximately 35% higher than in Ebb which is to be expected as it is more turbulent in nature. The integral length scale tends to be proportional to the mechanism of instability that is supplying turbulent kinetic energy to the flow. The difference between the Ebb and Flood flows suggests that the turbulence in the flow is triggered from different sources i.e. boundary layer velocity shear for Ebb and bluff bodies shedding vortices for Flood in addition to the boundary layer.

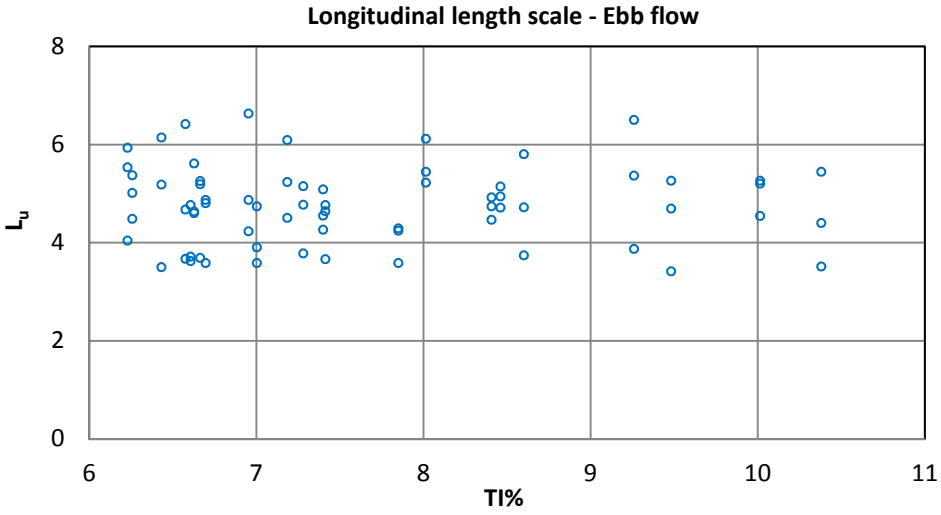

Figure 57 - Ebb flow length scale

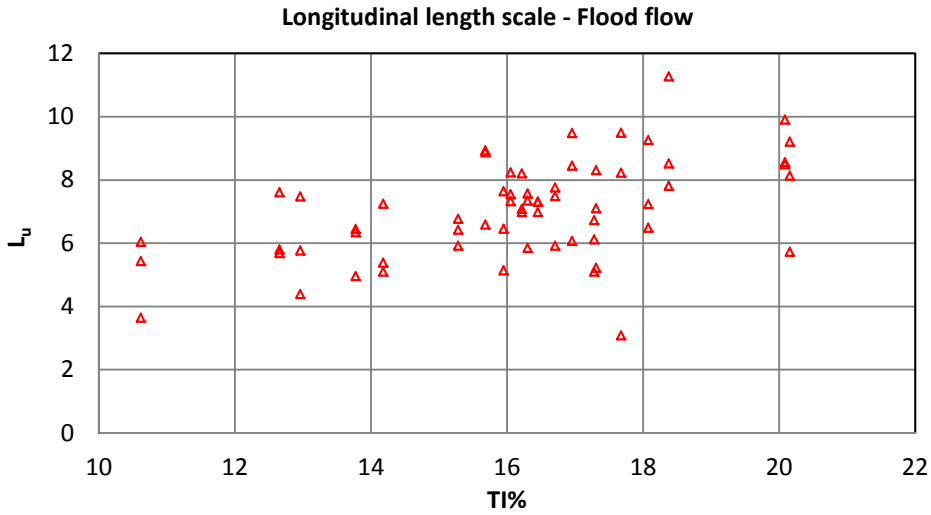

Figure 58 - Flood flow length scale

3.4.4 Turbulence spectra

A comparison of the spectral content of both the Ebb and Flood flow velocities with the Kaimal model overlaid in black is shown in Figure 59 below. The data used is a representative sample of both flows captured over a period of 10 minutes at the same mean velocity which is long enough to ensure equilibrium

statistics but is just short enough to avoid any low frequency harmonic components affecting the result.

As discussed in Chapter 2 the spectra can be split into three distinct regions along the frequency axis i.e. low, medium and high. The highest energy content corresponds to the lowest frequency range, on the order of several minutes, which is attributable to the largest eddies. The mid-range frequencies (approximately 0.25 - 0.05Hz) exhibit an inertial sub-range common to all flows. This range corresponds to a spectrum of spatial scales that range from those smaller than the integral length scale down to the Taylor microscale. The highest frequency components represent the smallest turbulent motions where viscosity dominates as kinetic energy is lost as heat.

Figure 59 shows the difference in spectral content between the Ebb and Flood tides against the Kaimal model. The Flood flow exhibits a stronger signal than the Ebb at the low frequencies suggesting more energy is present in non-equilibrium eddies which are not formed by the boundary layer shear and are not participating in the energy cascade. This corresponds with what has been discussed previously regarding the differences in TI and integral length scales of the two flows. The Ebb flow shows a remarkably close fit with the Kaimal model over the majority of the frequency range suggesting providing further evidence that the turbulence is mainly generated by boundary layer shear. However, care should be taken when analysing the high frequency range due to the potential uncertainty in the ADCP measurements at this frequency caused by the size of the measurement volume as discussed in Chapter 2.

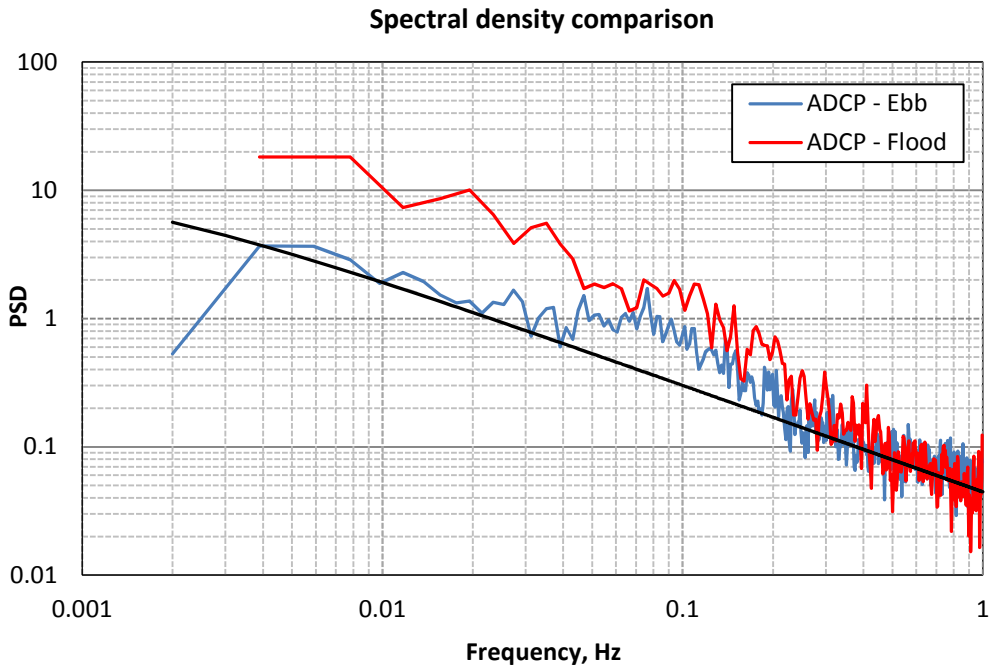

Figure 59 - PSD comparison

Quantification of the level of anisotropy in the flow is important for modelling the larger eddies which exist on the order of the blade length as turbulence on these scales will intensify the individual blade loads. An understanding of how these will affect the fatigue life and the interaction with the control system are important for safe operation of the turbine in the long term.

3.4.5 Coherent TKE

Coherence in the turbulent flow due to anisotropic turbulence has been identified as a potential source of unsteadiness for the turbine. Flow data from the ADCP has been analysed to identify points in the velocity record where coherent turbulent kinetic energy occurs. Based upon the stationary statistics of the turbulent flow the mean turbulent kinetic energy can be estimated as follows:

$$TKE = 3/2(U\,TI)^2 \quad [141]$$

Equation 73

Where U is the mean flow velocity and TI is the turbulence intensity. Therefore the mean kinetic energy of the bulk flow can be estimated to be used as a basis for assessing the statistical importance of peaks found in the TKE record when it is analysed in more detail using instantaneous velocity measurements from the ADCP. In this manner the turbulent kinetic energy is defined as follows:

$$TKE = 0.5\sqrt{\overline{u'}^2 + \overline{v'}^2 + \overline{w'}^2}$$

Equation 74

Where $u' = u - [u]$, $v' = v - [v]$ and $w' = w - [w]$ with the accent signifying a time average of the velocity component. The units of TKE are mean kinetic energy per unit mass associated with eddies in turbulent flow.

Figure 60 and Figure 62 show contour plots of the normalised TKE of the fluid for the 18 ADCP depth bins (which are spaced at 1m intervals) for a 10 minute period. The TKE has been normalised in respect to the mean TKE of each data set to make the coherent regions stand out more clearly. Figure 60 shows the level of TKE in the Ebb flow for a mean TI of 5% while Figure 62 is for a Flood flow where the mean TI is 16%. It should be noted that the units on the x-axis of Figure 60 are s/5. The Ebb flow exhibits only small regions of coherent activity compared with the Flood which exhibits numerous regions of strongly correlated flow. For example there is a large, well defined region of energetic flow between 250 and 300s that extends over an area equivalent to the dimensions of a turbine.

Plots in Figure 61 and Figure 63 show the level of TKE for the rotor hub height. The bold line is a 3s moving average value of the TKE. Coherent events are defined as when the time average of the TKE is greater than the threshold value of TKE[110]. There is no well-defined threshold limit as it must be judged based upon the background level of TKE within the flow. In this case the threshold (dashed line) is set at two standard deviations to ensure that only statistically significant levels of TKE are considered. This combined with the time averaging

of the signal provides a relatively robust way of identifying coherence in the velocity record by removing high frequency noise from the result. It can be seen that the occurrence of TKE lying above the threshold is significantly higher for the turbulence record with 16% TI suggesting that this flow contains a greater number of coherent events than for the 5% TI flow. In particular the large scale event previously mentioned in the Flood flow in Figure 62 is clearly identifiable from this method. This clearly shows the importance of the coherence model when considering generating inflow turbulence for the turbine simulations.

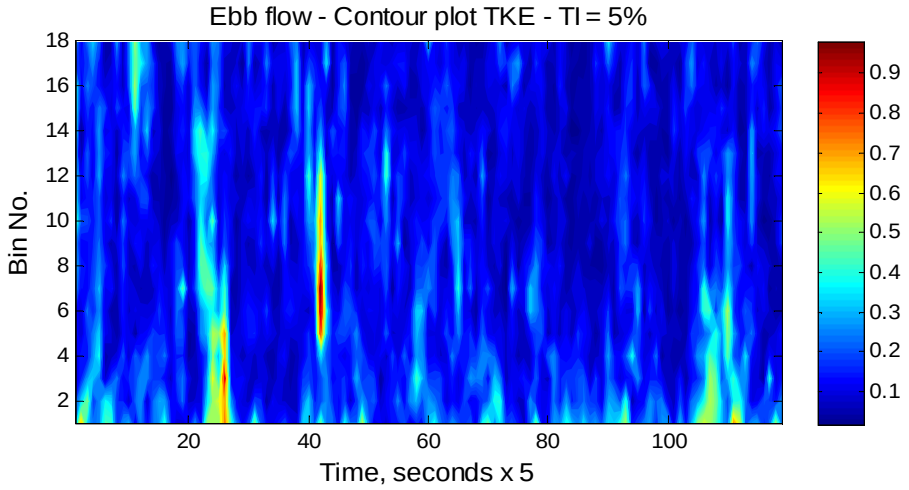

Figure 60 - Contours TKE Ebb

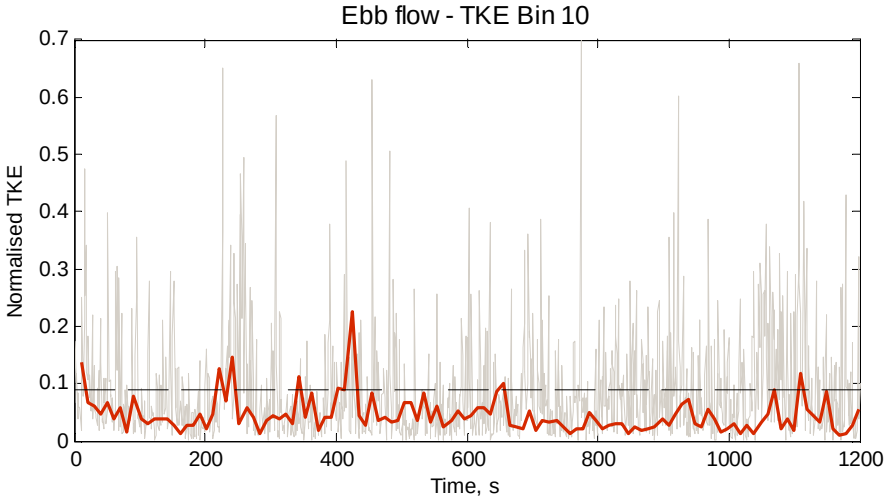

Figure 61 - TKE Ebb flow

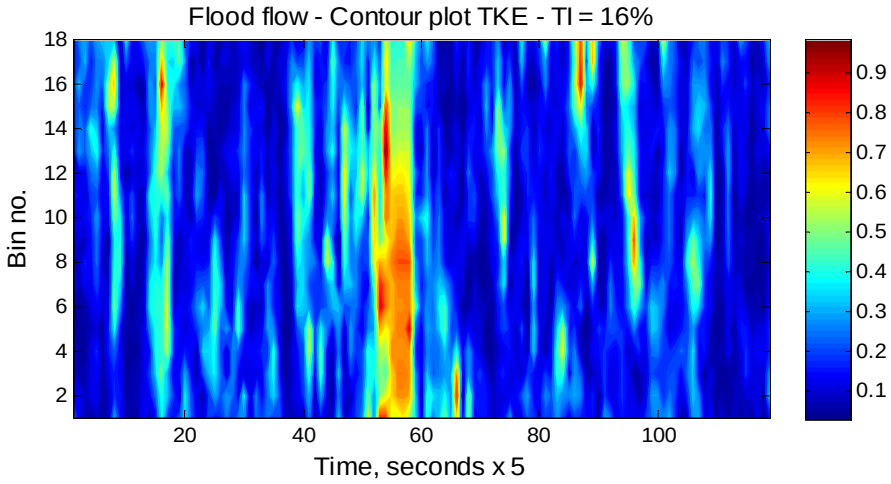

Figure 62 - Contours TKE Flood

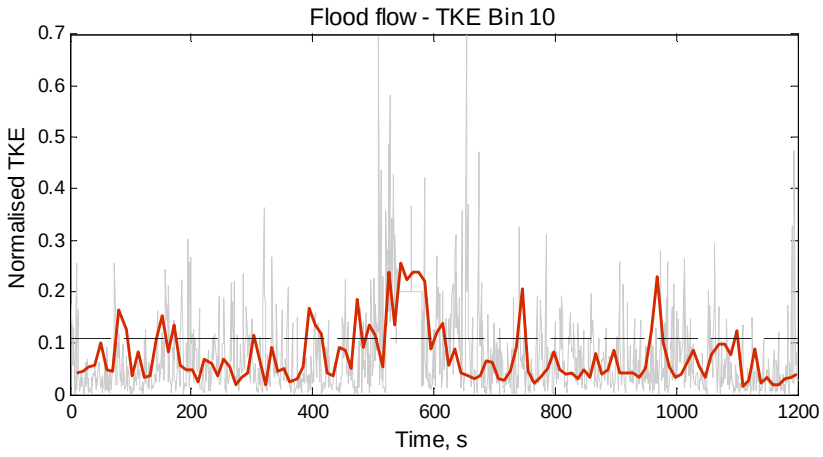

Figure 63 - TKE Flood flow

3.4.6 Shear profiles

The data shown in Figure 49 is taken from a single depth wise bin and does not give a full account of how the flow varies over the depth of the channel. Figure 64 below is a contour plot of a time series of the stream-wise velocity for all 18 data bins over a 2 minute period. This allows for a visualisation of the flow with depth and time and highlights structures within the flow not evident from the other velocity plots.

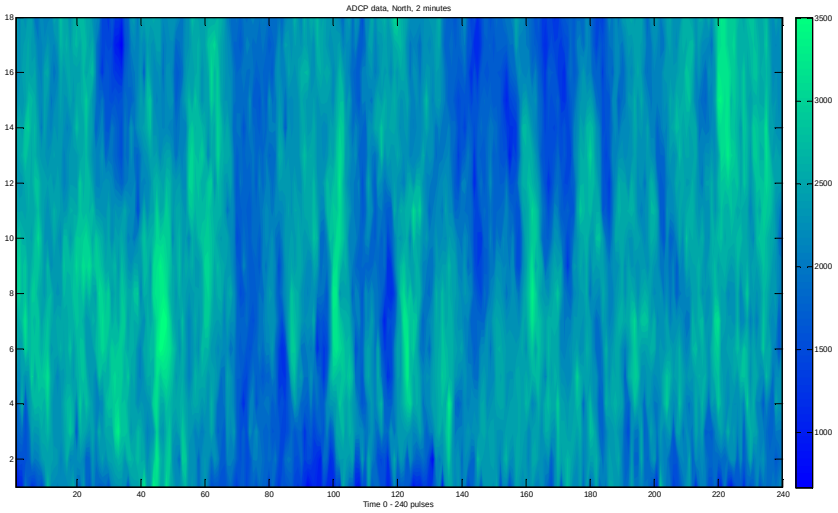

Figure 64 - Time series of stream-wise velocity

Using the data from the 18 bins it is possible to extract the velocity profile with depth in the channel for both Ebb and Flood tides. It is widely assumed that the velocity shear profile of the boundary layer follows a power law description in a manner similar to atmospheric flows of the form:

$$U_{shear} = U_{surface}\left({}^{z}/_{D_c}\right)^{1/n}$$

Equation 75

Where z is the depth below the surface, D_c is the total channel height and n is an exponent typically between 7 and 10. Both the Ebb and Flood tide shear profiles were calculated for several of the 10 minute data sets for a number of average hub flow speeds. These were then averaged to give the long term depth profiles shown in Figure 65 below. From this plot another difference between the Ebb and Flood flows becomes apparent as here the Flood flow exhibits a more pronounced depth profile particularly at higher flow velocities.

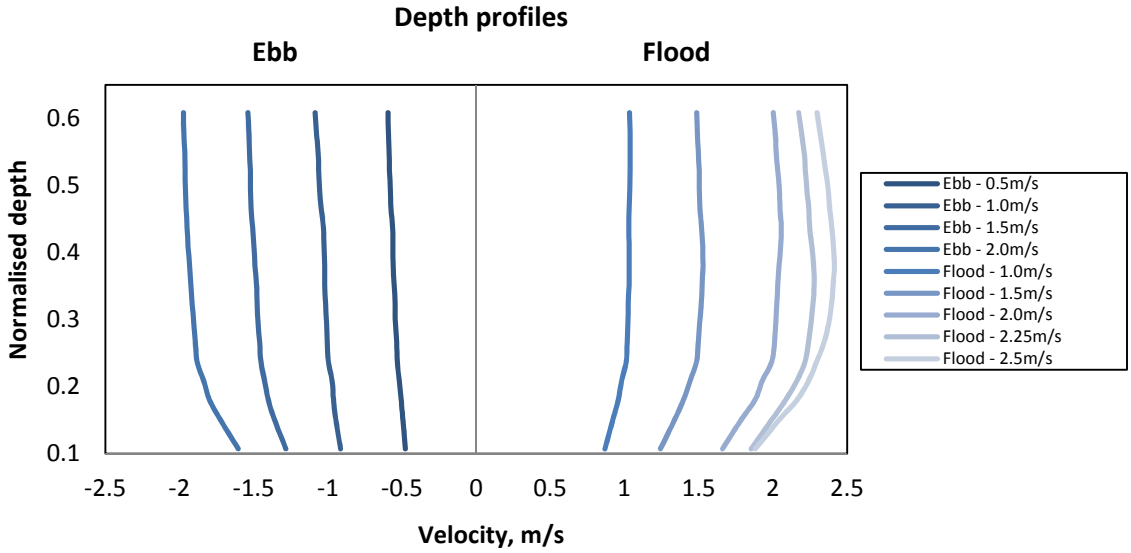

Figure 65 - Depth profiles

Figure 66 shows the Ebb profile for four different hub velocities between 0.5 and 2m/s, each of the four profiles is the average of four 10 minute data sets. The velocity profile is normalised against the mean hub velocity (the surface velocity is unavailable) and plotted against the normalised channel depth (the mean sea level is 35m at this point in the channel).

The Ebb shear profile closely resembles the classic wall boundary layer profile discussed earlier. Furthermore all four profiles agree reasonably well with each other indicating that flow velocity in the Ebb direction does not strongly affect the depth profile. Figure 67 shows that the Flood tide profiles (hub velocities between 1 – 2.5m/s) exhibit close agreement with each other but display a markedly different profile than shown for the Ebb tide. This can be attributed to the increased level of turbulence of the flow the source of which is not only shear in the boundary layer.

The difference between the Ebb and Flood tides is demonstrated in Figure 68 which shows the mean profiles from Figure 66 and Figure 67 as well as a plot of the power law for n = 7. In the lower part of the channel up to approximately 25% of the full depth all three profiles exhibit a similar shape with the Flood and

Ebb showing a strong similarity. Around 40% depth the Flood profile dramatically diverges from the Ebb profile and the power law approximation as the flow speed starts to reduce in the mid channel. It is at this point that the Ebb profile and the power law profile achieve best agreement.

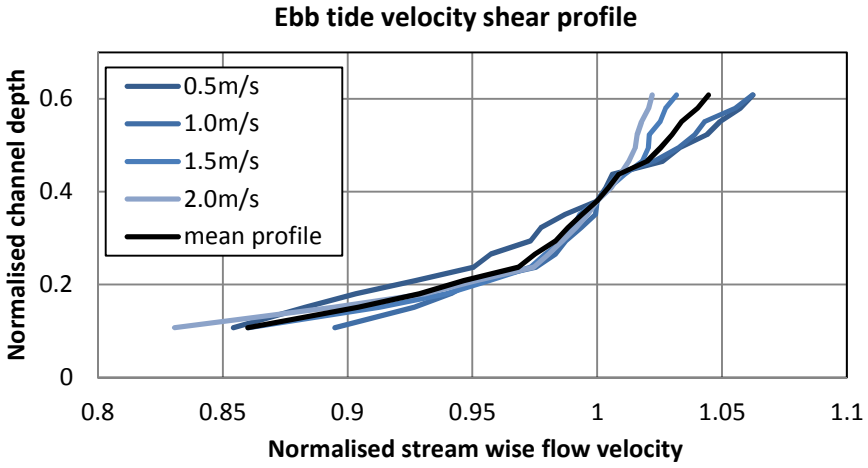

Figure 66 - Ebb shear flow

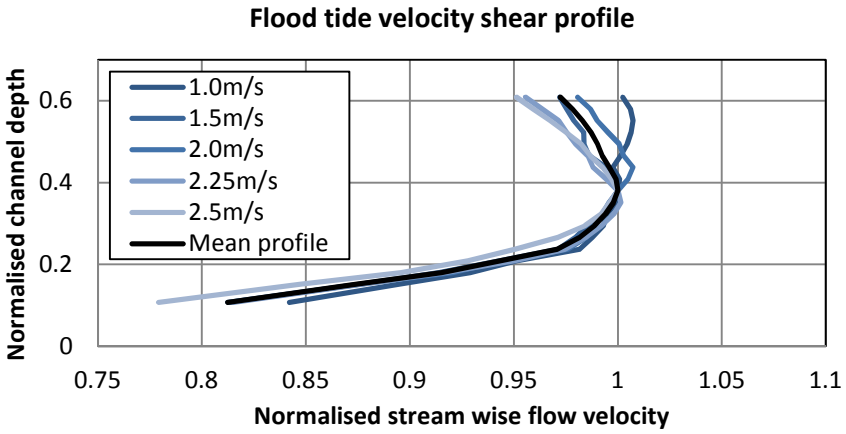

Figure 67 - Flood shear flow

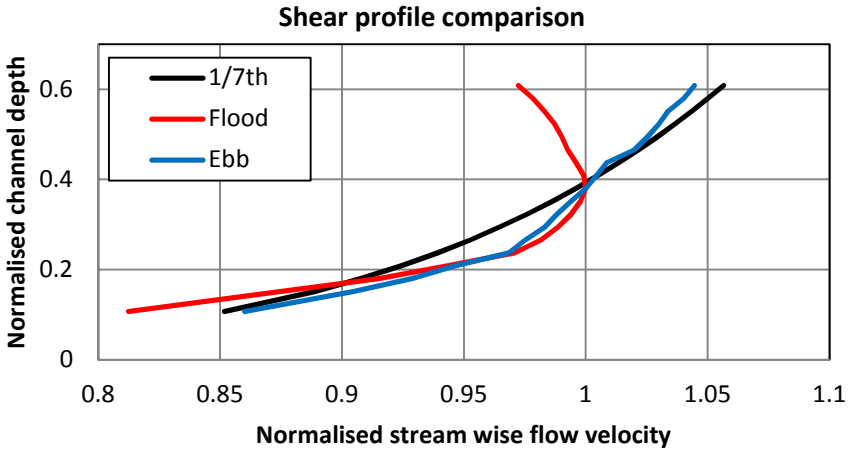

Figure 68 - Depth profile comparison

This result is an important one for flow modelling as the depth profile of the flow has a significant influence on the unsteady loading upon the turbine. As a rotor blade completes a full revolution it will experience a reduction in load with a minimum at bottom dead centre and an elevated load around top dead centre. Typically this cycle is considered as having a frequency equal to the rotor velocity which is valid of the Ebb flow. However, when one considers the inflection in flow velocity in the Flood profile at 40% depth the turbine blade will experience a twice per revolution load fluctuation that will have ramifications on fatigue life because the blade will experience two load reversals per revolution. This highlights the importance of using site specific data in order to achieve accurate modelling results.

3.4.7 Turbulent flow field generator

The previous section described in the detail the analysis of the turbulent flow measured in Ramsey Sound which was put into context by the literature sources reviewed. In order to generate synthetic turbulence data with which to drive the hydrodynamic model an open source code called Turbsim has been embedded within the authors Matlab model. Turbsim is a stochastic, full field synthetic turbulence simulation tool which uses a statistical model, rather than a

physics based model, to numerically simulate velocity time series. The velocity spectra and coherence are defined in the frequency domain and an inverse fast Fourier transform is used to generate velocity in the time domain.

Turbsim is a well-established model that was first written in 1988 and was known as SNLWIND as a single component wind velocity turbulence generator. It has subsequently been updated to generate three dimensional flow fields based on a number of different optional turbulence spectra including the von Karman and Kaimal models. Latterly it was re-written in Fortran 95 which simplified the process of updating the input parameters and made it compatible with Intel Visual Fortran compiler which is a widely available modern compiler. The purpose of Turbsim, as stated by Sandia National Laboratories who developed the code, is to provide the wind turbine designer with the ability to drive design code simulations of advanced wind turbine designs with turbulent inflow conditions so that the aero-elastic turbine response to important fluid dynamic features can be studied[112].

The turbulence data files generated using TurbSim prior to the simulation are converted into a time-dependent flow field matrix. At each time step velocity data is read sequentially into the flow field control script and the flow field matrix is populated according to the spatial position of the blade calculation nodes. Figure 69 below shows an example of the field matrix shown as a contour plot over four time steps in terms of the stream-wise velocity component to demonstrate the process. At each time step a field matrix is also generated in the same way for the cross-stream and vertical components of velocity which although they are much smaller in magnitude than the stream-wise component can significantly increase the unsteady blade loads.

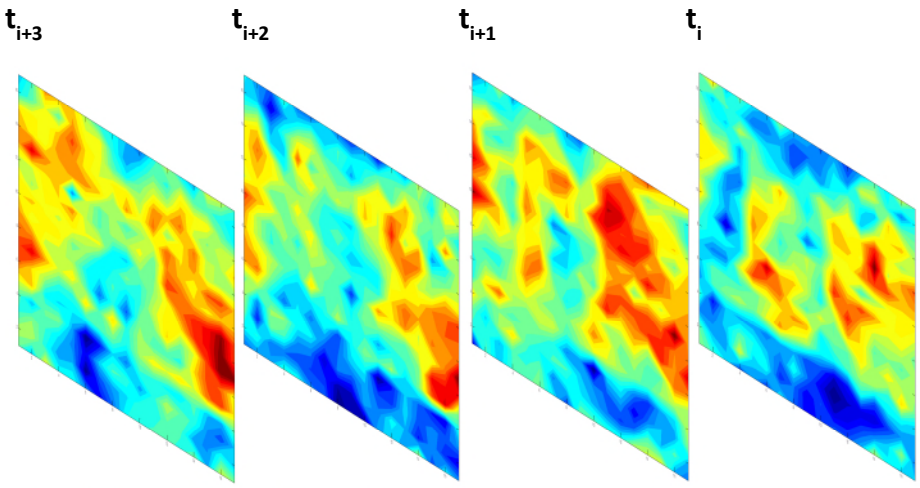

Figure 69 - Turbulent flow field matrix – stream-wise velocity contours

Care must be taken when using Turbsim that the turbulence is simulated at intervals equal to the time step implemented in the BEM code. This time step must be relatively small to capture the dynamic nature of the turbulence to reflect the appropriate spatiotemporal relationship of the three velocity components as the turbulence generated is non-homogeneous. To understand this phenomenon a convergence study was undertaken using the full time dependent model in combination with the Turbsim flow field and is discussed in the next section.

It has been shown the Ebb tide velocity spectra conforms well to boundary layer generated turbulence and can be represented well by using the Kaimal spectral model. It has also been found that due to the high level of anisotropy exhibited by the Flood tide the standard models do not fit with its behaviour. This is illustrated in Figure 70 below which plots both the Kaimal model and the Flood tide spectrum. The Flood spectrum is derived from Figure 71 which shows the power spectrum of a 10 minute window of flow. This shows that at the intermediate frequencies where eddy mixing is occurring there is good agreement between the two spectra. However at the low frequencies where eddies are being generated there is a very large discrepancy between the two

as the Flood spectra is an order of magnitude higher suggesting that different mechanisms are generating turbulence.

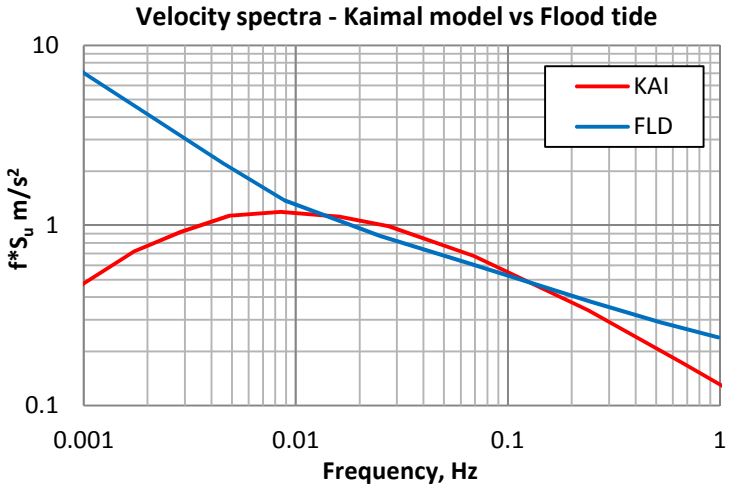

Figure 70 - Kaimal & Flood tide spectra

In order to generate meaningful turbulent flow data for Flood tide simulations the Flood spectra was implemented as a new model within Turbsim. This was undertaken as an MSc project to complement this work[142]. This took advantage of the open source nature of the code and used the Fortran compiler to insert an additional model tailored to the Flood spectra using the same methodology to generate the flow field. This model was validated against the Flood tide ADCP data available from Ramsey Sound.

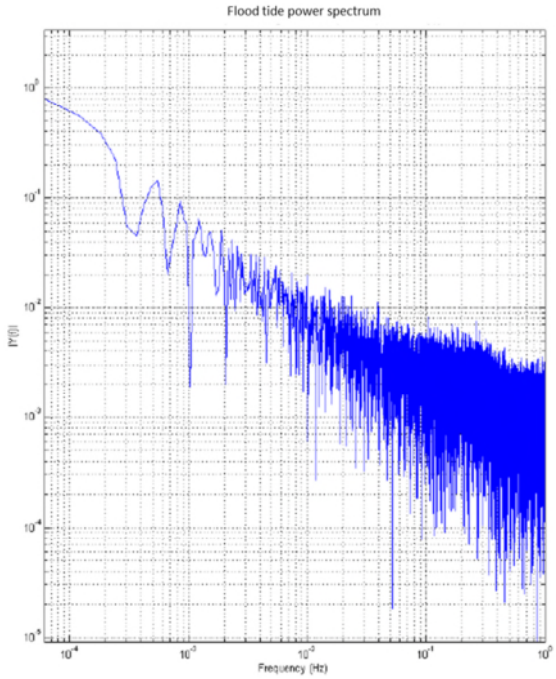

Figure 71 - Flood tide raw spectra

3.5 Summary of unsteady flow

Turbulence is an unavoidable consequence of the high Reynolds number in a tidal channel and is part of the environment in which a turbine operates. It is a key parameter when considering the design loads that must be accounted for in the development of the turbine.

It is likely that a large contribution to the turbulence in both flows is shear stress in the boundary layer. This is implied from the increasing levels of turbulence intensity with depth which matches with data reviewed in Chapter 2 from other tidal channel measurements. The turbulence increases towards the sea bed in a manner very similar to that seen in the Puget Sound as reported by Thompson[93].

The particularly extreme turbulence observed in the Flood tide could be the effects of bluff bodies in the boundary layer causing large structures in the mid channel as discussed earlier in section 3.4.2.

The level of turbulence varies between the tides and the damage to turbine will be greatly increased when operating in the Flood tide. The turbulence is dependent upon both the channel depth and the mean flow velocity.

The turbulence appears to show anisotropic characteristics in terms of length scale and standard deviation in the three Cartesian coordinates but further analysis required.

Furthermore it appears that the flow exhibits strong levels of coherence which could potentially increase the local kinetic by an order of magnitude. Further analysis to identify coherent events is required to determine their frequency.

3.6 Code setup parameters for reliable output

The following section discusses the results of the time dependency study in terms of three setup parameters; simulation time step, total duration and grid spacing. This is a verification process to ensure the modelling setup will always deliver consistent results. The time step and the grid spacing control the effective sampling rate of the dynamic turbulent flow field to the hydrodynamic code. If the sampling rate is too low then aliasing of the turbulence signal will occur and the resulting load spectrum will miss out higher frequency components and therefore the effect of the small eddies cannot be modelled. This will artificially reduce the unsteadiness of the flow and the results will under-predict fatigue loading. However, there will is a substantial computational penalty if the sampling rate is unnecessarily high which will reduce the number of simulations that can be practically conducted.

At the other end of the spectrum the overall simulation duration is dependent upon the large eddy turnover time scale. This can be estimated from:

$$t_L = {}^{L}/_{U}$$

Equation 76 [143]

Where L is the large eddy length scale which is of the same order as the tidal channel and U is the mean flow. Therefore it would be expected that the large eddy turnover rate is on the order of 10-30s which would be the absolute minimum duration to capture a single large eddy. However the simulation time scale will be significantly longer in order for the turbulent statistics to reach equilibrium.

The Damage Equivalent Load (DEL) which represents the load amplitude at one frequency that would cause the same level of damage as the full time history is defined as follows:

$$\boldsymbol{DEL = \left(\frac{\sum_i NiL_i{}^m}{Tf}\right)^{\frac{1}{m}}}$$

Equation 77

Where N is the number of load cycles of amplitude L at a constant frequency f. T is the duration of the time history used in the rainflow counting and m is the gradient of the blade material S-N curve plotted on log-log axes. The number of load cycles and load amplitude is determined from a rainflow analysis of the load time series. A rainflow matrix for an experimental load case shows the x-axis with the mean load value, the y-axis with load amplitude about this mean and a bin colour showing number of cycles, N. The material constant, m, is assumed as 10 for all cases as this is representative of a glass fibre based composite used in blade construction. This is a good comparator of the relative severity of the unsteady loads as predicted numerically compared to the experimental results. The material property and frequency is held constant for the entire analysis. Differences in the length of data time series are normalized to ensure compatibility.

The effect of time step is shown in Figure 72 below which shows a plot of non-dimensional DEL (thrust and torque) versus the time step size. This shows evidence of convergence to a repeatable result when the selected time step is below 0.25s. As the time step is further reduced to a minimum of 0.025 the

simulation result remains consistent which implies that there is no improvement to fidelity at smaller time steps.

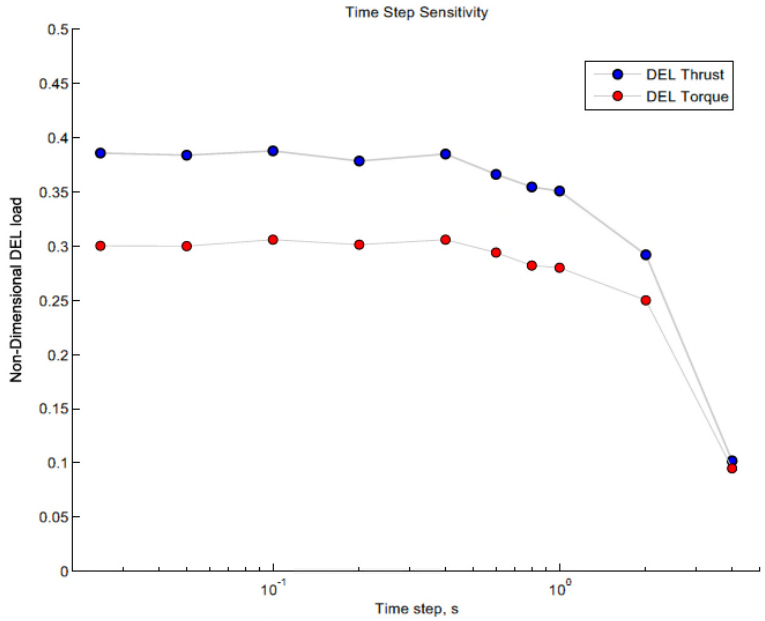

Figure 72 - Time step convergence

A similar plot for grid sensitivity is shown in Figure 73 which indicates convergence when the number of grid points reaches 25. This means that the minimum node spacing required is 0.48m as the grid size used in the study is 12x12m. This is a particularly important parameter to optimise as the memory allocation for the Turbsim algorithm is proportional to n^4 i.e. as grid points double the memory requirement increases by 16 times. .

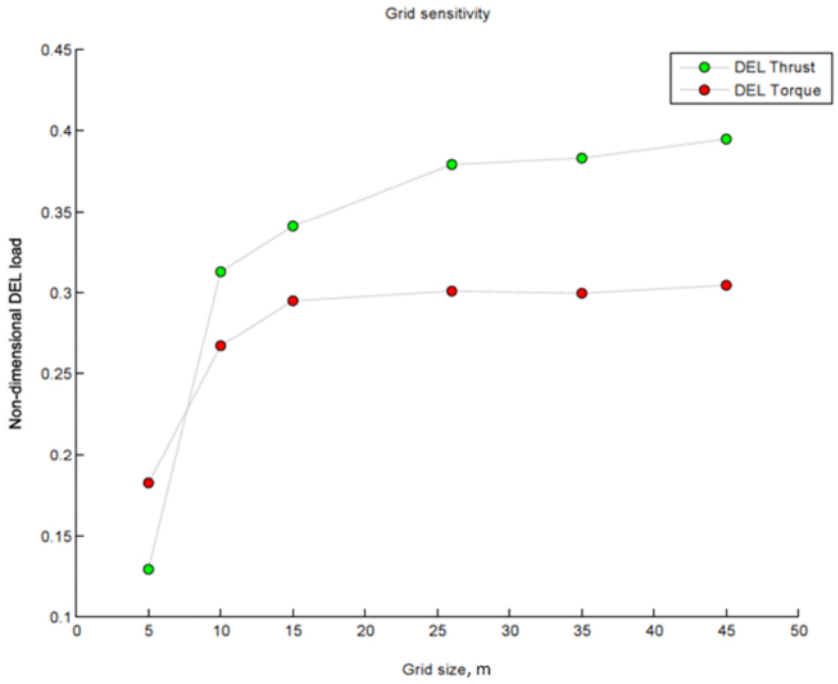

Figure 73 - Grid dimension

The final part of the study determined the minimum simulation duration required to achieve repeatable results. Figure 74 shows the convergence plot run for three levels of turbulence intensity. It was assumed that when the solution settled to a constant quantity the duration was sufficient that the stochastic turbulence statistics had achieved equilibrium.

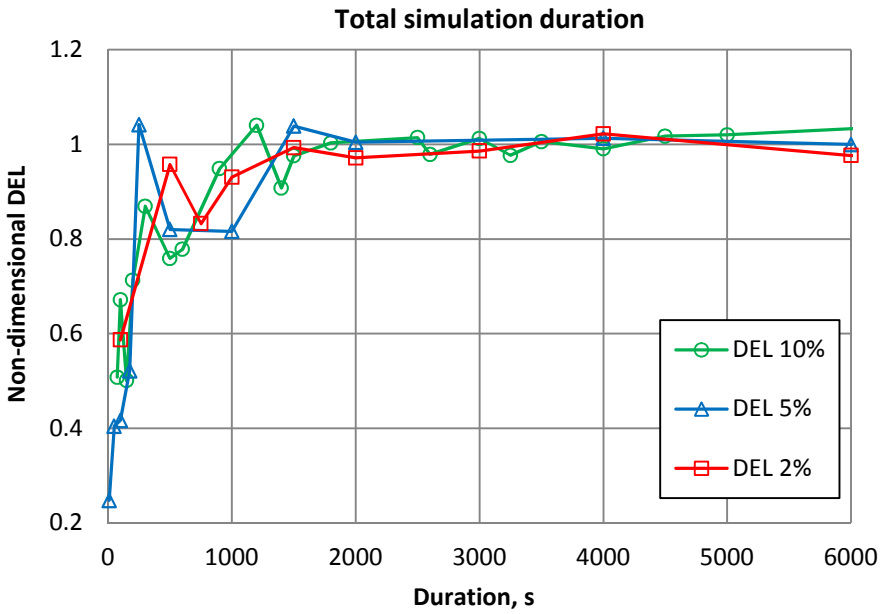

Figure 74 - Duration convergence

This shows that the minimum simulation that produces a consistent output is 2000s which is approximately 100 times the eddy turnover timescale. There does not appear to be any relationship between turbulence intensity and minimum duration for the range considered. Therefore all simulations are treated in the same way regardless of the turbulence parameters.

3.7 Stress analysis

A stress analysis model is required to determine the principle stresses from the blade loads in order that the fatigue life calculations can be carried out using the stress life approach. Furthermore because of the aspiration to develop a design tool that allows for rapid simulation of turbine life the stress analysis model must also meet this criterion. Therefore a finite element (FE) beam type model was developed in conjunction to this project for an MSc thesis to accomplish this activity[144]. Figure 75 and Figure 76 below demonstrate the blade construction from glass/epoxy composite layup. Figure 75 is a CAD render showing the

Deltastream load bearing spar cap in red and the aerodynamic fairings in blue. Figure 76 shows a blade under construction with the spar cap root section that bolts into the central hub in the foreground and the fairings in the background.

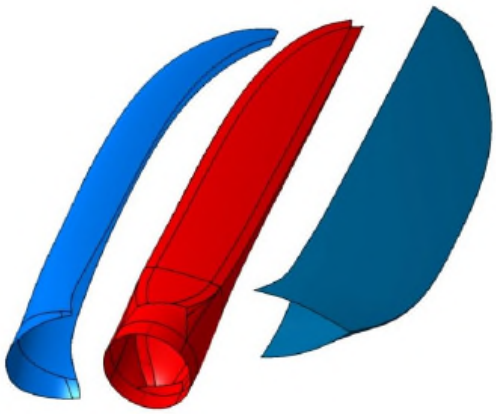

Figure 75 - Exploded view of blade design model

Figure 76 - End view of blade spar cap root section

The FE model is run in the proprietary code Abaqus and the blades are modelled as slender beams using the Timoshenko formulation which accounts for axial, bending, torsional, transverse and shear deformations. Although the beam formulation is one dimensional this model also involves a pre-processing step where the cross sectional properties of the blade are analysed at discrete span-wise intervals in order to allow coupling of the shear deformation using a so called warping function in the main one dimensional beam model. This was achieved using Abaqus's inbuilt meshed cross section analysis tool an example of which is shown in Figure 77 below.

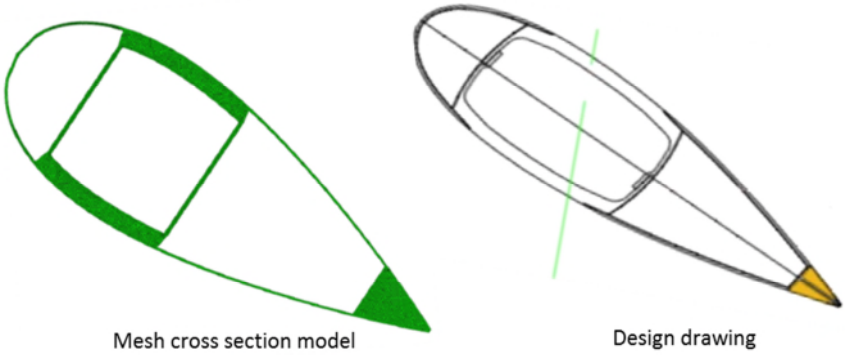

Figure 77 - Abaqus sectional model compared with the design drawing

Before application to the Deltastream turbine the model was validated using a literature source. This detailed an experimental wind turbine blade built by Sandia National Laboratories called the NPS-100 turbine. This is in many ways similar to the Deltastream blade as it is constructed from a glass/epoxy composite layup which consists of a spar cap surrounded by aerodynamic fairings. The turbine is an open source design so every detail of the blade construction and design are available for using in the validation case. The blade is modelled as a hybrid 1D beam. Two dimensional cross-sectional analysis is applied prior to load simulations to provide the one dimensional model with certain characteristics of the blade such as the warping function[139]. This is shown schematically in Figure 78.

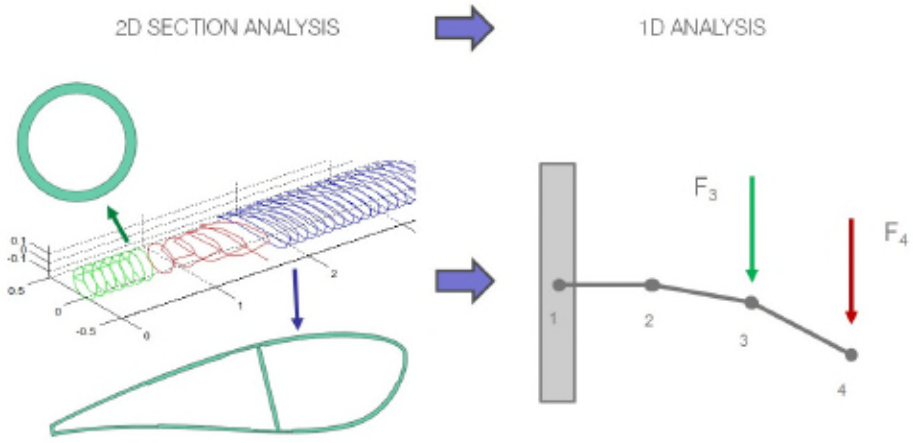

Figure 78 - Schematic representation of FE method

The main outcomes of the validation are shown in Table 5 below while the full description of the modelling process is described in the MSc thesis document[140].

Load case	Exp.	FEA model	Load direction
1	306.0 mm	309.0 mm	Flap-wise
2	89.6 mm	90.1 mm	Edge-wise

Table 5 - FEA model validation [145]

The blade was rigidly clamped at the root and a simple tip load was applied in both the flap-wise and edge-wise directions and the deflection under each case was measured. The FEA model predicts the deflections to within 1% of the experimental results which is a strong indication that the model is able to predict the linear elastic response of blades manufactured in this manner given accurate details of the material properties.

This gives confidence for application of the process to the Deltastream turbine. The geometry of the Deltastream is very similar to the validation case; both are constructed from a central spar cap with aerodynamic fairings making up the leading and trailing edges. The validation has shown the model can handle this particular setup when modelled as a beam type structure. Furthermore the cantilever boundary condition is applicable to both turbines as the hub is assumed rigid. The material layup for the Deltastream is not as complex as the validation case with less layers and fewer materials to be modelled which should simplify the procedure. The only difference between the validation case and the Deltastream model is the application of the blade loads. In the validation case tip loads were considered whereas a distributed load will be required for the Deltastream model. Given that the analysis is going to be undertaken using a robust linear elastic FE model (Abaqus), the agreement between the published literature and the validated model is very close and that

all other conditions are comparable it is assumed that changing the type of load from point to distributed will not add significant uncertainty to the results going forward modelling Deltastream.

The FE blade model was reconfigured for the Deltastream geometry, material properties and layup. The sectional analysis was completed to provide the warp function that couples the shear deformation to the one dimensional beam model. At this point loads from the hydrodynamic model were applied to determined stress distribution in the blade (as detailed in Chapter 5). These results allowed application of a simple transformation to convert bending moment to blade stress as shown in Equation 78

$$\sigma_i = \sigma_{ref}\left(\frac{BM_i}{BM_{ref}}\right)$$

Equation 78

Where σi is the nodal stress, σ_{ref} is the reference stress determined from the FE model, BM_i is the applied bending moment load from the hydrodynamic model and BM_{ref} is the reference bending moment applied in the FE model.

3.8 Deltastream turbine control modelling

3.8.1 Control Modelling Introduction

This section comprises the development of a control model that will be used in combination with the hydrodynamic model to simulate the effectiveness of the turbine design when operating in unsteady flows. As previously discussed the Deltastream is a fixed pitch, variable speed machine where load control is accomplished by governing turbine speed in accordance with the design curves shown in Figure 79 which were taken from the blade design process. More details of the design process are outlined in Chapter 4. The turbine can operate in two modes; mode 1 where the turbine runs at the design point and mode 2 the turbine runs to shed power. In mode 1 the turbine is operating at peak power, at a Tip Speed Ratio (TSR) of 3.25, which ensures the maximum possible conversion of kinetic flux to electrical power. This mode is employed when the machine is running in tidal flows below or at rated speed as observed on the left hand side of Figure 79 below. Conversely when the flow speed increases above the rated speed mode 2 is enabled to ensure the turbine does not generate more power than the electrical equipment has capacity for. Therefore the rotor speed behaviour must follow the curve on the right hand side of Figure 79 whereby the speed is rapidly increased for small changes in flow in order to move the operating point away from the design point to much higher TSRs such that the absorbed power remains constant. Furthermore this has the effect of reducing thrust load on the device to ensure stability at high tidal velocities.

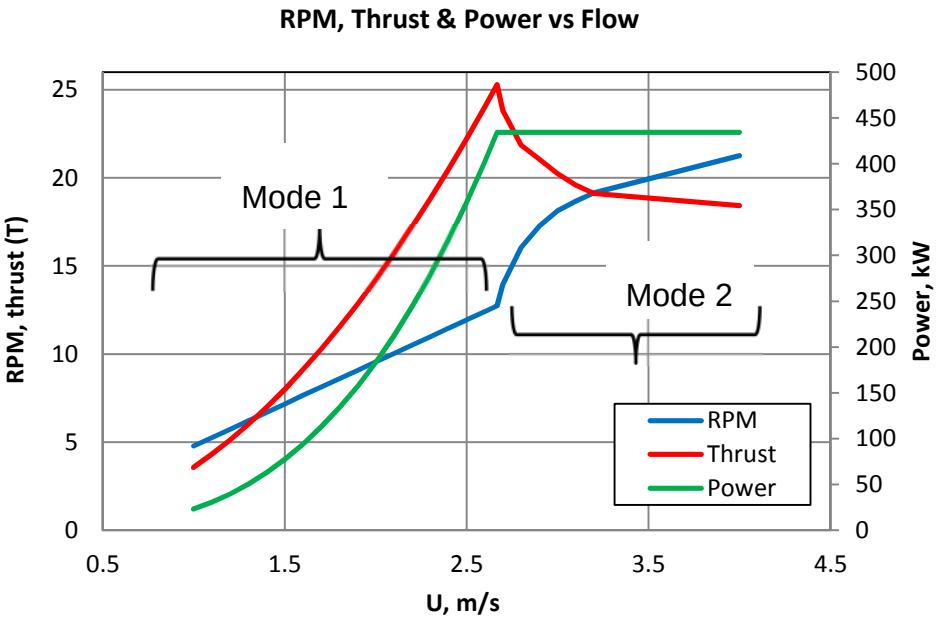

Figure 79 - Design curves

With realistic tidal flows the control system must act in a dynamic manner to fulfil the dual roles of maximising power capture and limiting load owing to the short timescales of the turbulent fluctuations that will act upon the device when compared to the semi-diurnal timescale. The spectral content of the tidal turbulence has been described in chapters 3 and it is envisaged that the controller will act to reduce the cyclic loading occurring as a result of the turbulent regime. However, knowledge of the inflow to the turbine is required in order to define the rotor running speed before a control law can be applied to govern the running speed.

The following section presents the development of an algorithm to predict tidal flow speed based upon the turbine operating data and implementation of a feedback control model that will act in conjunction with the hydrodynamic model. Substantiation of control system tuning for best performance is provided along with a detailed description of the differences between the two operating modes in terms of controlled behaviour that were established through conducting this research. Finally the results of simulations in which the control model was utilised in conjunction with the hydrodynamic model to control the turbine in realistic turbulence are presented and conclusions drawn on the

effectiveness of the model and its application in general terms to fixed pitch turbines.

3.9 Tidal flow estimation algorithm

As discussed in previous chapters' measurement systems for tidal velocity do exist and have been implemented successfully in Ramsey Sound. However, these are essentially measurements of a single point in the flow and in order to be useful for turbine control would have to provide the average velocity across the turbine rotor. Furthermore, even if velocity sensors were available that could provide this data it would not be desirable to rely totally on such systems as a malfunction could potentially result in catastrophic failure of the device. Therefore another method to determine flow velocity has been established for the Deltastream which is described in the proceeding section.

It is possible to measure the turbine power output and RPM which can be used in conjunction with the curve for Cp versus TSR to identify the operating point on the machine performance curve. This curve was predicted by the hydrodynamic model and has furthermore been validated through the IFREMER experimental campaign which lends a high level of reliability to the turbine performance model. The turbine power can be related to the power coefficient as follows:

$$Power = 0.5 C_p \rho A U^3$$

Equation 79

This provides the power coefficient as a function of the tidal flow speed and output power. From the performance curve the Cp can also be modelled by regression fitting of a 4th degree polynomial to the BEM Cp curve as shown in the Figure 80 and Equation 80 below as a function of the TSR.

For TSRs of 1 to 2.25 Cp is somewhat over predicted by the model, the experimental data decreases more rapidly than the simulation predicts. This is the model implemented in this work does not fully capture the flow physics of

the turbine when operating at high angles of attack. As the TSR tends towards 1 and the induction factor increases towards 0.5, the will rotor moves into the turbulent wake state where recirculation behind the rotor disc becomes stronger. As this is not accounted for by the model the estimation in this operating region diverges from the experimental data. However this shortcoming is not problematic in a practical sense as the Deltastream is only designed to operate at TSRs above 3 i.e. from peak power up to free wheel. Therefore as the model provides turbine load predictions with a sufficient degree of agreement with the experimental data in the operational range the shortcoming in model performance below TSR = 2 are not addressed. For a more detailed discussion on turbine performance see section 4.2.4.

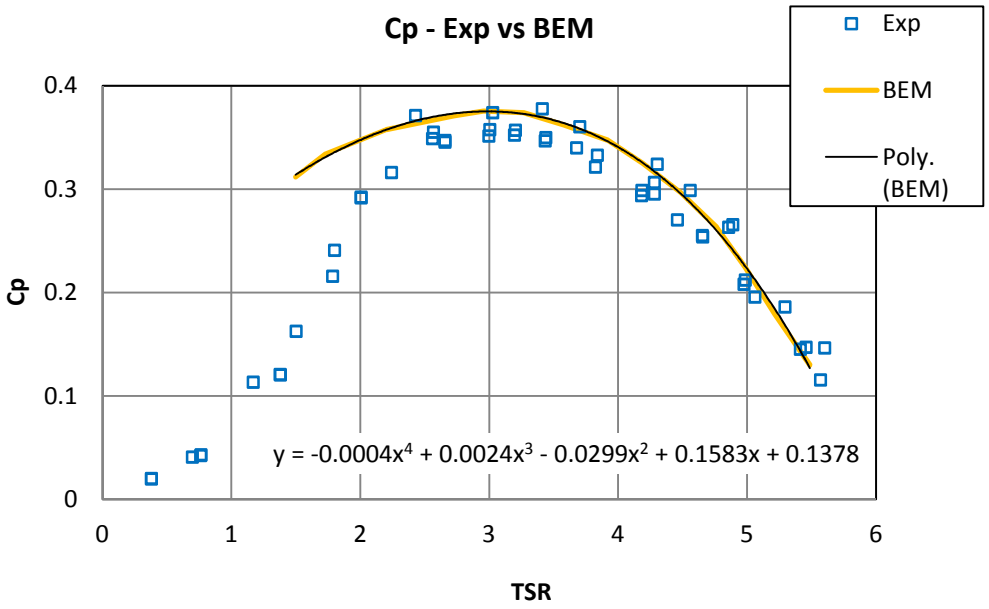

Figure 80 - Power coefficient

$$Cp = -0.0004TSR^4 + 0.0024TSR^3 - 0.0299TSR^2 + 0.1583TSR + 0.1378$$

Equation 80

Furthermore the TSR can be written in terms of rotor linear tip speed and flow speed in Equation 81

$$TSR = \left(\frac{\omega R}{U}\right)$$

Equation 81

By rearranging, the power coefficient can be substituted into the equation for power as follows:

$$Power(U) = 0.5\rho AU^2\left[-0.0004\left(\frac{\omega R}{U}\right)^4 + 0.0024\left(\frac{\omega R}{U}\right)^3 - 0.0299\left(\frac{\omega R}{U}\right)^2 + 0.1583\left(\frac{\omega R}{U}\right) + 0.1378\right]$$

Equation 82

The predicted flow velocity can then be determined by solving the power equation for U as power and rotational speed are both known variables. This is implemented within the time stepping hydrodynamic model to provide predicted flow speed for every iteration. A proportional control law is implemented to regulate the rotor speed such that it conforms to the pre-determined relationship with flow speed as per Figure 81 below.

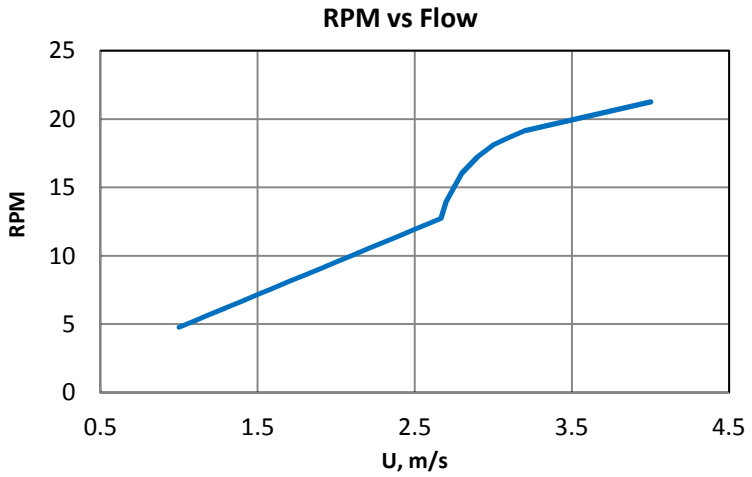

Figure 81 - Design flow vs RPM

Therefore the controller set point in terms of rotor speed can be determined through interpolation of this curve with respect to the estimated flow velocity as previously determined.

A closed loop feedback control model, as shown below, is used to regulate the turbine RPM once the set point is defined.

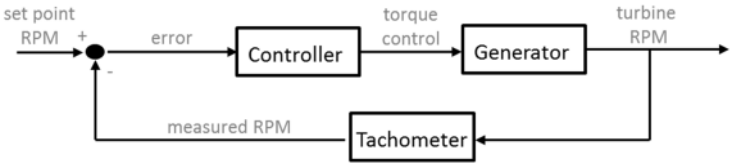

Figure 82 - Control loop model

The error, e, is determined by comparison of the set point with measured RPM i.e. the process variable. This is used as the input to the PID controller which is defined as follows:

$$Torque_c = K_p e(t) + K_I \int e(t)dt + K_D \frac{d}{dt} e(t)$$

Equation 83

Here $Torque_c$ is the torque demand on the generator required to alter the turbine speed. If the error is positive the rotor speed must increase and vice versa if negative. Rotor speed changes are enabled by temporarily absorbing more or less electrical power via the on-board generator. For example if an increase in rotor speed is required when the controller set point increases the generator will momentarily produce proportionally less power thereby allowing a change in RPM. This change in rotor speed is governed by the mechanical inertia of the system, I_r. The rate of change in RPM is therefore:

$$\Omega = Torque_c / I_r$$

Equation 84

Therefore the change in RPM per time step is:

$$\Delta\text{RPM} = \frac{60\Omega}{2\pi}$$

Equation 85

The updated rotor speed is fed as the initial condition of the next time step in the hydrodynamic model.

3.10 Tuning of the controller

After implementation of the closed loop feedback model within the main turbine model the controller was tuned to establish the set of feedback coefficients that will ensure the turbine can adequately track the demand curve as detailed in chapter 5. In many process environments a controller of this type is used for disturbance rejection so that the system can run in a stable manner. The Deltastream is slightly different as the set point of the controller is constantly changing with the rotor inflow so rigidly adhering to one speed is not so critical as compared to the systems reaction to large changes in flow to achieve the load shedding required for the integrity of the device. Furthermore, the Deltastream has two modes of control; Mode 1 – below rated power and Mode 2 – above rated which were found to have distinctly different system responses and therefore were treated separately.

Determination of the controller coefficients was based on the Ziegler-Nichols, Z-N, self-oscillation method which is a very widely used approach for feedback system tuning[146]. A well-defined step disturbance is provided to determine the ultimate gain, K_u, which is the gain that results in sustained oscillations after the disturbance has passed. From the wave form the oscillation period, $T_{u,}$ can also be determined.

As previously mentioned tuning is split into two parts to take account for the two modes in which the turbine operates. Mode 1 is when the flow velocity is significantly below rated and the controller set point is tracking along the linearly varying portion of the RPM demand curve i.e. where only small changes in RPM are required. Mode 2 is when the flow is close to or above the rated flow and the set point moves regularly into the non-linear portion of the control curve. The ultimate gain for both modes was determined by running simulations while varying the system gain, K_p. The results of these simulations are presented in

the next section and followed by a fuller analysis and comparison of the tuning outcomes.

3.11 Tuning at part power

In mode 1 the turbine will never reach the point of rated power and so load shedding is unnecessary. A step change in flow speed of 0.3m/s was applied to the turbine inflow conditions when the turbine was running in a steady flow of 2.2m/s. This 12% increase in flow represents a 25% increase in power on the turbine as the rotor power steps up from approximately 50% to 75% of rated power. Based on evidence from the Ramsey sound velocity data gathered by the ADCP (see chapter 2) this is a large but representative change in flow conditions that the Deltastream would have to be able to govern from a control perspective.

A total of seven simulations were undertaken at various control gains to determine the ultimate system gain ranging from K_p = 50 - 2250. Figure 83 below shows this step change in flow conditions ('Hub flow') plotted along with the control system response in terms of estimated flow speed as determined by solving the turbine power equation as described in the preceding section i.e. measured process variable in control theory parlance. As this is a time averaged variable there is a short lag before the estimated flow tracks up to the new steady state with a small overshoot and a settling time of around 3.5s in all cases. The size of the overshoot is determined by the magnitude of the gain with the overshoot increasing for decreasing values of K_p. This is a very important element in the control of the turbine as the estimated flow speed determines the rotor RPM set point and hence the error fed to the controller. If this estimated value lags the real flow then the governing of the RPM will be artificially sluggish.

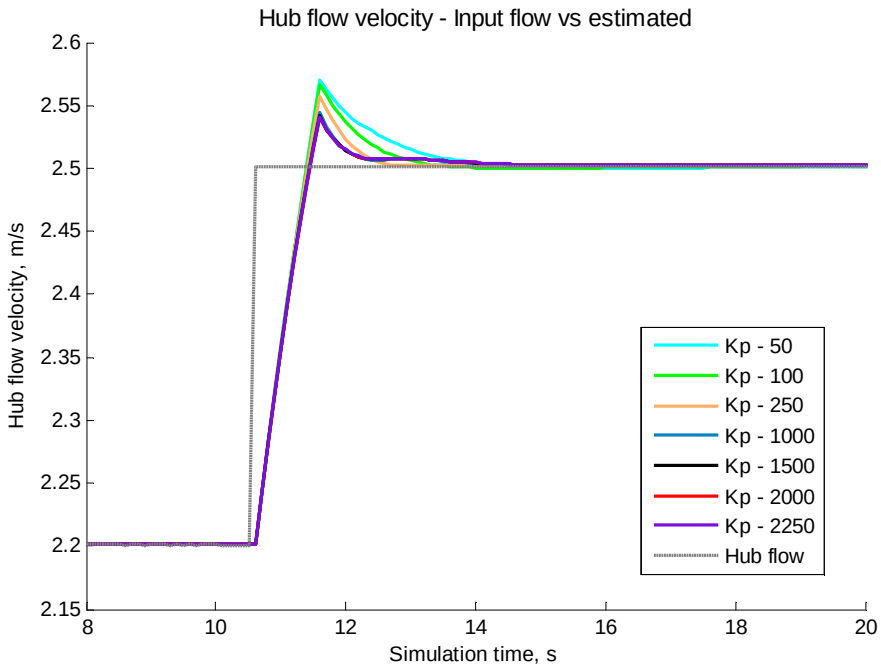

Figure 83 - Mode 1 estimated flow velocity

The measured rotor RPM in response to the step change is shown in Figure 84 below for all system gains. This shows very clearly that as K_p increases from 50 to 250 the settling time decreases but a threshold is reached at 1000 beyond which there are no further reductions in the settling time. Furthermore it is also clear that the system stability margin is reached when K_p = 2250. This is therefore the system ultimate gain, K_u, and increasing the gain further will lead to unstable behaviour based on the Ziegler-Nicholls self-oscillation method. It should be noted that for all gain values less than Kp = 2250 there are no oscillations in turbine response.

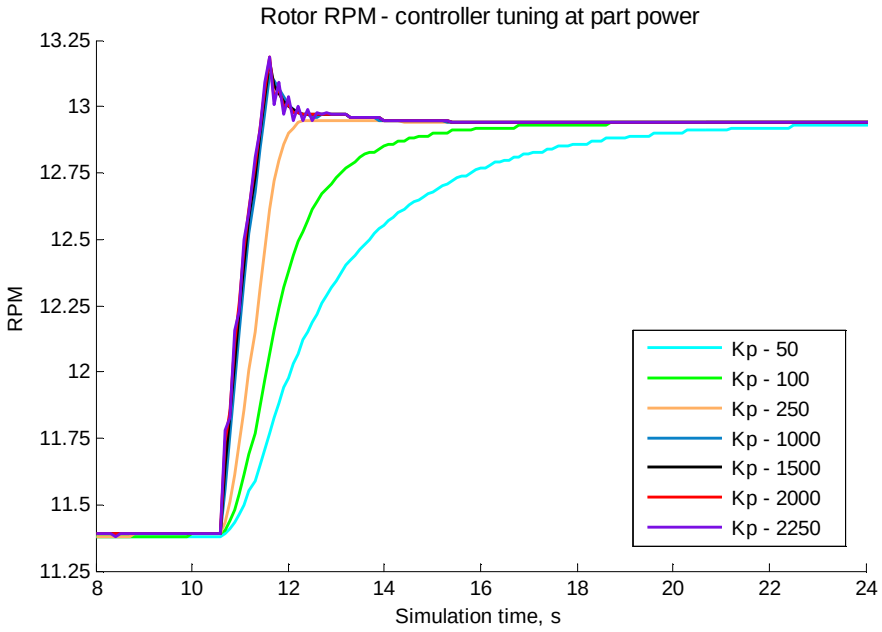

Figure 84 - Part power tuning

Figure 85 shows the turbine thrust load during the step change and subsequent control action. This shows that the settling time is similarly affected by the gain as for the RPM again with the gain threshold at approximately 1000. However it does not appear that the gain affects the level of load overshoot as in every case the maximum value is identical at around 24.5T. This suggests the overshoot is not dominated by the controller at this time scale but rather by the hydrodynamic model which is shown in section 3.12, Figure 89.

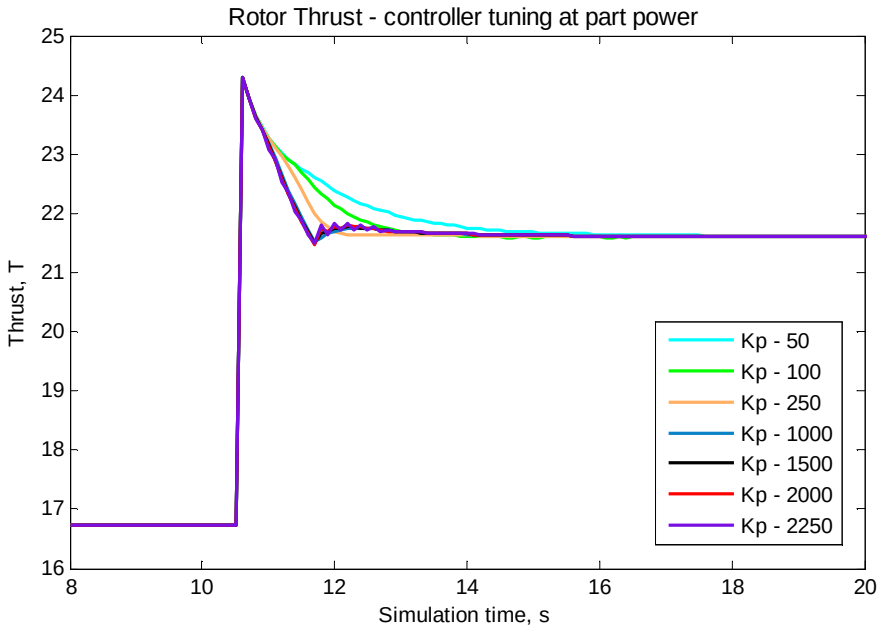

Figure 85 - Part power tuning: Thrust

3.12 Tuning at full power

In common with tuning at part power a step change of 0.3m/s was chosen as being a representative large change in environmental flow conditions for the full power tuning. In mode 2 the turbine will be moving in and out of the load shedding regime depending upon turbulence fluctuations. Although the flow velocity step is identical to mode 1 the control system will force a much larger change in RPM on the rotor as the device is subjected to a much more energetic regime. For a step change from 2.5-2.8m/s the available power increases by 40% from 326 to 458kW. However, the turbine can only absorb a maximum of 434kW in order not to overload the electrical equipment which must be achieved through the load shedding algorithm. Based on the turbine design curves a 5 RPM increase in rotor speed is required to maintain rated power which is four times greater than for mode 1.

Figure 86 shows the step change in flow conditions ('Hub flow') plotted along with the control system response in terms of estimated flow speed as determined by solving the turbine power equation. The response is fairly similar

to mode 1 if K_p is less than 1000 i.e. there is a slight overshoot before the estimation settles to the new equilibrium. Furthermore, it is also evident that the magnitude of the gain is important to the settling time which reduces as gain increases. However, there is a threshold at K_p = 1000 where the estimated value does not actually exceed the real flow before oscillating towards the equilibrium. In all cases the settling time is considerably longer than for the mode 1 cases.

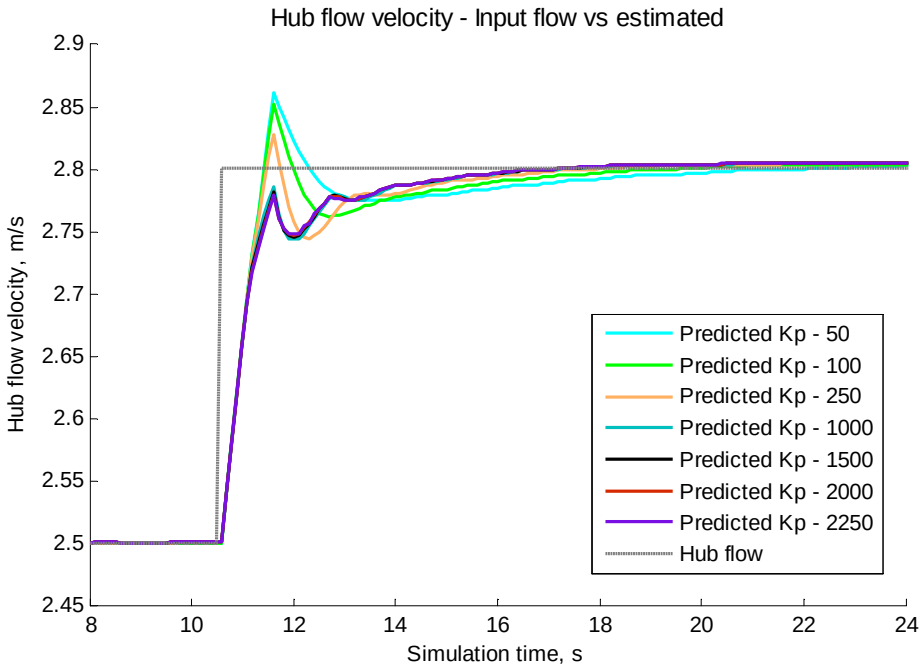

Figure 86 - Estimated flow velocity

This is reflected by Figure 87 below which shows the measured RPM response to the control action from the step change in flow as the settling time is around 5 times longer than mode 1. This also shows the effect of gain on settling time and stability. As expected the threshold gain is determined from RPM stability as 2250. For system gain values above 1000 no reduction in settling time is observed as for the mode 1 simulations.

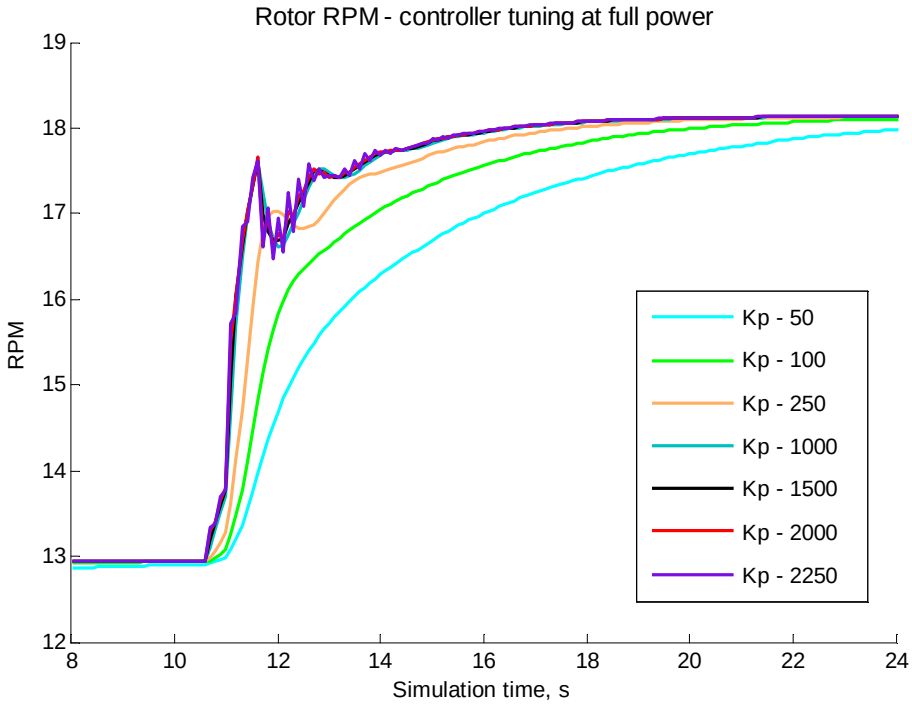

Figure 87 - RPM response at full power

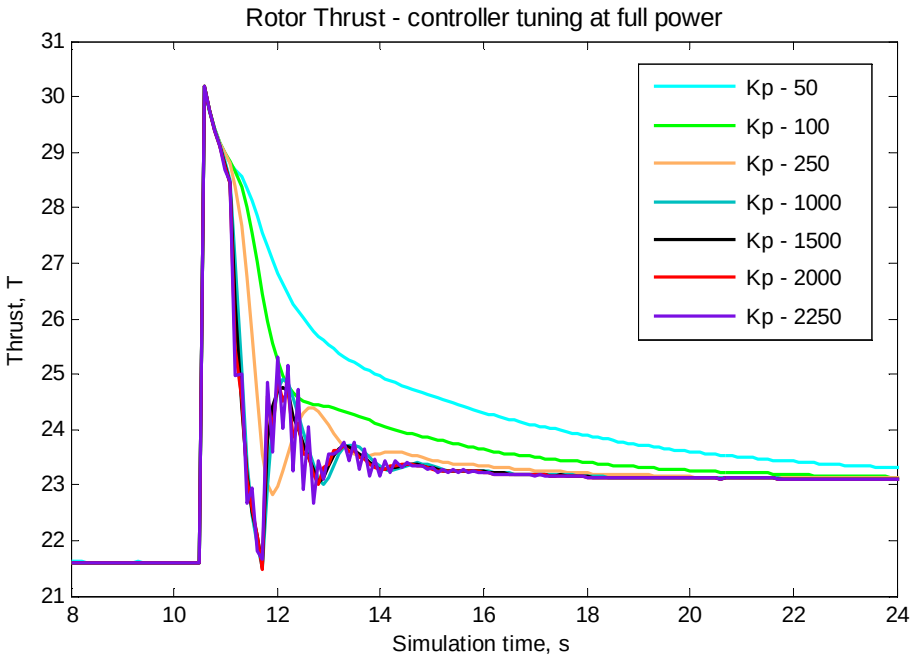

Figure 88 - Thrust load response at full power

The time history of turbine thrust is shown in Figure 88. This shows behaviour similar to mode 1 where the maximum value of the overshoot is not determined by the system gain however the settling time is strongly influenced by K_p. In contrast to mode 1 the load appears to show stronger oscillations at lower system gains as there is evidence of oscillation when K_p = 250, significantly lower than mode 1.

In order to compare the two control modes the peak overshoot ratio, decay ratio and settling time are calculated for simulations run at $K_p = 0.45K_u$. This is the value of gain for a PI control system that will deliver a ¼ decay ratio which is traditionally considered appropriate for a wide range of applications (see Table 2 above). Table 6 below lists these metrics for both the turbine RPM and thrust load.

Control mode	Mode 1	Mode 2	Ratio (2)/(1)
POR RPM	0.16	0.3	1.875
POR Thrust	0.53	4.72	8.906
DR RPM	0.021	0.064	3.048
DR Thrust	0.091	0.183	2.011
Ts 95% RPM	2.2s	5.5s	2.500
Ts 95% Thrust	2.1s	7.5s	3.571

Table 6 - Comparison of tuning in mode1 & 2 (POR – peak overshoot ratio, DR – damping ratio)

In each instance the mode 2 simulation has inferior performance compared with the mode 1 case. The decay ratio (DR) for both RPM and thrust is considerably larger than for the full power mode which is borne out by the increased the settling time. However, although the peak overshoot ratio (POR) is higher in mode 2 for thrust this is most likely a result of the high rate of change in load rather than the impact of the controller gain and is influenced mainly by the hydrodynamic model. This highlights a potential weakness of the fixed pitched

rotor design as the controller is unable to influence the overshoot in load caused by rapidly changing rotor speed. Therefore a balance must be found such that the gain selection allows rapid reaction to turbulent fluctuations but not at such a high rate that additional excessive cyclic loads are forced on the blades that will negatively influence fatigue life.

The effect of the hydrodynamic model was investigated in more detail by running the same flow cases but with the dynamic inflow solver switched off such that the code became quasi steady. The results of this are shown in Figure 89 below which plots the quasi steady results against the dynamic results for three values of controller gain. Settling time is greatly reduced when the dynamic inflow model is not employed as would be expected when the modelling process does not account for the changing load over the chord length of the blades as discussed earlier this chapter. The characteristic time constant for the Deltastream rotor in this flow (2.5m/s) is approximately 5s calculated from the ratio of the turbine diameter to mean flow velocity, D/U. This accounts for the increase in settling time between the two cases shown in the Figure 89.

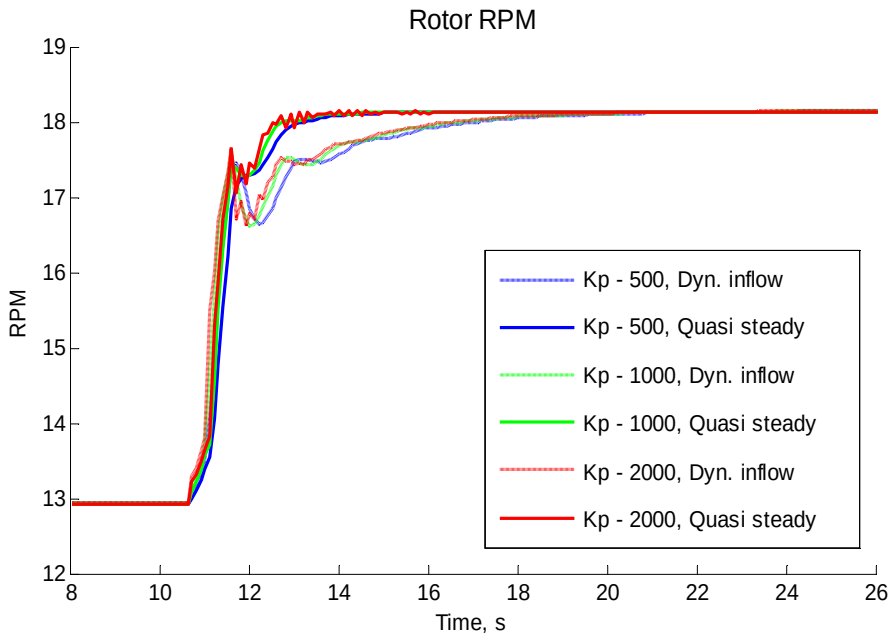

Figure 89 - Quasi steady vs unsteady simulation

For the quasi-steady model steady state is reached at 13.5s into the simulation (3s after the step change in mean flow) whereas with the dynamic inflow model the RPM does not reach a new steady state until 18.5s (8s after the step change).

3.13 Effect of the controller

In the proceeding section the effect the controller has on the turbine will be discussed in comparison with the open loop and ideal response as well as how the power demand is affected by system gain. Furthermore an example of the controller leading to turbine instability will be shown and the threshold at which this occurs.

Figure 90 below illustrates the performance of the turbine control algorithm in comparison to the open loop and ideal response of the Deltastream to a step change in flow conditions in terms of thrust. The open loop response assumes a steady rotor RPM independent of the flow step. This exhibits the same peak in overshoot as the other cases but the equilibrium load, as expected, is much higher. In fact it shows the turbine would operate at well above its maximum load capability at over 30T. The ideal case is for a situation where the control system is not predicting the flow speed rather the model is being artificially provided the area weighted mean flow such that there is no error in the set point. The benefit of this is clear; the decay ratio is minimised and the settling time is reduced when compared with the two other control cases where the mean flow has been estimated by the control algorithm for gains of 250 and 1000.

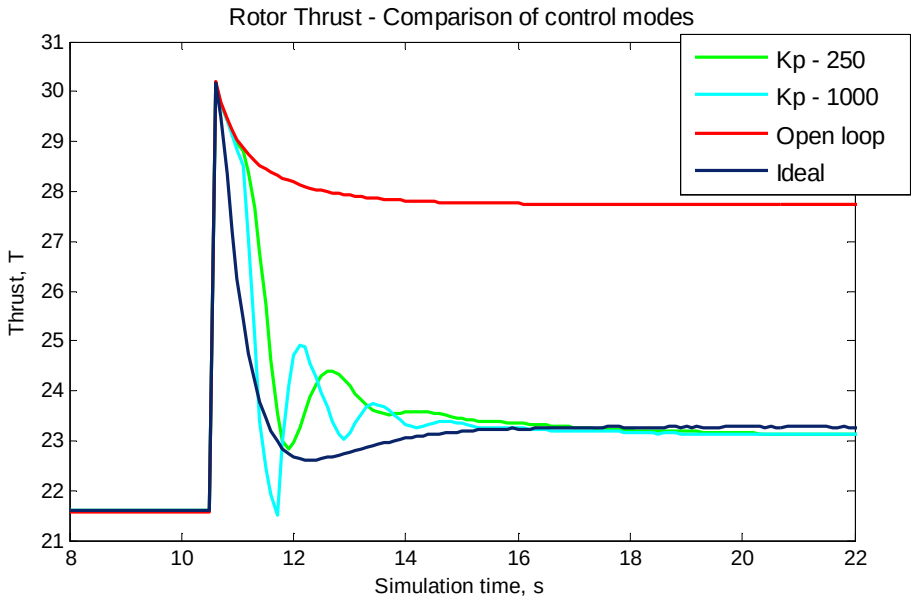

Figure 90 - Control modes

The error in the estimation is clear from Figure 90 which shows the ideal case compared with the estimation using two values of gain that may be realistically applied to the controller; K_p = 250 & 1000. As described in Table 2 values of gain significantly below the ultimate gain are desired for satisfactory functioning of the controller. To explore this design space values of 10 and 50% of the ultimate gain are therefore used as these are the lower and upper thresholds of gain that may be practically applicable. This shows a slight initial overshoot followed by an oscillation in estimated flow before the controller settles at the new equilibrium at 17s into the simulation, a settling time of approximately 6s. The uncertainty in set point leads to fluctuations in the turbine load but also rapid changes in the power demand from the generator to alter the rotor speed as shown in Figure 91. This shows high frequency changes in power demand, from positive to negative, of almost 5% of the total load i.e. from +10kW to -5kW. Positive power relates to when the controller demands that power is sacrificed from the generator in order to increase the rotor speed. Negative power means the generator must temporarily absorb more power than there is available from the flow in order to reduce the turbine rotational inertia. It is clear

from Figure 91, the power demand, that controller gain is the principle factor in the size of the load and power oscillations which occur after the step change in flow. The more aggressive gain leads to larger amplitude oscillations which are undesirable from a fatigue perspective. Therefore a lower gain should be used which does not significantly increase the settling time in any case.

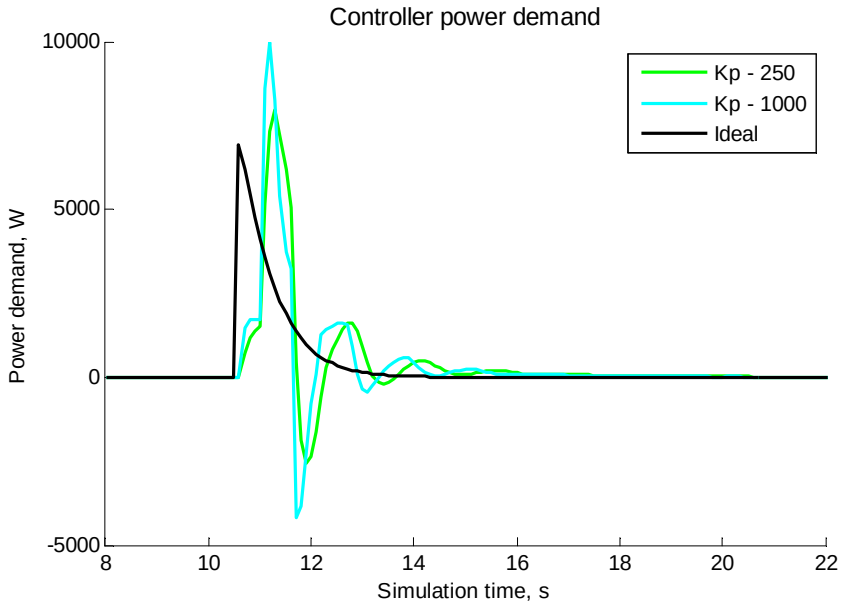

Figure 91 - Power demand

In order to illustrate controller instability the same simulation was run with the proportional gain set at around 10% above the ultimate gain as determined previously. The result is instability in the load signal for no change in set point as shown in Figure 92 below. This shows the thrust load response to the flow step for two gain values; above (K_p = 2520) and well below (K_p = 1000) the ultimate gain. While the low gain case reaches equilibrium and stabilises the high gain case apparently settles around the same equilibrium before starting to diverge. Although this is an important result it will not affect the control system design as it is undesirable to run the system at such large gains because as previously mentioned the optimum gain lies in the range 12-25% of the ultimate gain.

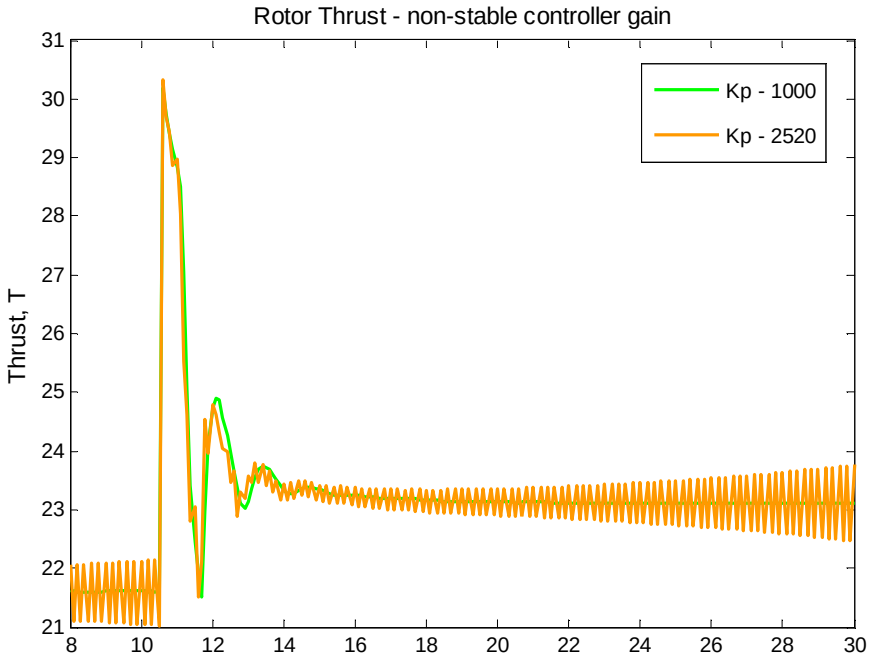

Figure 92 - Threshold of instability

3.14 Controller Performance with Turbulent Flow

The following describes the simulation of the turbine and control model operating with a realistic turbulence flow input and compares a range of gain settings to determine the best gain schedule for the Deltastream operating in Ramsey Sound's flow conditions. The flow regime used is representative of the turbine running close to rated flow, 2.65m/s, with 10% turbulence intensity. This provides a challenging case but is representative of very turbulent Ebb flow and relatively benign Flood flow that would be expected to occur with a probability of approximately 2% of the annual tidal flow but account for more than 5% of available flux. This is intended to provide a deeper insight into the capability of the control model beyond that offered by a simple step input. The control gains being studied vary from open loop through to the ultimate gain.

Figure 93 below shows the time history of the hub height flow velocity generated for this simulation using Turbsim. The turbulence model ensures realistic changes in flow speed both above and below rated, which is also

plotted for comparison, to test the turbine response. When the flow increases above 2.67m/s the turbine should enter the load shedding mode and increase TSR to release power and reduce maximum loads. The figure shows that the maximum velocity reached over the 8 minute simulation was 2.88m/s (marked at 428.8s), approximately 8% above the simulation mean which is due to large scale coherent eddies present in the flow. The nature of this is similar to the flow data extracted from Ramsey Sound on the Ebb tide shown in Figure 49.

Figure 94 shows how the turbine TSR changes during the simulation in response to the estimated inflow velocity. This appears to show the controller is responding appropriately as the TSR increases above the design point when the hub flow swings above the rated velocity threshold. Furthermore, the differences in the rotor response for three different levels of proportional gain can also be observed. The low gain (K_p = 50) response lags the hub velocity input during peaks in the flow speed by several seconds. It also does not appear as stable below the load shed threshold, where the controller is intended to firmly hold the rotor at the design TSR, when compared to the higher gain values as it appears to meander. Both the mid and high gain appear to produce a similar response to each however when the maximum and fatigue loads are evaluated significant differences appear between the two. It is shown in Figure 95 that the difference in DEL for simulations run with Kp = 250 compared to Kp = 2000 are around 16% which is an important difference when considered over the lifetime mission of the turbine.

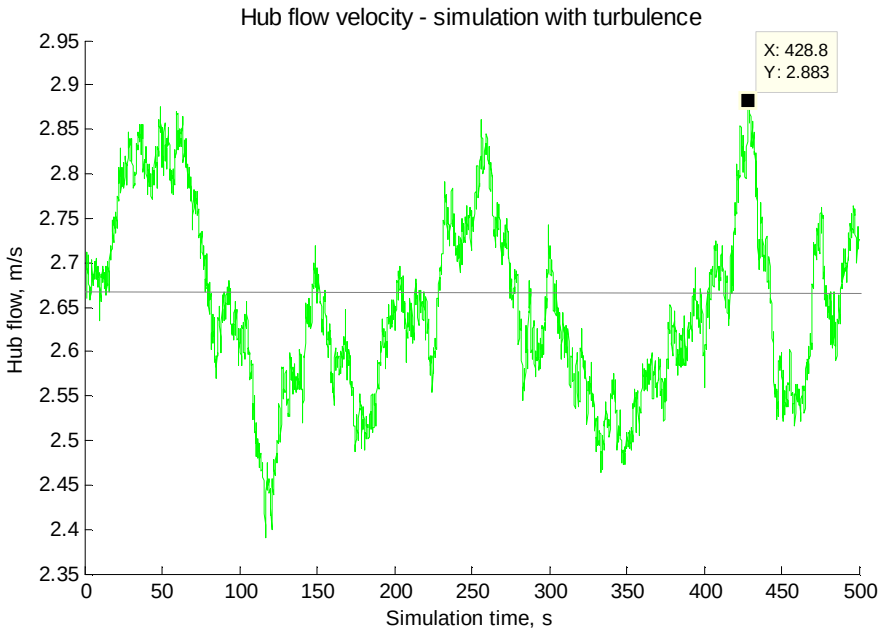

Figure 93 - Hub flow velocity

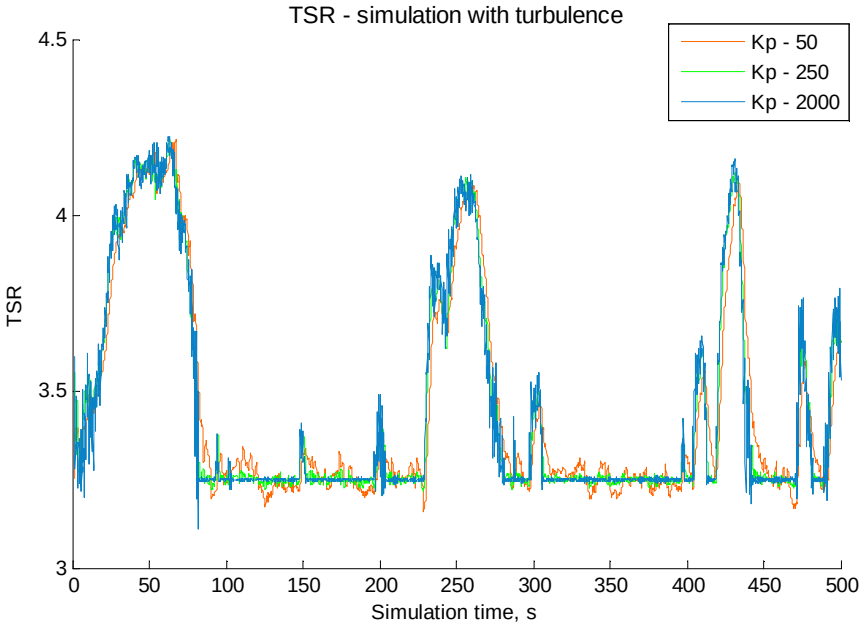

Figure 94 - Tip speed ratio

Figure 95 below shows the normalised DEL for this simulation when the gain is varied from 0 to 2000. This shows that the open loop response compared to the turbine response under the controller has a much higher DEL. Introduction of

the control model dramatically reduces the simulation fatigue loading (i.e. DEL) by approximately 47% when directly compared with a fixed speed rotor operating in identical turbulence inflow. Further this also shows that while the control model is effective at diminishing undesired cyclic loads across the full range of feasible gain values there is a distinct point at which the controller is most effective. This varies depending upon if the turbine is running at part or full power. At part power the most beneficial proportional gain constant is K_p = 500 while for the full power case K_p = 250 is most suitable i.e. when DEL is minimised. This suggests that the modified Z-N method holds true for the part power case as it is found that the optimal gain is K_p =0.25K_U as outlined in Table 6 in the previous section. However, it is also noted that the Z-N method is not suitable when applied to the full power case as the optimal gain is K_p =0.125K_U which is 50% lower. This can be explained by the influence of the dynamic inflow model which will produce large overshoots in load for rapid changes in RPM. For this case it is beneficial to sacrifice rate of response in order to minimise load peaks caused by excessively large changes in the rate of the blade lift (see Chapter 2 section 2.1.5 for a full description of this phenomenon). Figure 95 shows that when the gain is less aggressive a 5% reduction in DEL can be achieved. However reducing the gain further, towards the open loop response, results in a system that is too slow to respond to flow changes and the fatigue load rises again. For example when K_p is reduced to 50 an 11% increase in DEL above minimum is observed. This shows that simulating realistic turbulence allows for quantification of the gain settings and definition of an effective gain schedule that can be implemented in the control model.

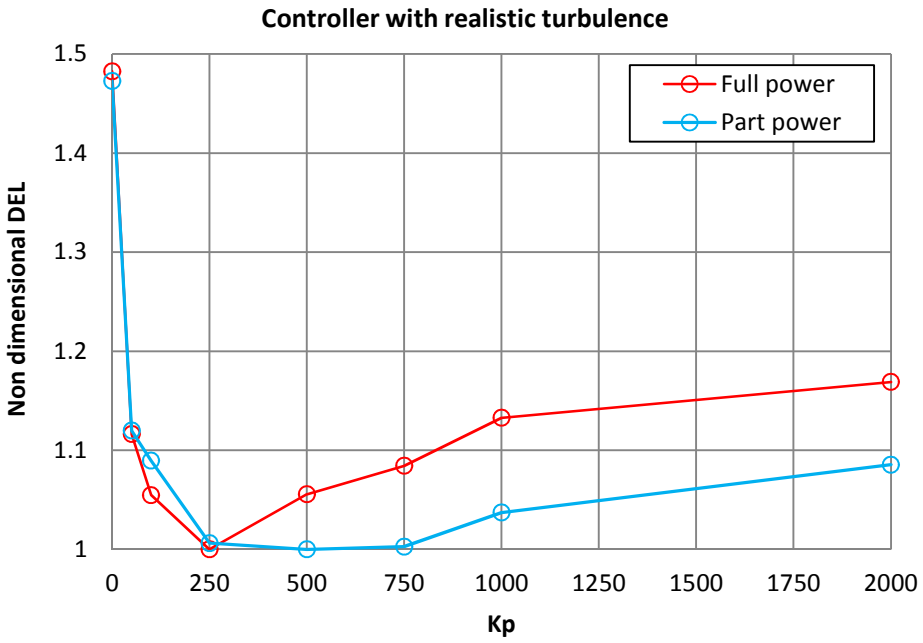

Figure 95 - Comparison of DEL vs controller gain

Finally, Figure 96 below demonstrates the peak thrust load experienced by the turbine versus RPM for the entire simulation at low, mid and high gain values. This gives an indication of how effective the control model is at limiting maximum load in relation to the pre-defined thresholds required to ensure the turbine remains fixed to the sea bed. The desired maximum thrust threshold is also plotted for reference and shows that a substantial majority of the points lie below it but there are times when the peak thrust exceeds the threshold. When the turbine thrust load exceeds the threshold it places the device in danger of over-turning and foot slippage. Movement of the device along the sea bed would have major implications for the safety of Deltastream and supporting equipment such as power cables as discussed in the thesis introduction. In general terms the effect of the control function can be seen from this figure, at the left side the closely bunched points between 12.5 and 13.5 RPM are when the turbine is operating in flows lower than rated and the set point RPM is in the linear range. The points become much more widely spread in the load shedding, non-linear, regime as the controller attempts to limit thrust below the threshold by rapidly increasing RPM. In terms of achieving a quantitative

comparison between gain values the maximum simulated values are 5.2%, 2.7% and 6.9% above threshold for low, mid and high gain respectively. This further reinforces the suitability of using $K_p = 0.125K_U$ (i.e. $K_p = 250$) as it performs better at limiting both fatigue and maximum loads (turbine operability will be discussed in detail in Chapter 5).

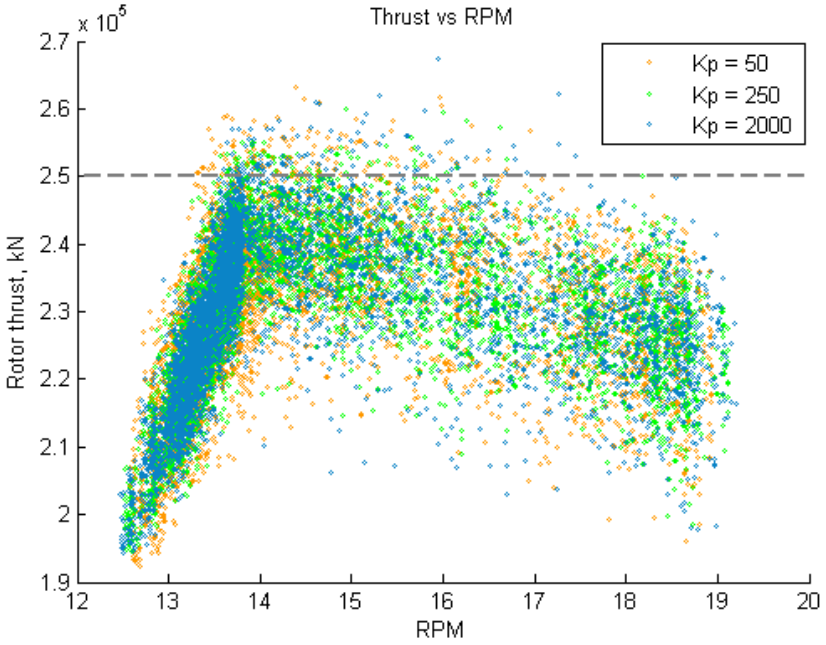

Figure 96 - Thrust data vs turbine RPM

3.15 Summary of turbine control

This chapter discusses the implementation and tuning of a control model which allows the turbine to estimate the tidal inflow velocity and then govern the rotor RPM in one of two modes. Mode 1 is intended to hold the rotor speed at the design TSR where the maximum available tidal flux can be absorbed for conversion to electrical power. This mode extends from minimum flow velocity (i.e. 1m/s) up to the turbine rated flow speed where the electrical output reaches the on-board installed capacity. At this point the control systems enters mode 2 which is a load reduction scheme that has two aims; hold the power constant at maximum power while at the same time limit the peak loads to protect the

device from damage. This is achieved through rotor speed control made possible by the turbine blade geometry which has been designed such that as TSR increases both power and thrust coefficients reduce.

The control system is a feedback loop but due to the nature of the tidal environment the system must operate without direct knowledge of the inflow current velocity. Therefore an algorithm has been successfully developed based on postdictive knowledge of the turbine performance to estimate flow speed for use as the controller set point.

During the development of the control model several observations have come to light with respect to the system performance when coupled with the turbine hydrodynamic model. Firstly there is a requirement for controller gain scheduling depending upon whether the turbine is operating in mode 1 or 2. In mode 1 the controller performance closely follows the classical Ziegler-Nicholls control theory. However in mode 2 due to the nature of the non-linear RPM design curve, which requires much larger changes in RPM for relatively small changes in flow, the Z-N method has proven too aggressive and a substantially lower gain was implemented to reduce load oscillations induced by the controller which led to a further 5% improvement in fatigue load reduction. It has also been proven that implementation of the control model has improved the level of fatigue loading on the turbine, as measured in terms of blade DEL, by around 47% when compared to a fixed speed turbine which will likely have a profound impact on the service life of the device (NB: the change in life is also a function of the turbine mission cycle which will be discussed in Chapter 5). When the ideal gain factor is utilised as compared to operating the turbine at constant speed (i.e. $K_p = 0$) the DEL is reduced by 47%. This is a large reduction in DEL and will contribute significantly to extending turbine life. Evidence for this is shown in Figure 95.

At high gain, close to and above the ultimate gain, the controller causes instability within the system that has been shown to lead to rotor load divergence which is a region that must be avoided to prevent damage to the device. Furthermore it must be noted that the gain schedule that has been

optimised for this rotor configuration is a function of the turbine geometry and rotating inertia of the drive train. A method has been developed to establish the system control model but it is not a universal model and it must be developed for each design iteration of the Deltastream device.

4 Model Validation

This chapter provides evidence that the code developed in the previous chapter can be used to accurately model a wide range of both wind and tidal turbines. Three literature sources have been selected to compare the experimental results of other authors with the results of this model. These sources were selected based upon the completeness of the information provided in terms of turbine geometry and operating conditions. All sources provided detail of the turbine blade profiles and airfoil lift and drag characteristics. Furthermore a sufficient description of the fluid inflow characteristics were provided to be able to satisfy all input parameters required of the code developed in this work without resorting to any assumptions.

There are a several comparisons made with steady state experimental results which are then proceeded by evaluation of two cases in which the transient turbine loads have also been made available. The aim of this is to provide a reliable validation of all aspects of the author's code in terms of its aerodynamic computation capabilities. In particular the transient cases studied allow for the effects of the dynamic inflow model to stand out very clearly.

The chapter is concluded with a summary of the experimental work carried out on a scaled version of the Deltastream turbine. The turbine is operated in turbulent flow and the experimental results are compared with the predictions from the author's code. This provides a further level of validation through implementation of the turbulent inflow generator.

4.1 Model validation summary

In the following section the performance predictions for five experimental turbines has been carried out using the authors code and are compared with both experimental data and the results from three other pertinent models. Steady state and transient simulations have been carried out on three wind turbine and two tidal turbine geometries at both model and full scale. The results from two research codes have been included in the validation study to demonstrate the state of the art in the research community both in Europe and

the US. The US code is called AeroDyn and was developed by the National Renewable Energy Laboratory (NREL) which is part of the US Department of Energy. The European code was developed at Delft University of Technology (DUT) during a large EU sponsored research project. Furthermore comparisons are made with the commercial analysis code Bladed which was developed by Garrad Hassan Ltd and is widely regarded as the standard industry tool for this type of analysis of wind turbines. The data available from the two full scale wind turbine experimental programmes comes from the Unsteady Aerodynamics Experiment (UAE) carried out by the NREL and from field tests of a 2MW Danish wind turbine in Tjaereborg.

4.1.1 UAE Phase VI research wind turbine (NREL)

The wind turbine research community has made significant improvements in the ability to simulate wind turbine performance and loading. However, certain deficiencies in the modelling led to poor descriptions of wind turbine performance in extreme conditions such as gusts, sudden direction changes, yaw, wind shear and tower shadow[147]. It is important to model such conditions in order to design for long life under high loading. The National Renewable Energy Laboratory (NREL) developed a test program called the Unsteady Aerodynamics Experiment (UAE) to address these problems.

The NREL built an extensively instrumented horizontal axis research wind turbine which was field tested for 10 years at the National Wind Technology Centre (NWTC)[147]. Field testing of the UAE rotor highlighted the extremely complex nature of the aerodynamics of the rotor. In conjunction with European researchers it was deemed that better progress would be made if a full scale machine could be tested under precisely controlled conditions in order to isolate aerodynamic phenomena caused by specific inflow conditions. The result of this was the research program based around the UAE rotor in the NASA Ames large wind tunnel. This is a very large facility (80 x 120 ft test section) allowing for a full scale device to be run under conditions analogous to commercial turbines.

The UAE rotor is a 2 bladed, constant speed (72rpm), upwind, stall regulated machine. It has a rotor radius of 5.03m with tapered and twisted blades which utilise the NREL S809 airfoil along their full span except for a small part at the root where it transitions to a circular cross section[148]. The blades are designed with the inbuilt capability to measure the chordwise pressure distribution along the upper and lower surfaces from 22 pressure tappings located at 5 spanwise locations (30%, 47%, 63%, 80% and 95% radius)[149]. The pressure distribution can be used to determine the local aerodynamic coefficients, Cn and Ct from which the lift and drag coefficients can be estimated. Probes located in front of the blades measure the wind inflow angle from which the angle of attack can be approximated. Together these provide experimental data of the chord and span-wise pressure distributions, streamline direction and local blade loads.

In conjunction with this experimental work the NREL invited various wind turbine research groups to undertake a study of the performance of the UAE rotor using their own research codes in a blind test in order to validate their models and in exchange for the experimental results. The technical specifications of the UAE rotor were supplied in order for the analysis to be carried out. This included the blade geometry in terms of chord and twist distribution. The airfoils lift and drag data for the S809 blades was supplied by Ohio State University (OSU) at a Reynold's number of 7.7E5 from wind tunnel tests. This was provided from a non-rotating wing section and as such is considered as two dimensional data.

Post testing, a data set of localised lift and drag was reversed engineered using readings from the blade pressure taps and inflow angle for each of the five span positions. This data is shown in Figure 97 below along with the 2d data from (OSU). As previously discussed in the section on stall delay simply using 2d section data as the input to a BEM code will not capture the inherently 3d nature of the flow, particularly in the region from the root to around the 50% span-wise position. Usually the only option available is to use a stall delay model to estimate the effect of rotation on the flow over the blade at a specific radial position. However, a more accurate alternative is to directly implement the data gathered from the rotating blade, possible in the case of the UAE rotor.

Therefore for this validation study the 2d data from OSU, the 3d data gathered at Ames and a stall delay model data will all be used as inputs to the authors BEM code in order to understand how accurate the code is following each approach.

Figure 97 shows how in the pre-stall region, below 15 degrees, the data from all span-wise points is similar to the 2d data provided by the OSU wind tunnel tests. However, once into the stall region the stall delay effects of rotation become more pronounced. The inboard (30%) part of the blade shows, as expected, the greatest degree of stall delay with maximum lift above 2 at 28 degrees whereas for the 2d data lift is approximately 0.75 at this same angle, a very large under prediction. This effect is obvious out to the 63% span-wise position. At the 80% position the 3d and 2d data are very similar while in the blade tip region (95%) the 2d lift data is higher than the measured 3d data even in the pre-stall area. The effects on the drag data are different. While the inboard section appears to be affected by a large drag increase after 20 degrees the other data for the outer part of the blade appears to adhere more closely to the 2d data.

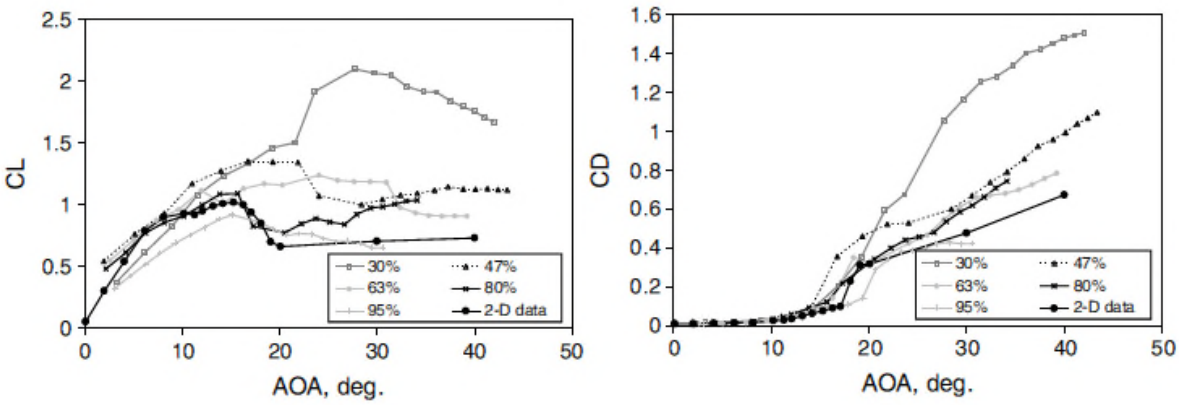

Figure 97 - 2d and 3d section data for the S809 airfoil[149]

Part of the UAE testing included gathering data during steady inflow conditions. This included measuring the rotor shaft torque and power and estimating the blade loads from the pressure measurements. The UAE rotor geometry[150] as shown below in Figure 98 was implemented in the present BEM code to

calculate the steady state values of power, torque and blade root bending at various wind speeds.

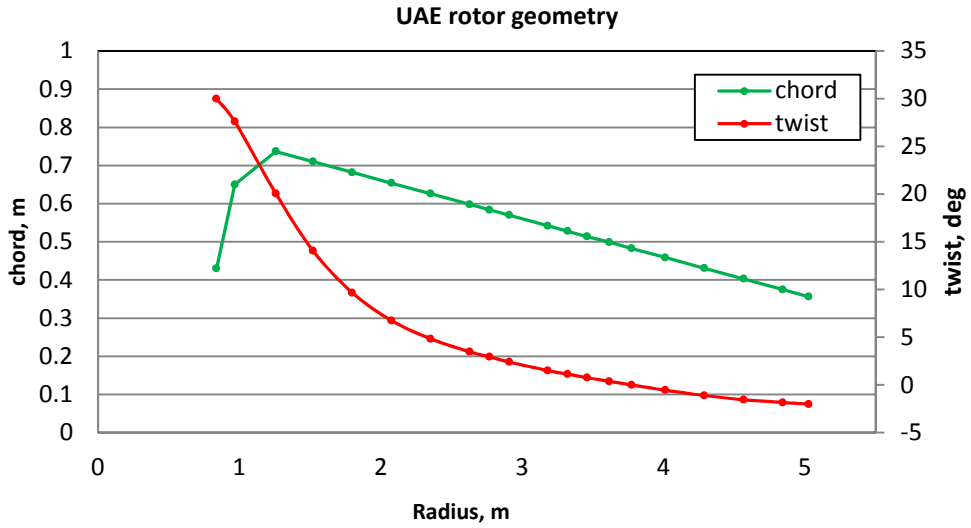

Figure 98 - UAE geometry

Figure 99 below shows the power curve vs wind speed for the UAE rotor in the previously discussed configuration with the prediction from the BEM code and also a prediction from Bladed using the 2d section data[104151]. It can be seen that Bladed agrees closely with the measured results for wind speeds less than 10m/s, this is when the turbine is operating below its rated power and without stalling effects. The present BEM code also provides a good prediction in this region as would be expected as the span-wise flow is insignificant.

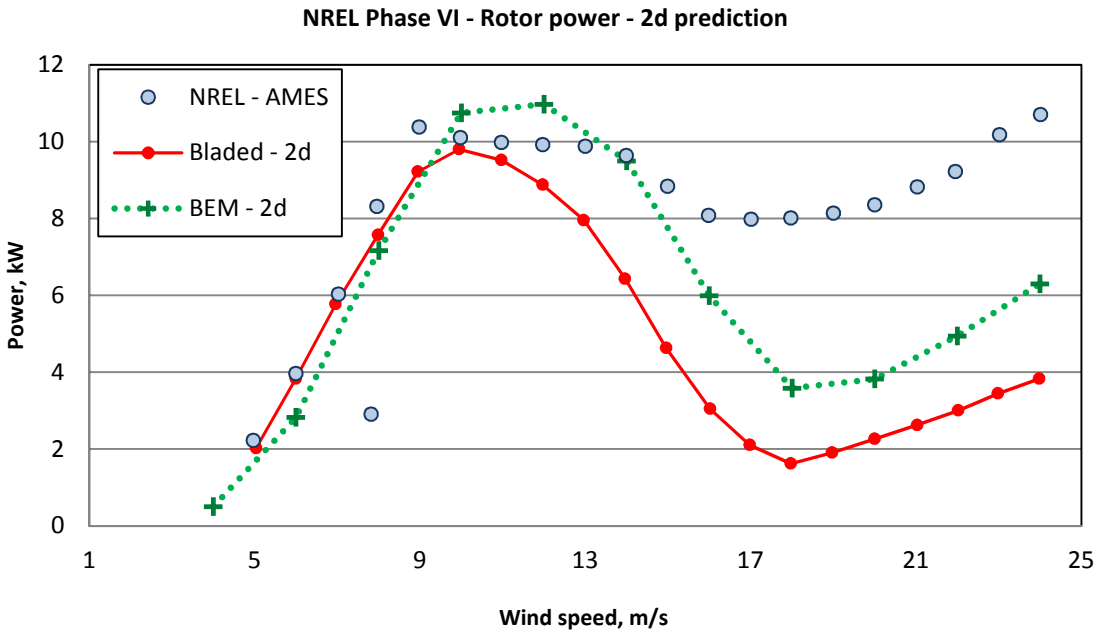

Figure 99 - UAE power curve - 2d

In the stalled regime above 12m/s Bladed tends to under-predict the power output. Similarly this occurs for the BEM code above 15m/s. While both codes predict the general shape of the power curve, a reduction in power after peak and then a recovery, neither is very accurate beyond 15m/s. This is because the 2d data does not account for the stall delay effects caused by rotation.

Figure 100 shows the same as Figure 99 but the Bladed prediction is based upon using a stall delay model[151] and the BEM code uses the reverse engineered 3d section data as previously described. For wind speeds up to 10m/s both predictions are identical as per the 2d data case. Just beyond this point, close to peak power, both codes tend over predict the maximum power. This could be due to the turbine transitioning into stall but rotational effects are weaker than after peak power. In the fully stalled region for wind speeds greater than 15m/s the BEM code delivers a prediction very close to the experimental data as would be expected when using the 3d data. In this region Bladed slightly under-predicts the power at high wind speeds but is much closer than when the 2d data is used.

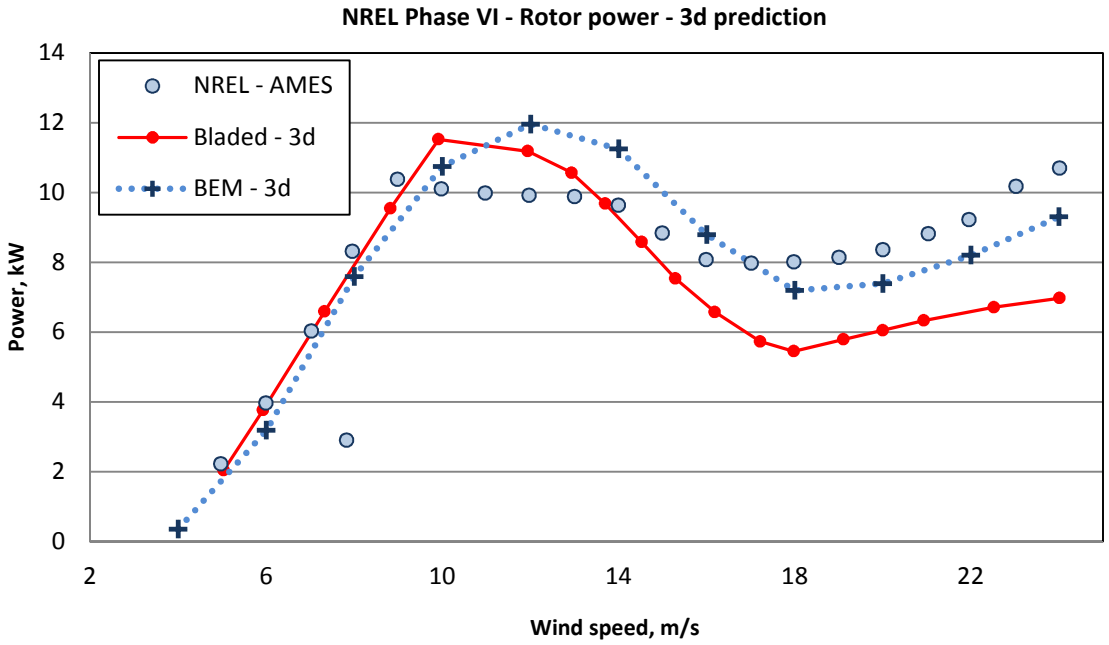

Figure 100 - UAE power curve - 3d

In order to compare how the stall delay model proposed by Snel performs when utilised within the BEM code a comparison between the 2d, 3d and stall delay data was undertaken and presented in Figure 102 against the measured power data. The stall delay model lift data is shown in Figure 101 below. It is shown in terms of the original 2d lift data as well as the prediction for each of the 5 span-wise stations measured at Ames and can be compared directly with the lift data in Figure 97.

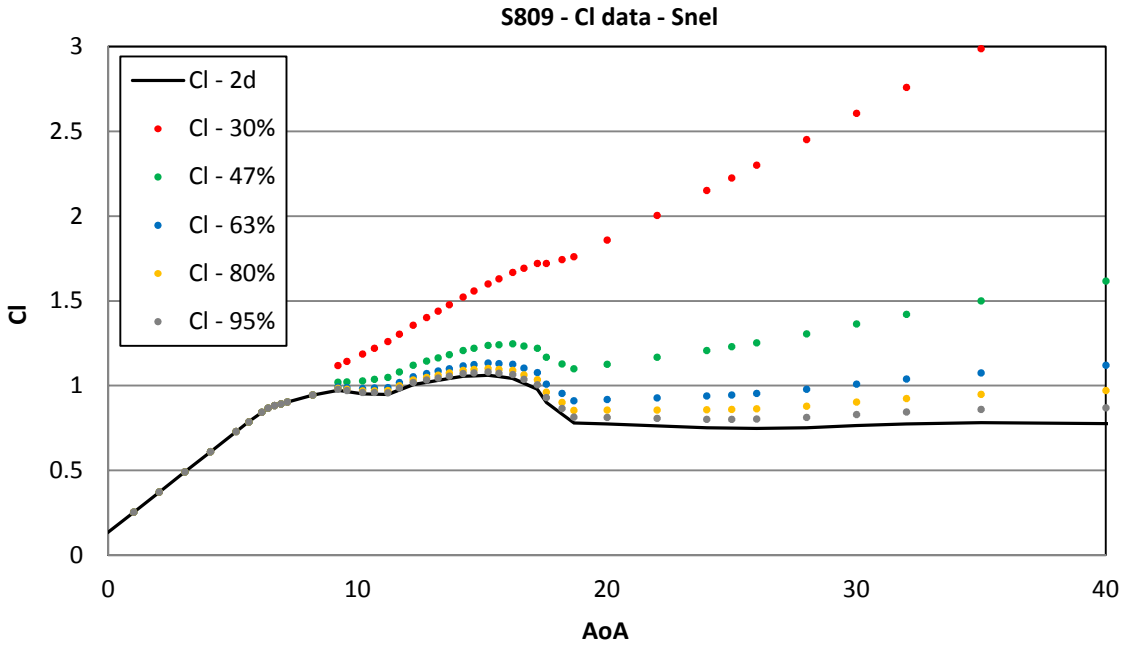

Figure 101 - Stall delay data - S809

The inboard station (30%) is over-predicted at all angles above the linear section of the lift curve. It is marginal between 10 and 15 degrees but after this the difference with the measured data increases with AoA. Most of the other stations are in good agreement with the experimental data which is shown in Figure 97. The agreement is particularly close at the 47% span element.

The result of the over-prediction can be seen in Figure 102 where the values of power as predicted by the BEM code are considerably higher around peak power than the experimental values which include the error bars for each data point. Thereafter, at higher wind speeds, the prediction using the stall model is consistently higher than the measured values but the difference is not any larger than the under-prediction when using the 3d data. In fact both the 3d and stall delay predictions lie within the error bounds of the measured data after approximately 18m/s.

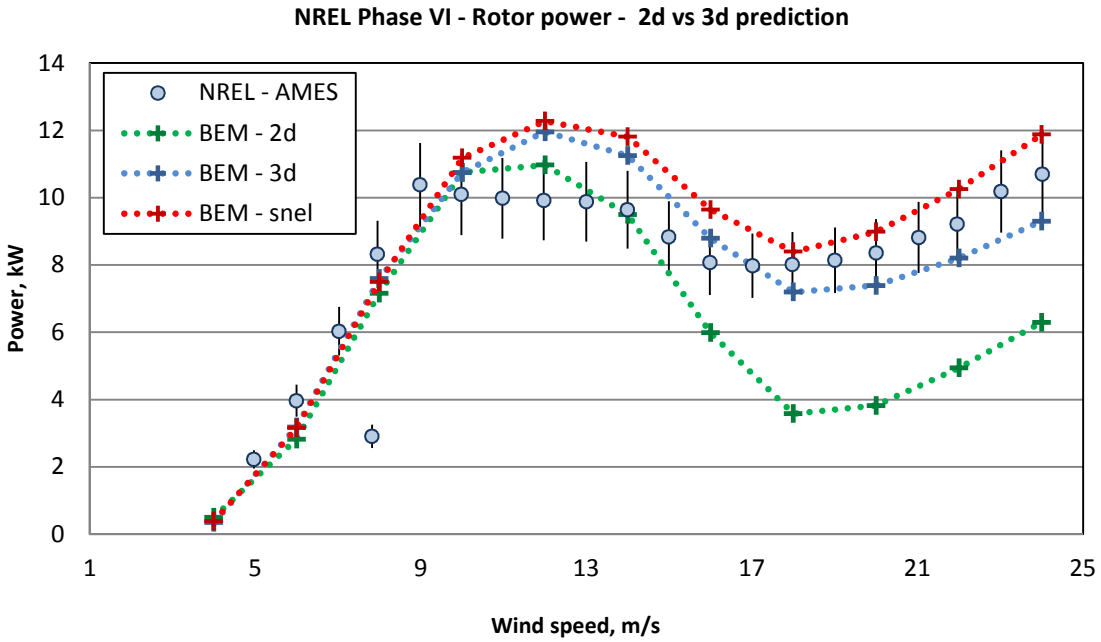

Figure 102 - UAE power curve - 2d vs 3d

Figure 102 clearly shows the importance of using appropriate section data when predicting turbine performance when operating in stall. The under-prediction of the power when using the 2d data in the stalled region is on the order of 50% whereas the difference when using the 3d data is only around 10-15%.

Figure 103 shows the power curve in terms of TSR for the 2d and 3d data plus the stall model. When the rotor is lightly loaded at high TSR's there is little difference between using 2d and 3d data because the rotor inflow angle is relatively low and hence the AoA is in the linear region of the lift curve. As TSR decreases the predictions begin to diverge, just after peak power as the rotor becomes more heavily loaded, but they are still comparable. However, at low TSR's where the rotor is operating in deep stall the predictions become increasingly divergent as rotation effects play a larger part in determining the blade loads.

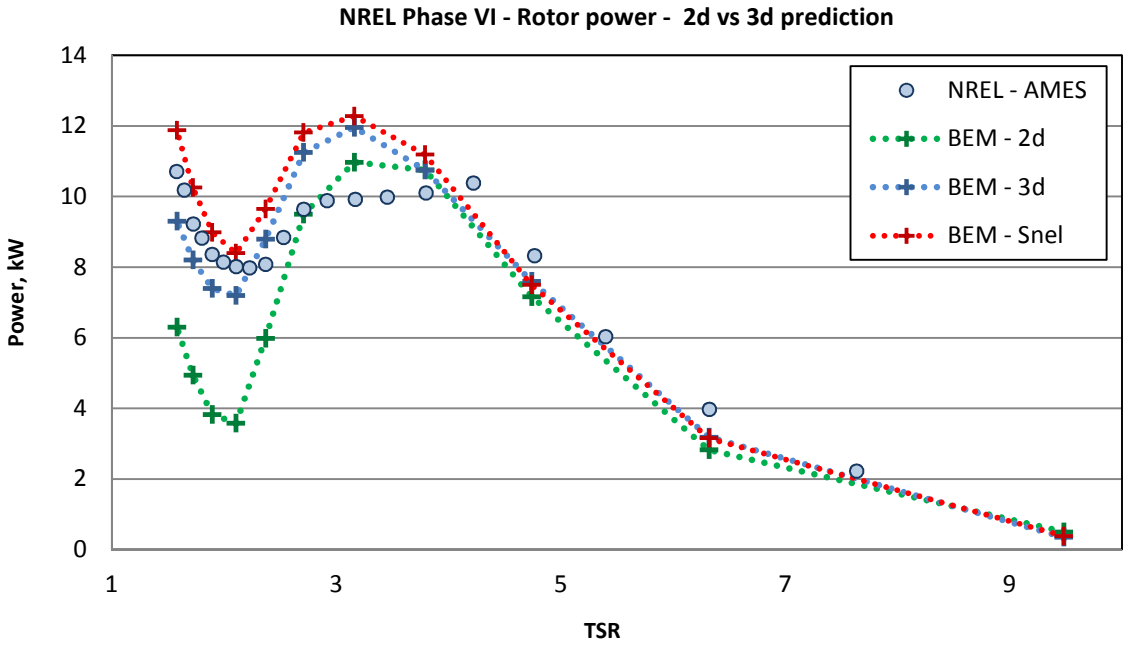

Figure 103 - UAE rotor - Power vs TSR

This is evident from observation of Figure 104 which shows the AoA distribution over the blade span for three different wind speeds as predicted by the BEM code. For low wind speeds (7m/s in this case) and high TSR's the AoA is quite low and relatively constant with span at approximately 5 degrees. Clearly the whole of the blade is operating in the well behaved linear portion of the lift curve which is very similar for both rotating and stationary blades. This is where the blade has been designed to operate best as the lift to drag ratio is very large and hence the power coefficient achieved is high. This is where the BEM code is most accurate because the assumptions about the flow conditions are hold true. In particular the assumption that each of the radial stations that make up the blade are independent of each other fits well.

At medium wind speeds (12m/s) around TSR's of 3 to 4 the AoA varies from 5 to 25 degrees from root to tip and therefore the blade is partially stalled. Stall occurs from the root outwards as TSR decreases. At low TSRs, high wind speeds (25m/s), the whole blade is operating post stall and therefore accurate prediction of its performance is reliant on trustworthy airfoil data such as from a stall delay model. Figure 103 shows that the BEM code, in conjunction with 3d

airfoil data, gives a good prediction of the power output at high TSRs and low TSRs. However, for TSRs around 3-4 where the blade transitions into stall the code prediction differs the most from the experiment. The 2d data tends to give a better fit with the experimental data suggesting that the 3d stall data is an over prediction of the post stall lift characteristics at this point.

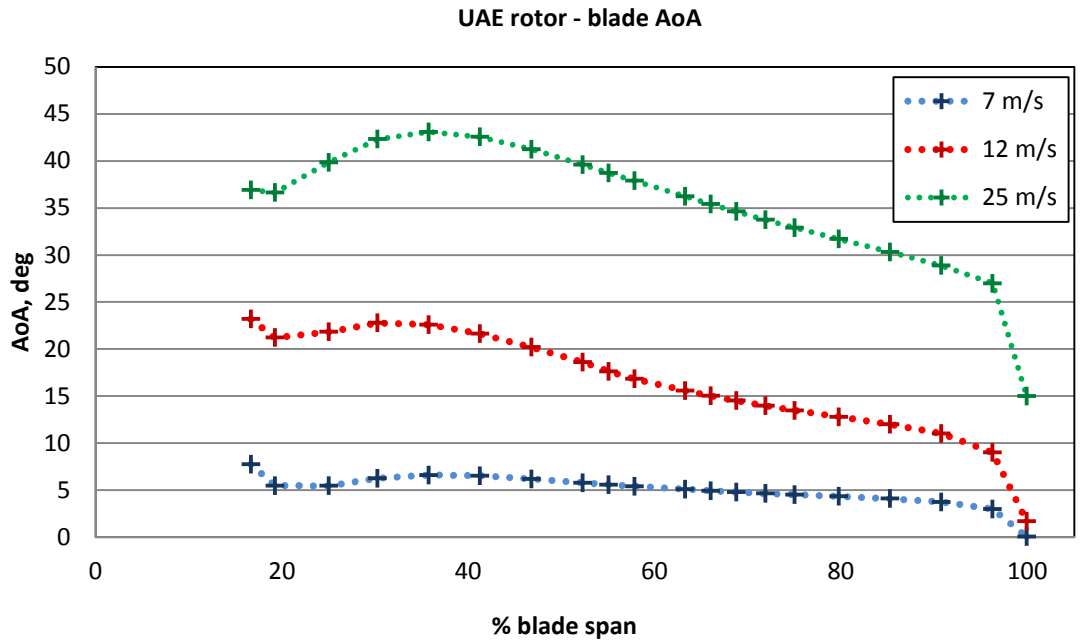

Figure 104 - UAE rotor - blade AoA

In another analysis of the UAE results data for both torque and blade root flap-wise bending moment is available. One of the groups involved in the blind test used the code AeroDyn and YawDyn to simulate various loads on the UAE rotor for a number of the inflow conditions. AeroDyn is a code for handling wind turbine aerodynamics in conjunction with dynamics analysis programs such as ADAMS and YawDyn. It uses machine and blade geometry information, airfoil aerodynamic data and wind inflow information to calculate aerodynamic loads on horizontal axis wind turbine blades. As with the previous simulations of rotor power both the 2d and 3d data were used in comparisons of the rotor torque and the blade flap-wise moment.

Figure 105 shows the torque measurements from the Ames test and the predictions of the BEM code and AeroDyn (YawDyn) for the same inflow conditions using the 2d data. As before both codes give good results for low wind speeds up to approximately 15m/s but as stall progresses from this point the accuracy of the predictions appears to reduce.

This deficiency is addressed when either the 3d data is used and when the stall delay model is applied, the results of which are shown in Figure 106. Here the same experimental results are plotted but the AeroDyn simulation includes the 3d data which then affords much closer predictions for the high wind speed inflow. The 3d data and stall delay model have been applied to the BEM code in the manner as for the power data discussed previously and both show the same trend as for the power curves i.e. an over-prediction at medium wind speeds but a much better prediction at high wind speeds than for the 2d data.

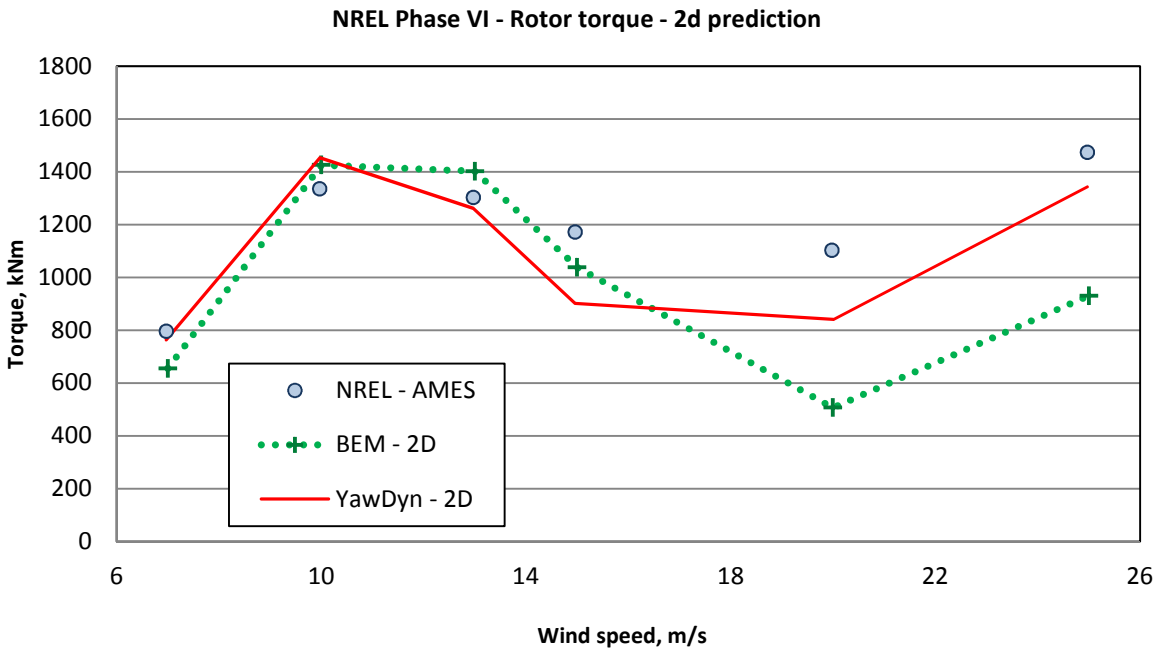

Figure 105 - UAE rotor - 2d torque

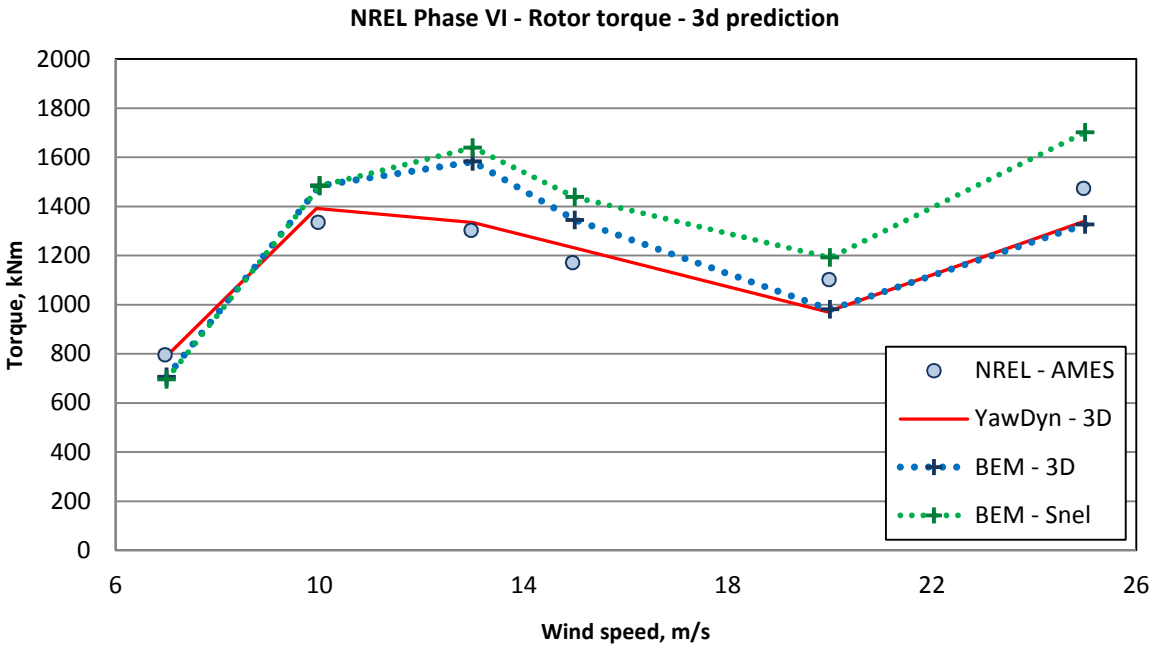

Figure 106 - UAE rotor - 3d torque

The final dataset from the UAE examined as part of this validation study is that of the blade root flap-wise moment. The previous authors also compared the AeroDyn results with the estimations of blade moment determined from the pressure measurements gathered on each blade. Figure 107 shows the AeroDyn and the BEM code prediction using the 2d airfoil data. At low wind speeds it is clear the AeroDyn prediction is very close to the experimental results while at high wind speeds it significantly under-estimates the bending moment. This is generally similar for the BEM code except the low wind speed prediction is poorer in places than AeroDyn but the high speed prediction is better.

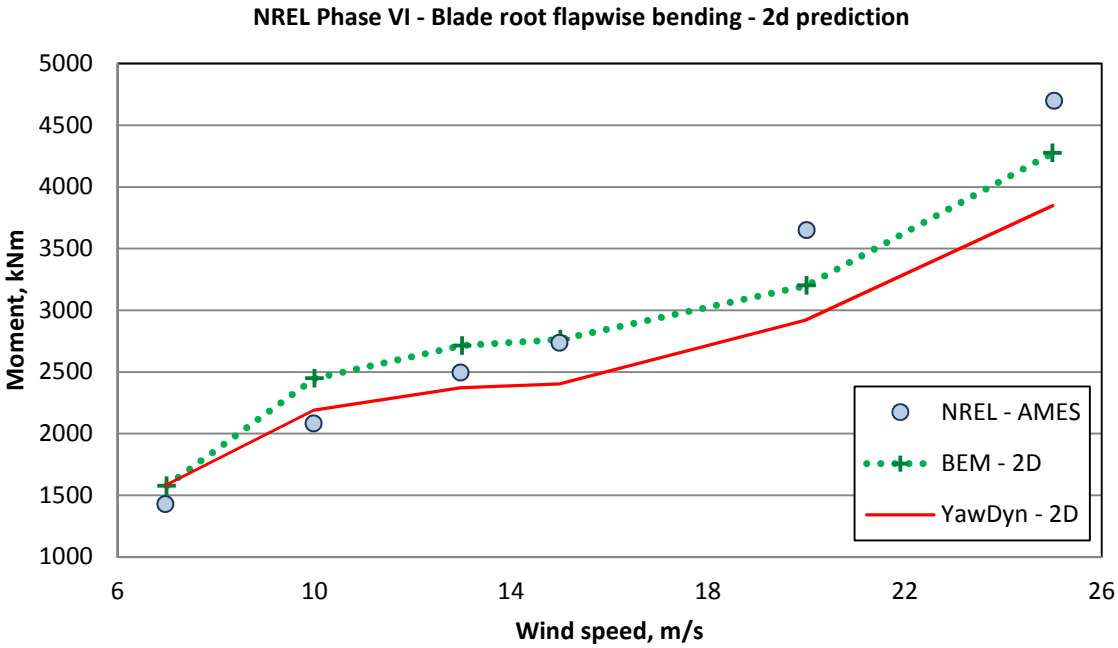

Figure 107 - UAE rotor - 2d bending

Figure 108 shows the results using the 3d airfoil data and with the stall delay model (BEM). Using this data significantly improves the AeroDyn results as the difference in the high speed data decreases from 25% to less than 5%. The same trend is noticed for the BEM code where the discrepancy between the results drops from around 14% to 8% for the 3d case.

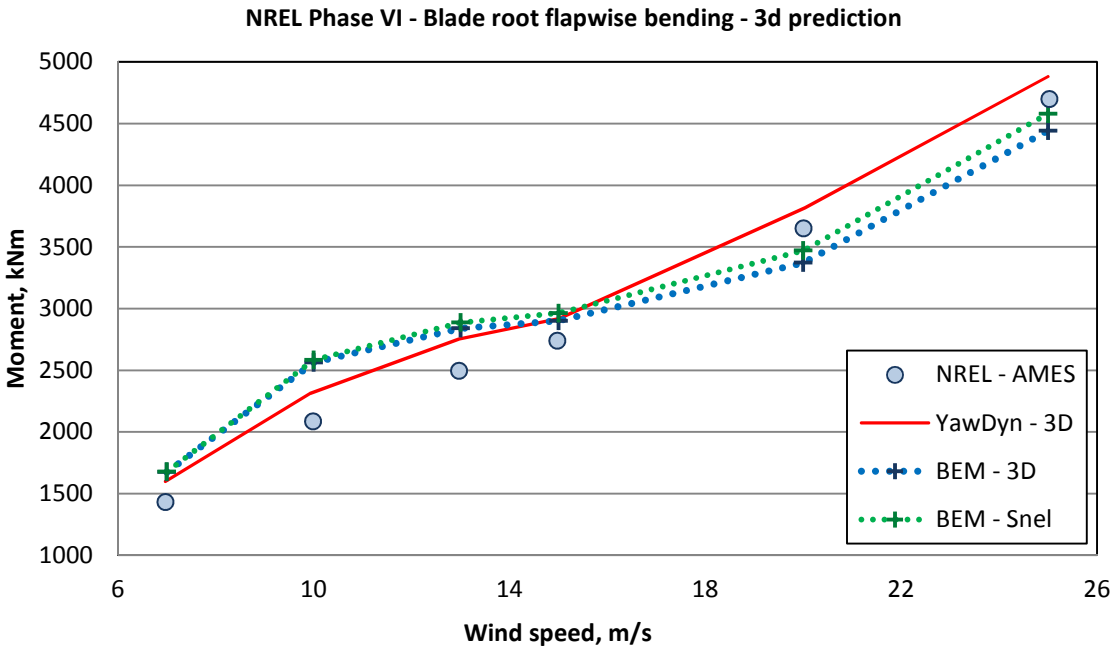

Figure 108 - UAE rotor - 3d bending

Due to the wide range of wind speeds over which the rotor was tested it was possible to compare the numerical results with data for pre-stall, stall transition and post stall rotor operation which is generally not available from experimental data. Based on the unique dataset available for the UAE rotor the BEM code generally delivers robust results with good agreement to the experimental results, most of the results lie within the error bounds of the measured data.

The validation study shows that the BEM code is only as good as the airfoil aerodynamic data available for the rotor. It is vital to apply a correction for stall delay when operating beyond the linear lift region of the data although prediction when operating in medium to high TSRs can be reliably achieved using 2d data of appropriate Reynold's number. Generally only constant speed machines are likely to be operated at low TSRs as variable speed machines are able to increase rotor RPM when encountering high wind speeds to avoid stalled operation which is the case for all modern tidal turbine devices.

4.1.2 University of Southampton model turbine

Researchers at the University of Southampton (SOTON) carried out a series of a tests on a scaled tidal turbine test rotor to investigate a number of phenomena important to axial flow rotors. While much can be transferred directly from the design and operation of wind turbines a number of fundamental differences exist. SOTON carried out torque and thrust measurements on an 800mm diameter rotor to investigate the effect of the proximity of the free surface, velocity inflow profiles and cavitation. The other aim was to compare the performance of two numerical codes with the experimental results[152]. SOTON developed an in house code called SERG-Tidal which is designed as a tidal turbine prediction code based on a BEM code for wind turbines developed by Barnsley and Wellicome[153]. The other code used to provide initial predictions of power and thrust coefficient was Tidal-Bladed.

The rotor used in the study had a diameter of 800mm this being a trade off between Reynold's number and blockage ratio in the test facility. The rotor has adjustable pitch NACA 63-8xx blades with chord and twist distribution as shown in Figure 109 below. The rotor features an inline strain gauge dynamometer mounted on the rotor shaft which measures the torque and thrust. All the results are presented as if the rotor is running in the free-stream as the results are filtered with a blockage correction model. The data is presented in terms of power and thrust coefficient at four blade pitch angle settings based upon the torque, thrust and inflow velocity measurements.

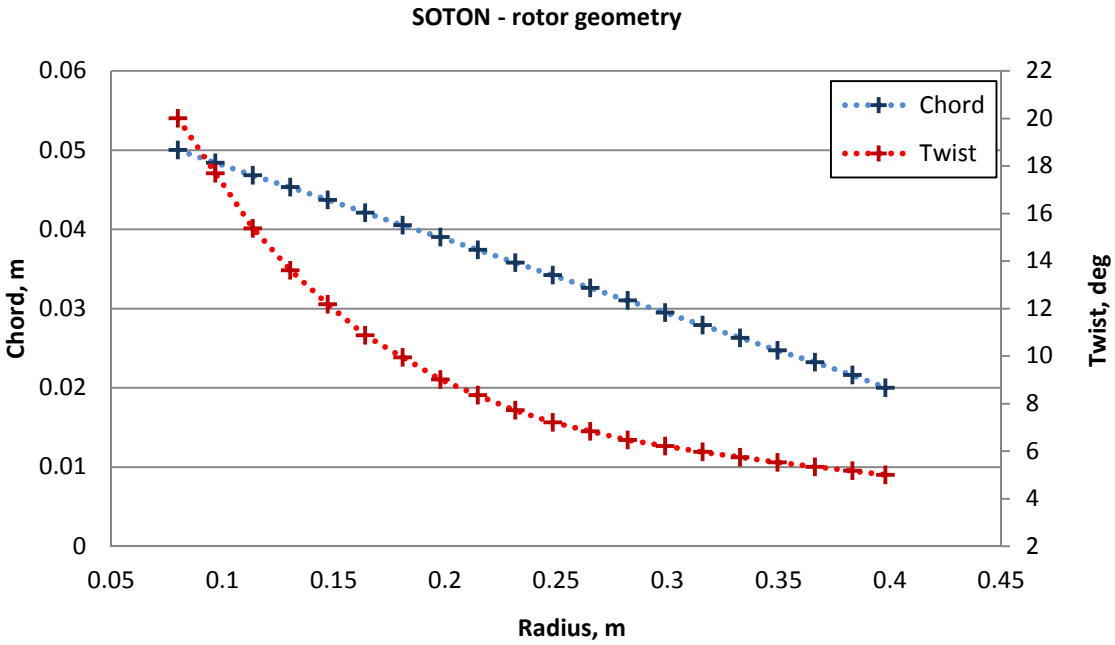

Figure 109 - SOTON - rotor geometry

Figure 110 shows the Cp data for the first pitch angle setting of 0 degrees for when the rotor was run in the cavitation tunnel. Four sets of data are compared here; the experimental data after correction for blockage, the BEM code prediction and the predictions made by SOTON using SERG-Tidal and Tidal Bladed.

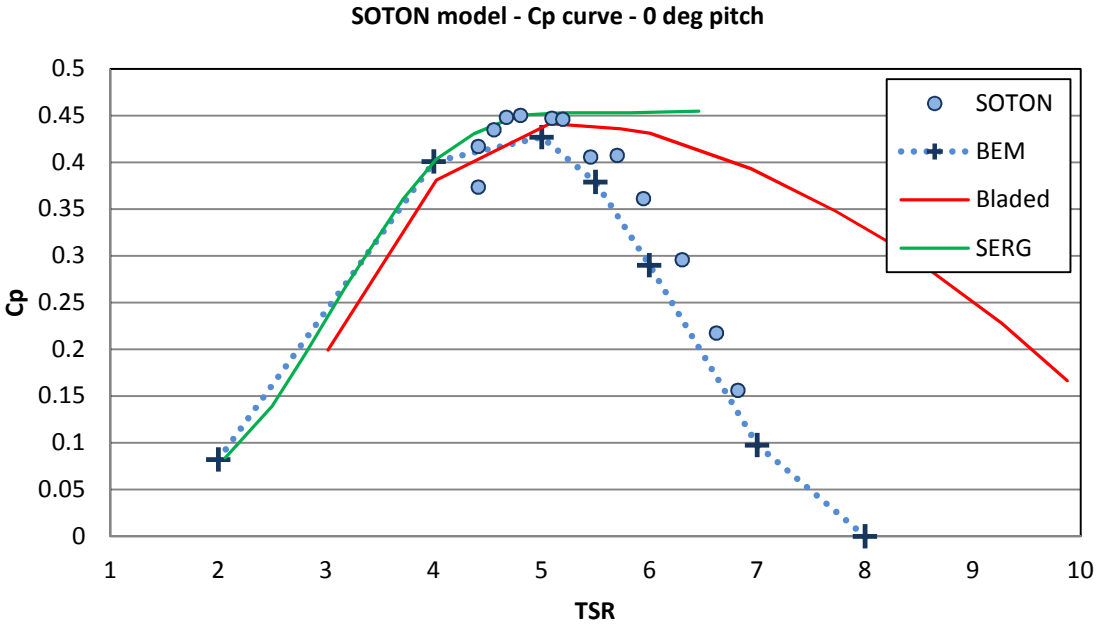

Figure 110 - SOTON - Cp curve - 0 deg

All the codes predict peak Cp at around a TSR of 5 and the values presented agree well with the experimental results. At lower TSRs none of the codes appear to predict the trend exhibited by the measured data although data in this region is limited as the rotor tended to stall in this region. At higher TSRs as the rotor load decreases SERG and Bladed offer an increasingly poor prediction while the BEM code follows the trend reasonably well.

Figure 111 is the equivalent of Figure 110 but instead shows the Ct data. Again the range of measured data is limited by stalling problems to between TSRs of 4.5 – 7. Here the BEM code is in agreement with the other codes and the experimental data below a TSR of 5.5 but above this point deviates significantly as it predicts a sharp decrease in thrust which is not supported by the data.

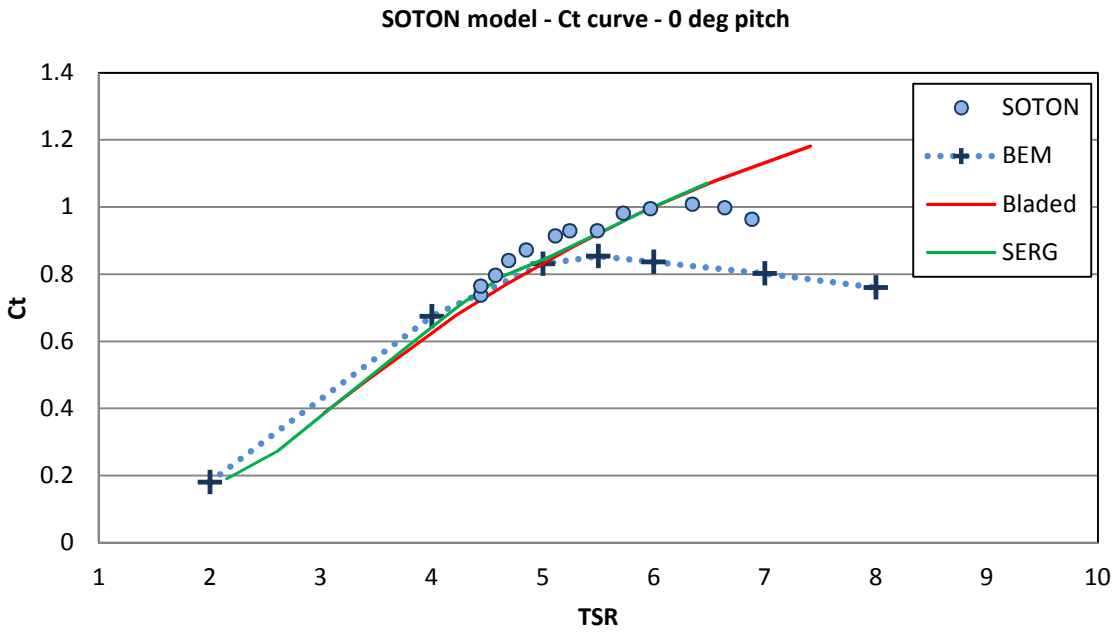

Figure 111 - SOTON - Ct curve - 0 deg

Figure 112 and Figure 113 show the data for the 5 degree pitch setting where the rotor is running at the blade design point. This is where the BEM code predictions match best with the experimental results and is in agreement with both the other codes. However, it seems to under-predict the values of Cp at high TSRs above 7 i.e. the BEM code anticipates that the Cp curve drops off more quickly than it actually does. In general for the Ct predictions all three codes match the experimental data very well including for high values of TSR.

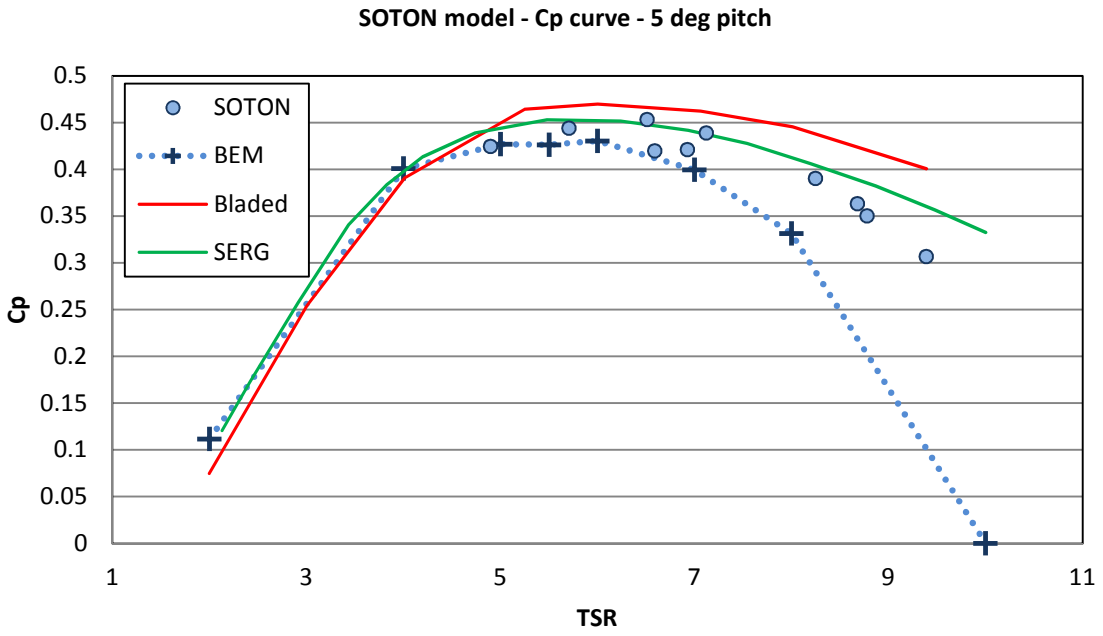

Figure 112 - SOTON - Cp curve - 5 deg

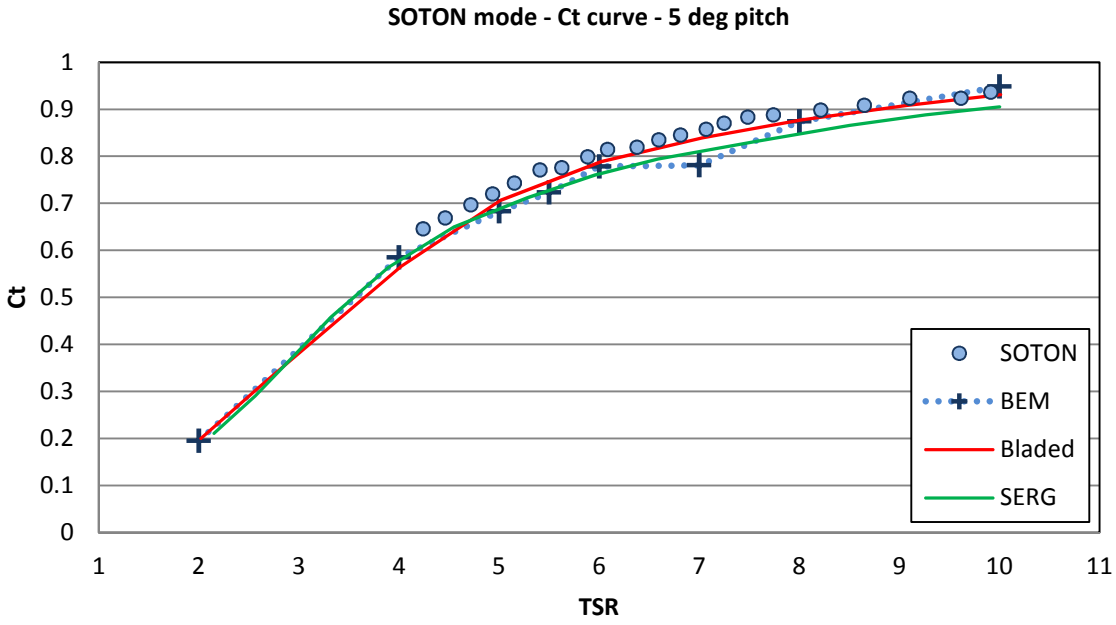

Figure 113 - SOTON - Ct curve - 5 deg

Figure 114 and Figure 115 shows the data for the 10 degree pitch setting where the blades are beginning to be angled more deeply away from the flow with the

result that the loads are decreased from the design point. All three codes predict this reduction in performance well with SERG-Tidal and the BEM code matching the experimental results most closely for Cp whereas Bladed predicted the Ct curve slightly better.

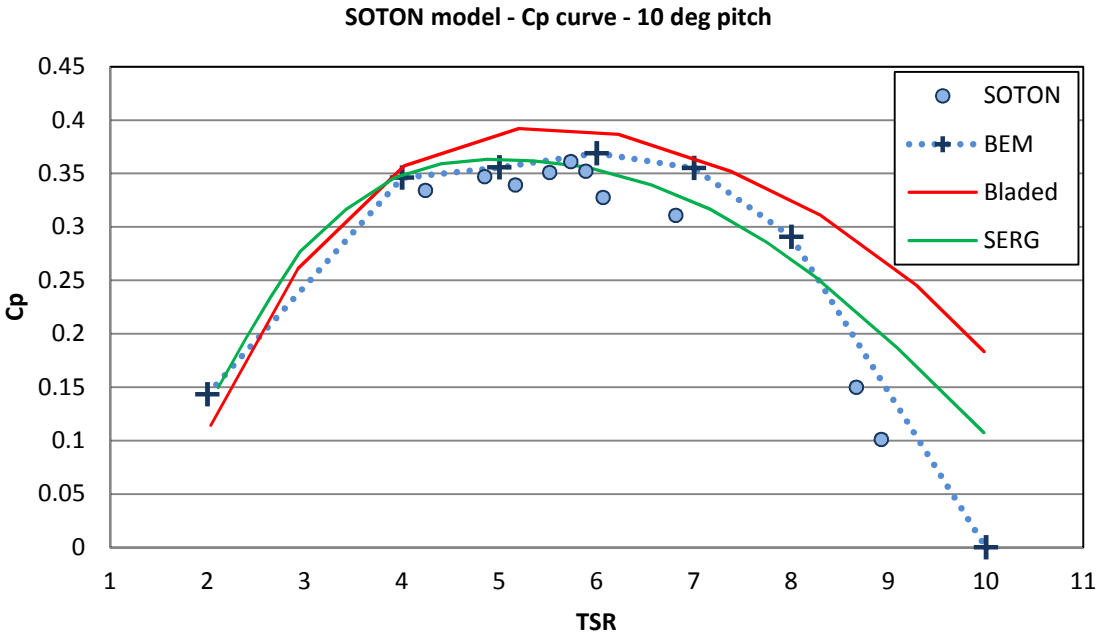

Figure 114 - SOTON - Cp curve - 10 deg

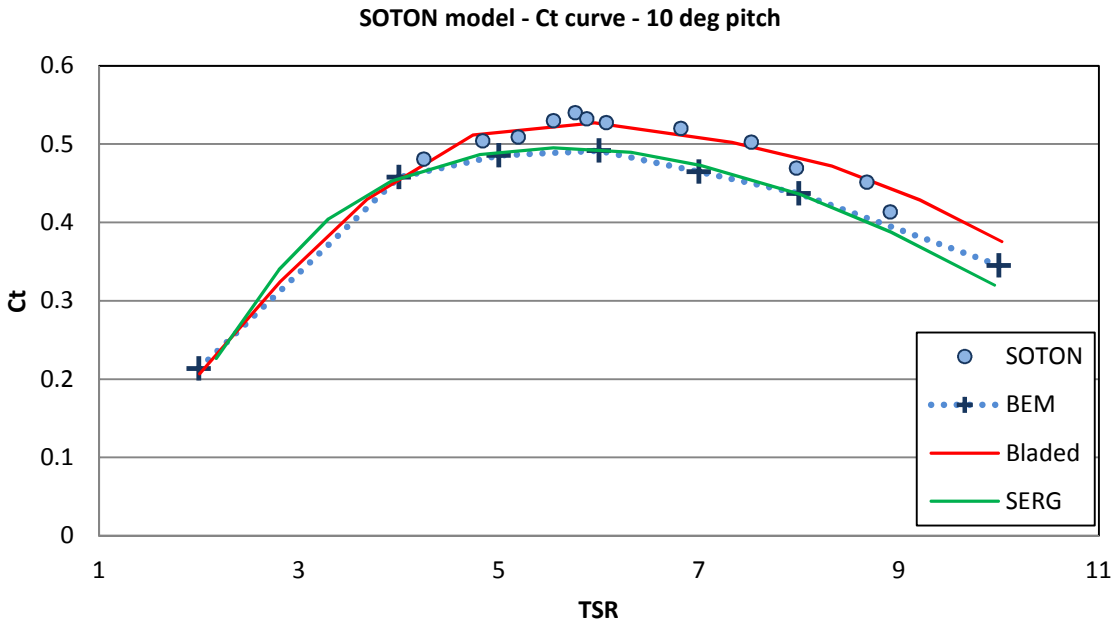

Figure 115 - SOTON - Ct curve - 10 deg

The final results for the SOTON rotor testing are plotted in Figure 116 and Figure 117. For both cases the BEM code tends to under-predict the values of Cp and Ct but does appear to follow the general trend exhibited by the experimental results. For both Cp and Ct Bladed has a tendency to over-predict the data, particularly for Cp as seen in Figure 116.

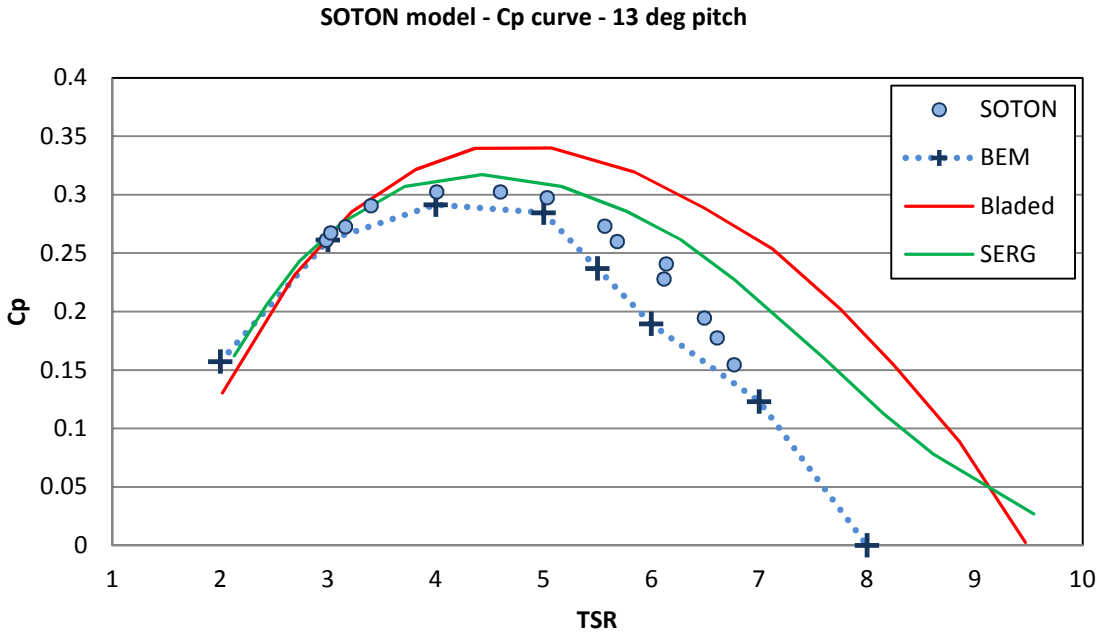

Figure 116 - SOTON - Cp curve - 13 deg

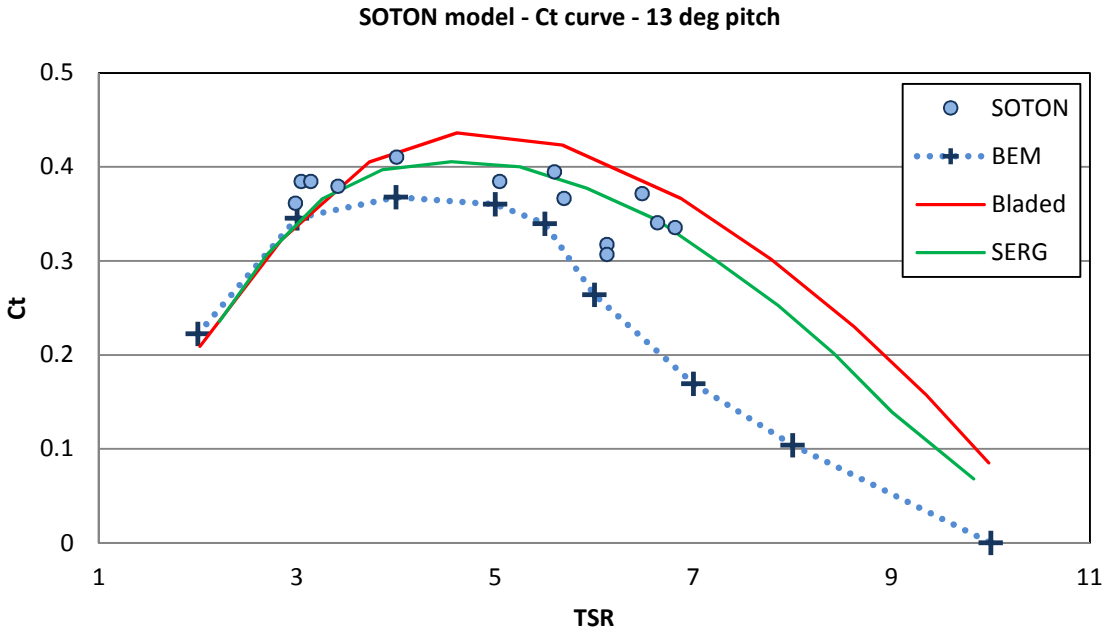

Figure 117 - SOTON - Ct curve - 13 deg

Comparison with the SOTON experimental data shows that the BEM code can predict with reasonable accuracy the performance of a turbine operating over a

range of pitch angles and a range of TSRs. This demonstrates the codes ability to calculate both torque and thrust loads applied to the rotor by the individual blades when the rotor is operating in an environment where the inflow is constant over the whole rotor plane. It also compares well with the research code SERG-Tidal and the commercial code Tidal-Bladed which is the industry standard. The BEM code performed best for blade pitch angles of 5 and 10 degrees i.e. close to the design point of the blades where the assumptions of the BEM theory are closest to reality.

4.1.3 CEC JOULE 1 project

As part of the European sponsored CEC JOULE program a project was carried out with the aim of improving aerodynamic and aero-elastic wind turbine response codes. It was known that wind turbines operate in a non-stationary environment, the effects of which can be broken down into two parts; dynamic profile aerodynamics and dynamic inflow. Dynamic profile aerodynamics accounts for the dependence of sectional aerodynamic force on time varying angle of attack which typically has a timescale on the order of 0.1s. Dynamic inflow accounts for the influence of the time varying trailing wake vorticity on the inflow velocity. The wake vorticity is the result of varying circulation strength along the blade and has a characteristic timescale of 1 to 2 orders of magnitude higher than the profile scale.

For wind turbines dynamic inflow effects become important during coherent wind gusts, blade pitching actions and also during yawed operation. It was the aim of this project to validate with experimental data a number of dynamic inflow models from several research institutions for use with wind turbine performance codes. Two of the participants were Delft University of Technology (DUT) and Garrad Hassan. Experimental data was gathered from two research turbines; the Tjaereborg 2MW turbine operated in Denmark and a 1.2m diameter test rotor run in the open wind tunnel at DUT. It is possible to directly compare the results of the BEM code when running unsteady simulations with the

experimental results from the DUT wind tunnel and the measurements from the Tjaereborg turbine.

The wind tunnel model is a 2 bladed rotor using NACA 0012 profile blades operating at approximately 700 rpm. The wind tunnel has a maximum working flow speed of 14.5m/s, a turbulent intensity of 0.8% with a uniformity of flow across the working section better than 2.5%. The measurements available are the blade flap-wise bending moment, rotor torque and thrust, angular position, speed and the tunnel flow speed. The blade geometry is shown in Figure 118 below.

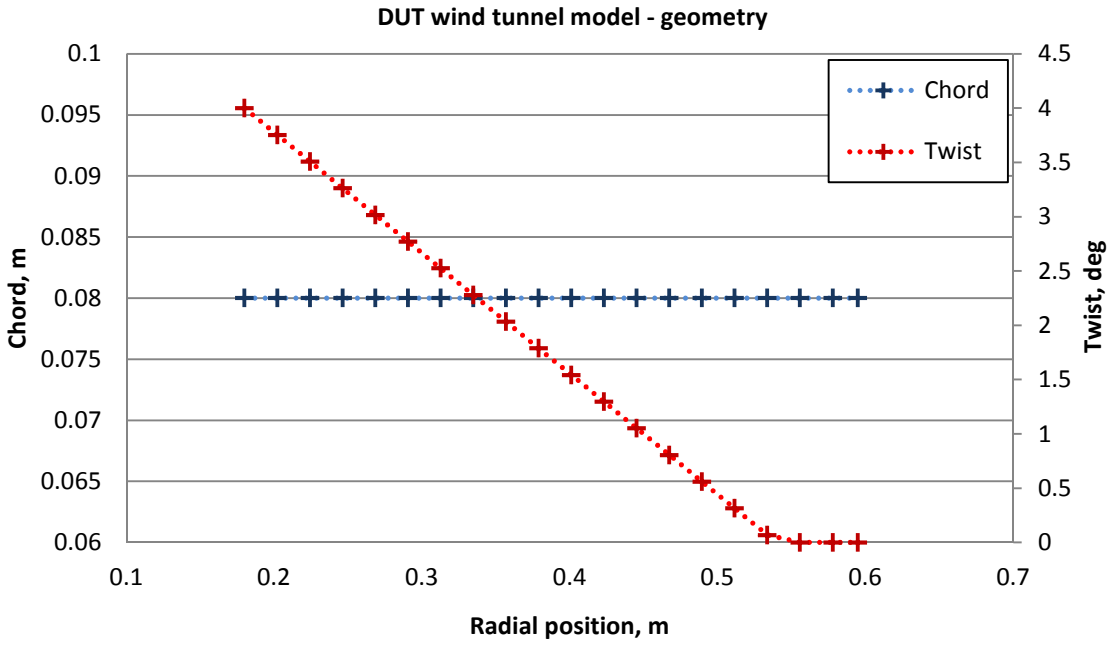

Figure 118 - DUT model – geometry

The full scale Tjaereborg turbine is a 3 bladed machine with a 61m diameter rotor running at 22.3rpm and reaches its rated power of 2MW at a wind speed of 15m/s. The section used for the blade is a NACA 44xx series airfoil of varying thickness shown in Figure 119 below. The data available for this turbine is the blade root bending moments, rotor torque and measurements of the flow field. An upstream met mast with 5 anemometers and wind vanes was used during all stages of the testing to give velocity data over the plane of the rotor. Because

the Tjaereborg machine is situated outside it is impossible to achieve control over the inflow conditions as it would be in a wind tunnel. Therefore the measured values for blade and shaft loads have been averaged over a number of realisations and over the three blades to filter out the stochastic wind influences and deterministic effects such as wind shear.

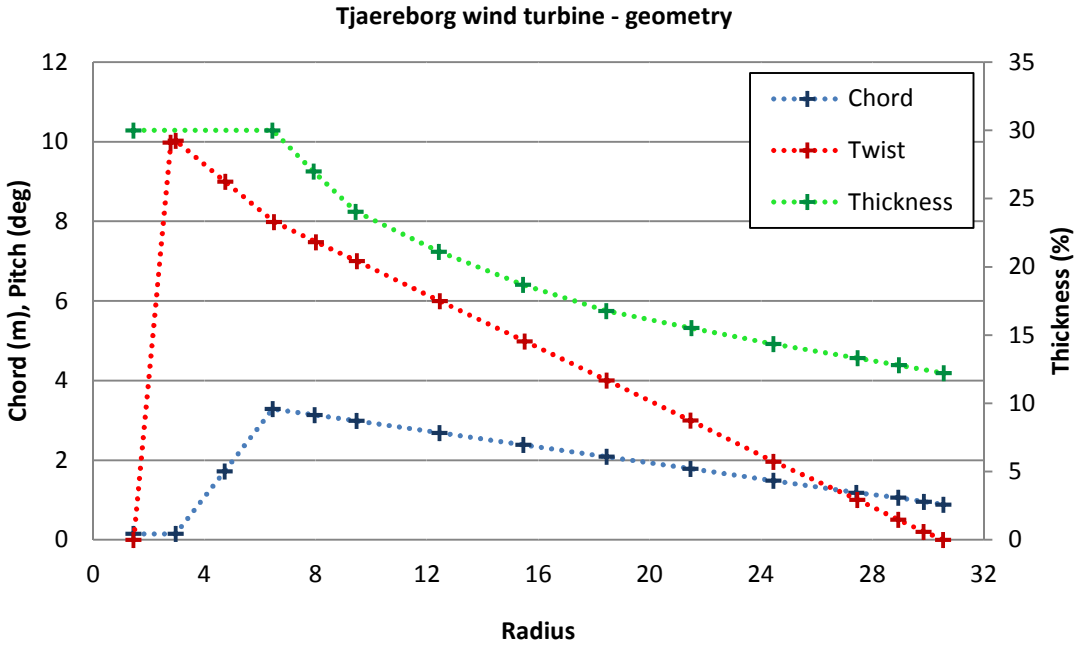

Figure 119 - Tjaereborg – geometry

4.1.3.1 DUT model data

The DUT model offers the chance to validate the BEM code when operating in unsteady mode under uniform inflow conditions. The data used for the comparison was collected at the DUT open jet wind tunnel of the university's Institute of Wind Energy. There were three experimental campaigns run; prediction of rotor characteristics, measurement of the flow field in the wake and performance during a coherent wind gust[154]. In addition to the experimental data predictions of the rotor loads from the in-house DUT code are also available.

The DUT code is based upon asymptotic acceleration potential theory. The pressure perturbation on the flow field is solved by the Laplace equation which acts as an acceleration potential function. Integration of the acceleration field determines the velocities on rotor plane from which the aerodynamic loads can be calculated[155, 156]. This method is equivalent to a lifting surface model and has been validated for use in helicopter aerodynamics[157].

Initially the steady state performance (prediction of rotor characteristics) was compared with the power and thrust coefficient curves from the wind tunnel data. Figure 120 shows the Cp data as measured in the DUT tunnel alongside predictions by the BEM code, the in-house DUT code and Bladed. None of the codes appear to accurately predict the experimental data over the entire range. The BEM code and Bladed offer very similar results in that the predictions are relatively close at low and high TSRs but peak performance is under estimated. This is in contrast to the DUT code which predicts peak performance best, around a TSR of 7, but appears to significantly over estimate the performance at higher TSRs.

The performance of the three codes is more consistent when compared with the Ct curve shown in Figure 121. Up to a TSR of 7 all the codes predict very similar values of thrust coefficient which is a slight under-prediction of the available data. However, past this point the codes diverge with Bladed offering the closest match to the experimental values and general trend of the data. As the TSR increases the BEM code under-predicts the values of Ct whereas the DUT code does the opposite.

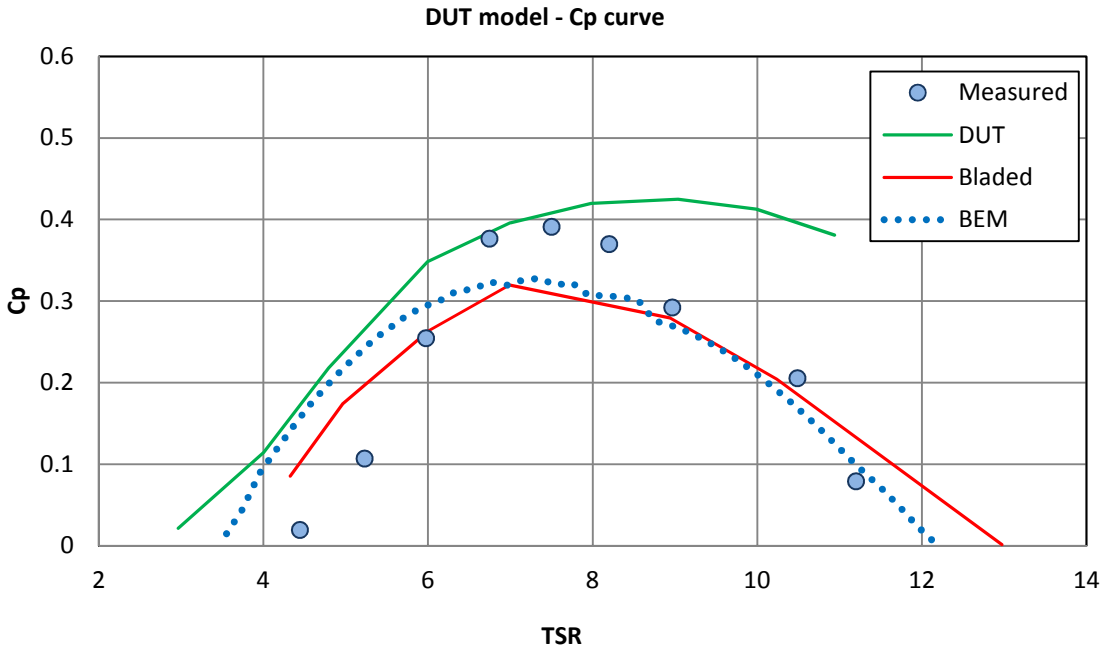

Figure 120 - DUT - Cp curve

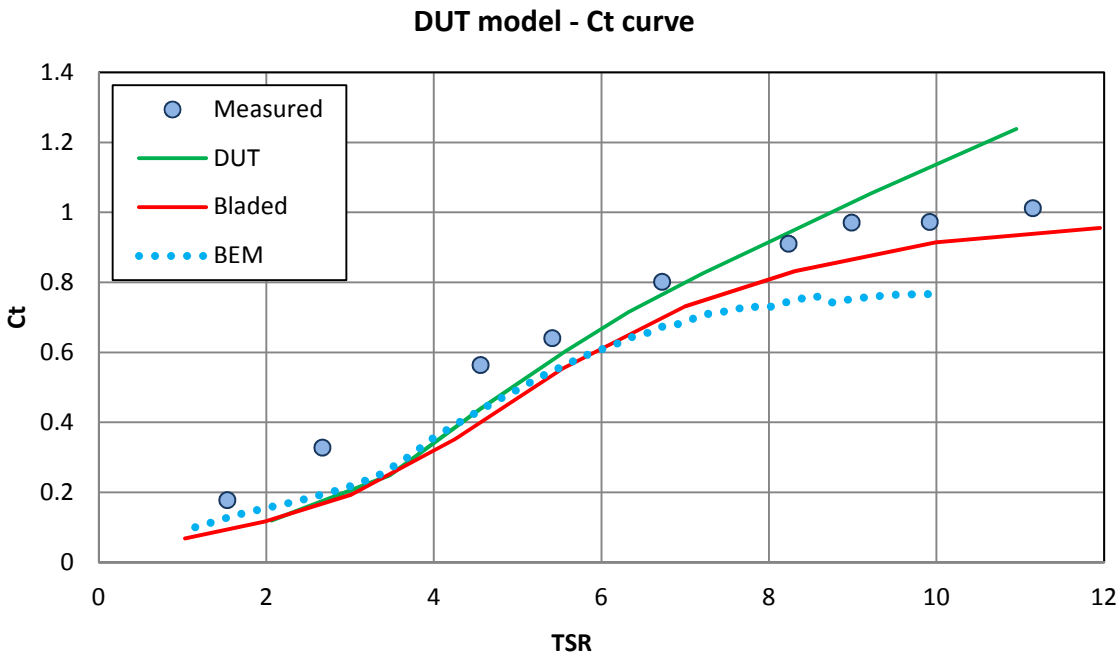

Figure 121 - DUT - Ct curve

Once the performance of the rotor had been experimentally confirmed and compared with numerical predictions the time dependent behaviour of the rotor when exposed to coherent wind gusts was examined. In order to generate the

coherent gusts two gauzes were placed in the wind tunnel. The gauzes could be opened very quickly which altered their porosity thereby changing the wind speed in the tunnel. The gauze could be opened or closed in approximately 0.2s and it took a further 0.2s for the tunnel velocity to reach an equilibrium value according to the hot wire anemometers placed at the tunnel exit and directly above the rotor.

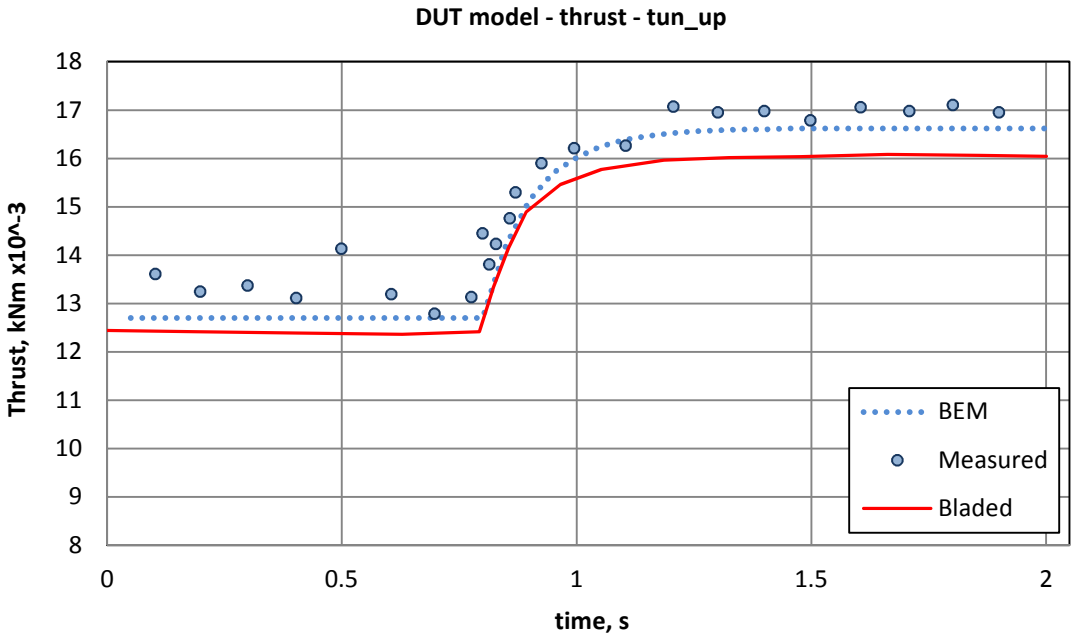

Figure 122 - DUT - thrust - tun_up

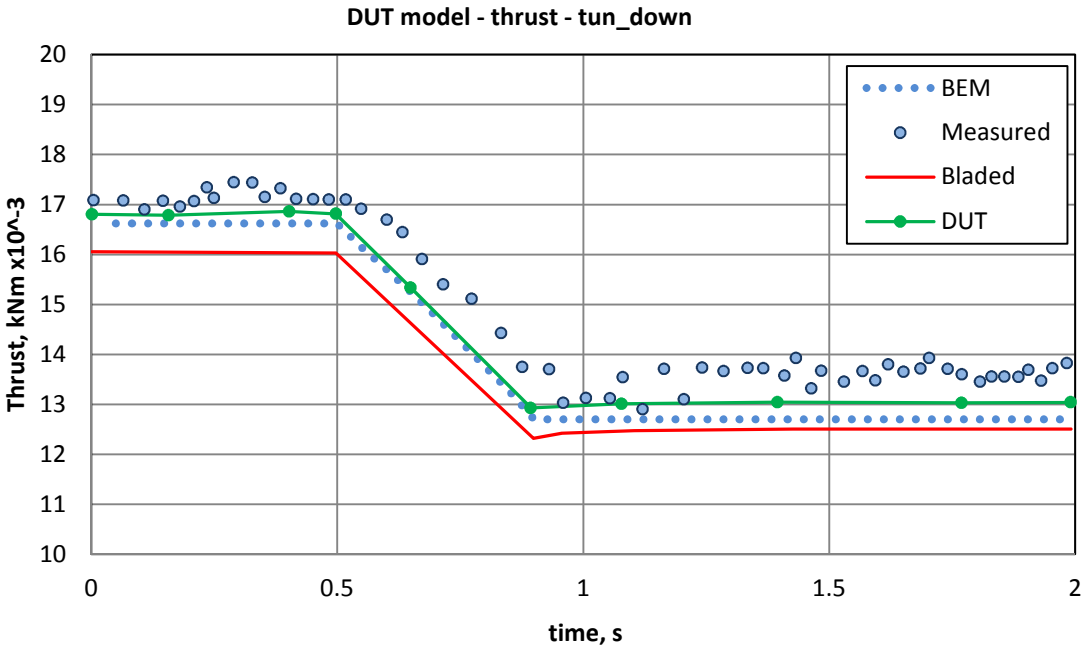

Figure 123 - DUT – thrust – tun_down

Figure 123 above shows a time history of the rotor thrust during a coherent gust along with the predictions of the BEM code and Bladed. The porosity of the gauzes was rapidly decreased in order to achieve a rapid increase in tunnel speed which behaved according to an inverse exponential. The tunnel speed was held constant at 4.9m/s for 0.8s at which point the gauze was opened and the speed increased to the new equilibrium value of 5.7m/s less than a second later. Both the BEM code and Bladed predict well the trend of the thrust force but the BEM code estimate is closer to the values of thrust. There is considerable high frequency noise in the thrust signal of the experimental data due to small differences in velocity across the rotor plane caused by turbulence in the flow which neither the BEM code nor Bladed account for.

Figure 123 shows a thrust change caused by a second gust of decreasing velocity but with a slower change in porosity of the gauze. Here the tunnel velocity was decreased from 5.7m/s to 4.9m/s in approximately 0.4s at a constant rate of change. Figure 123 also includes the prediction of the thrust by the in-house DUT code which was not available for the previous comparison in

addition to Bladed and the BEM code. Again all three predictions follow the trend very closely with the DUT code and the BEM code matching the measured values of thrust very closely.

For both cases there is no evidence of dynamic inflow effects caused by the changes in operating conditions. This is because although the velocity changes are relatively fast the characteristic time scale of the dynamic inflow effects is approximately 0.1s for these particular wind speeds. As the change in speed is considerably greater than this no overshoots in load are observed in the experimental data and none of the codes predict that there should be.

4.1.3.2 Tjaereborg wind turbine data

The experimental campaigns for the full scale Tjaereborg turbine included load measurements when undergoing blade pitching actions. The pitch transient data was collected when the inflow conditions were deemed axi-symmetric and a number of realisations were carried out in order to filter other dynamic effects from the results. The data available from these campaigns is the rotor torque and the blade root flap-wise bending moment. Due to the non-stationary nature of the conditions of the field tests the turbine was subjected to turbulence, wind shear and tower shadow and these effects could not be completely filtered out and so there is some noise in the signal.

Two of the pitch transient experiments have been selected for comparison with the BEM code. They were chosen as they had the fastest pitch changes which should result in the most pronounced load overshoots and hence are the most extreme conditions that the code should have to cope with. Both cases involve first an increase in pitch and then a reduction in pitch back to the initial state.

The first case (II.3) was run at a wind speed of 9m/s (TSR = 7.8) with an initial pitch angle of 0.2 degrees and a final pitch of 3.4 degrees. The rate of change of the first pitch change is not known precisely as it was not constant. However the reversal of pitch was carried out at a constant rate over 0.6s, a rate of around 7 degrees/s. This case can be seen in Figure 124 and Figure 125 below

as a time history of the torque and flap-wise bending load. The second case (II.4) was carried out at a wind speed of 8.7m/s (TSR = 8.1) from an initial pitch angle of 0.1 degrees to a final pitch of 3.7 degrees. Both the pitch actions were carried out at a constant rate of 7.2 degrees/s. The load time histories are presented in Figure 126 and Figure 127 below. Both sets of time histories are also compared with the DUT and Bladed predictions.

The characteristic timescale of the dynamic inflow effects for the Tjaereborg turbine is approximately 7s when operating in these conditions as approximated from consideration of the diameter and the wind speed. For both sets of measurements the time taken for the load signal to reach equilibrium from its peak value is approximately 18s. However, the load tends to return to within 10% of the equilibrium value after only 5s which is in agreement with the predicted characteristic timescale.

Examination of the BEM code results suggests that the approximation of the bending load is better than for rotor torque as in both cases the extreme value of the overshoot load is very closely predicted as is the rate of load change back to the equilibrium value. For the torque load the rate of change is quite similar to the experimental loads but the extreme load tends to be under-predicted. Part of the discrepancy is due to the difference between the predicted and the experimental equilibrium loads. In case II.3 the torque is over-predicted while in II.4 it is under-predicted hence there is a steady state offset (approx. 5% for II.3 and 8% for II.4) which is not the case for the bending moment where both transient and equilibrium loads are well matched to the experimental data. The difference between the torque and bending predictions is due to a magnification of the steady state error in the torque as it is calculated as the sum of the three blade loads which are assumed equal. Therefore the discrepancy between the experimental results and the code prediction is multiplied by a factor of three. This behaviour is also evident for the DUT prediction whereas Bladed appears to better predict the torque load behaviour.

When the rate of change of pitch is not well defined (II.3) none of the three codes predict the rate of change of load well compared to the other pitch

changes. It is therefore clearly important that the rate of change of flow conditions is known precisely to achieve good results using the dynamic inflow model which will usually be the case.

Generally the behaviour during the pitch change is well modelled by the BEM code but achieving accuracy when predicting the extreme overshoot load is dependent upon a close approximation of the equilibrium value. Accuracy of modelling this type of behaviour is important for two reasons; for good prediction of the fatigue life of the machine and to provide realistic inputs for the control system. For fatigue damage assessment the important parameter is only the magnitude of the overshoot whereas for the control system both the size of the load as well as its time dependent behaviour is important.

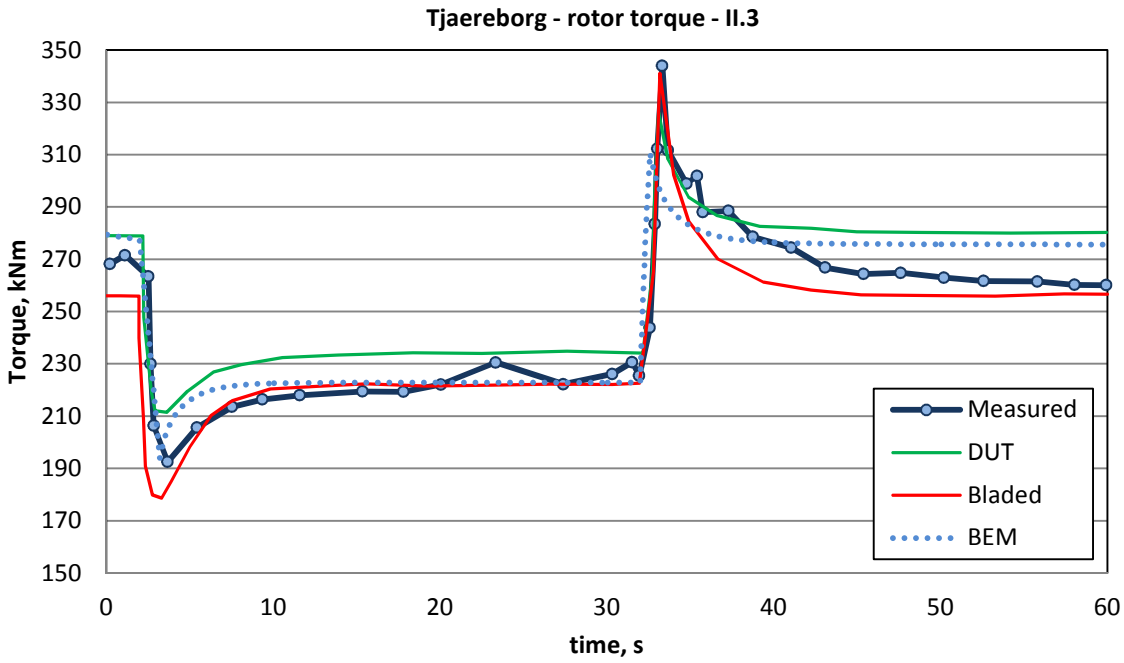

Figure 124 - Tjaereborg - rotor torque II.3

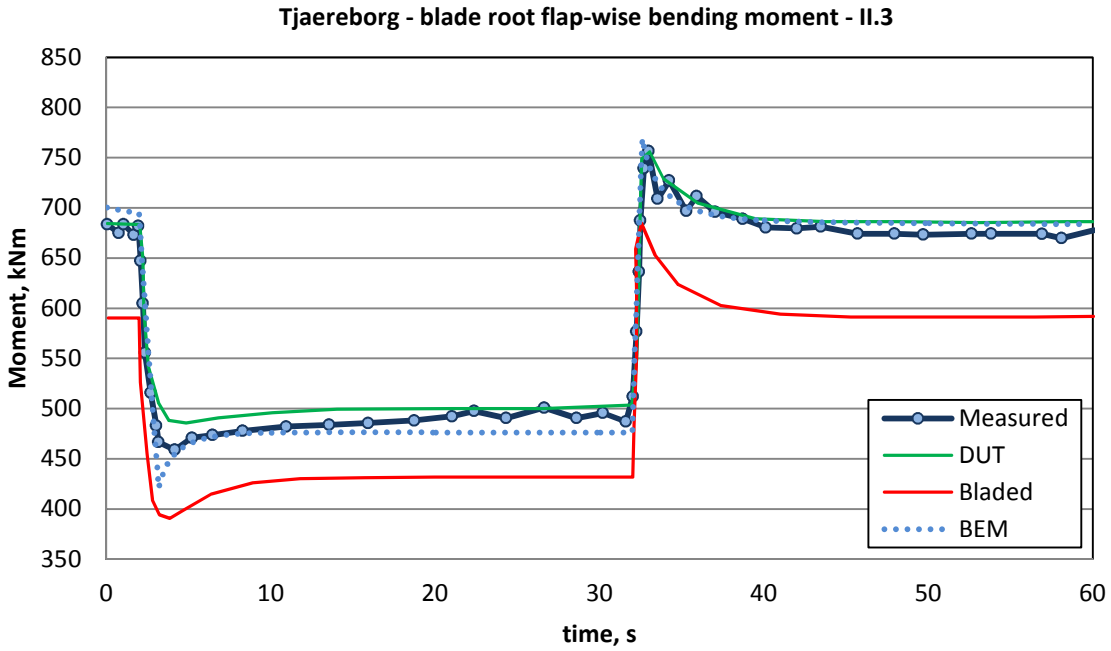

Figure 125 - Tjaereborg – flap-wise bending- II.3

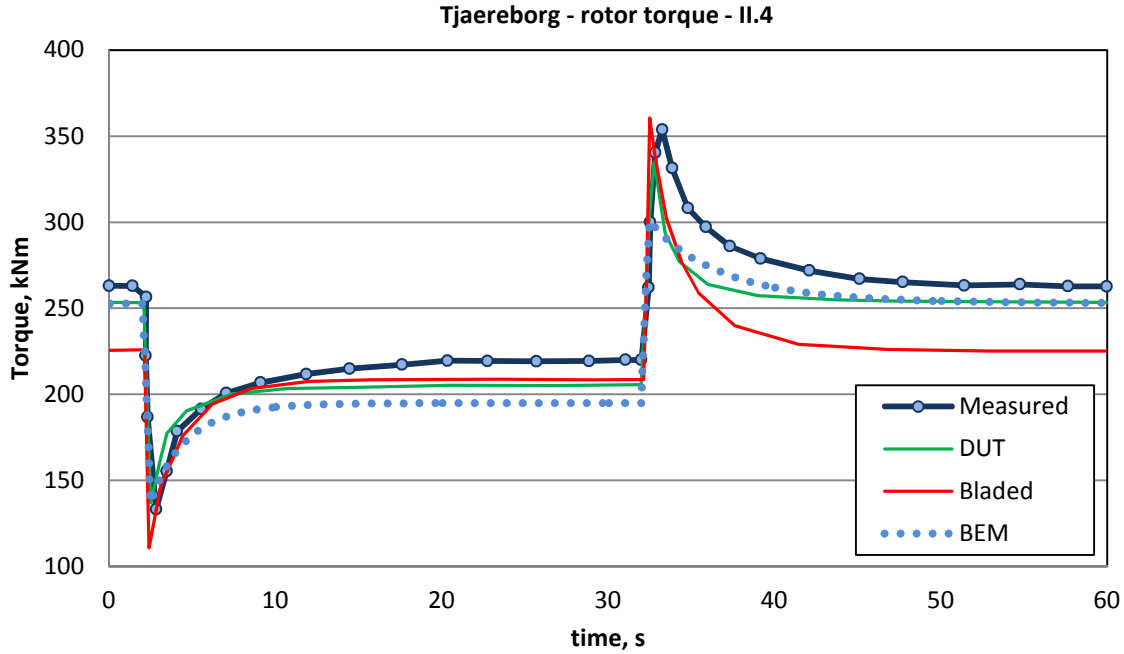

Figure 126 - Tjaereborg –rotor torque - II.4

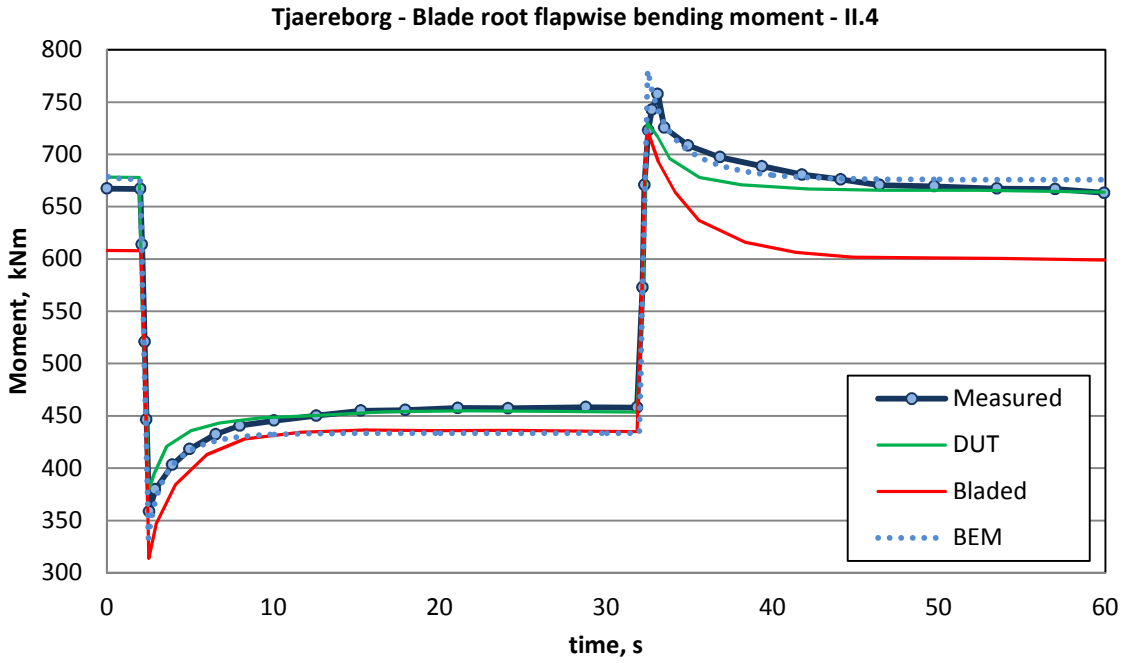

Figure 127 - Tjaereborg - flap-wise bending - II.4

4.2 Deltastream tidal turbine experimental validation

The final part of this validation study concerns the DeltaStream turbine rotor and the test data available from testing in the flume tank at IFREMER (Institut Francais de Recherche pour l'Exploitation de la Mer) in France which was conducted by the author. The following section covers the test rig setup and discusses in detail the data available from the test campaign which is used to further validate the author's turbine code. A detailed explanation of the experimental setup and a characterisation of the turbulent flow to which the turbine was subjected are given. This is followed by a note on the design of the test scale rotor and the validation of the steady state performance with the experimental date. Finally the results of the unsteady test data are compared with the output of the model to determine the validity of the code at predicting fatigue loads.

4.2.1 Experimental setup at IFREMER

The rotor under test was a 750mm diameter three bladed horizontal axis, fixed pitch turbine as shown in Figure 128 which is a 1:16th scale model of the turbine developed for the Deltastream device by the author. This is as large as is feasible for test in the circulating water channel at IFREMER given the working section dimensions of 4x2m. At this size the turbine caused a maximum blockage ratio of less than 6% when the rotor was operated at maximum thrust loads. Maintaining a low blockage ratio (i.e. around 5%) is important to ensure the inflow to the turbine is not distorted by its presence. A large blockage ratio would create a bow wave above the position of the turbine.

The effect of scaling the rotor is twofold; both the Reynold's number, with respect to the blade chord length, as well as the reduced frequency are decreased by an order of magnitude i.e. Reynold's from $2x10^6$ to $2x10^5$ and the reduced frequency from 0.5 to 0.08. However, neither effect is detrimental to the validity of the test data in terms of the comparison to the model outputs as Reynold's number similarity can be accounted for by using 3d airfoil curves and the flow is always considered to be in the unsteady regime. The reduced frequency is significantly above the threshold of k=0.01 for all test conditions undertaken. When the model is configured for the model rotor the 2d airfoil data, which is used as the basis of section lift and drag data, takes account for Reynolds number. Furthermore, the stall delay model has been applied to the geometry of the experimental rotor in order to determine the three dimensional lift coefficients for the scaled version. In terms of the reduction in unsteadiness this will be automatically captured by using the turbulence inflow generator with the input parameters set to those observed experimentally in the IFREMER tank (as previously discussed).

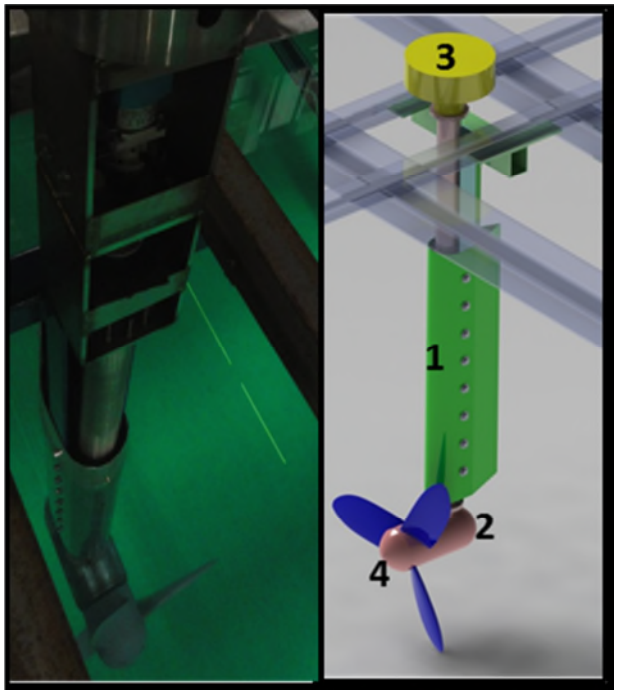

Figure 128 - Experimental rotor

The experimental setup comprises the turbine (4) which transmits torque through the drive train (2) to a permanent magnet generator (3) which was used to vary the load absorbed by the rotor thereby allowing rotor speed control. The rig was mounted on the facility 6 axis load cell which measured thrust. In order to ensure only turbine rotor loads were transmitted to the load cell a fairing (1) was fitted around the drive tube. The data recorded from the test setup included shaft speed, shaft torque and rotor thrust which allowed the turbine performance to be characterised in terms of power and thrust coefficients. The details of measurements are summed up in table below:

Measurement	Accuracy	Uncertainty
Flow velocity	n/a	0.05 m/s
Shaft speed	1.0% FSO	2 rpm
Shaft torque	1.0% FSO	0.5 Nm
Rotor thrust	0.2% FSO	1 N

Table 7 - Measurement fidelity

The TSR was determined from measurements of shaft speed and mean tank velocity. The propagation of measurement errors, determined using error calculus, was taken into consideration to determine that the uncertainty in TSR is around 3.4% which is equivalent to 0.1 at the design point (as per data in Table 7). The power coefficient was derived from data recorded from the torque sensor and the thrust coefficient was determined from data taken from the load cell which was slightly more accurate. The uncertainty in Cp and Ct were resolved as 4% and 3.3% respectively.

4.2.2 Flow Characterisation

The facility can deliver flow velocities of up to a maximum of 2m/s with either of two turbulence characteristics. The turbulence was controlled at the inlet to the working section by a set of flow straighteners. Depending upon the configuration the mean turbulent intensity could be altered between two levels of turbulence intensity. Velocity measurements using the facility laser Doppler anemometer were taken prior to turbine testing in order to characterise the flow field. Data was recorded at 20 points from near the surface down to the lower boundary. The equipment was able to deliver a data rate of 10Hz so that turbulent characteristics could be determined. Figure 129 below shows the velocity profile with depth in the working section with the flow straighteners in position. As expected near to the bottom of the tank the profile shows a classic boundary layer profile where the velocity rapidly decreases on approach to the

wall and the maximum velocity occurs at the surface. For the mid channel, where the rotor is positioned (hub centre line at -1m), the flow profile increases linearly with depth. There is approximately 2.5% difference in velocity between TDC and BDC which must be taken into account in the modelling process as this will result in around a 6% variation in blade load per revolution.

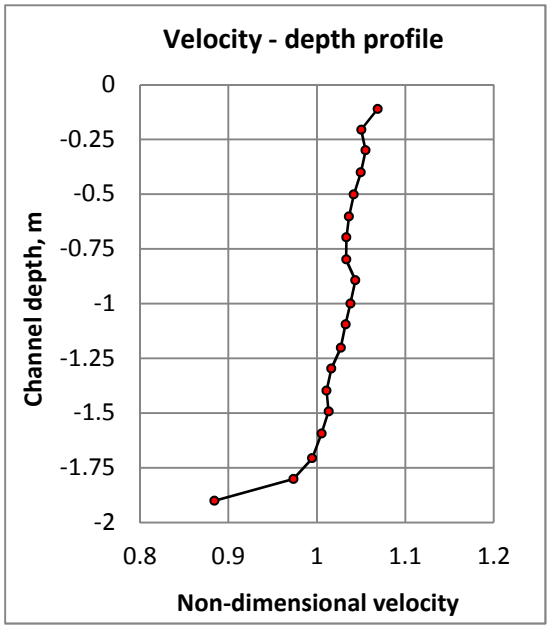

Figure 129 - Non-dimensional flow profile [158]

The turbulence profile shows the opposite trend to the velocity profile with the highest intensity nearest the bottom and the minimum values at the surface. Figure 130 below shows the turbulence intensity profile when the honeycomb inlet is fitted at the same mean velocity as shown in Figure 129 above. There is less than +/-0.5% variation in turbulence in the region in which the rotor is operated and therefore for modelling purposes it is assumed that the turbulence intensity is constant across the rotor plane. Depending upon the configuration of the facility inlet the mean turbulence intensity at the hub centre line was either 5 or 14% as measured using the facility equipment.

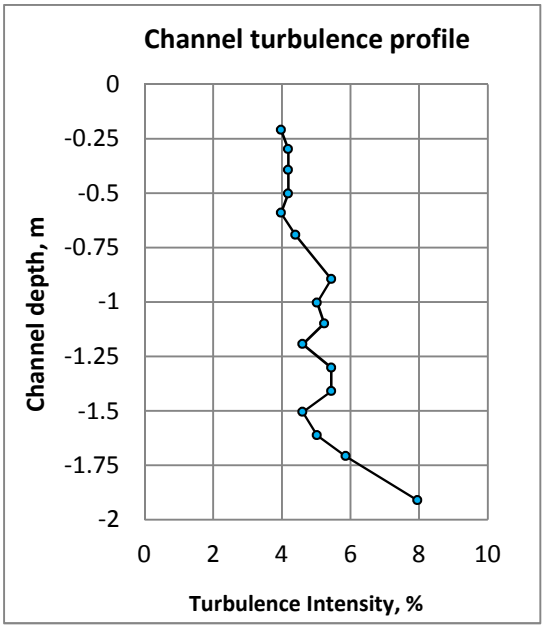

Figure 130 - Turbulence intensity profile

In order to characterise the turbulence the velocity spectrum was measured at a point by acoustic Doppler velocimetry (ADV) before the turbine was fitted in the tank. The tank velocity was sampled over 15 mins at the rotor centre line position with the u component of velocity being recorded at 10Hz. A comparison of the two inlet configurations is shown in terms of power spectral density in Figure 131 below.

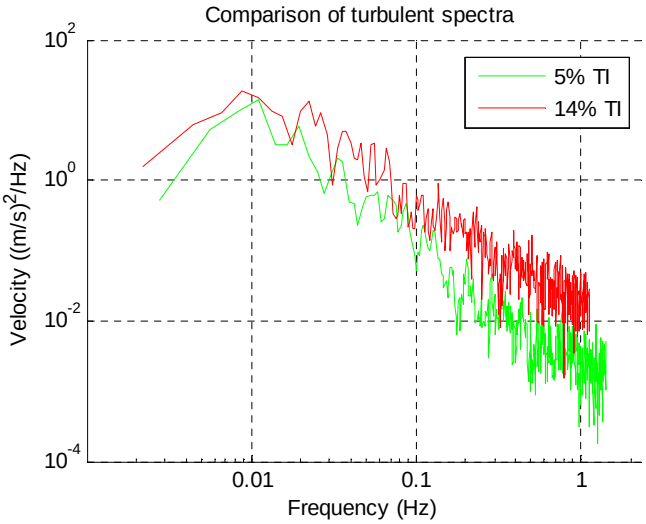

Figure 131 - Velocity spectra

This shows the difference between the energy content of the two flows is most pronounced in the mid-range frequencies of between 1 and 0.1Hz (NB: the ADV output was recorded at 10Hz but then digitally filtered through a high pass filter at 2Hz due to Doppler noise in the signal). This would imply that the eddy size and the time constant of the 14% turbulence as seen by the turbine would be larger than for the 5% flow which would potentially cause higher levels of unsteadiness in the rotor loading.

This is confirmed through calculation of the integral length scale of both flows. This was achieved by applying a two point auto-correlation function to the ADV velocity measurements. Unlike for the ADCP data (see section 3.4) time dependent velocity measurements were only taken at a single point during the test program therefore Taylor's frozen turbulence hypothesis is drawn upon in this instance and the correlation is made between two points at different times. Figure 132 below shows the values of the correlation function, Rxx, for both flows in the stream-wise velocity utilising the same 15 minute sample as was previously used to calculate the spectral energy content (this technique is discussed in greater detail in chapter 3). The area under each curve, found through integration of the trend line polynomial from zero to the x-axis intercept, is equivalent to the integral length scale. This shows that Lu (5%) is 0.36m which is slightly smaller than for Lu (14%) at 0.40m. The small difference between the two turbulence scales is due to the eddy size being governed by the dimensions of the flume tank.

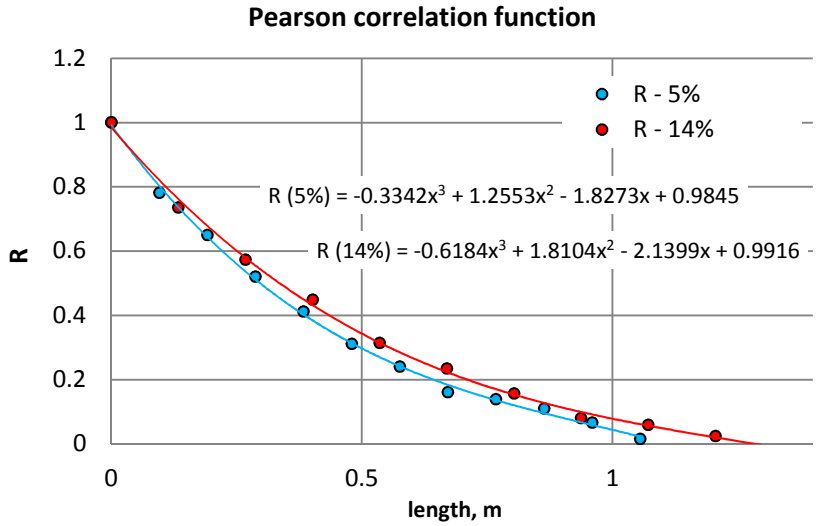

Figure 132 - Autocorrelation function

A significant observation made in comparison between the two flows is that when they are plotted alongside the standard von Karman model it is clear that the 5% flow matches more closely as can be seen in Figure 133. Here the mean of the data from figure above has been plotted over the von Karman model using the data from Figure 131 above. The 5% flow gradient trends more closely to the characteristic -5/3 isotropic gradient than the high turbulence case. This makes intuitive sense as the 5% turbulence is generated by a smaller, uniform grid which should result in reasonably isotropic turbulence once the flow develops downstream of the honeycomb.

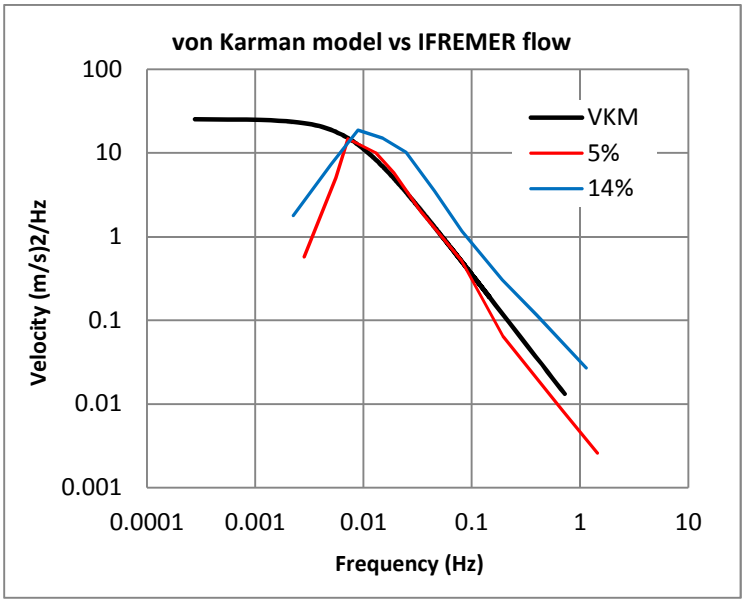

Figure 133 - Flow spectra comparison

4.2.3 Turbine Design

As noted in the introductory chapter one of the key design challenges for the DeltaStream device is in limiting the thrust load below the design threshold. As the device incorporates gravity stabilised design a robust solution must be in place before progressing to the full scale machine device. As the machine is to be held in place by its own weight i.e. the thrust force on the device must always be less than the available frictional resistance. However the turbine will be also be subjected to sudden increases in flow velocity from the turbulent environment so it is imperative the device has some mechanism to quickly alleviate unsteady loads.

The way in which the thrust is limited is by hydrodynamic design of the rotor blades and the choice of rotor operating speed. A large pitch angle has been used in the design of the rotor as it was found that as pitch angle increases the C_T/C_P ratio decreases i.e. the drag load for a given power reduces. This philosophy was employed to minimise fluctuating thrust loads close to peak rotor power in work previously undertaken by Cranfield [159]. As the blade pitch angle is increased the peak CP falls at lower TSRs. Therefore the rotor must be

run at lower speeds the greater the pitch angle. In addition to reducing the thrust loads, running at low speeds ensures cavitation is extremely unlikely. A three bladed rotor was used in order to achieve a trade-off between reducing tip loss and using robust blades. Using more blades results in a slower rotor, which reduces losses, but this requires slender blades which are susceptible to damage from extreme loading.

For the IFREMER tests a modified version of TEL's original rotor was designed by the author. What follows here is a brief outline of an internal report submitted to Tidal Energy Ltd on the turbine rotor design[160]. The fundamental thrust alleviation philosophy was followed but an improved Ct/Cp ratio was achieved such that at full scale, 12m in the case of the Deltastream prototype, the rotor thrust at the design flow peaks at the design threshold limit. The power and thrust coefficients for the test rotor at several pitch angles are shown in Figure 134 and Figure 135 as predicted using the hydrodynamic model, the geometry used for the IFREMER tests is labelled 'design'. This is a fixed pitch device but the curves show how sensitive the turbine performance is to small changes in the pitch angle that were considered during the design phase. For example a 5 degree increase in pitch above the design value results in a 20% increase in Cp and a 35% increase in Ct when operating at TSR = 3.25.

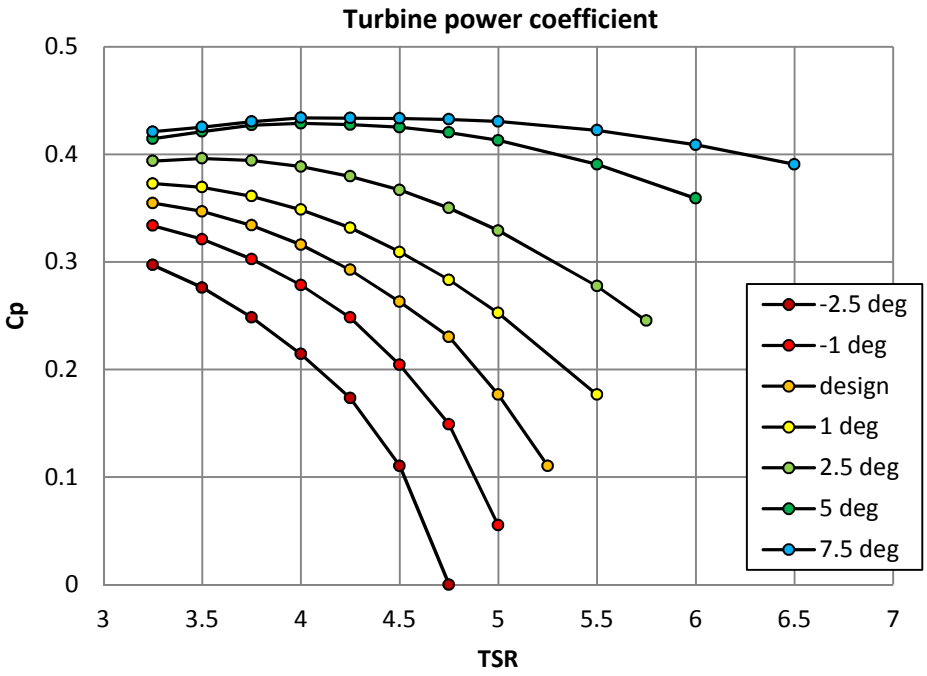

Figure 134 - Power coefficient

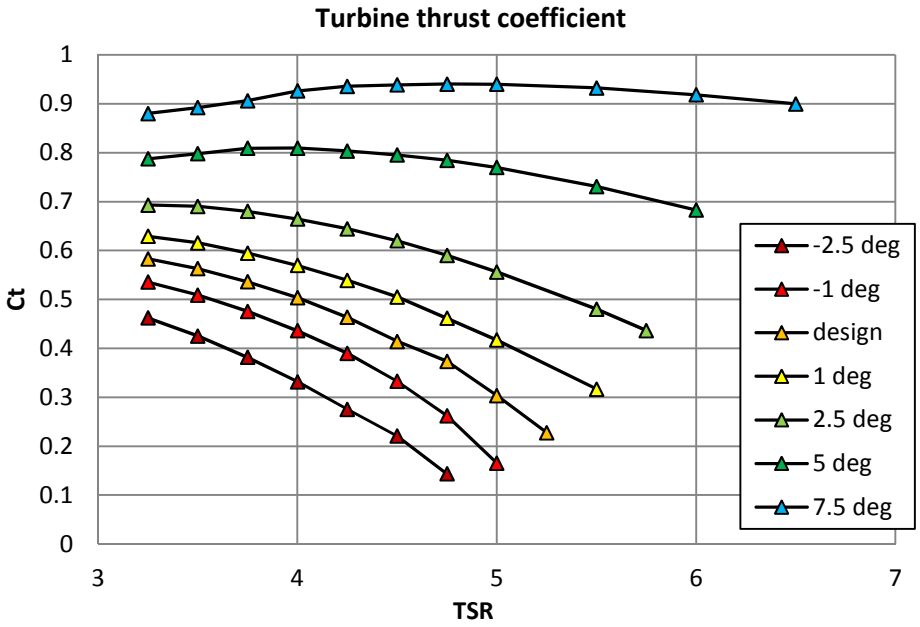

Figure 135 - Thrust coefficient

If the turbine curves are viewed in terms of non-dimensional performance, as shown in Figure 136 below, it is clear that as pitch is increased the ratio of power to thrust generally improves. The higher Cp/Ct the more power can be

extracted with less thrust penalty which is a crucial design metric to consider as the Deltastream is a gravity stabilised device. This also shows more clearly that as pitch is reduced the turbine operating range increases as for a pitch reduction of 7.5 degrees the maximum operational TSR increases dramatically.

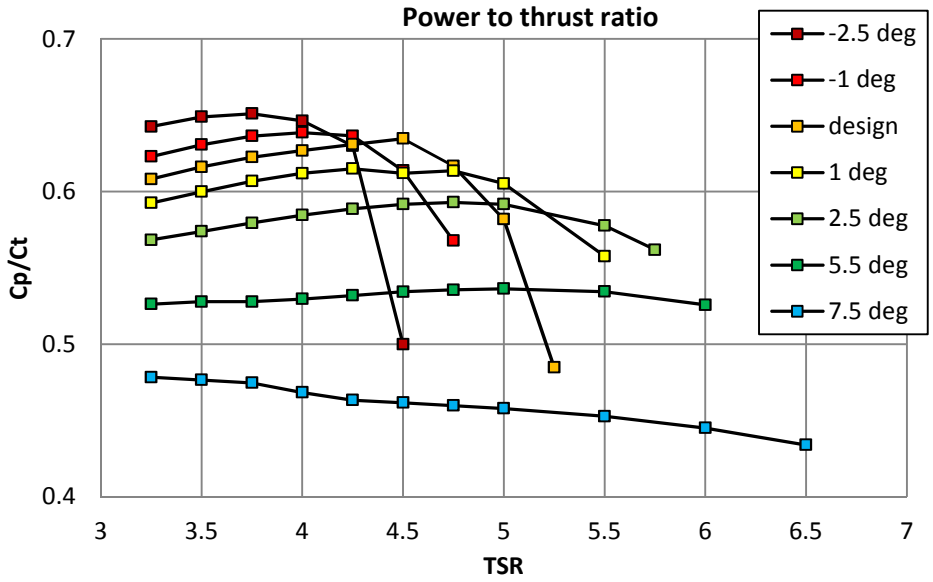

Figure 136 - Power to thrust ratio

There are three qualities that need to be achieved in order to reach a successful turbine design when considering the Deltastream; the machine must deliver reasonable power at rated flow, it must be reactive to load shedding but the maximum rotor speed cannot be too high for ecological constraints. The pitch angle chosen for the Deltastream was therefore established as a trade-off between these opposing requirements. When compared with the design point as the pitch is increased the performance characteristic suffers from diminishing returns as the Cp drops away very quickly with blade angle which would require a higher rated flow speed than is achievable in Ramsey Sound. Furthermore the dynamic range of the turbine is reduced as observed in Figure 134 above where the power falls to zero very quickly when TSR is increased. This would make for a turbine that was difficult to control as small changes in RPM would result in very large changes in rotor load. Control of the turbine is discussed in detail in Chapter 3. In contrast if the pitch is reduced by a few degrees the Cp/Ct ratio reduces rapidly which leads to a much less efficient rotor even though the

operating range is very wide. However this is not an improvement as, particularly for angles above +2.5deg, the Ct curve does not tend quickly to zero as TSR is increased which renders the control strategy ineffective. Furthermore it would require very high rotor RPM to reduce load at high speed which is unacceptable from an ecological perspective. Therefore the design angle chosen places the turbine in a narrow window bounded by a rotor that is unstable on one side and not very responsive on the other.

Figure 137 below shows the design values of RPM, thrust and power versus flow for the full scale Deltastream prototype turbine under steady state conditions. These curves were produced from the non-dimensional performance curves produced using the hydrodynamic code. The power is limited to 434kW (mechanical) at the turbine rotor as this corresponds with the on-board generating capacity of the electrical equipment taking into account for gearbox and drive train losses of around 8%. The gearbox will be particularly susceptible to heat loss due to the high gear ratio of 78:1. The peak thrust is constrained to 25.3T which coincides with the turbine reaching its rated power at a flow velocity of 2.67m/s. The left hand side of the curve is a result of allowing the turbine rotor to absorb maximum power by running at constant Cp. Therefore the rotor RPM increases proportionally with the flow speed until maximum power is reached. At this point the control system must start to act to restrict the power.

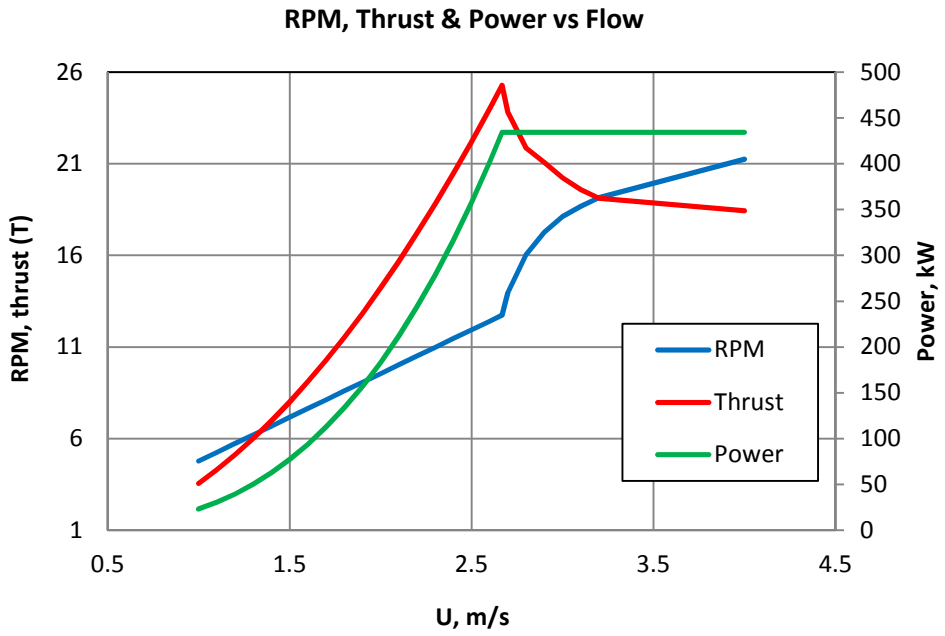

Figure 137 - Design curves

The rotor has been designed to be power rather than thrust limited i.e. the peak thrust load lags the maximum generating capacity of the device. In order to maintain a constant power above rated flow speed the turbine must operate at constantly decreasing Cp. This is achieved by increasing the TSR as flow increases which results in the shape of the right hand side of the RPM curve. Here the RPM increases exponentially above the rated flow speed to maintain constant power. This is governed by the trend of the Cp-TSR curve shown in Figure 134 above. The thrust load decreases somewhat because the rate at which Ct decreases is higher than Cp at this point of the turbine non-dimensional operating curve (as shown by the positive gradient of the design curve in Figure 136) which ensures the turbine can never exceed its over-turning moment. The rotor performance validation is discussed in greater detail in the proceeding section.

The parametric blade profile defined in terms of chord and pitch for the 1/16th scale model is shown in Figure 138 below. For the model scale tests at IFREMER the chord has been scaled by 16 while the twist angle remains constant. Therefore to achieve equivalent flow angles the rotor RPM during testing will be scaled up by 16 times to account for the reduced diameter. It is

assumed that the model rotor blades are made to a similar level of surface roughness as the full scale turbine.

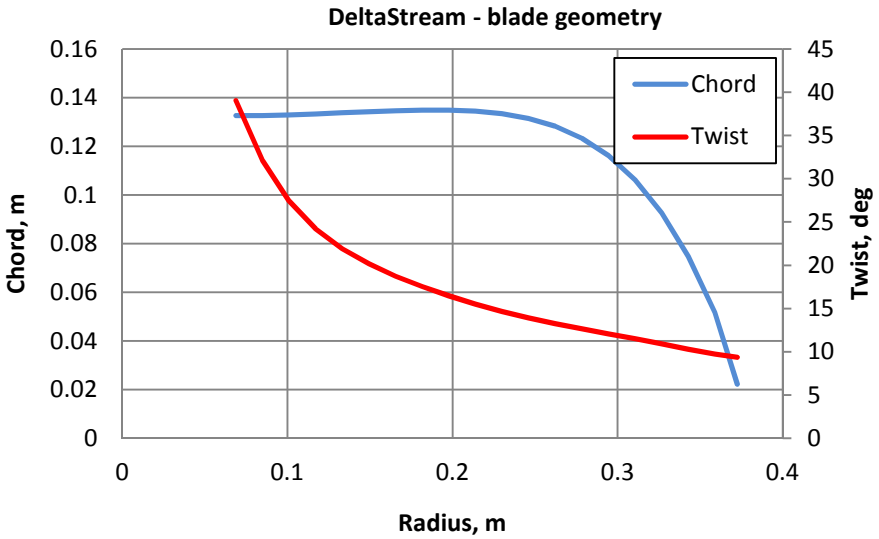

Figure 138 - Blade geometry

The blade airfoil is constant with span utilising a non-cambered NACA 0015 section profile from the root to the tip. The sectional data, in terms of lift and drag, used in the code to predict blade loads are shown in Figure 139 and Figure 140below. The red curves show the model scale data calculated for a Re of 2E5 which is predicted in the flume tank at design conditions. The blue curves account for the higher Re of the full scale machine which is expected to be 5E6 when operating in rated flow. As expected the model scale airfoil will stall earlier as indicated by the roll off in Cl at a lower angle of attack than for the full scale data. However this will not particularly impact the machine performance as the turbine design point is not close to the stall angle. Typically for a TSR of 3 to 4 the effective angle of attack will be approximately 4 to 7 degrees. The effect of scaling will manifest itself through the increased drag coefficient at lower Re. This will reduce the Cp and increase the Ct of the IFREMER model rotor which is evident when the Cl/Cd ratio is observed as even at low angles of attack the Cd is higher.

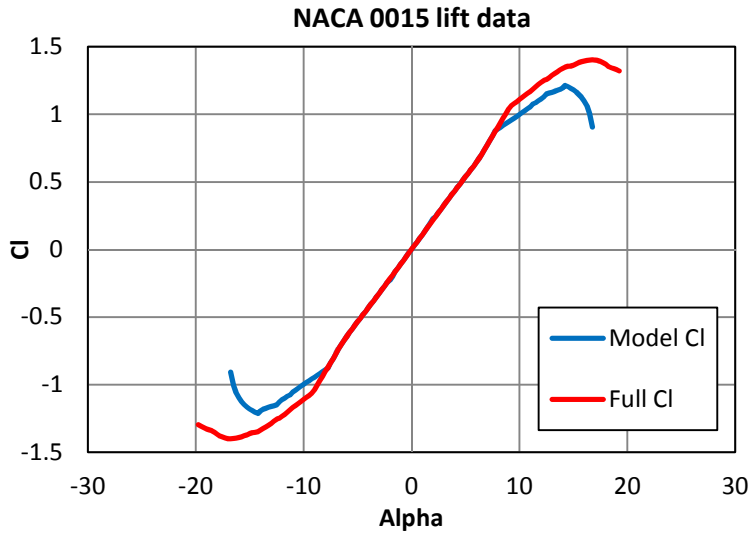

Figure 139 - 0015 Cl

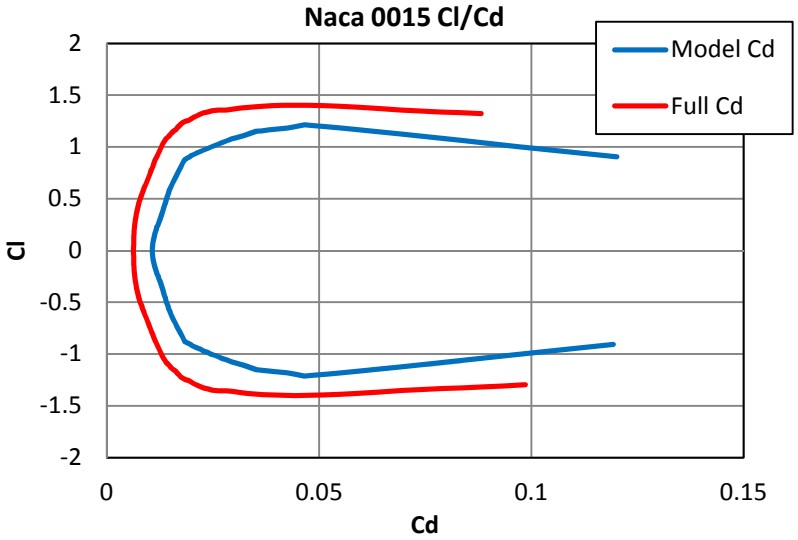

Figure 140 - 0015 Cd

4.2.4 Steady state results

The main aim of the experimental program is to study time dependent behaviour of the turbine but it is critical to characterise the turbine rotor performance to validate the turbine steady state design as discussed previously. Furthermore, it provides insight into the operating range over which the code can be deemed reliable. The Figure 141 below shows the steady state

turbine performance for both levels of turbulence determined from the post processed power and thrust measurements. The predicted power coefficient is shown in red and the thrust coefficient in black while the experimental results are in blue and green for low and high turbulence respectively. Each experimental point represents the mean of 100s of data acquired at 100Hz which ensures all turbulent fluctuations have been averaged out. The results for both the low and high turbulence flow are plotted together and this shows there is no relationship between the turbulence intensity and the steady state power or thrust coefficient. This result is expected as the unsteady fluctuations are smoothed out by the averaging procedure. This is a reassuring result from the perspective of the turbine operator because it shows that the turbulence level in of itself should not impact the turbine power capture performance (although it will have an influence on load mitigation strategies as discussed later in section 5.3.3)

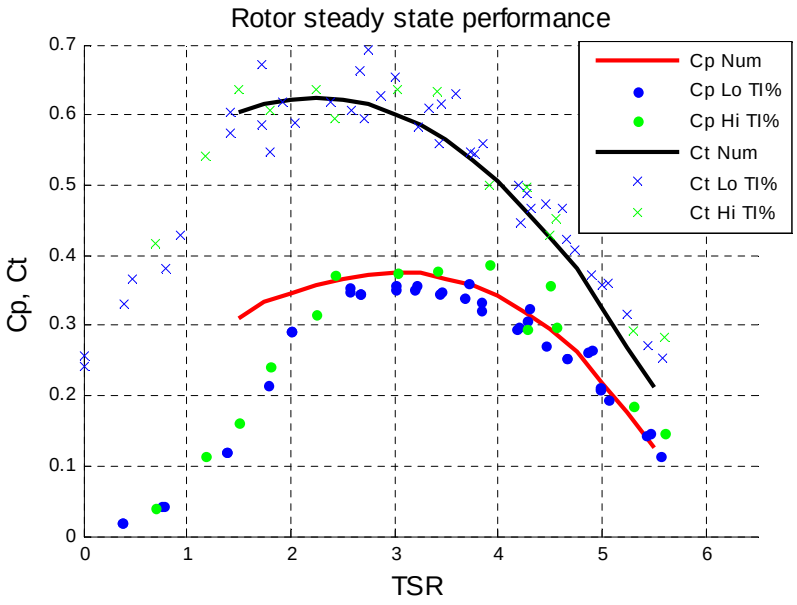

Figure 141 - Steady state performance

Overall this shows that the code provides a robust prediction of the turbine performance for both Cp and Ct. The prediction of trend and magnitude match well with the experimental data over much of the turbine' operating curve. Around the design point the discrepancy between numerical and experimental

data for Cp is approximately 3.5% and 2.3% for Ct. These differences are of similar magnitude to the measurement uncertainty previously discussed.

At low TSRs the code breaks down when the airfoil angle of attack is high. For TSRs of 1 to 2.25 the Cp is somewhat over predicted by the model as the experimental data drops off much more rapidly than the simulation predicts. This is the result of deficiencies in the model that do not fully capture the flow physics when the turbine is operating at this point. As the TSR tends towards 1 and the induction factor increases towards 0.5, the rotor moves into the turbulent wake state where recirculation behind the rotor disc becomes stronger leading to span-wise flows. This of course leads to the breakdown of the assumption in momentum theory that the annular stream tubes do not interact (see Chapter 2). Furthermore it is assumed that the blade stalls more suddenly than the theoretical airfoil data suggests possibly due to manufacturing defects in the blade. Certainly the NACA 0015 will be relatively sensitive to leading edge defects when close to stall as these may act as a trip leading to premature flow separation and transition to a turbulent boundary layer. However, due to the operational profile of the Deltastream turbine this is not deemed a problem. The turbine peak Cp occurs near at TSR = 3.25 i.e. this is where the peak power from the turbine can be absorbed. Furthermore when the device is in load shedding mode the TSR will increase towards freewheel around TSR = 6.0. Based on this no further effort was put into providing better predictions at low TSRs as this will only affect the starting performance of the turbine (which will probably be assisted by the on-board generating set motoring the rotor over).

The predicted trend of the turbine performance from peak power through to free wheel is well matched to the experimental data. Both the code and the experimental data indicate that peak Cp occurs at a TSR of 3.25 which is a key result. It is critical that the point of maximum power absorption is well defined so as to maximise electrical output. This ensures that the turbine operator is able to extract the most energy from the flow. Furthermore the drop off in both Cp and Ct towards freewheeling closely matches with the experimental data. This

is also an important result in terms of predicting turbine loading when the device is operating in flow speeds above rated to ensure the maximum over turning moment is not exceeded. This result validates the design curves in Figure 137 above and shows that the RPM vs velocity profile is justifiable. This is crucial for implementing the load alleviation control system by means of increasing turbine RPM which will be discussed later in chapter 5.

4.2.5 Scaled Deltastream Turbine Experimental Results

In this section fourteen experimental load cases are compared with numerical simulations when the turbine was running in 5% turbulence intensity flow at two flow speeds. A wide range of operating points has been selected starting close to stall at a TSR of 2.6 through to near freewheeling at a TSR of 5.5. The turbine rotor speed control was undertaken manually and therefore the TSRs for the two cases are slightly different. However this does not affect the analysis as the range of TSR for which the turbine was tested for both cases is very similar. Only cases where there are no additional dynamic loads such as those caused by structural resonance were chosen in order that the turbulent loads could confidently be isolated. The cases are detailed in Table 8 below:

#	TSR	RPM	Thrust	Torque	DEL Thrust	DEL Torque	U, m/s
1	2.83	90.03	216.66	12.66	91.88	4.9	1.25
2	3.3	105.64	209.48	10.5	80.94	4.23	1.25
3	3.77	119.6	187.25	7.95	85.74	3.5	1.25
4	4.24	135.13	167.2	5.86	68.72	2.53	1.25
5	4.71	150.62	140.2	3.47	62.34	1.74	1.25
6	5.18	166.32	108.38	1.02	48.02	0.594	1.25
7	2.62	101.6	329.29	24.24	127.04	9.35	1.5
8	3.01	114.7	324.15	21.98	131.78	8.69	1.5
9	3.4	13.38	305.07	18.87	125.9	7.33	1.5
10	3.8	146.46	277.14	15.88	117	6.76	1.5
11	4.19	159.9	247.83	13.19	103.03	5.48	1.5
12	4.58	177.92	209.8	10.17	100	3.97	1.5
13	4.97	190.39	176.74	7.84	104.39	3.63	1.5
14	5.5	207.72	134.43	5	63.23	1.97	1.5

Table 8 - Load cases

Comparisons between the experimental and numerical data are made on the basis of the following measures:

- The mean thrust and torque loads are compared in each case to ensure the steady state performance of the code matches the average experimental results. This is used as an initial check to confirm the numerical setup is well matched with the experimental case.

- An inspection of the overlaid load spectra, as calculated using a power spectral density function, gives an indication of the energy contained in the datasets and whether the numerical loads coincide with the experimental in terms of magnitude and wave number.

- A further more robust approach is taken to provide a quantification of the unsteady loads caused by the turbulence which is to calculate the

Damage Equivalent Load (DEL). The DEL provides a means of directly comparing the cyclic load component of each case by application of a method used in fatigue load analysis.

Figure 142 below shows a typical torque spectrum from an experimental run of 100s. The peaks occurring at the higher frequencies from 2-20Hz are from mechanical sources within the test rig and are not hydrodynamic forcings. To prevent this from corrupting the results all the experimental data is passed through a low pass filter to eliminate any signals that are not produced from unsteadiness in the flow. This is deemed a robust approach based upon the fluid velocity spectral analysis discussed in previously which indicates that the flow is well inside the inertial sub-range at this frequency.

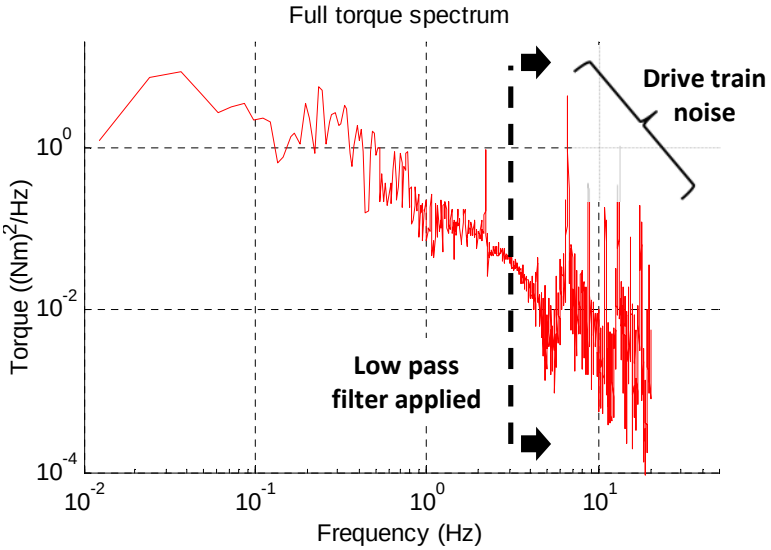

Figure 142 - Experimental torque load spectrum

The peaks in the spectrum labelled as 'drive train noise' occur at characteristic frequencies of the test rig including at the rotor running speed and the step up gearbox output speed. They are most likely due to slight misalignments in the rig construction and are not caused by the flow environment and therefore are

ignored. This was established through detailed vibration spectral analysis.

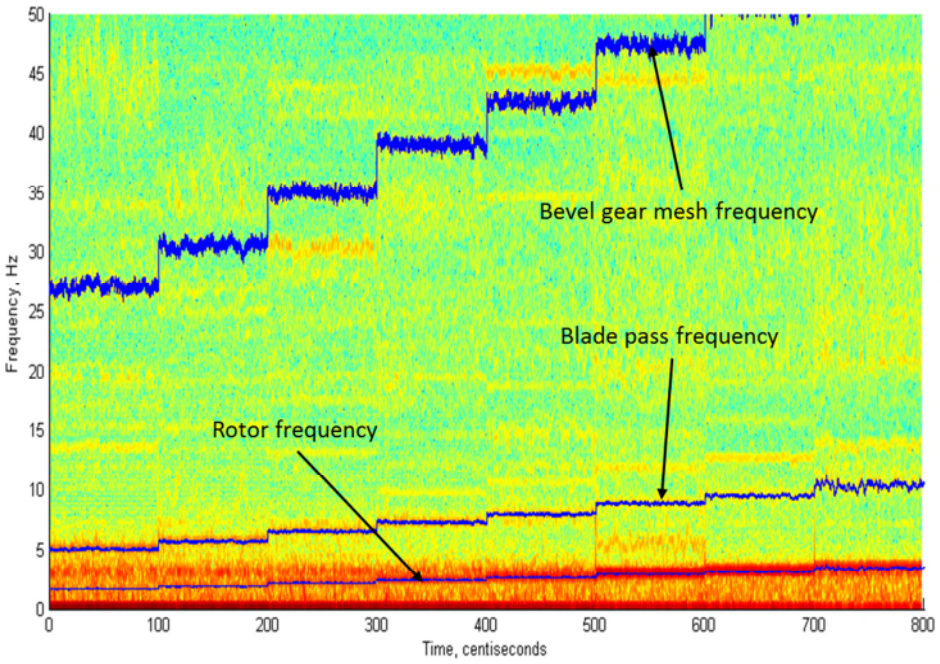

Figure 143 shows a spectrogram of the rig running over a wide range of speeds in a constant velocity flow. The spectrogram is a measure of the energy content of the spectral component at specific frequencies. Therefore in turquoise and yellow regions there is little spectral activity whereas in the red areas there is strong signal being detected by the vibration instrumentation. Overlaid on the spectrogram is the time history of the shaft speed, blade pass and gear mesh frequencies in blue. This shows that the spectral activity matches with the discrete machinery operating frequencies.

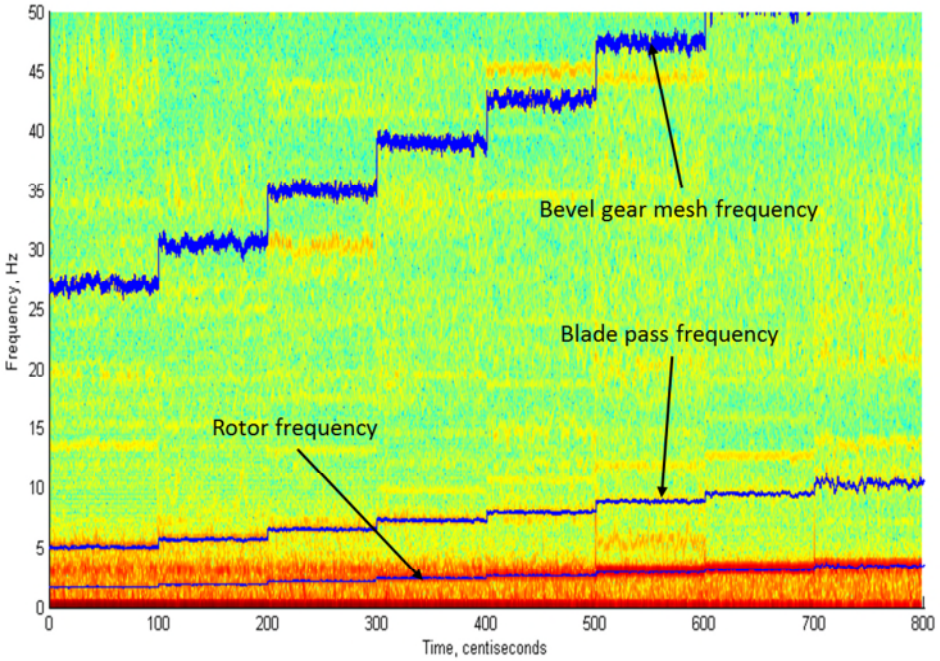

Figure 143 - Spectrogram of rig running frequencies

To show this in more detail data from two different running speeds were selected, 360 and 540rpm, and their spectral content is plotted in Figure 144. The distinctive peaks at the right hand side are the rotor shaft frequency which shift with running speed (i.e. move from 6Hz to 9Hz) whereas the turbulence frequencies remain unchanged at the left hand side. Further evidence that this is a valid technique is the presence of peak at 3Hz which is the result of a system natural frequency. It should be noted that this peak does not change as the running speed changes.

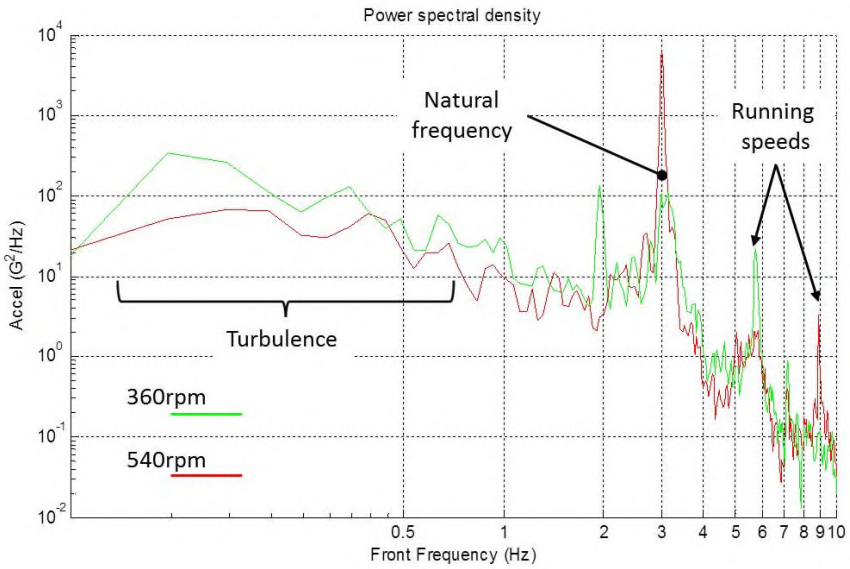

Figure 144 - Drive train spectrum

Figure 145 and Figure 146 below compare the mean torque and thrust loads from the 14 experimental cases with the numerical results from a large number of simulations at flow speeds of 1.25 and 1.50m/s. In general this shows good agreement between the experimental and numerical data particularly at the lower flow speed which is to be expected considering the non-dimensional results in Figure 141. There is a slight over prediction of mean torque for the high flow at TSRs less than 3 and a similar under prediction in thrust. These differences are explained due to the combination of experimental error and uncertainty in the model data.

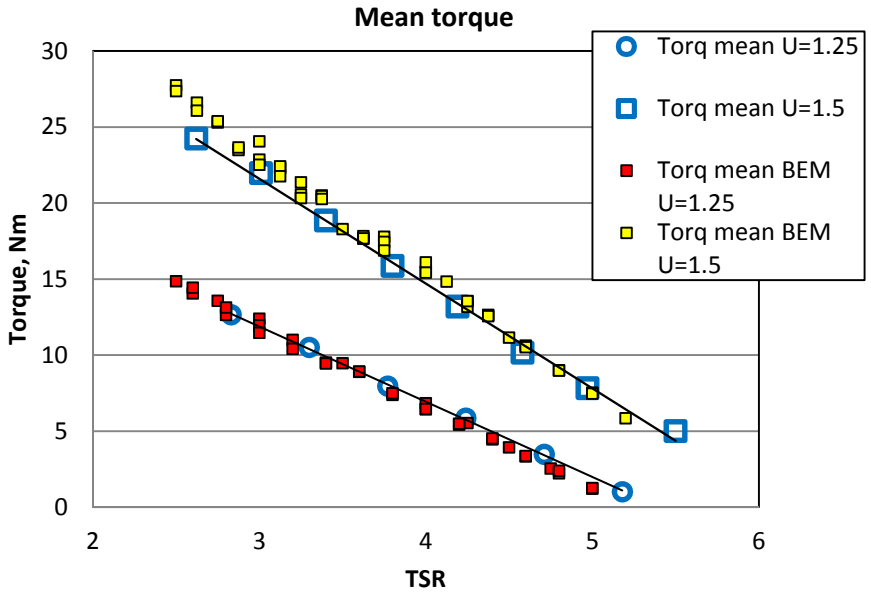

Figure 145 - Exp. mean torque

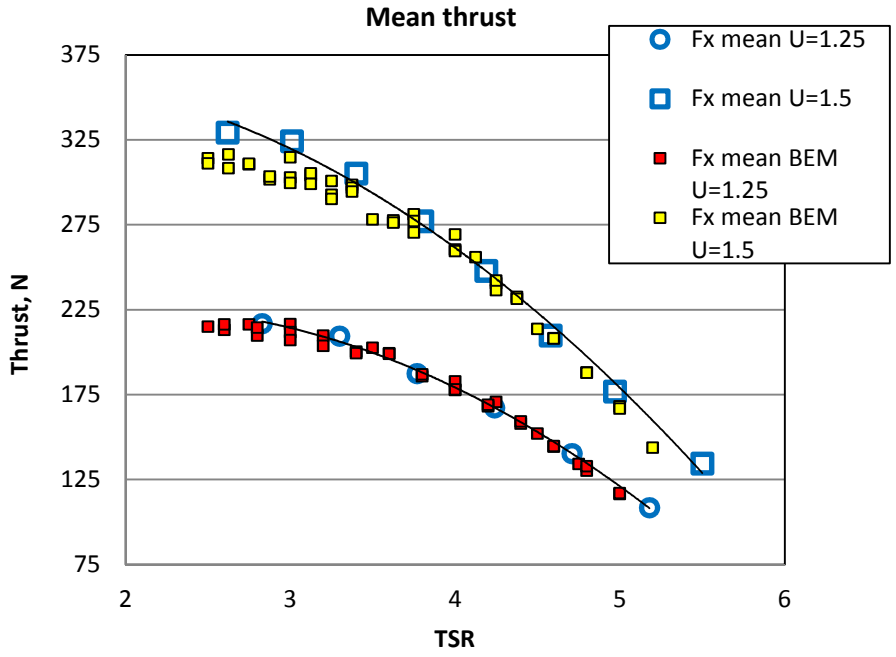

Figure 146 - Exp. mean thrust

The equivalent comparison of the unsteady loads is made in Figure 147 and Figure 148 which plot the DEL for torque and thrust for the same 14 experimental cases. The comparison of torque is very close between the prediction and the experimental data. As is expected there is degree of scatter

in the numerical results between simulations run at the same TSR. This is due to the simulations being less than 10% of the duration required for statistical steadiness. As previously outlined in section 3.6 a simulation duration of 2000s is required to produce statistically stationary results i.e. two simulations run with the same input parameters will result in the same output in terms of DEL. This is not a weakness in the model but rather a characteristic of the flow as it takes this length of time for the largest eddies to repeat enough times to become statistically stationary. However, due to constraints beyond the authors control each experimental point could only be run for 100s. When comparing experimental and numerical results the appropriate time step and grid size were still utilised. However, Figure 74 shows that the simulation will not produce DEL outputs that are invariant between simulations and a variation on the order of 10% should be expected. This variation is observed in Figure 147 and Figure 148. Here the same simulation has been repeated three times and there is a difference in the numerical result on the order of 10-12% typically. In order to be consistent with the experimental technique all variables were kept equal in the process of simulating the experimental results. Furthermore each simulation was repeated several times to provide a higher level of reliability to the data trend.

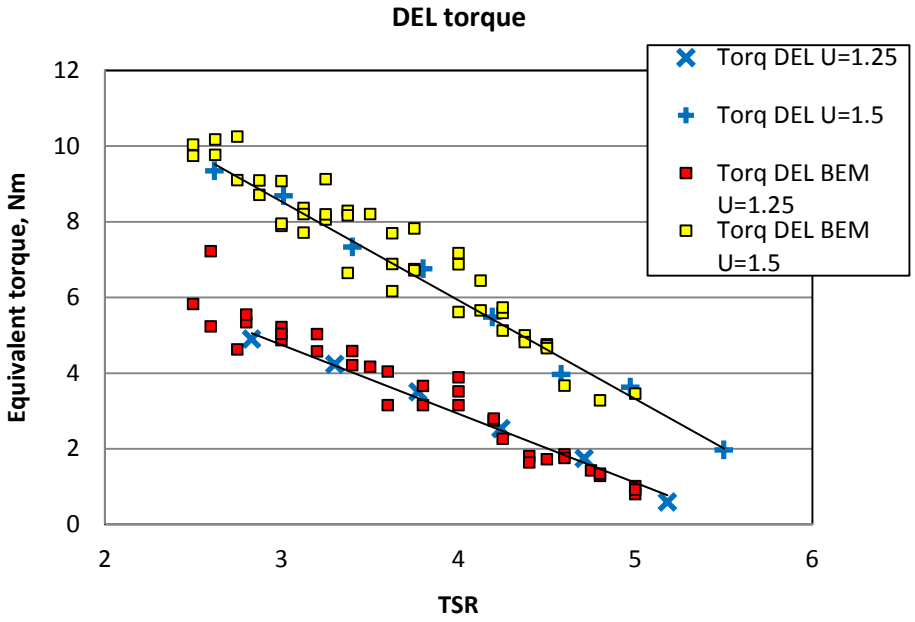

Figure 147 - DEL torque

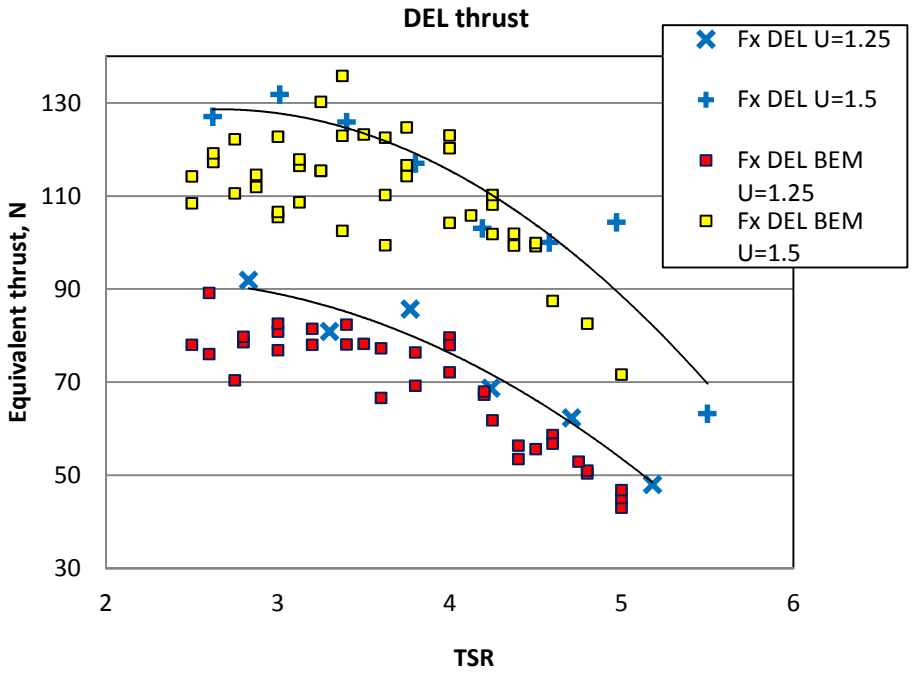

Figure 148 - DEL thrust

4.3 Validation summary

The BEM code has been compared with both numerical predictions and experimental results from five different turbine geometries of both wind rotors and tidal rotors. A number of aspects of the code have been highlighted and validated in isolation through both steady state analysis and transient simulations. The validation study progressed from steady state load analysis of the UAE rotor and the SOTON model turbine to the analysis of the unsteady DUT wind tunnel experiment and then to the time dependent behaviour of the Tjaereborg turbine undergoing pitching transients.

The steady state analysis provided the opportunity to study the performance of the code over a wide range of operating conditions including at low TSRs where the blades tend to operate in a partially stalled state. This highlighted the importance of using the appropriate aerodynamic section data to take into account the stall delay phenomenon caused by blade rotation. Comparison between using 2d and 3d section data emphasised how the 2d data will lead to under-prediction of loading in the stalled region but generally good performance at higher TSRs. This stressed the requirement of implementing the stall delay model for analysis of stall regulated turbines. In the majority of the steady state comparisons the BEM code performed well as the results were in agreement with the experimental data. Over the course of the validation study four of the major rotor loads (torque, thrust, blade bending and power) compared well with the experimental results. In some of the validation cases from literature the authors model exhibited quite large disparities with the published data however this is not a limitation in regards to the application of the model with the Deltastream turbine as there is good agreement with all the experimental data from the scaled rotor tests measured during IFREMER campaign that the author undertook.

The unsteady experiments carried out with the DUT wind tunnel model allowed the opportunity for validation of the transient capability of the code without using the dynamic inflow solver. The wind gust simulations demonstrated the codes ability to calculate loads in the time domain with variable inflow conditions. This

intermediate step is known as the equilibrium wake model between steady state load calculations and full dynamic simulations and is not time dependent. The dynamic inflow model was then tested using data from the Tjaereborg machine. The results for the bending loads were found to be in closer agreement than for torque. This was largely attributable to the steady state load calculation capability rather than the dynamic model as the time constants for both load cases appeared to match well with the experimental results.

The key results from the experimental test campaign are:

- The hydrodynamic code accurately models the turbine performance in terms of the absolute magnitude and the general trend in behaviour for both C_p and C_T which give confidence to the unsteady time marching formulation.
- The model validity holds over the range of interest to the Deltastream turbine from TSR = 3-6 i.e. from peak power through to free wheel. The behaviour when the turbine is close to stall is not as accurate however.
- The model can replicate the unsteady load results in terms of torque and thrust from the turbulent flow which is required for using the model to determine fatigue life.

5 Modelling of Turbine Operation

5.1 Introduction

This chapter covers the application of the turbine model to the full scale Deltastream prototype device. The model will be used to investigate the turbine operability and fatigue life performance in conditions replicating the tidal environment in Ramsey Sound. Furthermore the relationship between turbulence intensity and fatigue load for both Ebb and Flood tides is examined explicitly with the aim of deriving an empirical formulation to estimate damage equivalent load. Finally modifications to the turbine control methodology are explored to determine their viability for improving turbine operability and fatigue life performance.

5.2 Deltastream turbine duty cycle

In order to determine the turbine fatigue life when operating in Ramsey Sound it is necessary to accurately define the turbine duty cycle in terms of the flow regime and as well as the limits set on turbine operation. The site specific flow in which the Deltastream will operate has been discussed in Chapter 3 in terms of the flow velocity and turbulence profile which has been determined by analysis of the ADCP data taken at the turbine site as shown in Figure 8 in Chapter 1. The following is a summary of these conditions and a description of a sequence of simulations that have been conducted which are aimed at capturing how the turbine will be affected in terms of operability, fatigue life and performance. The turbine operability is defined in terms of how successfully the system works at holding the device below the maximum load threshold for thrust and blade bending as well as ensuring the power does not exceed the rated capacity. The fatigue life will be assessed in terms of stress cycles using the fatigue model previously described driven by the data gathered from the sequence of simulations described next. Finally performance will be measured in terms of energy captured over the Ebb and Flood tides with the effect of control taken into account.

The annual tidal velocity probability distribution for the Ebb and Flood tides is shown in Figure 149 below as derived in Chapter 3 from ADCP data. This appears to show that the Flood tide is more energetic than the Ebb tide as the Flood runs for a higher proportion of the year and peaks at a higher velocity i.e. 3.2m/s instead of 2.5m/s.

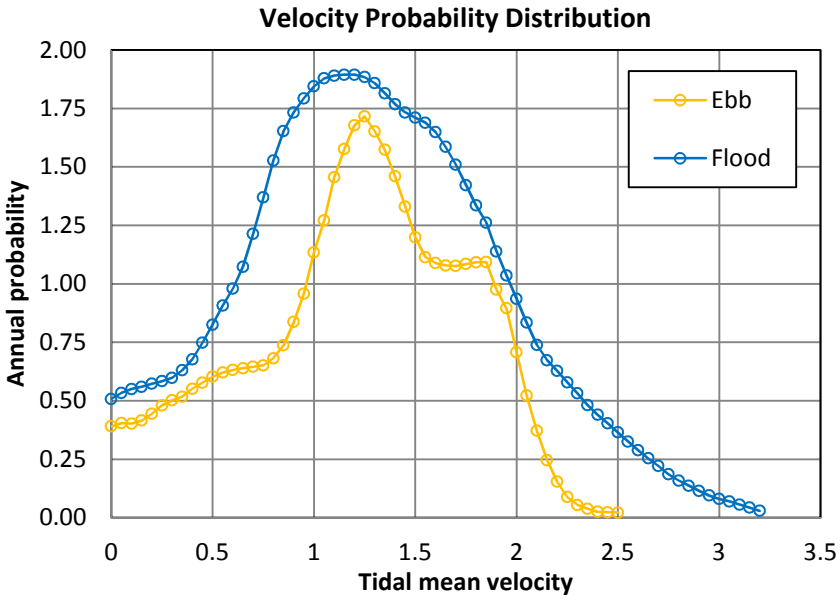

Figure 149 - Tidal flow velocity probability distribution

This is confirmed by Figure 150 below which shows the annual energy distribution, in terms of MWhrs, for both tidal flows. When a disc of the dimensions of the rotor is considered the annual kinetic flux available on the Ebb tide is approximately 4,800MWhrs and 10,200MWhrs for the Flood i.e. twice the energy. For flows below 1.5m/s the energy availability is similar between the tides but above1.5m/s there is a significant difference in the distribution. This is highlighted more clearly by Figure 151 which shows the proportion of the total annual energy of each tide (NB: the proportion is not of the total tidal energy available but the proportion available from each tide) for five flow bins for both tides. This shows that more than half the energy available from the Ebb tide lies in the band 1.5-2m/s whereas for the Flood tide the energy is more evenly distributed above 1.5m/s. Furthermore 30% of the annual energy available in the Ebb cycle lies between 1 and 1.5m/s and therefore more than 80% of the total energy available falls between 1 and 2m/s.

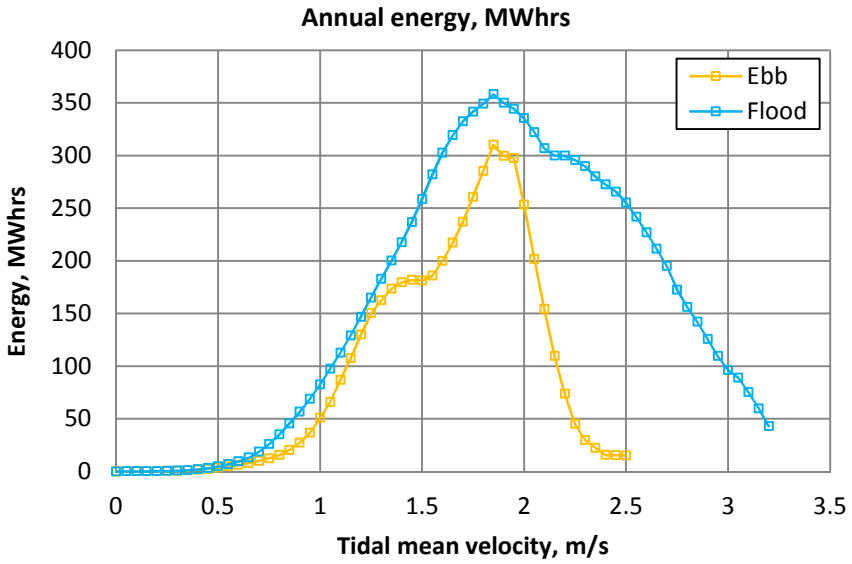

Figure 150 - Energy probability

As the Flood tide energy is much more evenly distributed the turbine will have to operate over the full velocity range in order to generate maximum revenue in comparison to the much narrower band for the Ebb flow. Operation in the Flood regime will be far more damaging to the turbine than in Ebb when the distribution of turbulence intensity is also taken in account as shown in Figure 152.

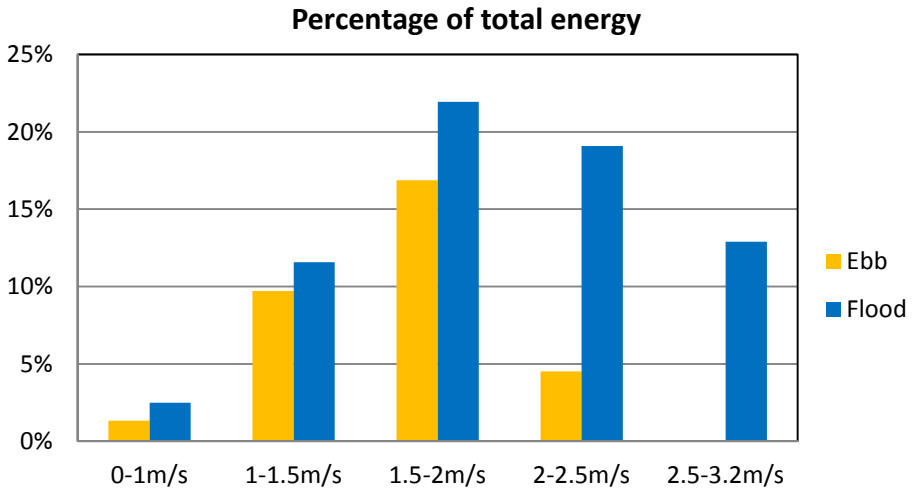

Figure 151 - Energy distribution

This shows the stream-wise turbulence intensity data gathered using the ADCP during a 3 month deployment period. Each point on the plot represents the average of one minute of flow at a sampling rate of 2Hz. There is a distinct difference in the behaviour between the Ebb and Flood tides with the Ebb turbulence being around 8% lower in the turbine operating range. Furthermore there is a much greater spread in the Flood tide data which is the result of the nature of how the turbulence is generated which is discussed in detail in Chapter 3. At the rated flow the turbine will be subjected to close to three time's higher turbulence in Flood (14%) than Ebb (5%). It should be noted that turbulence intensity increases as the flow velocity tends towards zero. This does not indicate that flow in this regime is particularly damaging compared to the flow above, say, 1.5m/s but it is an artefact of the calculation of turbulence intensity i.e. TI will tend to infinity when velocity tends to zero (see Equation 70). Therefore only flow velocities above 1m/s are considered in any analysis.

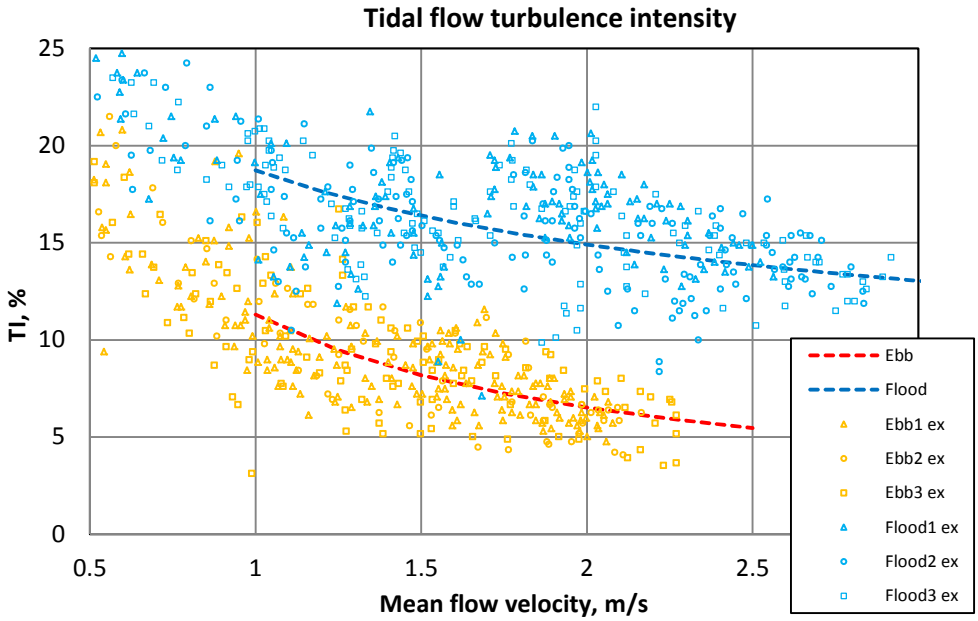

Figure 152 - Ebb vs Flood TI%

A set of simulations to model the turbine loading conditions has been established based on splitting the flow into a series of bins with turbulence intensity, a turbulence model and the annual probability attributed to each

based on the previous analysis of the flow data. The first set was aimed at determining the turbine energy capture, operability and the fatigue loading on Deltastream for an Ebb tidal cycle as shown in Table 9. The simulations were run for both constant velocity and for the Ebb tide shear profile shown in Figure 153 below in order to examine the effect of turbulence in isolation from the cyclic loads caused when the turbine runs in a shear layer.

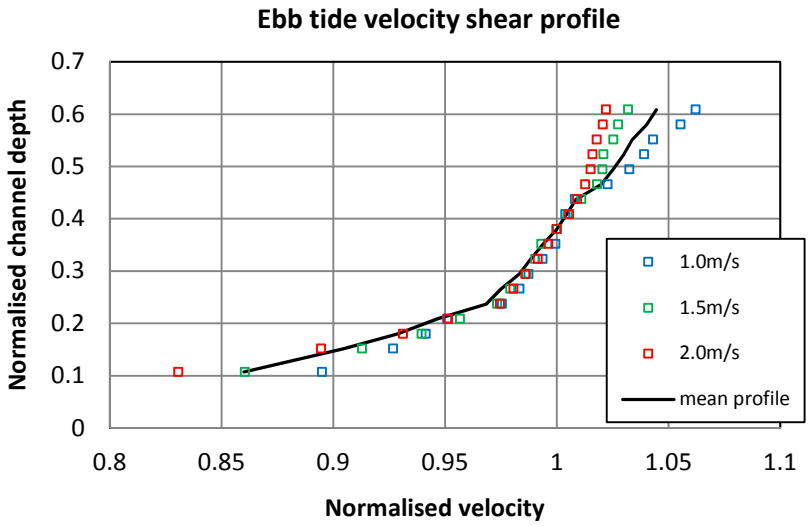

Figure 153 - Ebb shear profile

It is assumed that below 1m/s the turbine will not be operating due to the very low energy available from the flow. Therefore during an Ebb tide the turbine will be operating approximately 67% of the time with the cut in velocity set at 1m/s and no cut out. The flow has been split into 7 bins of 0.25m/s in size between 1 and 2.5m/s with each bin assigned a turbulence level based on the data from Figure 152 above. For the high power cases the turbulence intensity is approximately 5.0-6.0%. A single value of turbulence intensity has been chosen as the turbulence follows a normal distribution and so using the mean value for the bin is a valid approach in this instance.

Case	U_{hub}	TI%	Model	Occurance
E1	1	11.30	KAI	5.51%
E2	1.25	9.46	KAI	14.91%
E3	1.5	8.19	KAI	19.11%
E4	1.75	7.24	KAI	26.98%
E5	2	6.51	KAI	24.85%
E6	2.25	5.93	KAI	5.77%
E7	2.5	5.46	KAI	0.09%

Table 9 - Ebb energy and fatigue cases

The second set of simulations covers the Flood tide in a similar manner, as shown in Table 10 below, however 12 simulations are used to better capture the overall tidal flow. The Flood cases are only run once with the Flood shear profile included in all simulations (see Chapter 4).

Case	U_{hub}	TI%	Model	Occurance
F1	1	18.72	FLD	3.52%
F2	1.2	17.63	FLD	6.07%
F3	1.4	16.76	FLD	8.88%
F4	1.6	16.04	FLD	12.03%
F5	1.8	15.43	FLD	13.60%
F6	2.0	14.90	FLD	12.73%
F7	2.2	14.44	FLD	11.53%
F8	2.4	14.04	FLD	10.44%
F9	2.6	13.67	FLD	8.51%
F10	2.8	13.34	FLD	5.80%
F11	3.0	13.04	FLD	3.60%
F12	3.2	12.77	FLD	0.10%

Table 10 - Flood energy and fatigue cases

The two sets of simulations detailed above are used to determine the fatigue life of the turbine when operating in both tides. An additional set of simulations were run to look in more detail at the turbine operability across the entire range of turbulence which can feasibly occur in Ramsey Sound in relation to the Ebb tide flow. Less importance is placed up the Flood tide as, due to the nature of the prototype Deltastream turbine, only very limited running will be conducted in the higher turbulence, higher energy flows. This is not a rotor performance related problem but rather due to the nacelle yaw system which has a maximum flow speed during which the system is able to turn out of the flow into ‘safe’ mode. It is expected that the turbine will remain yawed for much of the Flood flow.

In terms of turbine operability in relation to the effectiveness of the control system the entire range of Ebb turbulence is considered from 3.5% to 10%. Three velocity cases are considered; 1.5, 2.0 and 2.5m/s, which represent the

flow from which the turbine can extract the majority of the annual energy from the site. As discussed previously more than 50% of the annual energy lies in flows between 1.5 and 2m/s. At the high power condition of 2.5m/s load shedding will become prevalent and so acquiring a strong understanding of how the turbine behaves near its peak loading is vital in order to highlight potential limitations of the system. In addition to the effect of turbulence the importance of the boundary shear layer is also considered in relation to the effect it has on the turbine cyclic loading in combination with the turbulent inflow. A discussion of the results of these simulations is presented in the following sections.

5.3 Unsteady Flow Analysis

5.3.1 Effect of Turbulent Intensity

The effect of the turbulence intensity on full scale turbine loading is investigated in this section. Simulations were run for three tidal velocities (1.5, 2.0 and 2.5m/s) representative of the Ebb tide across a range of turbulence from 3.5 to 11%. Although the emphasis was placed on Ebb flows, as these are representative of general tidal flows, the full range of Flood flow was also simulated to understand the difference in the two tidal flows given the different turbulence models being used.

In order to assess the effect turbulence has on operability and fatigue loading both blade and rotor loads are compared to each other. The blade root flap-wise and edge-wise bending moments, being the principle blade loads, are considered as critical design loads while the rotor torque and thrust are used as examples of the total load on the turbine. These four loads are plotted below in Figure 154-Figure 157 for each flow and turbulence level in terms of the damage equivalent load which was defined in Chapter 4. The load simulations were run for time histories of 2000s as it has previously been established that turbulence statistics can be considered stationary over this duration. The DEL was then calculated based on a constant number of load cycles, which are

representative of a full year, as this is a direct comparison of the effect of turbulence and not an attempt to calculate fatigue life.

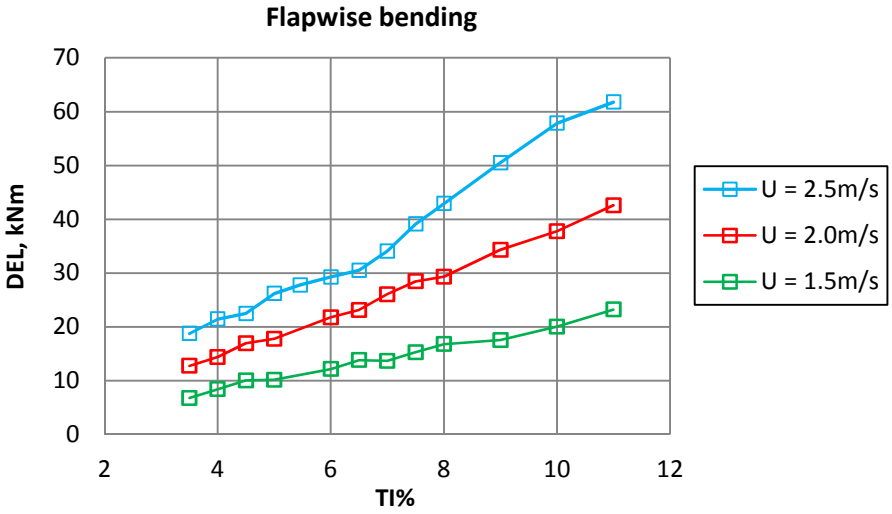

Figure 154 - Flap-wise bending moment DEL

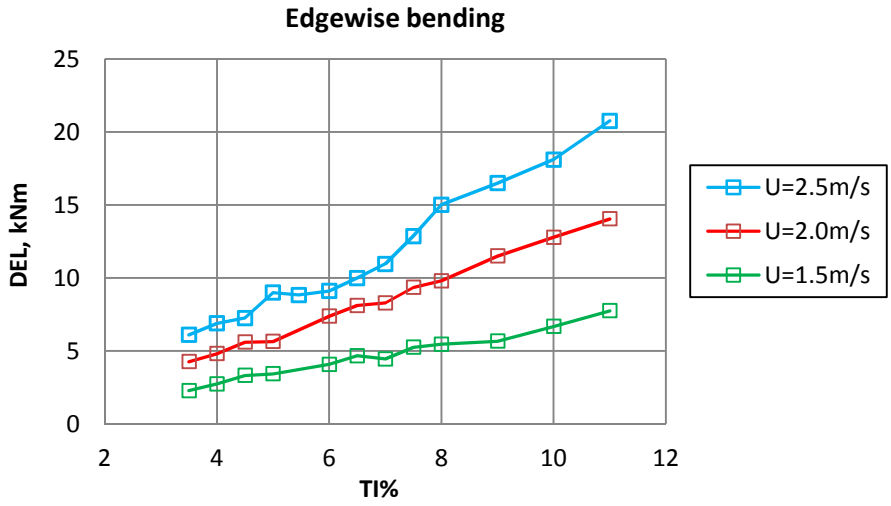

Figure 155 - Edge-wise bending moment DEL

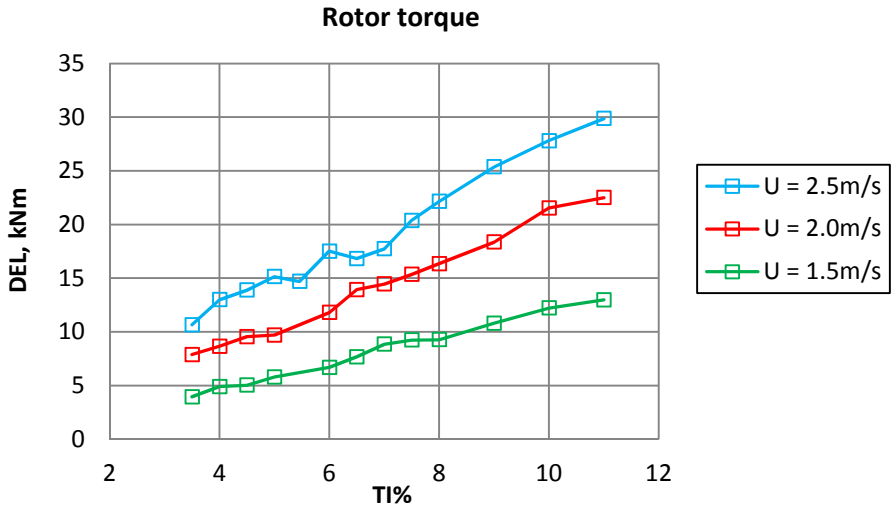

Figure 156 - Rotor torque DEL

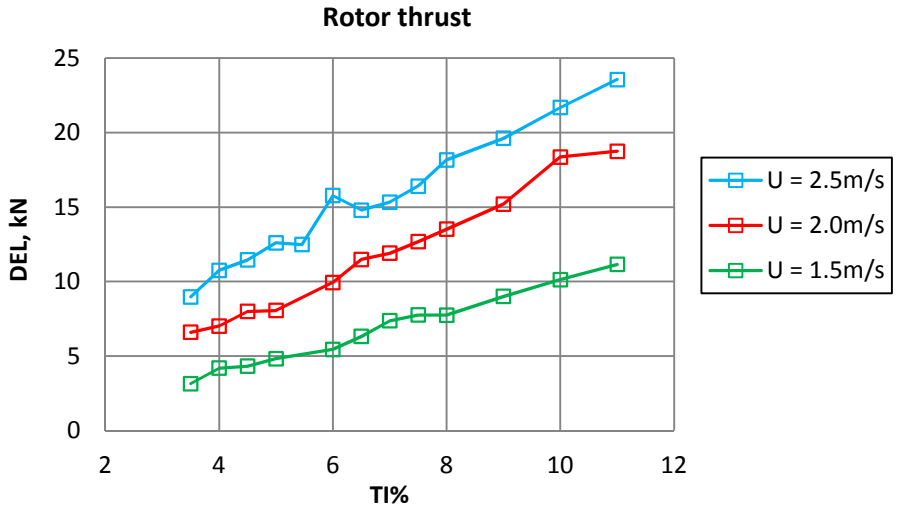

Figure 157 - Rotor thrust DEL

The behaviour immediately evident from the four load plots is that they all exhibit a directly proportional relationship with turbulence. However, in order to understand the relationship with flow speed the loads have been non-dimensionalised in terms of mean load as shown in Figure 158. This reveals two points; a clearly distinct difference in load magnitude that separates the blade loads from the rotor loads and furthermore the normalised DEL is independent from velocity magnitude which is to be expected.

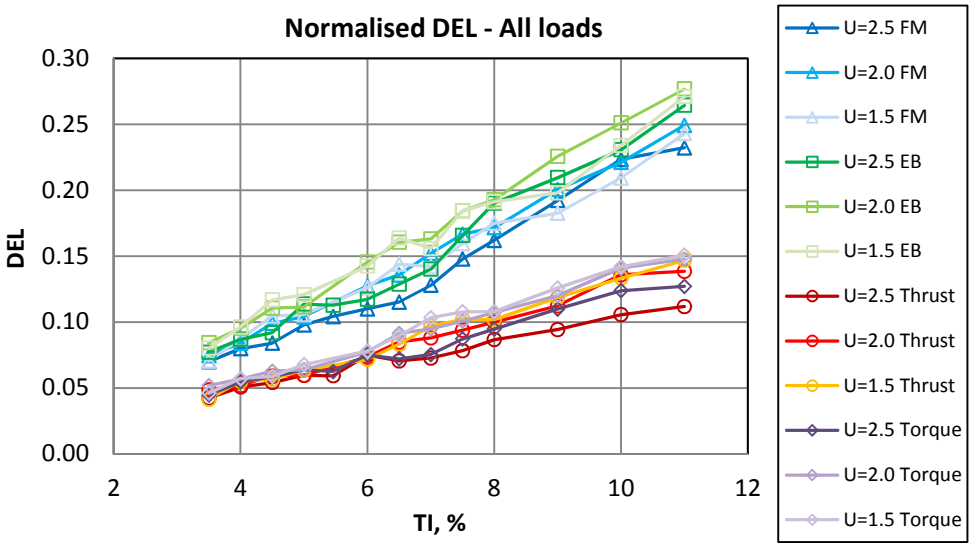

Figure 158 - Non-dimensional DEL loads

It must be noted however that this is only the case below the load shedding limit. Above U=2.67m/s the control system will play an important role in the behaviour of the DELs when the rotor is no longer operating at a fixed TSR. But this simplifies the numerical simulations required to fully map the turbine behaviour however as a single tidal velocity below rated will be sufficient. An examination of the load shedding regime will be presented in later sections. When the normalised loads are then averaged in terms of flow speed the difference between the blade and rotor loads becomes even more apparent as indicated by Figure 159. Linear regression of the trend-lines reveals that the cyclic load on the blades is more aggressive than for the rotor by almost a factor of two. This suggests that the blading will be subjected to a greater level of fatigue than the rotor for the same flow regime which will have design implications for the blading to ensure they do not limit the fatigue life of the device prematurely.

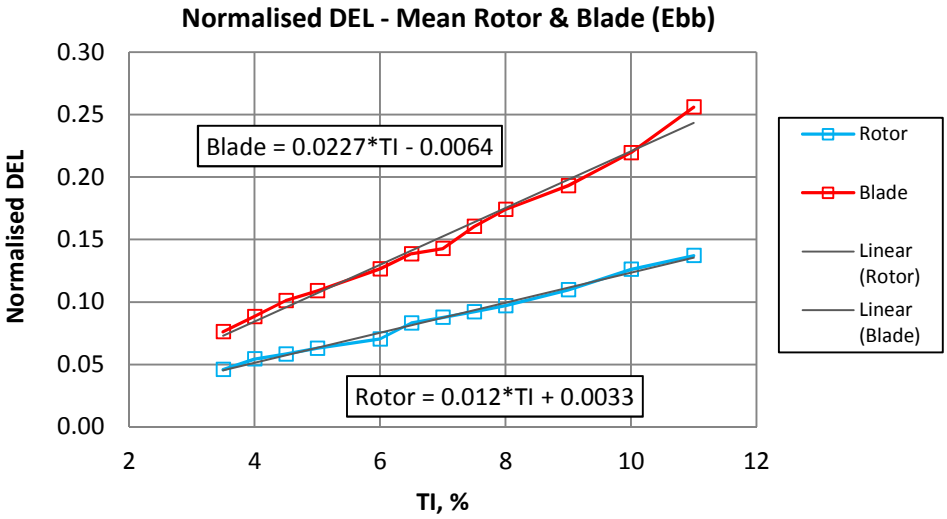

Figure 159 - Averaged DEL loads

This is also a useful result in terms of estimation of design loads on the turbine as it leads to an empirical law that can be applied to determine fatigue load as shown in Equation 86 and Equation 87 below.

$$\boldsymbol{Blade_{DEL}} = \mathbf{[0.0227} * \boldsymbol{TI}\% - \mathbf{0.0064]} * \boldsymbol{Blade_{MeanLoad}}$$

Equation 86

$$\boldsymbol{Rotor_{DEL}} = \mathbf{[0.012} * \boldsymbol{TI}\% + \mathbf{0.0033]} * \boldsymbol{Rotor_{MeanLoad}}$$

Equation 87

This will allow a first order approximation of DEL at any flow speed or turbulence intensity which dramatically simplifies any postdictive modelling or design. It is also applicable to other turbine diameters as the blade design can be scaled up to develop a turbine that can deliver more power for any given tidal location.

Based on the understanding gained from the Ebb turbulence modelling the results of the fatigue simulations for the Flood tide were used to compare the Flood and Ebb turbulence models. As the fatigue loads are independent of

velocity only the Flood envelope is required to fully quantify the behaviour in Flood turbulence. The normalised blade and rotor DEL loads are shown in Figure 160 below in equivalent fashion to the Ebb data in Figure 159 above.

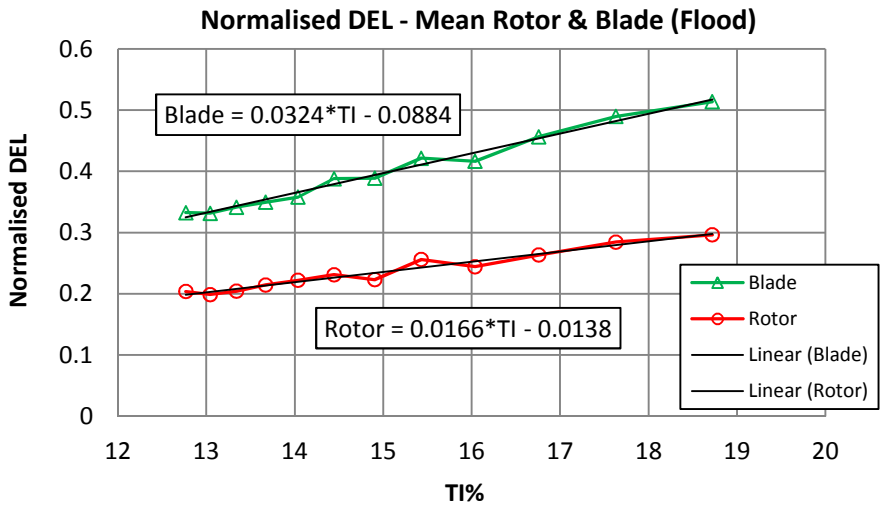

Figure 160 - Average DEL load Flood turbulence

This shows a very similar behaviour to the Ebb data where the rotor and blade loads are affected differently by the same level turbulence with the blade loads being more aggressive. The mean ratio between the normalised blade and rotor loads for Ebb is 1.89 and the ratio for Flood is 1.95 suggesting that the Flood tide causes slightly more damage than for the Ebb tide. The difference between the Ebb and Flood flows is further emphasised by Figure 161 below which shows the normalised blade DELs plotted against turbulent intensity where the steeper gradient for the Flood data confirms the more aggressive flow regime.

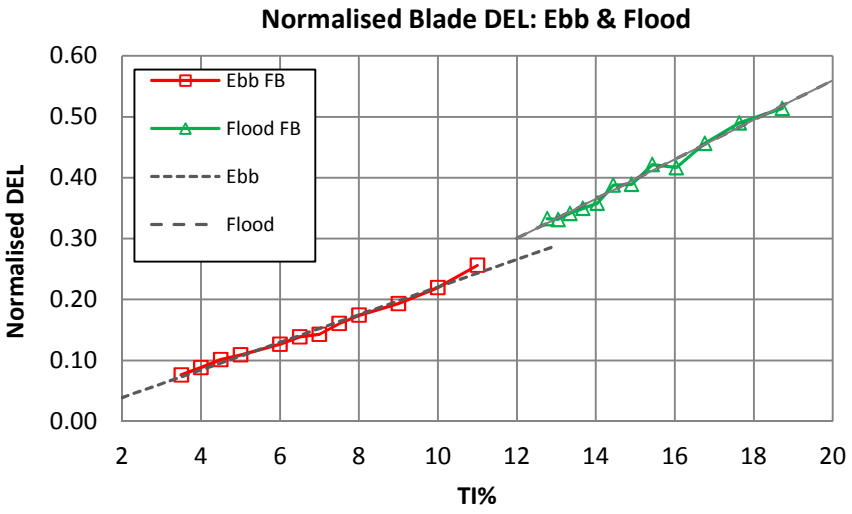

Figure 161 - Summary of blade DEL: Ebb & Flood

This result allows for an empirical approximation of the DELs for the turbine in the Flood tide as expressed below in Equation 88 and Equation 89 which are of the same form as the equations describing the Ebb DEL.

$$Blade_{DEL} = [0.0324 * TI\% - 0.0884] * Blade_{MeanLoad}$$

Equation 88

$$Rotor_{DEL} = [0.0166 * TI\% - 0.0138] * Rotor_{MeanLoad}$$

Equation 89

The damage equivalent load is independent of flow velocity when normalised against the mean load. Furthermore a linear, proportional relationship exists between DEL and turbulent intensity which can be written in empirical form as a means of simplifying turbine design. The difference in the fatigue loading between Flood and Ebb has been quantified with Flood being shown to be more damaging than the Ebb which is to be expected given the larger integral length scale and the degree of anisotropy at the largest length scales observed in the velocity spectra (see Chapter 3, Section 3.4.3 & 3.4.4).

5.3.2 Effect of the shear layer

Presented below are the results of simulations for turbine loading which compare operation with and without the boundary layer shear profile active (see Figure 153). Figure 162 shows the damage equivalent load in terms of blade flap-wise (FB) and edge-wise (EB) bending moments, torque and thrust for these simulations. It is clear that the blade only loads are significantly affected by the shear profile but the total rotor loads, torque and thrust, do not appear to change between the two cases. There is a substantial difference in the bending moment DEL when running the turbine with a flat inflow profile compared to the power law expression and this is seen for entire flow range. Conversely the torque and thrust results show no clear trend between the two cases indicating shear will not influence rotor fatigue loading. The bending moment DEL shows a very substantial 30% increase when the shear model is used applied.

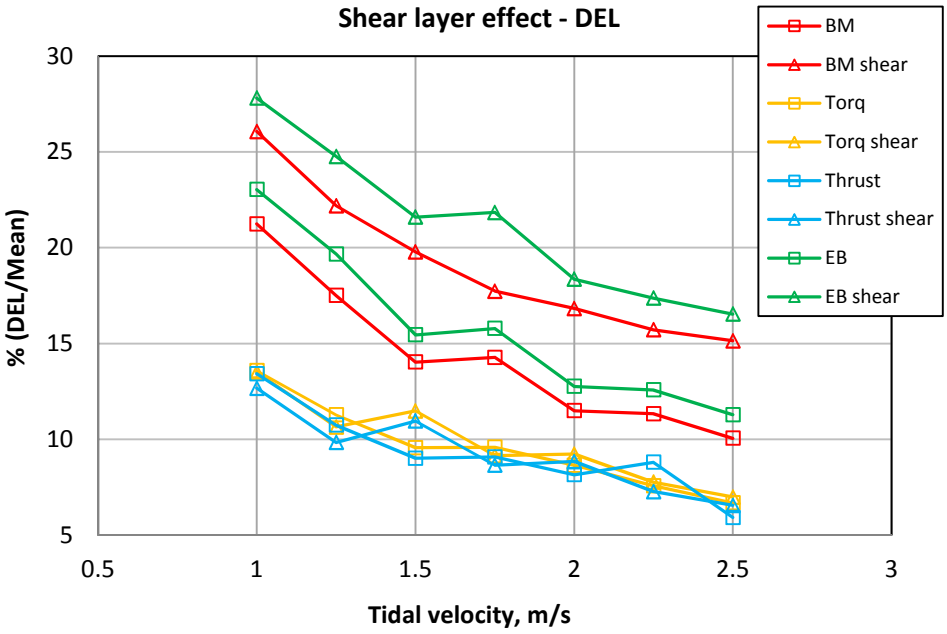

Figure 162 - DEL load boundary shear

The effect is further quantified in terms of the cyclic load ratio plotted in Figure 163 below. The cyclic ratio is defined as the ratio of the simplified minimum to maximum alternating load calculated from the rainflow cycle counting algorithm.

Therefore, as the stress ratio is decreased the amplitude of the cyclic load is increased. This makes it apparent that turbulence alone is driving the cyclic loading for the rotor loads (torque and thrust) as the results of the simulations including the shear layer are indistinguishable from those without. Whereas for the blade only loads the simulations that include shear clearly stand apart as being significantly more damaging. The influence of turbulence on fatigue load for the blades is already appreciably higher than for the rotor loads i.e. the blade loads are 0.1 lower than the overall loads. However, when shear is included the effect is an additional 20-30% increase in DEL and a further reduction of 10-12% in stress ratio which confirms the importance of including the shear layer in modelling effort when considering the life of the turbine blading. This is an important result in terms of selection of the appropriate S-N curve from the constant life diagram as this shows that the blade loads and the rotor loads must be treated separately from each other.

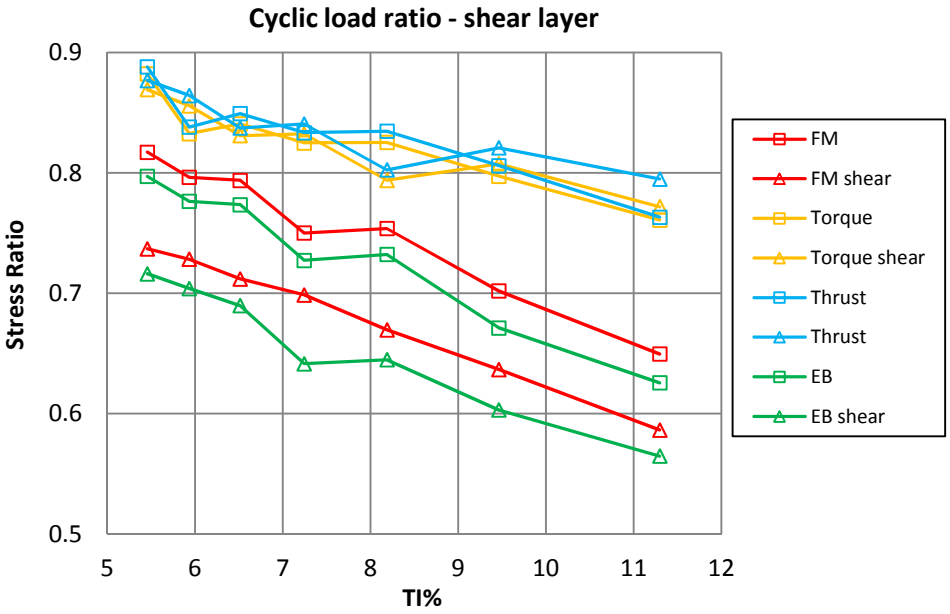

Figure 163 - Cyclic load ratio

To illustrate how the shear profile interacts with the turbine a time history of the three blade loads is plotted in Figure 164 for two simulations that include the

same shear profile. The first simulation, as per the figure legend, is run at 5% turbulence and the second has the turbulence model switched off completely. This serves to illustrate that the cyclic load amplitude produced by the blade in the shear layer is more substantial than that caused by the turbulent inflow for low levels of turbulence intensity. Therefore boundary layer shear can be a primary factor in driving high cycle fatigue.

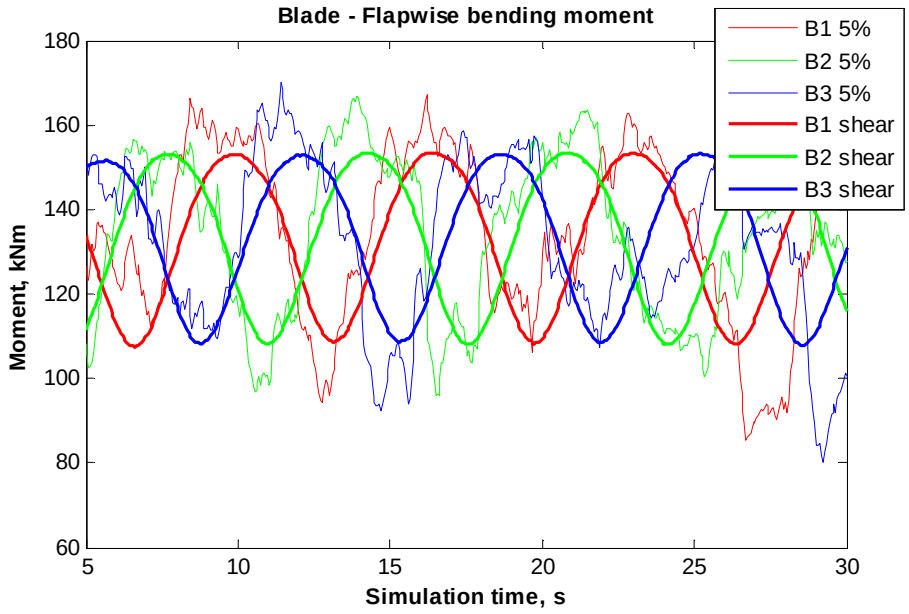

Figure 164 - Blade bending loads; shear layer flow

In contrast Figure 165 shows the results of the same simulation but in terms of rotor torque which further strengthens the assertion that the shear layer does not substantially affect the overall rotor load as the torque signal is virtually constant for the shear only case (green) compared to the very unsteady torque load profile when turbulence is introduced (blue). In this instance torque has been used to illustrate the comparison between the effect of shear layer and turbulent flow field. For the sake brevity the bending moment and the thrust have not been plotted but they would show the same result i.e. shear is not as significant to rotor fatigue as the turbulence. In the proceeding sections all fatigue calculations take account of the shear layer profile.

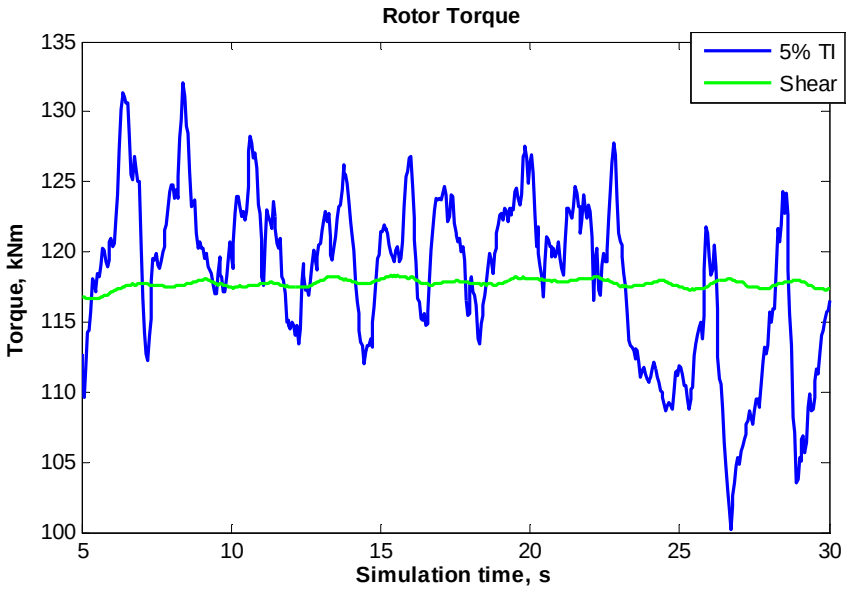

Figure 165 - Rotor torque loads; shear layer flow

5.3.3 Turbine Operability

This section examines the turbine system operation in turbulent flow from the perspective of the effectiveness of the control over rotor loading. As noted previously both thrust and power must be limited to the hard thresholds defined by nature of the device hardware. The turbine thrust is limited by the rock foot holding capacity which is dependent upon the available sea bed friction and the total weight of the device. Based on geological surveys of the tidal channel site the working coefficient of friction has been estimated at 0.38 and with a device weight of 67T the maximum allow rotor thrust load is therefore 25T (245,250N). The power is limited to the on-board generating capacity of the electrical equipment selected to convert the shaft power to grid quality electricity which for the Deltastream prototype is limited to 400kW electrical power output. Given system losses of 8% the maximum allowable rotor power the device can handle is therefore 434kW.

Over-loading of the turbine with respect to power and thrust will have potentially dangerous and costly consequences. Excess thrust load will result in device instability and potentially allow movement of the turbine frame which could put strain on power and control cables, alter the turbine alignment with respect to the flow direction or damage support equipment near the device. Within limits managing excess power is likely to be less problematic as the electrical equipment will be rated to handle temporary loads above maximum continuous rating through heat rejection. However, the objective of designing the control system is to maintain power and thrust below these thresholds.

In order to assess the control system performance over the full turbine operating envelope the load data from the hydrodynamic model for the Ebb tide duty cycle is plotted in terms of power, thrust and flap-wise bending moment versus tidal velocity in Figure 166-Figure 168 below. Each plot shows all the data generated from running simulations E1-E7 (see Table 9) in order to represent a full Ebb tidal cycle. The design intent load is over-laid on the simulation data to show the idealised performance. This allows for quantification of the controller performance over the rotor behaviour in turbulent conditions and demonstrates it capability to perform disturbance rejection in these conditions.

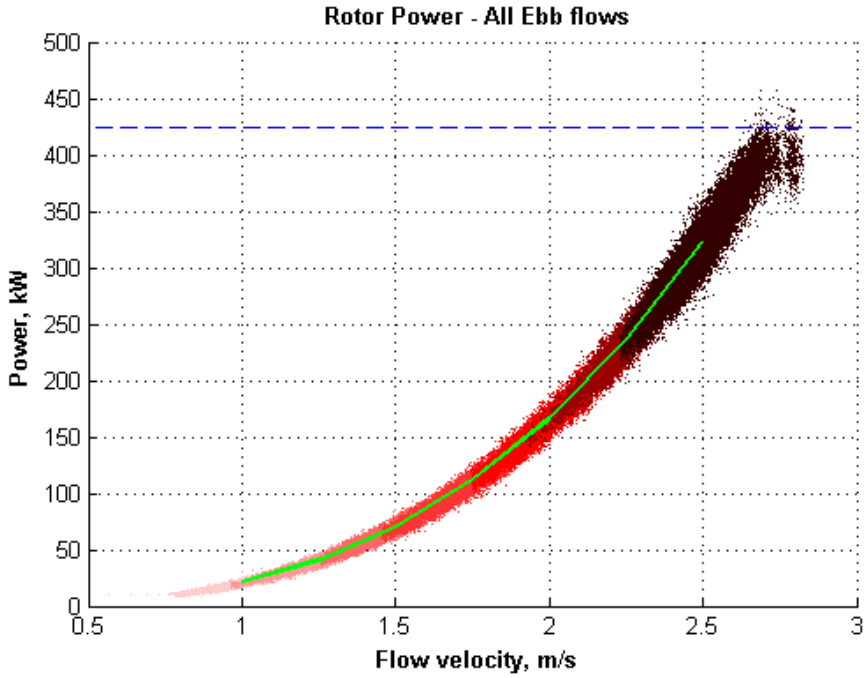

Figure 166 - Rotor power: 1.0-2.5m/s Ebb flow

Overall the rotor power simulation data follows the design intent closely for the entire flow range. The scatter in the data is a result of the turbulent load fluctuations where the controller is unable to maintain a steady value which is also reflected in the thrust and bending moment data. This is driving the cyclic fatigue loading which will be discussed in the following section. These plots also provide a clear demonstration of the greater level of unsteadiness when comparing the blade loads to the rotor loads. The deviation from the mean bending load is much greater for the bending moment than for the thrust and power loads which was explored in detail in previous sections.

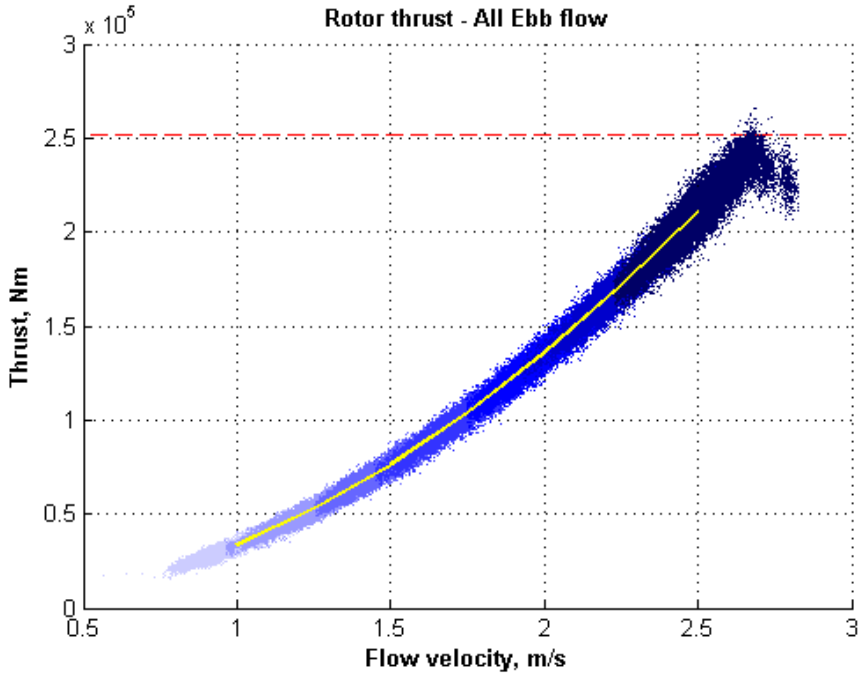

Figure 167 - Rotor thrust: 1.0-2.5m/s Ebb flow

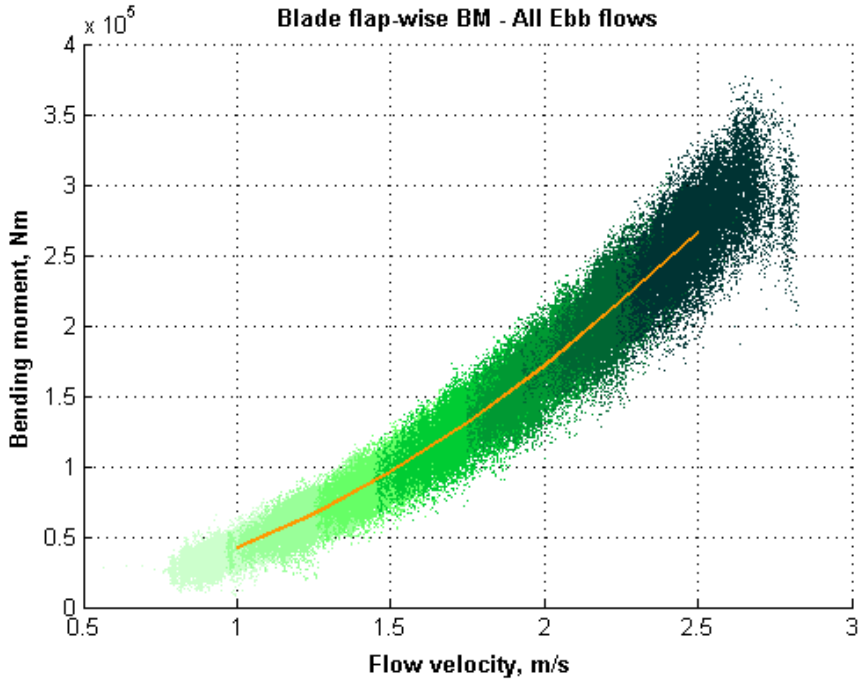

Figure 168 - Blade flap-wise bending moment: 1.0-2.5m/s Ebb flow

In terms of assessing the potential for turbine over-load Figure 166-Figure 168 shows how the device loads can exceed the hard limits when operating within the 2.5m/s speed bin as the limit is exceeded for several data points in both cases. Table 11 below specifies the over-shoot in terms of maximum load and occurrence. This shows the overshoot is around 5.5% in both cases but the occurrence of the thrust overload is four times higher than for power. In terms of annual duration the power will be at some level of overload for around 120s and the thrust 480s.

	Max. overload	Percentage overload	Occurrence
Power	456.95 kW	5.2%	120s/year (0.4%)
Thrust	265.51 kN	5.5%	480s/year (1.6%)

Table 11 - Operability in Ebb

This is unlikely to have a particularly adverse effect on turbine operability as the occurrence is low. Furthermore, when considering the thrust overload it is improbable that all three turbine rotors will be overloaded together so the total load on the device will not peak above the design load. However these results are for Ebb turbulence at 2.5m/s which is considerably lower than the Flood flow. Therefore a set of simulations were run to quantify the effect of turbulence intensity on the parameters affecting operability the results of which are shown in Figure 169 and Table 12 below. These cases were all run at a mean flow velocity of 2.5m/s, where the turbine is moving in and out of the load shedding regime, for three values of turbulence from 3.5-11%. Figure 169 shows the results in terms of thrust for the highest turbulence case with the control curve and the threshold overlaid on the simulation data. This shows the maximum overload reaches 21.1% above the load limit and the rotor was at some level of overload for 4.83% of the simulation.

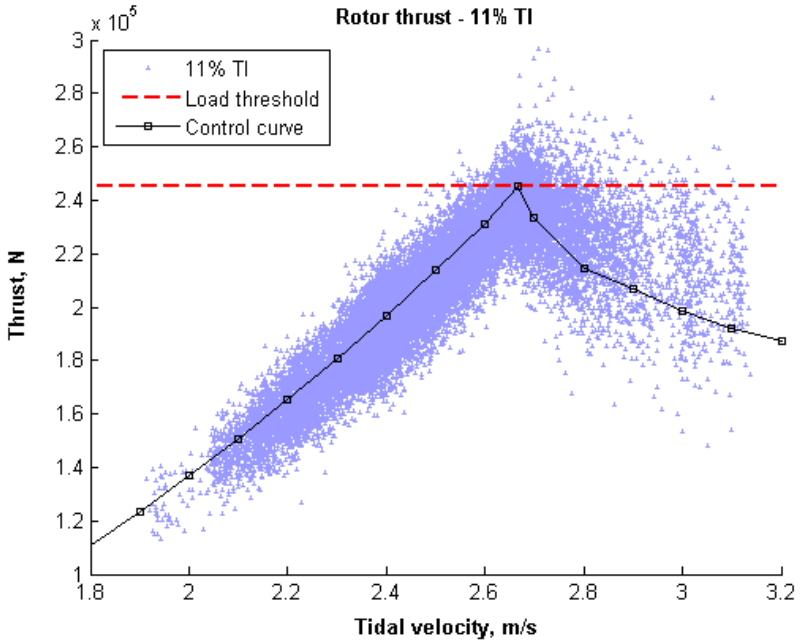

Figure 169 - Rotor thrust showing overload

Table 12 shows the results for overload of power are approximately half the level of thrust which is similar to the previous case for the Ebb flow. Furthermore it is evident that the peak thrust overload occurs around the load shedding velocity of 2.67m/s. For higher flows the trend is for the overload to reduce towards the threshold again. It is very unlikely that the device will be able to operate in flows where the overload peak values are higher than 20% of the threshold loads particularly as the occurrence is relatively high, almost 5% for thrust, at this particular flow. Therefore an understanding of how to improve control at this critical point is required.

TI, %	Power; overload	Thrust; overload	Power; occurrence	Thrust; occurrence
3.5	0.0%	2.1%	0.00%	0.12%
7	5.6%	9.4%	0.46%	2.12%
11	17.0%	21.1%	2.44%	4.83%

Table 12 - Overload vs turbulence

When the estimated flow velocity (used to define the rotor speed) is plotted against the mean tidal velocity for the entire simulation, as shown in Figure 170 below, a slight bias towards underestimating the velocity can be observed. This shows data for the 7 and 11% turbulence simulations and both reveal that, particularly at the higher flows, the velocity estimation algorithm prediction is slightly below the inflow velocity to the rotor plane by approximately 1% when averaged over the simulation. However this is not sufficient to account for the very large deviations in load above the threshold observed in the high turbulence case.

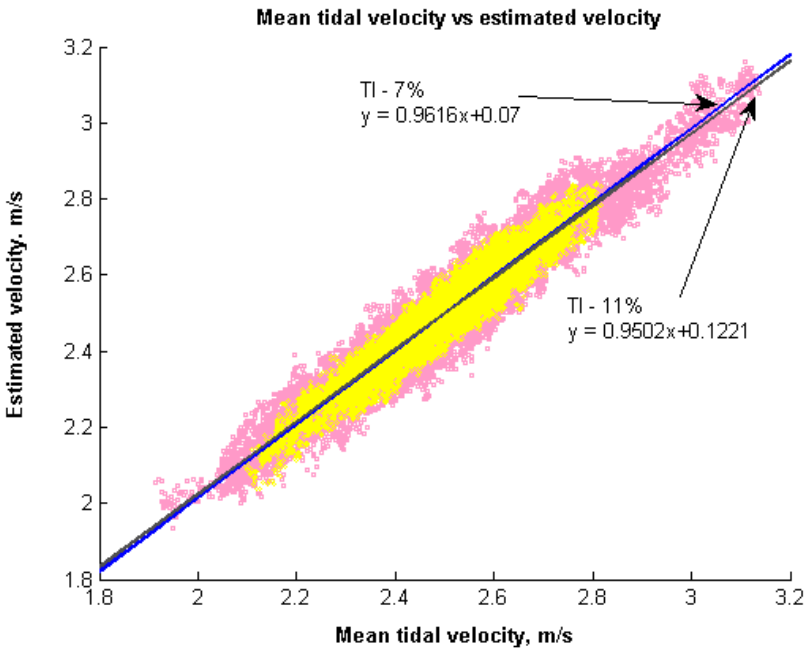

Figure 170 - Mean velocity vs estimated velocity

Furthermore, when the mechanical response of the turbine is examined, as in Figure 171 below, the rotor speed matches very closely to the control set point. This shows the rotor RPM response to tidal velocity with the control curve overlaid above the simulation data. It is evident that the simulation data fits extremely closely with the design curve. This is evidence that the control system tuning was successful at matching the mechanical system model with an effective control gain such that the turbine speed quickly matches the set point. Therefore it must be concluded that the overloads are caused by the inherent unsteadiness of the hydrodynamic response to the combination of rapid changes of the inflow conditions and the constantly fluctuating rotor speed. This phenomenon is described in Chapters 2 and 3 and the validation of the hydrodynamic model in relation to high frequency load changes is detailed in Chapter 4.

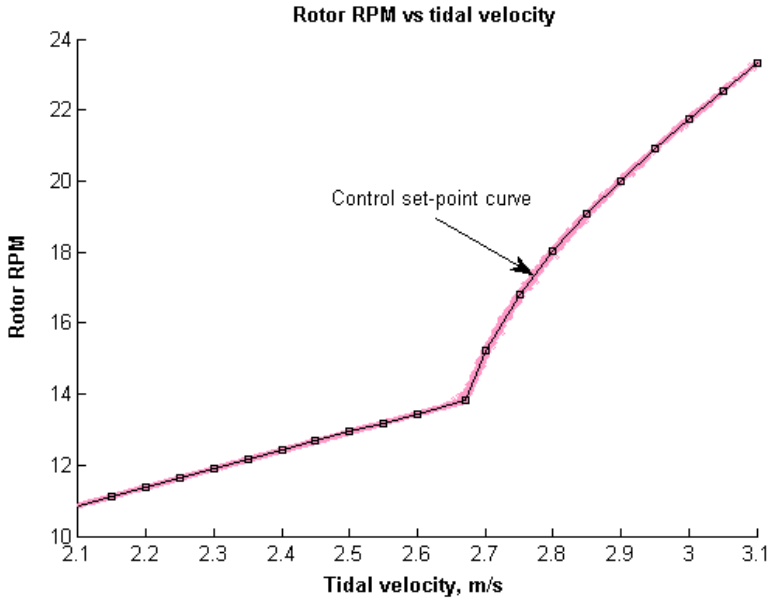

Figure 171 - Rotor RPM data

In summary the turbine performance is well matched with the design aims for the majority of its operating envelope. The turbine rotor response to the control inputs is rapid enough to ensure that the turbine operates very closely to the pre-defined RPM demand curve. However at medium and high levels of

turbulence the turbine experiences over-shoots in load directly around the rated tidal velocity where the load shedding mode initiates. This leads to a potential failure mode as it is possible for the thrust load to considerably exceed its limit. This is down to the fundamental unsteadiness of the flow regime and the interaction of the turbine to rapid load fluctuation being non-linear. In order to investigate corrections to this weakness a series of measures are considered later in this chapter that aim to address the load over-shoots to improve turbine operability as the turbine will not be able to operate at rated power without this problem being solved.

5.4 Turbine blade fatigue life

The proceeding section covers the analysis of the turbine simulations used to establish blade life when operating in both Flood and Ebb tides. Several factors are involved in predicting the fatigue life including the blade material properties, blade loading and resultant stress distribution as well as the number of load cycles for each stress bin under consideration. The methodology outlined in Ch3 is used to determine fatigue life but there are a number of assumptions in its application that must be justified before the results are presented.

All material data has been sourced from the blade manufacturer, Designcraft Ltd of Southampton, including the S-N curve. The S-N curve for the composite blades is shown in Figure 172 where the manufacturer's data is in red labelled 'New'. The other curves are the stress life predictions formulated to model stress degradation because of water diffusion into the blades over time as the blades are constantly immersed in sea water. The manufacturers S-N curve is their stress-life prediction based upon the blade layup design (+/- 45 degree) and volume fraction and tensile testing of sample material coupons to facture. The alternating stress is given in terms of the flexural strength which is equivalent to the tensile stress of the outer composite fibres. It is well known that the material flexural strength tends to exceed the tensile strength by a considerable margin as discussed in greater detail in Chapter 2.

The stress ratio, R, for both sets of simulations is plotted in Figure 173 which shows the mean of all the Flood tide simulations is just below R = 0.5. Meanwhile the Ebb simulations have an average of around R = 0.65. The lower the value of stress ratio the more damaging the effect of the load reversals is on components. The datum curve in Figure 172 (from the manufacturer) is based upon a stress ratio of R = 0.5 as this is the only data available for the material from which the blade is manufactured. It must be remembered that the S-N curve for composites is a function of the material properties and the specific layup orientation which is particular to this manufacturer. Therefore using this data will mean the results of this analysis are conservative for the Ebb tide simulations as the stress ratio is higher at around R = 0.65 (i.e. less aggressive than the conditions in which the material data has been provided). However, the S-N curve data matches closely with the Flood tide data which also has a mean R value of 0.5.

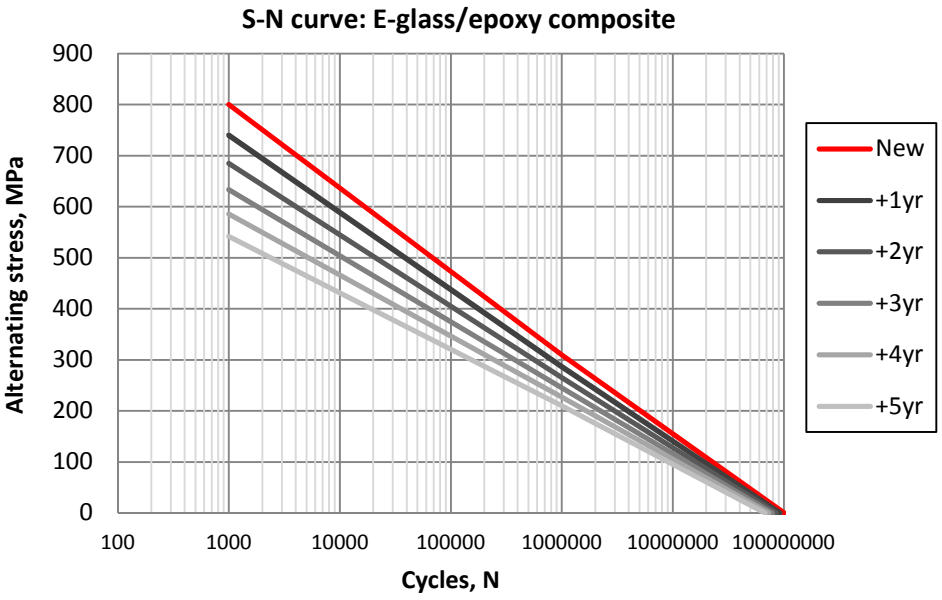

Figure 172 - S-N curve showing predicted degradation effect of water immersion

As there is no specific experimental data available for the effects of water diffusion therefore an approach based upon literature sources has been applied in order to account for the reduction in strength of the blades as they age in the

saltwater environment. Based on the discussion from the sources detailed in Chapter 2 (Section 2.3.2 & 2.3.3) it has been assumed that the glass/epoxy matrix will uptake water at a rate of 0.5% of total component weight per annum when immersed in sea water. For both glass and carbon composites it has been found that water diffusion will cease after weight gains of between 1 and 5% of total weight. Therefore it has been assumed that equilibrium will occur after five years of immersion (i.e. after 2.5% weight increase at 0.5% per year). Furthermore, degradation in flexural strength has been found to advance in proportion with the water diffusion until saturation is reached where the strength reduction is approximately 50-75% of the 'as new' condition. Therefore, in this study, the degradation rate of 7.5% per year has been assumed and applied to the S-N curve (i.e. a reduction in flexural strength of 7.5% per year). The fatigue life is then calculated for each year using a modified S-N curve (Figure 172) from which the cumulative blade damage is determined. The effect of this is a reduction in component life even though the alternating stress and annual stress cycles remain constant.

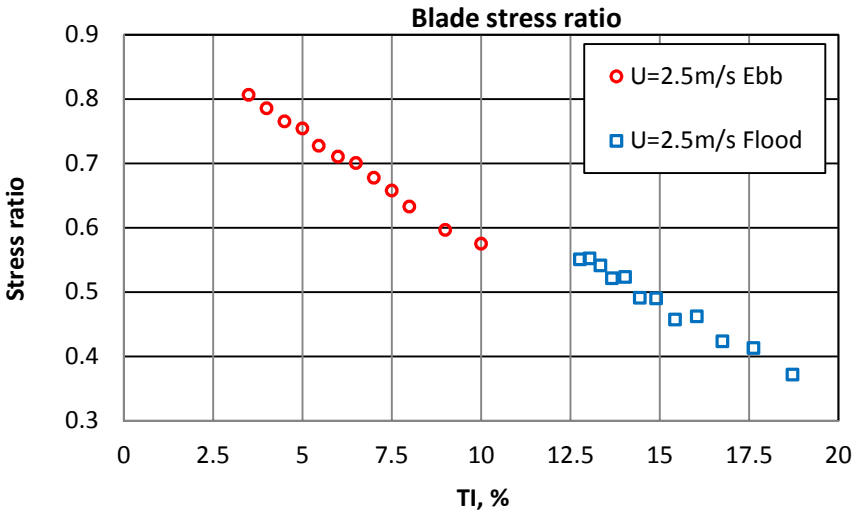

Figure 173 - Stress ratio; Ebb and Flood simulations

The blade stress is derived using the finite element model described in Chapter 3 using the loads calculated by the hydrodynamic model as inputs. As the bending stress caused by the turbulence fluctuations is relatively small compared to the ultimate tensile strength of the material all deformations are

assumed to be linearly elastic and therefore the following relationship between bending moment and stress can be applied:

$$\sigma_i = \sigma_{ref}\left(\frac{BM_i}{BM_{ref}}\right)$$

Equation 90 [114]

Where σ_i is the stress at time i, σ_{ref} is the reference stress calculated from the finite element model (see Chapter 3) using the reference load BM_{ref}. Therefore for any load BM_i generated by the hydrodynamic code the blade stress distribution can be quickly calculated. Figure 174 below shows a typical normalised bending load distribution along the blade span (labelled 'BM') which is the result of averaging over an entire simulation. This is shown alongside the resultant stress distribution ('Sigma') calculated using the 1D beam model. The stress distribution has been normalised with respect to the blade root stress (i.e. at 0% span) and this shows that the peak stress is not found at the peak bending moment (at the first blade node) but rather at 2.7m along the blade (45% of the blade span) which is in the spar cap. The peak stress is used as the limiting stress in the subsequent fatigue life calculations as this will determine where failure occurs.

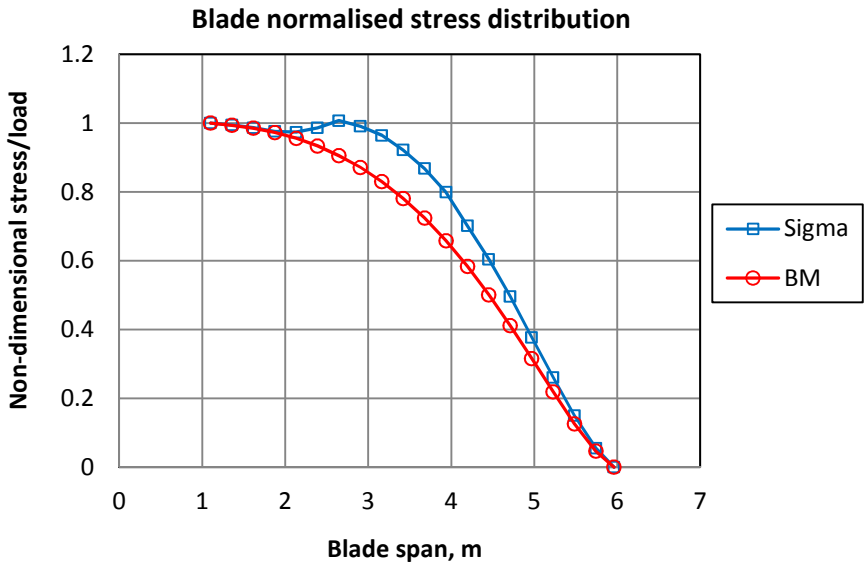

Figure 174 - Blade stress distribution

The following details the results of the fatigue analysis dealing with the Ebb and Flood tides separately in order to compare the damage severity of each tide. Table 13 below lists the simulation cases (E1-8) run in order to determine the annual fatigue damage caused by the Ebb tide. The turbulence level, mean flow velocity and number of cycles are listed as the inputs to the hydrodynamic model.

Case	TI, %	U bin, m/s	Cycles, n_i	Root BM, kNm	Alternating stress, MPa
E1	11.296	1.00	304198	10.987	28.7
E2	9.462	1.25	823079	14.524	37.9
E3	8.187	1.50	1054451	18.695	48.8
E4	7.244	1.75	1488748	22.809	59.6
E5	6.515	2.00	1371166	28.360	74.1
E6	5.933	2.25	318611	33.515	87.5
E7	5.457	2.50	5234	39.860	104.1

Table 13 - Stress amplitude and cycles for fatigue life calculation: Ebb tide

The root bending moment is the result of the hydrodynamic simulation listed in terms of the mean of the root flap-wise bending moment DEL. This is then converted to a stress value using the finite element model and the peak blade stress, in MPa, is used in the fatigue life model. The damage fraction is calculated in line with the Palmgren-Miner rule which defines failure as when the cumulative damage equals the damage limit when D = 1.

$$\sum_{i=1}^{N} D_i = D$$

Equation 91

Where the cumulative damage from each set of alternating stresses is defined as:

$$D_i = \sum \frac{n_i}{N_i} = \left(\frac{n_1}{N_1} + \frac{n_2}{N_2} + \cdots + \frac{n_i}{N_i}\right)$$

Equation 92

Using the alternating stress calculated from the FE model the number of allowable cycles, Ni, can be extracted from the S-N curve. The damage fraction is then determined as the ratio of stress cycles, n_i, to allowable cycles which are shown in Figure 175 below for 6 successive years. Here the damage fraction is plotted for each flow bin for 6 sets of annual cycles. This reveals two aspects of how the fatigue life of the blade progresses; firstly the increase in annual damage due to strength degradation is evident as the damage fraction almost doubles between year 1 and year 6 and secondly the distribution of damage versus flow velocity is revealed. This shows that the 2m/s flow bin causes the greatest damage fraction and is followed closely by the 1.75m/s bin. This ties in well with the energy absorption apportioned to these flow velocities as shown in the energy distribution plot in Figure 150. It is also interesting that the 2.5m/s flow bin contributes virtually nothing to the fatigue damage with an alternating stress that is almost 15% of the tensile strength because of the very low duration spent operating in this flow.

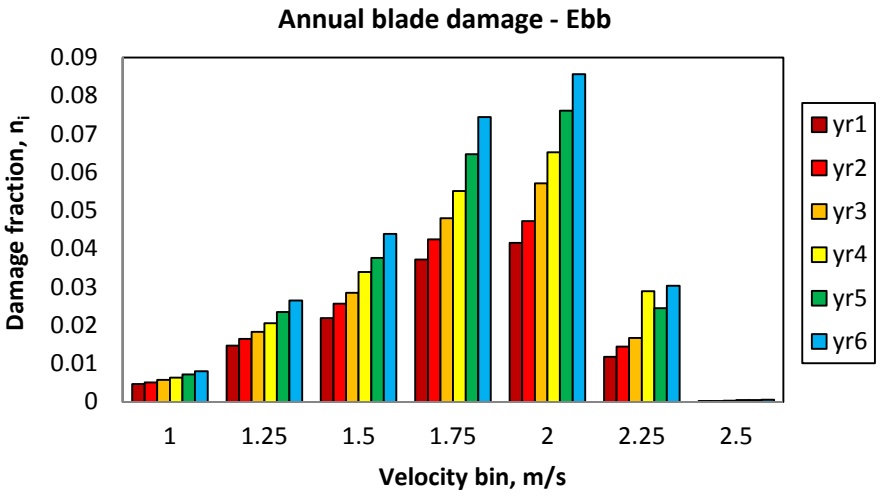

Figure 175 - Annual damage for all velocity bins: Ebb

The total damage for each set of annual cycles is then summed and the result plotted in Figure 176 below which shows the cumulative damage versus

duration in years. It also shows when the predicted damage crosses the damage limit, at D=1, at which point the blade is assumed to fail at the most highly stressed point span-wise. From this analysis failure can be expected after approximately 5.3 years assuming the turbine runs for the prescribed duty cycle in all Ebb flows above 1m/s which equates to operational life of 15,600 hours.

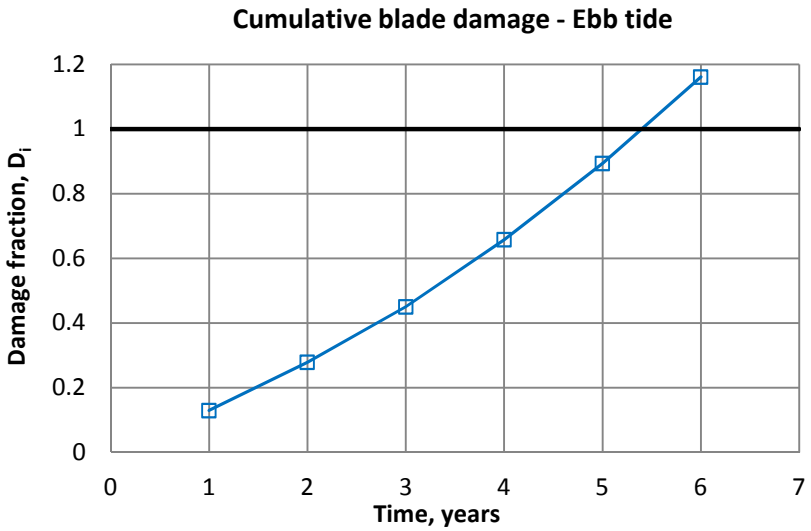

Figure 176 - Cumulative damage indicating time to failure: Ebb

This process is repeated for the Flood tide using the simulations detailed in Table 14 below as the inputs to the fatigue life model. All the assumptions previously applied to the analysis of the Ebb tide are valid in this case. As discussed previously the cyclic load amplitude for the Flood tide is significantly higher than the Ebb tide due to the much greater level of turbulence across all flow velocities and so it is expected that the fatigue damage caused by the Flood tide will advance at a much higher rate. Furthermore the flow range in Flood is more extensive leading to yet further increases in fatigue load assuming the turbine is allowed to operate in this region.

Case	TI, %	U bin, m/s	Cycles, n_i	Root BM, kNm	Alternating stress, MPa
F1	18.72	1.0	194412	21.912	57.224
F2	17.63	1.2	335070	28.859	75.365
F3	16.76	1.4	490062	38.386	100.245
F4	16.04	1.6	663869	45.745	119.464
F5	15.43	1.8	750772	58.558	152.925
F6	14.90	2.0	702393	66.651	174.061
F7	14.44	2.2	636095	80.373	209.897
F8	14.04	2.4	576070	88.140	230.180
F9	13.67	2.6	469456	103.853	271.216
F10	13.34	2.8	319840	114.250	298.368
F11	13.04	3.0	198892	127.219	332.237
F12	12.77	3.2	5555	145.176	379.131

Table 14 - Stress amplitude and cycles for fatigue life calculation: Flood tide

Figure 177 below shows the predicted annual damage fraction for the Flood tide for three consecutive years. This shows higher magnitudes than for the Ebb tide across all flows for all years which is to be expected given the turbulence level. In the case of the 2m/s flow bin which is the most damaging case of the Ebb tide the damage fraction is 2.25 times higher in Flood and is one of the more benign cases for this tide.

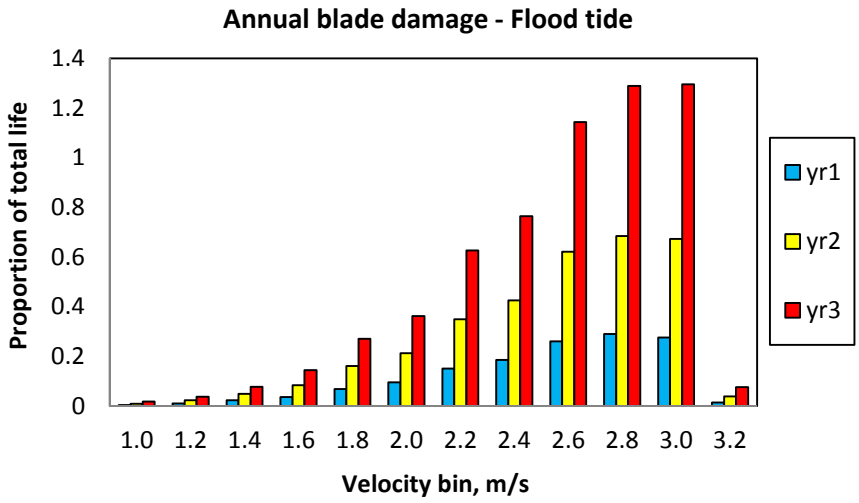

Figure 177 - Annual damage for all velocity bins: Flood

What the cumulative damage fraction shown in Figure 178 below demonstrates is the dramatic reduction in blade life when compared to the Ebb tide. If the full range of Flood flow was utilised to generate power the life is significantly less than one year. However, a more appropriate comparison is when the turbine operation is limited to flows of up to 2.4m/s which is close to the peak flow in the Ebb tide. Even in this scenario the predicted fatigue life is only just over 1.5 years or around 4,700 hours of operating time which is around 30% of the Ebb tide life for the same range of mean flow velocities.

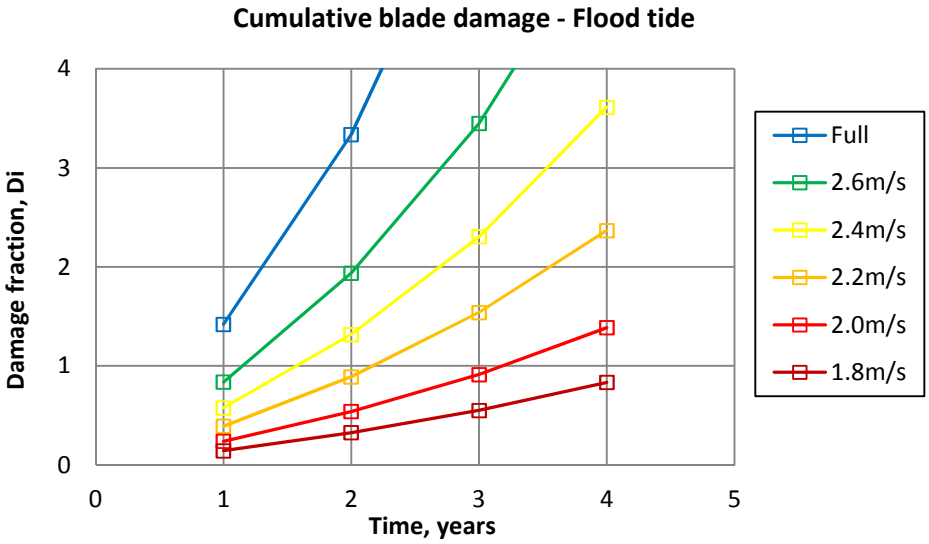

Figure 178 - Cumulative damage indicating time to failure: Flood

A comparable life could be achieved if the operation in the Flood tide was limited to operating the turbine from 1-1.7m/s. This will have a significant impact on the energy capture however reducing the potential energy available from 10,264MWhrs down to 3,356MWhrs. This reduction would mean the Flood tide would yield approximately 70% of the Ebb tide for equivalent fatigue damage.

This is more clearly demonstrated in Figure 179 below which directly compares both damage fraction distributions against flow for both tides. The damage is equivalent in flows of 1-1.7m/s but as flow increases the damage rapidly diverges as the Ebb data plateaus at 1.75m/s while the Flood data continues to increase until 2.8m/s. The higher damage rate observed for the Flood tide is mainly due to higher turbulence intensity across all flows but also to a lesser extent because the flow probability is more evenly distributed than the Ebb tide and so a greater proportion of stress cycles occur at higher flows even through the total cycles for both tides is similar. This analysis suggests that the turbine operation in Flood will have to be severely restricted in order to maintain service life beyond a few months.

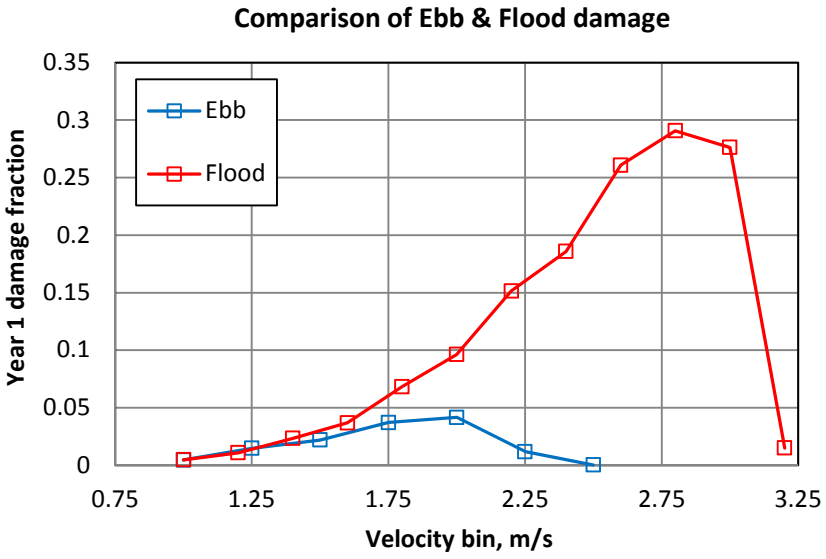

Figure 179 - Comparison of damage fraction distribution

5.5 Improving Turbine Operability

As discussed in the section covering turbine operability there are areas of the operating envelope where the turbine load breaks the design thresholds. Figure 169 shows the turbine thrust exceeding the load limit when the turbulence intensity of the flow is 11%. The importance of regulating thrust and power below the design limits has been discussed extensively in previous chapters. Figure 180- Figure 182 below highlight the area of the operating envelope where the turbine is susceptible to overload which is slightly different for thrust than power. Simulations were run to investigate the response of the turbine running in three tidal velocities; 1) 2.5m/s just below rated, 2) 2.7m/s at rated and 3) 2.9m/s just above rated speed. Figure 180 shows how the turbine RPM reacts to tidal velocity as the turbine controller switches between the two operating modes; full power and load shedding. This shows the turbine behaves as planned with the RPM data tracking closely to the control intent over the entire operating envelope. Figure 181 shows the turbine rotor power characteristic in response to the three flow velocities with the power threshold overlaid in red. The overshoots in power plateaus as the flow velocity increases beyond rated i.e. the overshoot at 2.8m/s is the same as for 3.2m/s.

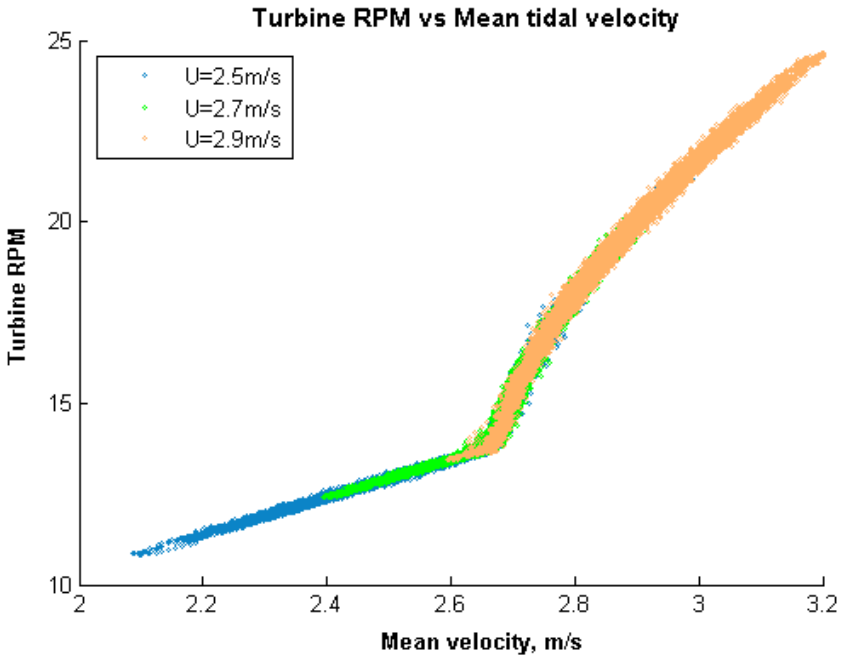

Figure 180 - Turbine RPM response simulation data

Figure 182 demonstrates the thrust loading characteristic which is also subject to over load but for a less extensive flow range. The characteristic peaks at the rated flow velocity and then diminishes again as flow velocity increases. This is more clearly shown in the comparison between the three flows in Figure 183 below. This is driven by the design of the rotor; the thrust load will drop off more quickly than the power load as the TSR is increased. This was a fundamental element in the design of the improved rotor dictated by the gravity stabilised frame.

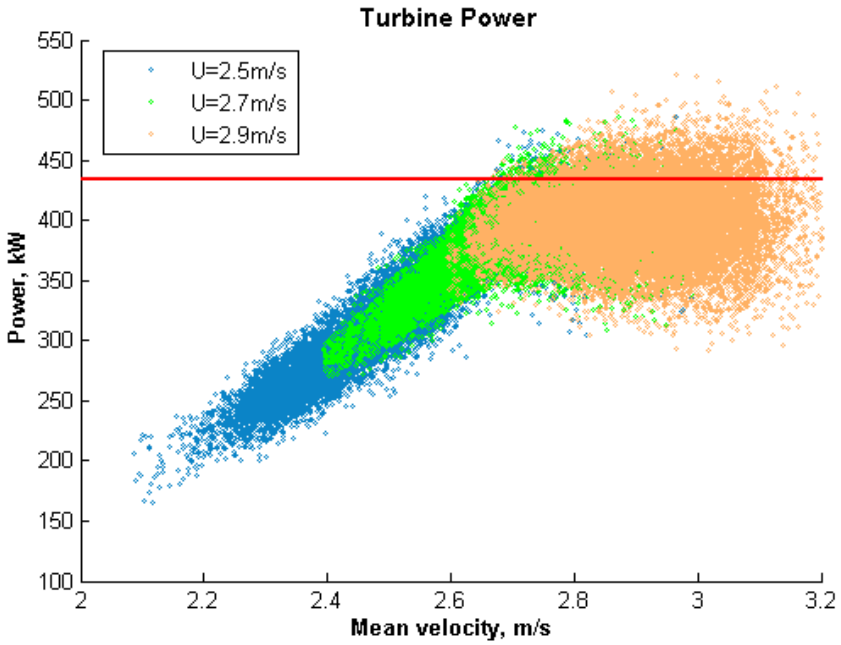

Figure 181 - Turbine power response vs tidal flow simulation data

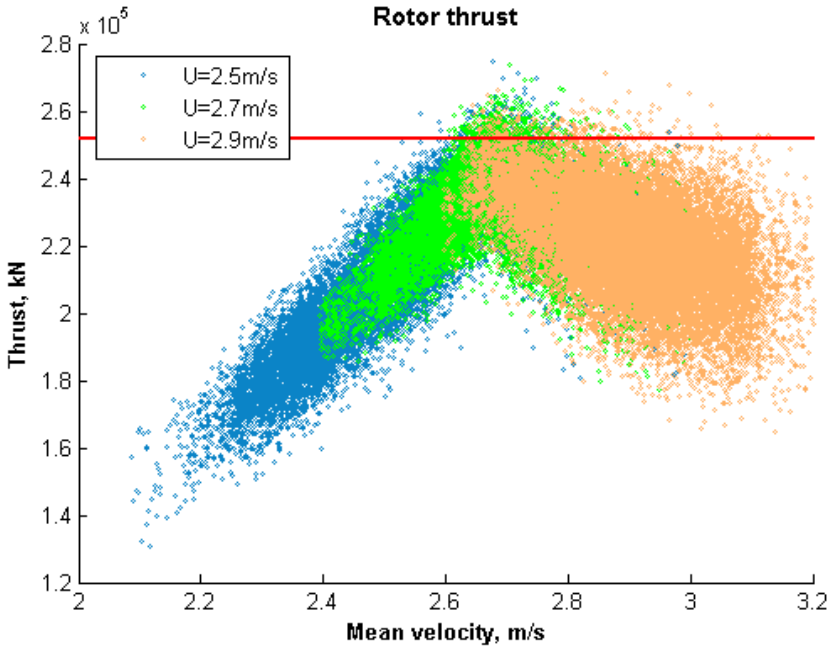

Figure 182 - Turbine thrust response simulation data

It is crucial that the turbine can operate in high velocity flows that are above the rated flow although not necessarily to extract power from these flows but because of limitations of the device yaw system. The yaw system can only manoeuvre the nacelle into the parked position in periods of slack water because to do so otherwise would require an extremely powerful drive system and would subject the turbine to yawed flow. Therefore if the peak flow of a particular tide is greater than the turbine cut out velocity the entire tide will have to be abandoned and no energy harvested. As most of the energy is captured at the lower flows (1.5-2.0m/s), but which may briefly peak at much higher velocities, this would have a harmful effect on the commercial viability of the device. This means it is important for the turbine to be able to continue operation at high flows even if the power output is not maximised in order to be able to absorb power from the flows.

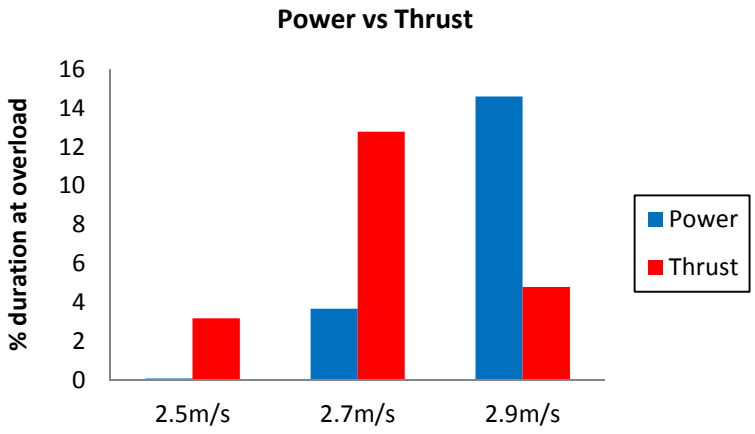

Figure 183 - Power vs Thrust

To this end two revisions to the turbine control methodology were considered to establish their effectiveness at improving turbine operability in higher flows. Improvements in operability were defined in terms of power and thrust duration spent at overload. The first modification was aimed at reducing the necessity for a large rate of change of rotor RPM when the turbine first enters the load shedding mode as this is considered a key mechanism causing over-loads. It has been demonstrated that the reduced frequency, in terms of blade-flow interaction, increases with rapid changes in blade lifting load. The physical phenomenon which drives the unsteadiness is the blade trailing edge vorticity running in a transient, non-equilibrium state. Therefore the load shedding tidal velocity demand curve was modified as shown in Figure 184 below. The rated flow was reduced from 2.67m/s (as per the datum curve) down to 2.45m/s 'mod 2' in order to decrease the gradient at this sensitive point on the curve. Therefore the turbine will switch from mode 1 to mode 2 earlier, at lower tidal velocities, and the rate of change of RPM will decrease.

The second modification is a preliminary investigation of the potential benefits of utilising rotor blades that incorporate a pitching mechanism so that blade pitch angle can be increased to shift the turbine onto a new operating curve as described in Chapter 4. Small increases in pitch angle will substantially reduce both C_p and C_T.

These two modifications were also compared with the effect of derating the turbine to 75% of maximum power as a means of benchmarking performance. This is a different approach to softening the transition to load shedding as the de-rated curve shown in green in figure will never allow the mean turbine power to rise above 325kW whereas the modified demand curve will.

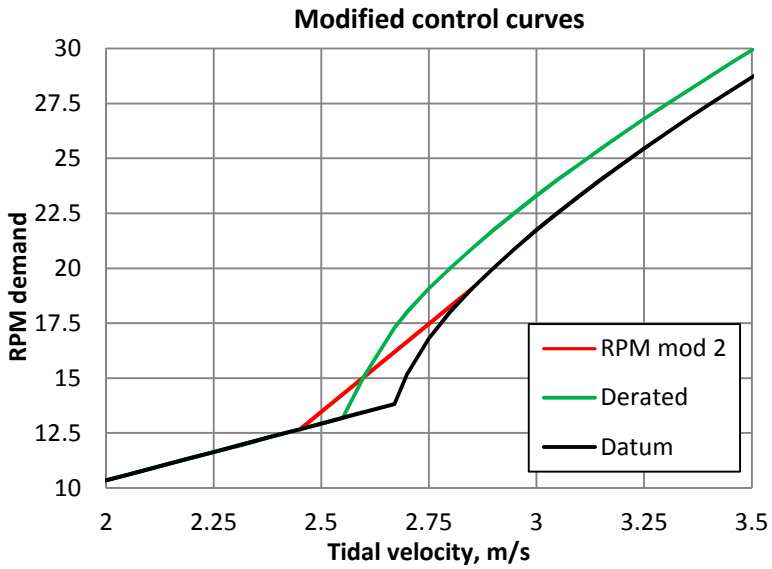

Figure 184 - Modified control curves

Simulations were run in flow conditions representative of the Ebb tide at a mean flow of 2.5m/s and turbulence intensities of 5% and 11% to compare typical low and high turbulence flow. In the 5% TI simulation the pitch angle is increased by only one degree, estimated from the steady state performance curves, shown in in Chapter 4. In this relatively benign flow state both the modified RPM control and the increased pitch show similar levels of improvement in reducing the overloads as shown in Figure 185. The pitch control simulation shows reduced power and thrust for all flow velocities by approximately 6% and 9% respectively.

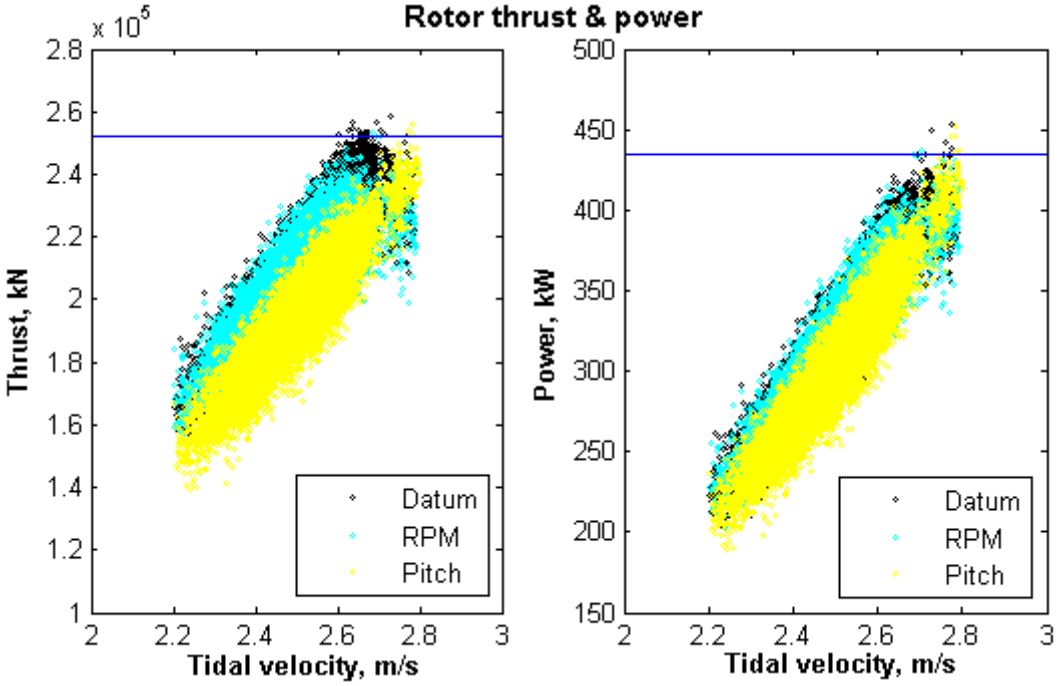

Figure 185 - Rotor thrust and power; TI = 5%

The simulations were repeated with the higher turbulence intensity of 11% to represent the upper end of what can be expected from boundary layer turbulence which is a marked contrast to the 5% TI simulation of Figure 186. A second pitch angle of 2.5 degrees was also included to complement the 1 degree pitch simulation which had shown significant load over-shoots above the thresholds. The results of the two simulations are compared in Figure 187 which contrast the differences in the low and high turbulence flow and shows the progression in overload reduction for the two methods.

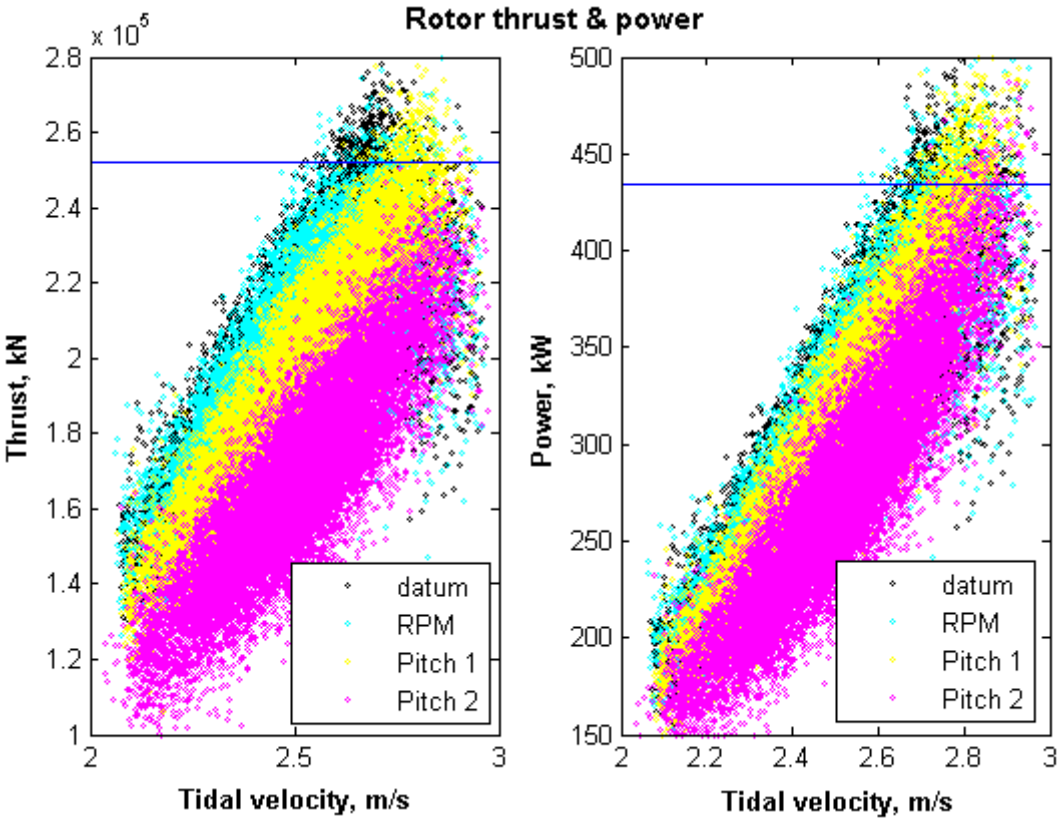

Figure 186 - Rotor thrust and power; TI = 11%

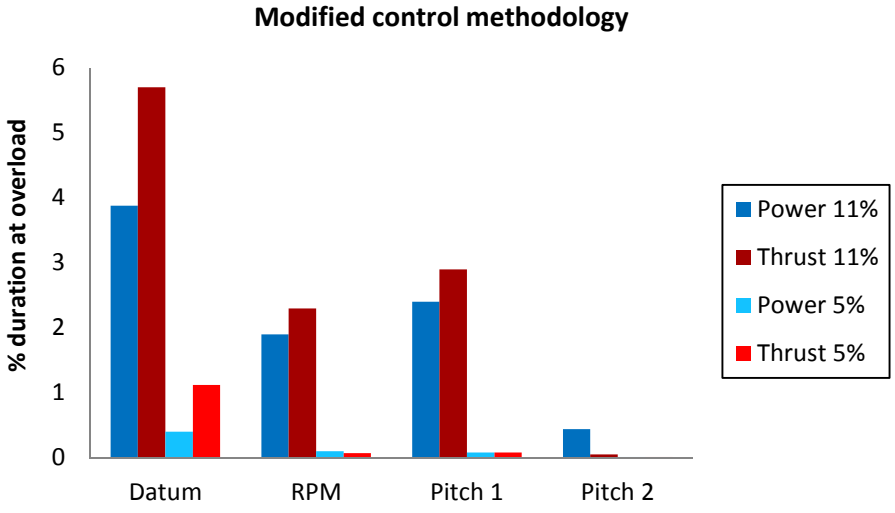

Figure 187 - Modified control methodology

Although this level of turbulence would be unusual on an Ebb tide in Ramsey Sound, flows of up to 11% TI and higher have been found to be common in literature and on the Flood tide. Therefore a mechanism to protect the Deltastream when running in all flows is sought. A set of simulations were run combining the de-rated RPM control with pitch regulation and the results are shown in Figure 188 below.

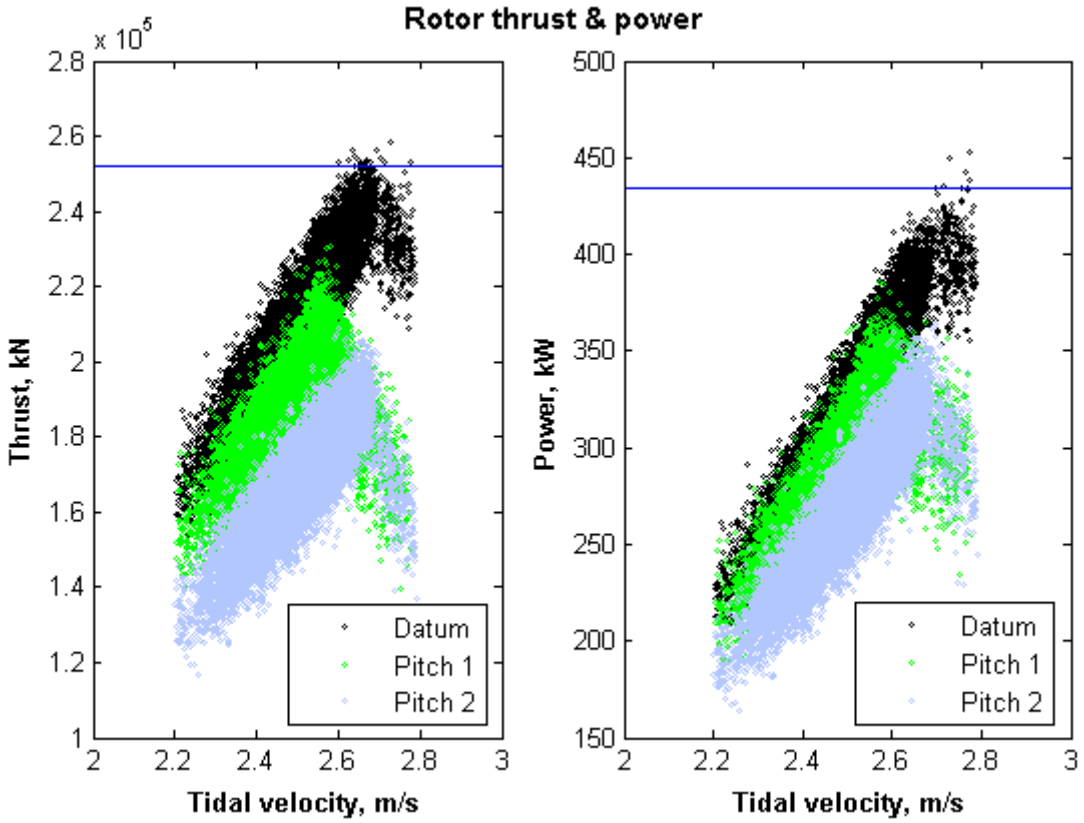

Figure 188 - Rotor thrust and power; combined pitch and speed control

This shows a radical reduction in the overload behaviour for the two modified control strategies in comparison to the datum simulation results. There is no overloading in either of the two cases where pitch control is introduced. This shows that the combination of using a de-rated RPM strategy and pitch control could be used to run the turbine effectively in high turbulence flows. Furthermore in both cases the turbine is still making considerable power and

there is also a reduction in DEL in terms of the flap-wise bending load. When the DELs for blade bending are compared to the datum case there is a 9.1% and a 15.3% reduction for the 1 and 2.5 degree pitch cases respectively. As discussed previously any improvement in fatigue life will be very beneficial.

A techo-economic assessment has not been carried out as part of this study to compare a pitch regulated version of the Deltastream with the current fixed pitch machine. The reason for this is two-fold. Firstly the analysis of this work has been carried out on a prototype device which does not function in the same way nor will cost the same as a production device. Therefore the economic assumptions will not scale to the marketable systems. Secondly, when this work commenced the aim was to produce a low cost tidal turbine that necessarily sacrificed energy capture in return for a simplified design with the philosophy of reducing the cost per unit energy captured and the challenge was to ensure the turbine design could facilitate this in terms of power capture and load shedding performance. Therefore this work focused on developing and validating an accurate turbine model.

However in the course of this work it has been shown that pitch control is potentially promising and may be worth considering in more depth. The study has shown that the application of a theoretical pitch control system is more effective at reducing fatigue load (than the variable rotor speed method alone) and increases the turbines range of operability (i.e. the maximum flow in which it can successfully generate power safely). It has also quantified the magnitude of the reduction in power capture required to achieve these benefits (approximately 14%). This interplay between extended operability and fatigue life while reducing power capture means an assessment of the overall benefit is non-trivial. It will also depend greatly on the site specific flow characteristics in terms of flow speed and turbulence.

An additional benefit of pitch control that has not been considered here is that the turbine could be made to operate at higher power coefficients when running in low flow velocities, in the range 1.5-2m/s for instance. This is illustrated by Figure 134 which shows that the C_p can be increased by approximately 16% for

a reduction of 5 degrees of blade pitch i.e. from Cp = 0.36 to Cp = 0.42 (although at the penalty of an additional 34% thrust).

Further work in this area would need to focus on a quantitative assessment of the cost of producing electricity by the two methods discussed to determine whether the simplified fixed pitch approach is more effective than a complex variable pitch method. This may involve a re-design of the blade geometry to be better suited to a pitching control mode in terms of C_p/C_t ratio across the range of pitch control being considered as it is currently optimised for fixed pitch operation.

6 Conclusion

A number of noteworthy outcomes have arisen from the application of the modelling process to the Deltastream turbine:

- The effect of turbulence intensity has been quantified independently from flow velocity in terms of the fatigue loads. This allows for an empirical formulation of the DEL rotor and blade loads as a function of turbulence intensity. Given the mean turbine load for a particular flow velocity the DEL can be calculated for blade and rotor load respectively. This provides a means for attaining design loads more quickly than by simulation. This method can be applied to any turbine operating in turbulent flow once the turbine performance characteristic is known.

- This led onto the discovery that blade fatigue loading is considerably more aggressive than loading on the rotor overall for the same given flow and operating conditions. This is due to the natural averaging effect the rotor experiences being the sum total load of all three blades. It has been shown that an the Ebb tide in Ramsey Sound the blade fatigue load is approximately 1.9 times larger than the rotor load. The situation is very similar for the Flood tide where the blade fatigue load is 1.95 times larger than the rotor load.

- A control algorithm that estimates the mean inflow velocity to the turbine has been developed and successfully implemented within the authors model. This algorithm determines the set point for the control loop to compare the running speed with the desired speed. The algorithm is based on solving an empirical function defining the turbine power in terms of flow velocity. The algorithm relies only upon knowledge of the rotor speed and output power and does not require any flow sensing system. This makes for a robust, self-contained system that will not be susceptible to external systems failure which is critical given that the nature of the load shedding mechanism relies on accurately controlling the turbine speed in relation to the transient tidal velocity.

- During development of the turbine rotor speed control algorithm it was proven that by using the previously mentioned velocity estimation algorithm a reduction

in fatigue load (DEL) of 47% is possible as compared to operating the turbine with a fixed speed in turbulent flow. In maximum power mode it ensures the turbine is running at peak C_p so that maximum energy can be harvested. In load shedding mode the rotor TSR is increased to reduce the effective power coefficient of the rotor thereby reducing the load on the blades. Therefore the controller allows the turbine to operate at maximum power in conditions below the rated flow while reducing fatigue loads in high velocity flows above the machine rated power.

- It has also been proven that the fatigue loads can be further reduced by implementing a scheme of controller gain scheduling. It has been found that the ideal controller gain differs depending upon the operating mode. An additional 5% reduction in fatigue load can be achieved if a suitable gain schedule is implemented. The most suitable controller gain in maximum power mode is approximately twice the gain of the load shedding mode. This is due to the influence of the non-linear fluidic loading driving over-shoots in blade load when the rate of change of RPM is high. This is modelled using the dynamic inflow solver.

- Using the duty cycle determined from analysis of flow data from Ramsey Sound coupled with the hydrodynamic model the fatigue life of the turbine blades have been quantified. This study showed that the blade life in the Flood tide would be considerably shorter than for the Ebb tide. A method for determining fatigue life based on site specific flow conditions has been developed.

- When the operability of the turbine is considered in relation to the probability a given flow will cause a power or thrust over-load it was found that the existing design and control strategy will allow the turbine to operate in the Ebb tide. However, for highly turbulent flows (such as a Flood tide) the turbine must be artificially de-rated to prevent over-load of thrust and power. It was found that this could be achieved using de-rated RPM control curves. It was found that a significant increase in turbine operability could be achieved for a modest reduction in energy capture.

6.1 Further Work

There are several areas of research that naturally lead on from this work:

- A full techno-economic assessment of implementing variable pitch blades into the Deltastream tidal turbine design. This would explore the benefits of improved turbine performance at flows less than rated and reduced blade loads at high flows where the current design struggles for operability but also take account of the costs associated with the extra complexity that variable pitch would bring.

- Optimisation of the load shedding schedule across the full envelope of turbulent conditions to maximise operability and further reduce fatigue loads. This would likely involve iteration in blade designs with the objective of increasing the C_p/C_T of the rotor.

- Investigation of the Deltastream's potential at turbine locations worldwide. The areas of high tidal flow are well documented. These sites should be investigated using the turbine model to investigate the effectiveness of the Deltastream at each with the objective developing a suitable range of rotor sizes that will meet market demand. It should also rank the sites according to suitability for Deltastream operation taking account of both technical and economic considerations.

REFERENCES

[1] Kvenvolden, K "Organic geochemistry – A retrospective of its first 70 years"
Organic Geochemistry, 37:1, 2006
[2] O'Rourke, Boyle & Reynolds, "Tidal energy update 2009"
Applied Energy, 87(2010) 398-409
[3] David J. C. MacKay "Sustainable Energy – without the hot air"
UIT Cambridge, 2008 ISBN 978-0-9544529-3-3
[4] David J. C. MacKay "Sustainable Energy – without the hot air"
UIT Cambridge, 2008 ISBN 978-0-9544529-3-3
[5] Charney, J.G., "Carbon dioxide and climate: A scientific assessment", 1979
[6] Stocker, Qin, Plattner, Alexander, Allen, Bindoff, Breon, Church, Cubasch, Emori, Forster, Friedlingstein, Gillett, Gregory, Hartmann, Jansen, Kirtman, Knutti, Lemke, Marotzke, Mokhov, Ramaswamy, Randall, Rojas, Sabine, Talley,Vaughan & Xie, "Climate Change 2013: The physical Science Basis. Contribution of working group I to the fifth assessment report of the intergovernmental panel on climate change", Cambridge University Press, 2013
[7] The Renewables Obligation Order 2002, No. 914, DTI
[8] Energy from the Sun and Moon, I Bryden, Presentation, 2006
[9] Physics of Waves, William Elmore & Mark Heald, Couries Dover Publications, 1985
[10] Sustainable Tides, I Bryden, 2006
[11] Sustainable Tides, I Bryden, 2006
[12]NASA Goddard Space Flight Center, NASA JPL Scientific Visualization Studio, Television Production NASA-TV/GSFC
[13] Egbert & Ray, "Semi-diurnal and diurnal tidal dissipation from TOPEX/Poseidon altimetry"
Geophys. Res. Lett., 2003, 30(17), OCE 9-1 9-4
[14] Flather, " A tidal model of the north-west European continental shelf"
Memoires Societe Royale des Sciences de Liege, 1976, 10(6), 141-64
[15] Cartwright, Edden, Spencer & Vassie "The tides of the northeast Atlantic Ocean"
Philos. Trans. R. Soc. Lond. Ser. A, 1980, 298(1436), 87-139
[16] Black and Veatch Consulting Ltd. "UK, Europe and Global tidal stream energy resource assessment"
Technical Report 107799/D2200/03, Carbon Trust, London, 2005
[17] European Commission "The exploitation of tidal and marine currents. Wave energy. Project results."
Technical report EUR 16683 EN, Commission of the European Communities. Directorate-General for Science, Research and Development, 1996
[18] Bryden and Couch, "Tidal current energy extraction: hydrodynamic resource characteristics"
PIMechE, 220, M, J. Eng. Maritime Environment, 2006
[19] U.S. Energy Information Administration, http://tonto.eia.doe.gov, (URL accessed June 2010)
[20] Bryden & Couch, "Tidal current energy extraction: hydrodynamic resource characteristics"
PIMechE, 220, M, J. Eng. Maritime Environment, 2006
[21] Bryden & Couch, "Tidal current energy extraction: hydrodynamic resource characteristics"
PIMechE, 220, M, J. Eng. Maritime Environment, 2006
[22] Myers & Bahaj, "Power output performance characteristics of a horizontal axis marine current turbine"
Renewable Energy 31 (2006) 197-208
[23] Yang, Wang, Copping, "Array Optimisation for Tidal Energy Extraction in a Tidal Channel", Proc. 2nd Marine Energy Technology Symposium, Seattle, 2014
[24] Owen & Bryden, "Energy extraction implications of structurally significant velocity variation in tidal currents", 2007
[25] Black & Veatch, "Phase II, UK tidal stream energy resource assessment"
Carbon Trust, 2005
[26] I. Bryden "Intoduction to ocean energy and technological developments: Tidal currents"
Presentation 2008
[27] I. Bryden "Intoduction to ocean energy and technological developments: Tidal currents"
Presentation 2008
[28] I. Bryden "Intoduction to ocean energy and technological developments: Tidal currents"

Presentation 2008
[29] O'Rourke, Boyle & Reynolds, "Tidal energy update 2009"
Applied Energy 87(2010) 398-409
[30] 'Analysis of tidal stream power', Wiley-Blackwell, 2009
[31] O'Rourke, Boyle & Reynolds, "Tidal energy update 2009"
Applied Energy, 87(2010) 398-409
[32] O'Rourke, Boyle & Reynolds, "Tidal energy update 2009"
Applied Energy 87(2010) 398-409
[33] Tidal Energy Ltd, 2015
[34] http://www.tidalenergyltd.com/?page_id=650, accessed Jan 2017
[35] www.tidalenergyltd.com, June 2010
[36] Freeman, Teixeira, Trarieux, Ayre, "Design of a gravity stabilised fixed pitch tidal turbine of 400kW"
Proc. 8th European Wave & Tidal Energy Conf., Sweden, 2009
[37] McCann, "Tidal current turbine fatigue loading sensitivity to waves and turbulence – a parametric study"
Proc. 7th European Wave and Tidal Energy Conf., 2007
[38] Turner and Owen, "The effect of boundary conditions on performance prediction model results for tidal turbines", Proc. 8th European Wave and Tidal Energy Conf., 2009
[39] T. O'Doherty, Mason-Jones, D.M. O'Doherty, Byrne, Wang, "Experimental and computational analysis of a model horizontal axis tidal turbine"
Proc. 8th European Wave and Tidal Energy Conf., 2009
[40] Fuglsang & Madsen "Optimisation method for wind turbine rotors"
J. Wind Engineering and Industrial Aerodynamics, 80(1999) 191-206
[41] Molland, Bahaj, Chaplin and Batten, "Measurements and predictions of forces, pressures and cavitation on 2D sections suitable for marine current turbines", Proc. Instn. Mech. Engrs, Vol. 218 Part M: J. Engineering for the Maritime Environment
[42] Manwell, 'Wind Energy Explained: Theory, Design and Application', Wiley, 2009
[43] http://www.esru.strath.ac.uk/EandE/Web_sites/05-06/marine_renewables/technology/Froude.htm
Accessed June 2010
[44] [44] Hansen, M.O.L "Aerodynamics of wind turbines" Chapter 6
2nd Ed, Earthscan, 2008
[45] Stock, Gharakhari, Stone, 'Modelling Rotor Wakes with a Hybrid OVERFLOW Vortex Method on a GPU Cluster', AIAA 2010-4553
[46] J. G. Leishman, "Challenges in modelling the unsteady aerodynamics of wind turbines"
21st ASME Wind Energy Symp., Reno, NV, 2002
[47] J. G. Leishman, "Challenges in modelling the unsteady aerodynamics of wind turbines"
21st ASME Wind Energy Symp., Reno, NV, 2002
[48] Bagai and Leishman, "Rotor Free-Wake Modeling using a Psuedoimplicit relaxation algorithm"
J. Aircraft, Vol. 32, No. 6, 1995, pp 1276-1285
[49] Hansen, J.N. Sorensen, Vontsinas, N. Sorensen, Madsen, "State of the art in wind turbine aerodynamics and aeroelasticity"
Progress in Aerospace Sciences 42(2006) 285-330
[50] Menter, "Zonal two equation k-omega turbulence models for aerodynamic flows"
AIAA paper 932906, 1993
[51] Hansen, J.N. Sorensen, Vontsinas, N. Sorensen, Madsen, "State of the art in wind turbine aerodynamics and aeroelasticity"
Progress in Aerospace Sciences 42(2006) 285-330
Hansen, J.N. Sorensen, Vontsinas, N. Sorensen, Madsen, "State of the art in wind turbine aerodynamics and aeroelasticity"
Progress in Aerospace Sciences 42(2006) 285-330
[53] Sorenson, "Evaluation of 3D effects from 3D CFD computations."
IEA Joint action, aerodynamics of wind turbines, 14th Symp, 2000
[54] Bermudez, Velaquez & Matesanz, "Viscous-inviscid method for the simulation of turbulent unsteady wind turbine airflow", J. Wind Eng. & Industrial Aerodynamics, 90 (2002) 643-661
[55] Tangler, J.L. "The nebulous art of using wind tunnel aerofoil data for predicting rotor performance"

Wind Energy, 2002; 5: 245-257
[56] Leishman, "Challenges in modelling the unsteady aerodynamics of wind turbines"
21st ASME Wind Energy Symp. and 40th AIAA Aerospace Sciences Meeting, Reno
AIAA paper 2002-0037
[57] Tonio Sant ,'Improving BEM based aerodynamic models in WT design codes', 2007, U. Delft
[58] Batten, Bahaj, Molland, Chaplin "The prediction of the hydrodynamic performance of marine current turbines"
Renewable Energy, 33 (2008), 1085 - 1096
[59] Clarke, Conner, Grant and Johnstone, 'Design and testing of a contr-rotating tidal current turbine' Proc. Institute of Mechanical Engineers Part A: Journal of Power and Energy, 2007, pp171-179
[60] Batten, Bahaj, Molland, Chaplin, "The prediction of the hydrodynamic performance of marine current turbines"
Renewable Energy, 33 (2008), 1085 - 1096
[61] Hansen, M.O.L "Aerodynamics of wind turbines" Chapter 6
2nd Ed, Earthscan, 2008
[62] Hansen, M.O.L "Aerodynamics of wind turbines" Chapter 6
2nd Ed, Earthscan, 2008
[63] Sorenson, Shen, Munduate "Analysis of the wake states by a full field actuator disc model"
Wind Energy, Vol. 1, 1998, pp73-88
[64] Hansen, M.O.L "Aerodynamics of wind turbines" Chapter 6
2nd Ed, Earthscan, 2008
[65] Sorenson, Shen, Munduate "Analysis of the wake states by a full field actuator disc model"
Wind Energy, Vol. 1, 1998, pp73-88
[66] Sorenson, Shen, Munduate "Analysis of the wake states by a full field actuator disc model"
Wind Energy, Vol. 1, 1998, pp73-88
[67] Glauert "Airplane propellers" in W. F. Durant
Aerodynamic Theory, 4, Division L, Dover, NY, 1963
[68] Burton, Sharpe, Jenkins & Bossanyi "Wind Energy Handbook", Chapter 3
John Wiley & Sons Ltd, 2001
[69] Burton, Sharpe, Jenkins & Bossanyi "Wind Energy Handbook", Chapter 3
John Wiley & Sons Ltd, 2001
[70] Himmelskamp "Profile investigations on a rotating airscrew", MAP Volkenrode Report, Translation No. 832, 1947
[71] Dwyer & McCroskey "Crossflow and unsteady boundary layer effects on rotating blades", AIAA Journal, 1971, 8, 1498-1505
[72] Milborrow "Changes in aerofoil characteristics due to radial flow on rotating blades", Proc. 7th BWEA Conf., Oxford, 1985
[73] Ronsten "Static pressure measurements on a rotating and non-rotating 2.375m wind turbine blade – Comparison with 2d data", J. Wind Eng. and Ind. Aerodynamics, 1992, 39, 105-118
[74] Simms, Schreck, Hand, Fingersh, "Navier-Stokes predictions of the NREL phase VI rotor in the NASA Ames 80ftx120ft wind tunnel", Wind Energy 2002, 5, 151-169
[75] Breton "Study of the stall delay phenomenon and of wind turbine blade dynamics using numerical approaches and the NREL's wind tunnel tests" PhD thesis, Norwegian University of Science and Technology, 2008
[76] Du & Selig "The effect of rotation on the boundary layer of a wind turbine blade", Renewable Energy 20, 2000, 167-181
[77] Tangler "An evaluation of an empirical model for stall delay due to rotation for horizontal wind turbines", Wind Power 97, NREL/CP – 440 - 23258
[78] Bak "3D corrections of airfoil characteristics based on pressure distributions" EWEC 2006, Greece, (Riso)
[79] Snel & Schepers "Engineering models for dynamic inflow phenomena"
J. Wind Engineering & Industrial Aerodynamics, 39 (1992) 267-281
[80] Wright and Cooper, "Introduction to aircraft aeroelasticity and loads", Wiley, 2007
[81] Leishman "Challenges in modelling the unsteady aerodynamics of wind turbines", AIAA 2002-0037, Proc. 21st ASME Wind Energy Symposium, 2002

[82] Pitt and Peters "Theoretical prediction of dynamic inflow derivatives", Vertica 5, 21-34 (1981)
[83] Dynamic stall and rotational augmentation in recent wind turbine aerodynamics experiments' Schreck and Robinson, Applied Research Division, NREL, AIAA 2002-2967
[84] Theodorsen 'General theory of aeroelastic instability and the mechanisms of flutter' NACA report 496, 1935
[85] Leishman & Crouse 'State-space model for unsteady airfoil behaviour and dynamic stall' AIAA, 1989
[86] Larsen, Nielsen & Krenk, "Dynamic stall model for wind turbine airfoils"
J. Fluids and Structures 23(2007), 959-982
[87] J. G. Leishman, "Challenges in modelling the unsteady aerodynamics of wind turbines"
21st ASME Wind Energy Symp., Reno, NV, 2002
[88] Fingersh et al, "Wind tunnel testing of NREL's unsteady aerodynamics experiment"
AIAA paper 2001-0035
[89] Leishman & Tyler, "An analysis of pitch and plunge effects on unsteady airfoil behaviour"
J. American Helicopter Society, Vol. 37, No. 3, 1992, pp 69-82
[90] J. G. Leishman, "Challenges in modelling the unsteady aerodynamics of wind turbines"
21st ASME Wind Energy Symp., Reno, NV, 2002
[91] Dewan 'Tackling Turbulent Flows' in Engineering', Springer, 2011
[92] Lesieur, 'Turbulence in Fluids', Springer, 2008
[93] Karlin, Ansumadi, Angelis, Ottinger, Succi, 'Entropic Lattice Boltzman Method for Large Scale Turbulence Simulation', J. Fluid Mechanics, 2003
[94] Pope, 'Turbulent Flows', Cambridge University Press, 2000
[95] Tennekes & Lumley "A first course in turbulence", The MIT Press
[96] Mycek, 'Experimental study of the turbulence intensity effects on marine current turbines behaviour: Part 1', Renewable Energy Vol. 66, pp729-746, 2014
[97] Thomson, Polagye, Durgesh, Richmond, 'Measurements of Turbulence at Two Tidal Energy Sites in Puget Sound, WA', IEEE J. Oceanic Engineering, Vol. 37, No. 3, 2012
[98] Osalusi, Side, Harris, "Structure of turbulent flow in EMEC's tidal energy test site", Int. Comm. Heat and Mass Transfer, 36 (2009) 422 - 431
[99] Osalusi, Side, Harris, "Structure of turbulent flow in EMEC's tidal energy test site", Int. Comm. Heat and Mass Transfer, 36 (2009) 422 - 431
[100] Simpson "Marine Turbulence: Theories, Observations and Models" Chapter 15, Cambridge University Press
[101] Lorke "Application of coherent ADCP for turbulence measurements in the bottom boundary layer" J. Atmospheric and Oceanic Technology, 2005, vol. 22, p1821
[102] Osalusi, Side, Harris "Reynolds stress and turbulence estimates in bottom boundary layer of Fall of Warness", Int. Comm. Heat and Mass Transfer, 36 (2009) 412 – 421
[103] Walter, 'Similarity scaling of turbulence spectra and cospectra in a shallow tidal flow', J. Geophysical Research: Oceans, 2011
[104] MacEnri, Reed, Thiringer, 'Influences of tidal parameters on Seagen flicker performance', Philos Trans A Maths Phys Eng Sci 2013
[105] I. Van der Hoven "Power spectrum of horizontal wind speed in the frequency range from 0.0007 to 900 cycles per hour" J. Meteorology, vol. 14, 1957
[106] Hau, 'Wind turbines: Fundamentals, Technologies, Applications, Economics', 2013, Springer
[107] Pedersen, 'Investigation and implementation of turbulent wind in a specialised software tool for offshore wind turbines', Thesis NTNU, 2014
[108] U. SOTON Oceanographic Grp, 2015, data set Fal Estuary
[109] A. Hussain "Coherent structures – reality and myth", 1981, Ann. Meet. Div. Fluid Dynamics of the American Physical Society
[110] Kelley, Jonkman, Scott, Redmond"The impact of coherent turbulence on wind turbine aeroelastic response and its simulation" NREL/CP – 500 – 38074, WindPower 2005
[111] Werne & Fritts "Stratified shear turbulence: Evolution and statistics", 1999, Geophys. Res. Lett. (26), pp439-442
[112] Jonkman, 'Turbsim User Manual', SNL, 2012
[113] *Harris,' Engineering Composite Materials', **1999***

[114] Kennedy, 'A preliminary design methodology for fatigue life prediction of polymer composites for tidal turbine blades', SAGE, 2012
[115] Kennedy, 'A preliminary design methodology for fatigue life prediction of polymer composites for tidal turbine blades', SAGE, 2012
[116] Gonabadi, Moharrani, Oila, Bull, 'Wet Flexural Fatigue Behaviour of Tidal Turbine Blade Composite Materials' 11th European Wave and Tidal Energy Conf, 2015
[117] Mandell, Sambursky, Agastra, 'Composite Materials Fatigue Issues in Wind Turbine Blade Construction', SAMPE 2008
[118] Maddox 'Fatigue strength of welded structures', Abington Publishing
[119] Waegter, 'Fatigue design based on S-N data', Denmark, 2009
[120] Almar-Naess et al 'Fatigue handbook – offshore structures, 1985
[121] Lars Damkilde University of Aalborg
[122] Harper & Hallet, 'Advanced numerical modelling techniques for the structural design of composite tidal turbine blades', Ocean Engineering, 2015, 96
[123] 'Marine Composites', Centro de Tecnologia Naval e Oceanica, University of Lisbon
[124] Kennedy, 'A preliminary design methodology for fatigue life prediction of polymer composites for tidal turbine blades', Proc. IMECHE Part L, 2012
[125] 'Marine Composites', Centro de Tecnologia Naval e Oceanica, University of Lisbon
[126] Boisseau, Davies, Thieboud, 'Fatigue behaviour of GFR composites for ocean energy conversion systems', Applied Composite Materials, 2013, 20(2)].
[127] Doremus, 'Static fatigue in Glass', Advances in Science and Technology of materials, Springer, 1974
[128] Renaud, 'Effect of glass fibres and environments on long term durability of GFRP composites, EFUC, Poland, 2005
[129] Li, 'Temperature and moisture effects on composite materials for wind turbine blades', 2000
[130] Davies, Germain, Gaurier, Perreaux, 'Evaluation of the durability of composite tidal turbine blades', Proc. Royal Soc. London, 2013, 371
[131] Price and Hull, 'Propagation of stress corrosion cracks in aligned glass fibre composite materials', J. Materials Sci, 1983, 18
[132] Wedel-Heinen, 'Optimat report OB_TG6_R002 rev 8, 2006
[133] Post, Cain, McDonald, Case, Lesko, 'Residual strength prediction of composite materials; Random spectrum loading', Engineering Fracture Mechanics, vol 75, 2008
[134] Antonio Visioli "Practical PID Control", Springer-Verlag, 2006
[135] Luyben 'Essentials of process control', McGraw Hill, 1997
[136] Bossanyi, "GH Tidal Bladed Theory Manual"
Document No. 282/BR/009, November 2008
[137] M.O.L. Hansen, "Aerodynamics of Wind Turbines", Chapter 6
2nd Ed., Earthscan, 2008
[138] Hansen, JN Sorensen, Voutsinas, N Sorensen, Madsen "State of the art in wind turbine aerodynamics and aeroelasticity", Progress in Aerospace Sciences 42 (2006), 285-330
[139] Hansen, JN Sorensen, Voutsinas, N Sorensen, Madsen l "State of the art in wind turbine aerodynamics and aeroelasticity", Progress in Aerospace Sciences 42 (2006), 285-330
[140] L.E. Myers & A.S. Bahaj, 'An experimental investigation simulating flow effects in first generation marine current energy converter arrays', Renewable Energy, Vol.37, Issue 1, 2012
[141] Pope "Turbulent Flows" Cambridge University Press, 2000
[142] Comparin, 'Modelling of Turbulent Effects on the Operation of Tidal Turbines', MSc Thesis, Cranfield, 2014
[143] McMurtry, 'Length and time scales in turbulent flow', U. Utah
[144] S. Buoso, 'Structural Investigation of a Tidal Turbine Composite Blade: Dynamic Analysis and Fatigue Assessment Employing a Mono-dimensional Approach, MSc Thesis, Cranfield University, 2012
[145] Buoso, 'Structural Investigation of a Tidal Turbine Composite Blade: Dynamic Analysis and Fatigue Assessment Employing a Mono-Dimensional Approach', MSc Thesis, Cranfield, 2012
[146] Astrom & Hagllund 'PID controllers; theory, design and tuning', 2nd ed. 1992

[147] Simms, Shreck, Hand, Fingersch, "NREL unsteady aerodynamics experiment in NASA Ames wind tunnel: A comparison of measurements to predictions", 2001, NREL
[148] Tangler & Kocurek "Wind turbine post stall airfoil performance characteristics for BEM methods" NREL
[149] Laino, Hansen & Minnema "Validation of the Aerodyn subroutines using the NREL unsteady aerodynamics experiment data" Wind Energy, 2002, 5:227-244
[150] Giguere & Selig "Design of a tapered and twisted blade for the NREL combined experiment rotor", April 1999, NREL/SR-500-26173
[151] Crawford "Advanced engineering models for wind turbines with application to the design of a coning rotor concept", PhD dissertation, University of Cambridge, 2006
[152] Bahaj, Batten, McCann, "Experimental verifications of numerical predictions for the hydrodynamic performance of the horizontal axis marine current turbine", Renewable Energy, 2007, 32 (2479-2490)
[153] Barnsley & Wellicome "Wind tunnel investigation of stall aerodynamics for a 1m horizontal rotor", J. Wind Eng. Ind. Aerodyn, 1992, 39 (1-3)
[154] Snel & Schepers "Joint investigation of dynamic inflow effects and implementation of an engineering method", ECN-C-94-107, 1995
[155] Coleman, Fiengold, Stempin, "Evaluation of the induced velocity field of an idealised helicopter rotor", WRL-126, NACA, 1945
[156] Drees "A theory of airflow through rotors and its application to some helicopter problems", J. Helicopter Soc., Vol. 3, 1949
[157] Gaonker "The use of the actuator disc dynamic inflow for helicopter flap-lag stability", J. American Helicopter Soc., 1982/3
[158] Bacchetti, Germain, Maganga, Gaurier, Facq, Pinon, 'Characterisation des conditions generees au basin de Boulougne-sur-Mer', Oct 2010
[159] Freeman, Teixeira, Trarieux, Ayre, "Design of a gravity stabilised fixed pitch tidal turbine of 400kW" Proc. 8th European Wave & Tidal Energy Conf., Sweden, 2009
[160] M Corsar, 'Design of a 12m diameter prototype rotor for the Deltastream tidal energy system', Internal report confidential to TEL, 2011

Appendix

7.1 Published Work

As a means disseminating the findings of this work a number of journal and conference papers will be published covering the key aspects of the research. Currently one paper has been presented at a conference which detailed the experimental campaign at IFREMER. Two other papers aim at publication in journals are under construction:

- M. Corsar, D. Mba, J.A. Teixiera, “Turbulent loads upon tidal turbines: Comparison between experiment and modelling predictions”, 1st AWTEC (Asian Wave and Tidal Energy Conference) Series, Nov. 2012

- M. Corsar, D. Mba, J.A. Teixiera, “Implementation of a novel variable speed control strategy for fixed pitch tidal turbines”, Submitted to IET Journal for Renewable Power Generation for editorial review, Dec. 2016

- M. Corsar, D. Mba, J.A. Teixiera, “Assessment of fatigue loads on tidal turbines operating in turbulent flow”, Work in progress.